UNIVERSITY OF SOUTHAMPTON

Aerodynamic Control of Bluff Body Noise

by

Matthew Spiteri

Thesis for the degree of Doctor of Philosophy

School of Engineering Sciences
Aerodynamics and Flight Mechanics Group

June 2010

UNIVERSITY OF SOUTHAMPTON

ABSTRACT

SCHOOL OF ENGINEERING SCIENCES
AERODYNAMICS AND FLIGHT MECHANICS GROUP

Doctor of Philosophy

Aerodynamic Control of Bluff Body Noise

by Matthew Spiteri

The main aim of this study was to investigate noise reduction techniques for bluff body noise. Three methods were investigated, using a splitter plate on a fairing-strut configuration, applying flow control to the surface of a fairing and fitting a splitter plate behind a isolated bluff body.

Aerodynamic tests were performed in wind tunnel facilities using particle image velocimetry (PIV), hotwire anemometry, pressure sensors and a force balance. Acoustic tests using a microphone array, on-surface microphones and freefield microphones were performed to investigate the noise generated by the models. The splitter plate fitted to the fairing-strut configuration was found to be dominated by large scale vortex shedding. The addition of the splitter plate blocked the interaction between the two opposing shear layers aft of the shell's trailing edge thereby reducing their interaction with the downstream strut. Broadband noise reductions were observed as well as reduction in the noise levels of the peaks associated with the shedding. Applying flow control showed noise reductions for both cases when suction and blowing were applied. These reductions were observed at the lower tested Reynolds numbers ($Re_{D_{shell}} = 1.75 \times 10^5$), at higher Reynolds numbers ($Re_{D_{shell}} = 3.5 \times 10^5$) the noise reductions decreased when compared to the baseline case. The splitter plate fitted behind an isolated bluff body modified the wake, decreasing shedding frequency and drag with an increase in the splitter plate length. Broadband noise reductions were observed with all three splitter plate lengths and the tonal peak of the vortex shedding noise was suppressed.

The study shed light on the possibility of achieving noise reductions using the three methods. However more research is required to apply these findings on a landing gear.

Acknowledgements

I would like to firstly thank Prof. Xin Zhang for his supervision and his guidance throughout the course of the PhD. I am in indebted to him for giving me this opportunity and for the encouragement and motivation he gave me when it was needed most.

I thank Airbus for their financial support and also Dr. Chow for his advice and suggestions.

Thank you to my friends and colleagues, Koen B, Dave, Ed, Sammie, Ben, Koen VM, Max, Kon, Cindy, Yong, Xun and Yuichi for their help, discussions and for making my time in Southampton memorable.

A special thanks to Prof. Goodyer for his assistance.

Thank you to the windtunnel technician staff, especially Mike Tudor-Pole. A special mention for Dr. Charlie William, may he rest in peace.

I would like to dedicate this work to my parents and my brothers, one big family who is always there for each other.

Finally, I also dedicate this work to Lexi for all the love and happiness she brings into my life.

Table of Contents

List of Figures

List of Tables

Nomenclature

All units are in SI

a_0	=	Speed of sound, m/s
C_μ	=	Blowing and suction coefficient
C_{DES}	=	Constant in DES model
C_D	=	Coefficient of drag
C_p	=	Coefficient of pressure
d	=	Distance, m
D_{shell}	=	Diameter of shell, m
D_{strut}	=	Diameter of strut, m
E	=	Total energy, J/kg
e	=	Internal specific energy, J/Kg
f	=	Frequency, Hz
f_{sample}	=	Sampling frequency, Hz
L	=	Length of splitter plate, m
l	=	Length scale, m
L_{model}	=	Length of model, m
M	=	Mach number
n	=	Block size
p	=	Static pressure, kg/ms^2

p_{ref}	=	Reference pressure, kg/ms^2
Pr	=	Prandtl number
Pr_t	=	Turbulent Prandtl number
Q	=	Volume flow rate, m^3/s
q	=	Dynamic pressure, kg/ms^2
Q_m	=	Mass flow rate, Kg/s
R	=	Riemann invariant, m/s
Re	=	Reynolds number
S	=	Surface area, m^2
S_E	=	Plenum exit area, m^2
S_W	=	Total plenum wall area, m^2
S_{ij}	=	Strain rate tensor, $1/s$
Str	=	Strouhal number
T	=	Period, s
t	=	Time, s
t_f	=	Trailing edge thickness, m
t_p	=	Pitch of the perforates, m
t_D	=	Non dimensional time
T_{ij}	=	Lighthill stress tensor, kg/ms^2
TL	=	Transmission loss in plenum chamber
Tu	=	Turbulence intensity, %
U	=	Velocity magnitude, m/s
u'_{RMS}	=	RMS value of velocity fluctuations in x-direction, m/s
u'_t	=	Average of RMS of velocity fluctuations, m/s
u_i	=	Velocity tensor, m/s

U_∞	=	Freestream velocity, m/s
u_t	=	Time averaged velocity magnitude, m/s
V	=	Integration volume, m^3
V'	=	Velocity of the acoustic source, m/s
v'_{RMS}	=	RMS value of velocity fluctuations in y-direction, m/s
W	=	Width and height of H-beam, m
x_i	=	Cartesian tensor, m
x_c	=	Distance between the shell and the strut, m
y^+	=	Non dimensional wall distance

Greek Symbols

Δf	=	Frequency resolution
$\Delta x, \Delta y, \Delta z$	=	Cell dimensions in x, y and z directions, m
δ_{ij}	=	Dirac delta function
Γ	=	Non-dimensional suction rate (-ve) and blowing rate (+ve)
γ	=	Ratio of specific heats
μ	=	Dynamic viscosity, kg/ms
μ_t	=	Turbulent viscosity, Ns/m^2
ν	=	Kinematic viscosity, m^2/s
ν_t	=	Eddy viscosity, m^2/s
Ω_{ij}	=	Vorticity tensor, $1/s$
ρ	=	Density, kg/m^3
σ	=	Porosity of the perforates, %
τ^*	=	Retarded time, s
τ_{ij}	=	Stress Tensor, kg/ms^2
θ	=	Polar angle from model leading edge, $^\circ$

$\tilde{\nu}$	=	Modified eddy viscosity, m^2/s
ζ	=	Lagrangian coordinate

Glossary

$NoSplt$	:	Model without splitter plate
$Perf$	:	Model fitted with perforated plate
SA	:	Spalart-Allmaras
$Sint$	:	Model fitted with sintered metal plate
$Splt$	:	Model fitted with splitter plate
SST	:	Shear Stress Transport
CAA	:	Computational Aeroacoustics
CFD	:	Computational Fluid Dynamics
DES	:	Detached Eddy Simulation
DNS	:	Direct Numerical Simulation
DPIV	:	Digital Particle Image Velocimetry
EPNL	:	Effective Perceived Noise Level
FFT	:	Fast Fourier Transform
FW-H	:	Ffowcs Williams-Hawkings
LES	:	Large Eddy Simulation
OASPL	:	Overall Sound Pressure Level
PIV	:	Particle Image Velocimetry
PSD	:	Power Spectral Density
RANS	:	Reynolds Averaged Navier-Stokes
RMS	:	Root Mean Square
SPL	:	Sound Pressure Level
URANS	:	Unsteady Reynolds Averaged Navier-Stokes

Chapter 1

Introduction

1.1 Background and Aim

Over the last few decades air travel has increased considerably giving importance to the noise pollution produced by aircraft in the vicinity of airports. This has led to increasingly stringent environmental standards pushing the aircraft industry to research ways to lower the noise emission on current and future aircraft. Noise generated by civil aircraft consists of engine and airframe noise [4]. A number of studies have been conducted to reduce the engine noise as it is a prominent noise source. This led to a number of development. Jet noise has been reduced by $15 - 20$ dB and as a consequence the average effective perceived noise level (EPNL) for large commercial aircraft has been reduced from approximately 110 to 90 EPNdB [5]. Modern commercial aircraft now possess high bypass ratio engines and nacelles with large diameters while still necessitating engine-to-ground clearance leading to longer landing gear [6]. It is generally accepted that further engine noise reduction must be coupled with airframe noise reduction to have an acceptable impact on the overall aircraft noise signature.

Flow around bluff bodies generates noise, which is detrimental in particular to aerodynamic applications where low noise emission is a design/regulatory requirement. Airframe noise is a problem mainly during the approach-to-landing phase when the engines are operating at low thrust. During this phase, the slats and flaps, high lift devices, are fully extended and the landing gears are deployed. This configuration gives rise to an unsteady flow field which leads to higher levels of noise. Landing gears on commercial aircraft have been identified as a major noise contributor during approach and landing [7, 8]. The design of a landing gear is

solely based on the fulfilment of its structural and dynamic function. The stringent mechanical criteria make it extremely difficult to consider noise requirements.

Landing gear fairings have been studied as a way to reduce the noise produced by landing gears [9]. The fairing shields components such as cavities, hose dressings and other protrusions from high speed flow, in turn the fairing will generate its own self noise as well as deflect high speed flow onto other components. A variation on solid fairings is perforated fairings, allowing air to be bled through the fairings redistributing the airflow around the fairing. Flight tests using perforated fairings have shown to decrease noise [9, 10]. This observation has been confirmed in wind tunnel tests [11].

From the initial few paragraphs of this introductory chapter the reader would be right to think that this investigation will focus on reducing the noise generated by aircraft landing gears but at the same time pondering why the title of the thesis makes no mention of landing gears. In order to clarify this it is necessary to give a brief account of how the PhD work started, progressed and developed into the work presented in the following chapters. Airbus, the sponsors of the PhD, conducted tests which showed that fairings applied to the landing gear reduced the noise of the aircraft during the approach phase, however, one main drawback of fairings is that due to their geometry they accelerate the flow and deflect it on other downstream components of the landing gear, hence reducing or cancelling out any noise reduction gains. Having tried to investigate using perforated fairings to bleed air through the fairing and reduce the velocity of the deflected flow, Airbus asked the University of Southampton to investigate perforated fairings in order to understand the physics involved. In addition, the University of Southampton was also asked to investigate applying suction or blowing to the surface of the fairing in order to control the deflected flow and hence improve the its performance. The objective and starting point of this PhD was the latter. The plan was to perform the initial tests on a simple model in order to investigate the effects of suction and blowing on the surface of the fairing to allow the physics to be understood better. The next step would have been applying the technology on a fairing fitted to a landing gear.

The aerodynamic and acoustic tests where progressing smoothly even though the noise reductions being measured where less then hoped for. During one of the tests, the measurements using on-surface microphones were being performed to try to identify the noise sources on the model. In an attempt to determine the noise generated in the fairing-strut cavity a piece of open cell foam was placed inside the

cavity. The results of this experimental run showed a sudden reduction in the noise levels, reductions which warranted attention. Further reductions were obtained when the open cell foam was replaced with a solid plate. At this point a decision was taken, together with Airbus, to change the main focus of the PhD and instead focus on the splitter plate technology investigating parameters such as separation distance and the size of the fairing with respect to the strut. Unfortunately this meant there was not enough time to test the splitter plate on a landing gear, however, the parameters being investigated on the simplified model were chosen keeping in mind their applicability to landing gears. The noise reductions were encouraging, which raised the question whether the splitter plate would still be effective even without the fairing. The effects of splitter plates placed behind bluff bodies were well known, however, not on the effect it has on the generation of sound, especially at the Reynolds number of interest. This lead to the testing of this configuration.

The scope of the thesis changed throughout its execution, however, its progression resulted in three different technologies which had the potential to reduce the noise generated by landing gears or at least the reduction of noise generated by bluff bodies.

1.2 Structure of Thesis

Chapter 2 reviews previous work in the field. This chapter includes a general explanation of aerodynamic noise generation, experimental and computational techniques, an overview of cylinder flow and relevant studies on landing gears. A research methodology inspired by literature is outlined in chapter 3. The wind-tunnel models, test setups and measuring techniques are also discussed in this chapter.

Chapters 4 to 6 discuss the experimental results of the various configurations. The fairing-strut using the splitter plate will be discussed in chapter 4 to be followed by the results of the fairing-strut configuration using suction and blowing. The results of the H-beam fitted with a splitter plate are discussed in chapter 6.

Conclusions and recommendations as well as proposals for future work are presented in chapter 7.

Appendix A describes the computational methodology including grid generation boundary conditions which were used for the DES results used in chapter 4.

Chapter 2

A Review of Previous Work

2.1 Introduction

A number of theories have been developed to deal with the generation of sound by flow and these are briefly presented in section 2.2. This background theory has helped experimental and prediction techniques to be developed to effectively understand the various noise mechanisms as well as the sources of noise on landing gears. Sections 2.3 to 2.5 explain the main aspects of these techniques to give a clearer idea of what is required in the development of methods to reduce noise. A clear understanding of the effects suction and blowing have on the fairing is needed. To do this effectively a very simple geometry (e.g. cylinder) is needed that reduces the number of parameters that could have an effect on the generation of sound. A simplified case consisting of a cylinder shielded by a half cylindrical shell is being proposed in order to investigate the effect of suction and blowing which requires some knowledge of the different flow regimes attributed to flow over cylinders. Section 2.6 gives a brief aerodynamic overview of the flow past cylinders and methods with which vortex shedding could be controlled.

2.2 General Theory of Aerodynamic Noise Generation

An introduction to the basics of sound generated by aerodynamic flow is given in this section. Lighthill [12] initially derived a theory that predicts the generation of sound in unbounded flows (Section 2.2.1). Curle [13] extended Lighthill's theory

to incorporate the presence of boundaries in the flow region (Section 2.2.2). These two theories are still not sufficient to predict noise of moving bodies. Ffowcs Williams and Hawkings [14] developed a theory that incorporates the effect of the motion of bodies on the generation of sound (Section 2.2.3).

2.2.1 Lighthill: unbounded flows

A theory of sound generated aerodynamically, simply as a byproduct of an airflow was developed by Lighthill [12]. The method adopted was to firstly estimate the details of the flow (density, velocity, pressure) and secondly to deduce the sound field which avoids the effects of the back-reaction of the sound produced by the flow field itself. It is argued that the sound produced is so weak in comparison to the motion producing it that no significant back-reactions can be expected. In this way quantitative estimates may be obtained only for sound radiated into free space, hence neglecting effects of reflection, diffraction, absorption or scattering by solid boundaries, hence unbounded flows.

In order to find the sound produced by unbounded flows, a fluctuating fluid flow is assumed to occupy a small fraction of a very large volume of fluid where the remainder of the fluid is at rest. The exact equations of motion which govern the fluctuations in the real fluid are compared to the equations of a uniform acoustic medium at rest which correspond to the wave propagation area. The difference between these set of equations would be the effect of the fluctuating external force field acting on the uniform acoustic medium at rest and hence radiating sound.

The exact equations of motion of a fluid ignoring external forces in tensor notation are given by:

$$\frac{\partial \rho}{\partial t} + \frac{\partial}{\partial x_i}(\rho u_i) = 0, \tag{2.1}$$

$$\frac{\partial}{\partial t}(\rho u_i) + \frac{\partial}{\partial x_j}(\rho u_i u_j + \tau_{ij}) = 0, \tag{2.2}$$

where x_i represent the Cartesian coordinates, ρ the density, u_i the flow velocity and τ_{ij} is the stress tensor given by equation (2.3)

$$\tau_{ij} = p\delta_{ij} + \mu\left[-\frac{\partial u_i}{\partial x_j} - \frac{\partial u_j}{\partial x_i} + \frac{2}{3}\left(\frac{\partial u_k}{\partial x_k}\right)\delta_{ij}\right], \tag{2.3}$$

where p is the pressure, μ is the coefficient of dynamic viscosity and δ_{ij} is the Kronecker delta function.

Now considering the governing equations of the propagation of sound in a uniform medium without sources or external forces, we have,

$$\frac{\partial \rho}{\partial t} + \frac{\partial}{\partial x_i}(\rho u_i) = 0, \tag{2.4}$$

$$\frac{\partial}{\partial t}(\rho u_i) + {a_0}^2 \frac{\partial \rho}{\partial x_i} = 0, \tag{2.5}$$

where a_0 is the speed of sound in the uniform medium. The linearised inviscid wave equation (2.6) is obtained by taking the time derivative of (2.4) and subtracting it from the spatial derivative of (2.5)

$$\frac{\partial^2 \rho}{\partial t^2} - {a_0}^2 \nabla^2 \rho = 0, \tag{2.6}$$

where ∇ is the gradient operator.

The equations of an arbitrary fluid motion can now be rewritten to incorporate the propagation of sound in a uniform medium at rest. Equation (2.2) may be expressed in a similar form as equation (2.5) to give rise to equation (2.8), whilst equation (2.9) is obtained in the same way equation (2.6) was derived.

$$\frac{\partial \rho}{\partial t} + \frac{\partial}{\partial x_i}(\rho u_i) = 0, \tag{2.7}$$

$$\frac{\partial}{\partial t}(\rho u_i) + {a_0}^2 \frac{\partial \rho}{\partial x_i} = -\frac{\partial T_{ij}}{\partial x_j}, \tag{2.8}$$

$$\frac{\partial^2 \rho}{\partial t^2} - {a_0}^2 \nabla^2 \rho = \frac{\partial^2 T_{ij}}{\partial x_i \partial x_j}, \tag{2.9}$$

where T_{ij} is the instantaneous applied stress or Lighthill stress tensor

$$T_{ij} = \rho u_i u_j + \tau_{ij} - {a_0}^2 \rho \delta_{ij}. \tag{2.10}$$

In the medium outside the flow itself the stress system equation (2.10) may be neglected meaning that equation (2.9) is the same as equation (2.6). This occurs as the velocity u_i relates to the small motions of sound propagation and as it also appears in a quadratic form in equation (2.10) it can be neglected. The viscous stresses in τ_{ij} and the conduction of heat constitute small effects and therefore can

also be neglected.

The instantaneous applied stress T_{ij} may be simplified further for most flows if the viscous stresses are assumed to be negligible when compared to $\rho u_i u_j$ and if at low Mach numbers the difference in temperature between the flow and the outside air is simply due to kinetic heating or cooling. Therefore using these assumptions T_{ij} may be approximated to:

$$T_{ij} = \rho u_i u_j. \tag{2.11}$$

Using Green's functions, the acoustic perturbation at position $\mathbf{x}$ for the field of a concentrated quadrupole at position $\mathbf{y}$ with tensor strength density T_{ij} can be written as:

$$\rho - \rho_0 = \frac{1}{4\pi {a_0}^2} \frac{\partial^2}{\partial x_i \partial x_j} \int_V T_{ij} \left(\mathbf{y}, t - \frac{|\mathbf{x} - \mathbf{y}|}{a_0} \right) \frac{d\mathbf{y}}{|\mathbf{x} - \mathbf{y}|}. \tag{2.12}$$

When differentiating the integrand in equation 2.12 with respect to x_i for large distances $|x|$, the spatial derivative of the term inversely proportional to $|\mathbf{x} - \mathbf{y}|$ can be neglected.

To determine how the sound produced varies with the flow constants one may assume that the frequencies are proportional to U/l. Using this assumption the fluctuations in $\frac{\partial^2 T_{ij}}{\partial t^2}$ are roughly proportional to $(U/l)^2 \rho_0 U^2$ and the density variations in equation (2.12) are proportional to the product

$$(\rho - \rho_0) \propto \frac{1}{{a_0}^2} \frac{1}{x} \frac{1}{{a_0}^2} \left(\frac{U}{l} \right)^2 \rho_0 U^2 l^3 = \rho_0 \left(\frac{U}{a_0} \right)^4 \frac{l}{x}, \tag{2.13}$$

where l is a length scale and U is a velocity scale.

The intensity of sound at a point where the density is ρ is ${a_0}^3/\rho_0$ times $(\rho - \rho_0)^2$. Therefore the intensity may be written as:

$$I(\mathbf{x}) = \frac{{a_0}^3}{\rho_0} (\rho - \rho_0)^2 . \tag{2.14}$$

Thus the quadrupole sound intensity is seen to increase to the 8^{th} power of the flow velocity U as shown in equation (2.15)

$$(\rho - \rho_0)^2 \propto \rho_0^2 \left(\frac{U}{a_0}\right)^8 \left(\frac{l}{x}\right)^2. \tag{2.15}$$

2.2.2 Curle: effect of solid boundaries

Lighthill [12] pointed out that solid boundaries may play an important role in sound generation such as in the case of fluctuating lift on a rigid circular cylinder. Curle [13] extended Lighthill's theory to take account of the presence of solid boundaries. Physically the solid boundaries will have an effect on the sound generated as the quadrupole noise will be reflected and diffracted by the solid boundaries. Moreover the quadrupoles will not be distributed over the entire space, instead they will be distributed only in regions external to the solid boundaries. Due to the interaction of the forces present between the fluid and the solid boundaries, dipoles are likely to be present as they correspond to externally applied forces. Curle modified equation (2.12) derived by Lighthill and added a surface integral over all the solid boundaries equation (2.16). The addition of the surface integral accounts for the impact of sound waves from the quadrupoles on the solid surface and for the hydrodynamic flow itself.

$$\rho - \rho_0 = \frac{1}{4\pi {a_0}^2} \frac{\partial^2}{\partial x_i \partial x_j} \int_V T_{ij} \left(\mathbf{y}, t - \frac{|\mathbf{x}-\mathbf{y}|}{a_0}\right) \frac{d\mathbf{y}}{|\mathbf{x}-\mathbf{y}|} + \frac{1}{4\pi {a_0}^2} \frac{\partial}{\partial x_i} \int_S P_i \left(\mathbf{y}, t - \frac{|\mathbf{x}-\mathbf{y}|}{a_0}\right) \frac{dS(\mathbf{y})}{|\mathbf{x}-\mathbf{y}|}, \tag{2.16}$$

$$P_i = -l_j \tau_{ij}. \tag{2.17}$$

where P_i is the strength of the dipoles per unit area, S represents the surface of the solid boundary, l_j is the direction of the outward normal (towards the fluid) on the surface.

Similar to the way Lighthill simplified the volume integral at large distances from the flow the surface integral introduced in equation (2.16) may also be simplified to give the density fluctuations due to the dipole term.

$$(\rho - \rho_0)^2 \propto \rho_0^2 \left(\frac{U}{a_0}\right)^6 \left(\frac{l}{x}\right)^2. \tag{2.18}$$

This illustrates that the sound field generated by the dipole term is larger then that generated from the quadrupoles at low Mach numbers.

2.2.3 Ffowcs Williams - Hawkings: effect of source motion

An extension to Lighthill-Curle's theory was presented by Ffowcs Williams and Hawkings [14] to include the arbitrary convective motion. The FW-H equation is a rearrangement of the Navier-Stokes equations and is appropriate for computing the acoustic field when solid boundaries play a direct role in the generation of sound. The forward motion of a source influences the radiation pattern of the sound and must be accounted for as this would change what a distant observer will perceive.

The FW-H equation deals with the motion of a surface by employing a Lagrangian coordinate ζ to the stationary surface.

$$\zeta = \mathbf{y} - \mathbf{V'}t, \tag{2.19}$$

where **V'** is the velocity of the source.

$$\begin{aligned}\rho - \rho_0 = \frac{1}{4\pi {a_0}^2}\frac{\partial}{\partial t}\int_S n_i \left[\frac{\rho(u_i - V_i) + \rho_0 V_i}{r|1 - M_r|}\right]_{\tau^*} dS(\zeta) + \\ \frac{1}{4\pi {a_0}^2}\frac{\partial}{\partial x_i}\int_S n_j \left[\frac{\rho u_i(u_j - V_j) - \tau_{ij}}{r|1 - M_r|}\right]_{\tau^*} dS(\zeta) + \\ \frac{1}{4\pi {a_0}^2}\frac{\partial^2}{\partial x_i \partial x_j}\int_V \left[\frac{T_{ij}}{r|1 - M_r|}\right]_{\tau^*} dV(\zeta),\end{aligned} \tag{2.20}$$

where M_r is the projection of the local Mach number $M = V_i/a_0$, $r = |\mathbf{x} - \mathbf{y}(\zeta, \tau^*)|$ and the notation $[...]_{\tau^*}$ indicates the quantity enclosed within the brackets is to be evaluated at position ζ and a retarded time $\tau^* = t - |\mathbf{x} - \mathbf{y}(\zeta, \tau^*)|/a_0$.

The solution is made up of two surface integrals which represent the contributions from monopole and dipole acoustic sources and partially from quadrupole sources and a volume integral represents sources in the region outside the source surface. The FW-H equation can be used both when the surface coincides with the solid boundaries and also when the surface is off the body and permeable.

2.3 Experimental Techniques for Aeroacoustics

Experimental methods used to investigate the flow and acoustic properties play an important role when simulating flows over complex geometries such as a land-

ing gear (figure 2.1). Wind tunnel and flyover testing are two main methods to experimentally test airframe noise.

2.3.1 Wind tunnel testing

A requirement of modern commercial aircraft is to have a high bypass ratio engine/nacelle diameter whilst maintaining engine to ground clearance which results in longer landing gears [6]. The increase in the length of the landing gear is a major contributing factor to today's landing gear noise, but it also poses another problem: wind tunnel testing. The size of a wind tunnel test section restricts the size of the model which makes most wind tunnels inadequate to accurately test scale model landing gears due to the insufficient geometrical detail they contain. Features such as hydraulic cables, dressings and bolts are responsible for high frequency noise. Dobrzynski *et al.* [7] concluded that in order to capture the true airframe noise of a landing gear full scale model testing was required. For this wind tunnels such as the German-Dutch Wind Tunnel are needed which can be operated in a free-jet configuration with a nozzle cross sectional area of $6 \times 8m^2$ and still allow the landing gear to be within the core of the flow.

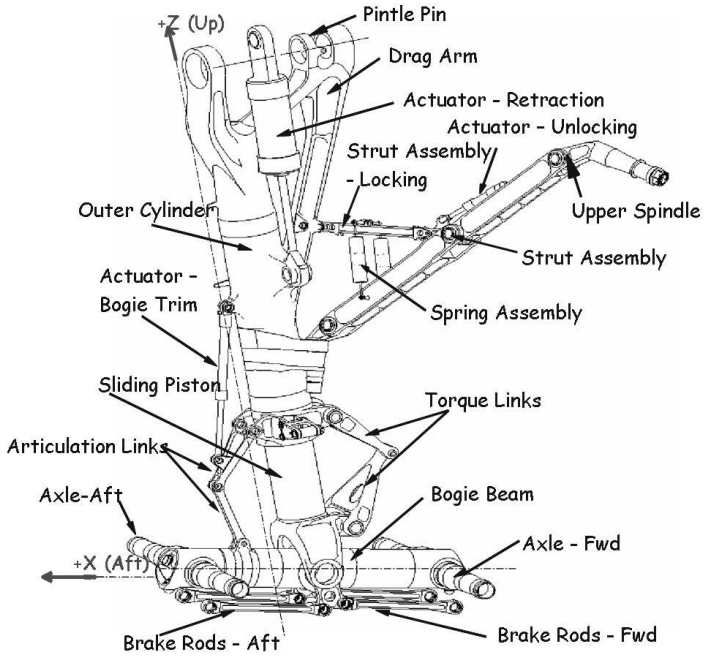

FIGURE 2.1: Schematic representation of a landing gear

2.3.1.1 Aerodynamic testing

Aeroacoustic noise is attributed to aerodynamic flow features such as vortex shedding. Previously, much work was done to demonstrate that frequencies in a fluid flow are equal to those of the noise generated [13]. Thus this underlying fact shows that appropriate flow measurement techniques are required to aid in understanding the noise generated by the flow. Measurement techniques such as hot wire anemometry and pitot-static measurements were used by Horne *et al.* [15] to investigate the wake behind a landing gear. They were able to map out the wake flow properties such as pressure, velocity and turbulence levels. Digital particle image velocimetry (DPIV) was used to capture an image of the mean flow field. Lazos [16] states that enough knowledge of the mean flow can be used to aid in the determination of noise sources.

2.3.1.2 Acoustic testing

Aeroacoustic testing of components using stationary facilities can be challenging. It would be ideal if full scale models could be tested at operating conditions to satisfy the Reynolds number criteria, and the only noise measured by the equipment is that of the model. This is not the case; stationary facilities generate their own sound which can be defined as background noise. Tonal noise is also a problem as was found in early stationary facility tests [1], in this case the tone was found to be independent of flow velocity and was associated with cavity resonance. Tests such as these were carried out in open section wind tunnels, with microphones placed around the model and outside the core flow.

When the data is acquired outside the core flow the sound pressure levels must be corrected for signal to noise ratio, for the effects of shear-layer refraction, for the effect of convective amplification and for atmospheric absorption.

As sound waves pass through a shear-layer (caused by the open-jet flow and the ambient air outside the test section) they exhibit a change in propagation direction and amplitude. A correction scheme from Amiet [17] was used and had been validated in full scale landing gear experiments [7].Correction of convective amplification accounts for the fact that the noise radiation of a stationary source is different to that in motion [18].

Anechoic test sections have been developed to reduce the effect of sound reflection and to reduce background noise. More accurate sound measuring techniques were

developed to measure and localise the sources of noise. An elliptical acoustic mirror microphone system was used by Grosche *et al.* [8] to measure the noise sources of a transport aircraft. The principle of such a system is to use a large elliptical mirror which focuses the sound onto a microphone in front of it. The mirror microphone unit can survey the sound sources by traversing the unit over the object being tested giving an image of the noise sources.

Another method to measure and localise noise sources is the use of a phased microphone array. This consists of a number of microphones at different planar (spiral, cross or grid although the former two options are preferred as fewer microphones are required) locations. Shifting the outputs of the microphones an amount equal to their propagation delay and then summing them together, an image of noise sources in a plane may be achieved [19]. Recent improvements to the microphone array has led to it being implemented in hard walled wind tunnels. The microphone array is recessed in a sidewall of the wind tunnel and is covered by a porous cloth. The cloth isolates the microphones from direct contact with the turbulent boundary layer which reduces background noise considerably [20]. Its implementation in hard walled wind tunnels creates the possibility for pressurised wind tunnels to be used to increase the Reynolds number of the flow [4].

2.3.2 Flyover measurements

Tests to determine the noise level of an aircraft are carried out by actually acquiring data from the ground whilst an aircraft is in landing approach. Flyover measurements have been developed to predict the noise levels of an aircraft by testing a scale model in a wind tunnel using a microphone array [7]. By using the farfield noise level directivity measured in the wind tunnel tests the Effective Perceived Noise Level (EPNL) can be determined. The EPNL is the metric for flyover noise certification which correlates highly with human response to environmental noise. However to do so, different transformations and level corrections must be done [21].

Correction of Flow Velocity: -

The flow velocity around the landing gears on aircraft is lower then that of the freestream velocity due to the circulation around the wings and fuselage. Previous studies [7, 22] have shown that the local velocity around a landing gear is about

78% of the flight speed for a typical landing configuration, which corresponds to a difference in noise of as much as $5.8dB$ according to the sixth power law [22]. Therefore corrections,depending on aircraft and the location of the landing gear, need to be made to the testing flow velocities in the wind tunnel to simulate the in flight flow velocities.

Correction for Convective Amplification: -

This effect is defined as the difference between sound propagation through a quiescent medium or a medium without zero mean flow or the difference between a stationary source and one in motion. Observed sound waves for an approaching source are compressed and expanded for a source moving away, resulting in a Doppler shift of the frequency. The well known Doppler formula can be employed to calculate the corrected frequency. Formulas for correcting the sound pressure, dependent on source type (monopole, dipole or quadrupole), are presented in [18].

Correction for Atmospheric Absorption: -

A method presented by Bass *et al.* [23] corrects for the effect of the atmospheric absorbtion of noise. As sound propagates through the atmosphere it is attenuated by the environmental conditions such as air temperature and humidity. This effect is dependent on the distance between the source and receiver.

2.4 Prediction Methods for Aeroacoustics

It is necessary to be able to predict the generation of noise early in the design stages as to minimise design modifications at later stages. This section deals with techniques to aid the prediction of noise generated by landing gears. Section 2.4.1 highlights empirical techniques that use simple analytic formulae. Computational techniques that include the use of numerical solvers for both aerodynamic and acoustic predictions are discussed in section 2.4.2.

2.4.1 Empirical methods

Prediction tools for landing gears have been developed to predict noise generation. Landing gear can be decomposed into three distinct component categories, the wheels, the main struts and the small features [24]. Each of these categories is responsible for different frequency domains. An early prediction model developed by Fink [25] was not capable of predicting the noise at high frequency as the test models considered to develop the prediction model only consisted of wheels and main struts. This lack of detail leads to an under-prediction of the EPNL of about 8dB.

Smith *et al.* [26, 27] developed a prediction model that uses a number of empirical constants to fit standard source characteristics to components such as struts, wheels and small features. The characteristic shape of each spectrum is a haystack with a peak centered at the natural vortex shedding frequency of the component. Using the basic scaling law based on Curle's equation [13] and a set of relationships for the different components the overall level of the landing gear noise during flyover could be determined. The prediction method was compared to wind tunnel tests of different landing gear configurations and was found to agree closely with the experimental measurements.

Since then more detailed models have been tested in wind tunnels leading to more accurate prediction models. Guo *et al.* [22] decomposed the noise spectrum into three frequency components, namely, low (wheels), mid (main struts) and high frequency components (small features). Using wind tunnel data from a full-scale landing gear it is shown that the low and mid frequencies scale well with the sixth power law using the flow Mach number, whilst the high frequencies scale with an eight power law (for overall sound level) which is typical of noise generated by turbulent flows. The sound pressure level for each frequency is estimated by addition of a frequency dependent function to the overall sound pressure level. The overall sound pressure level (OASPL) is denoted as a function of velocity, distance, a length scale (these vary according to the component), the number of struts and wheels and a complexity factor. It is argued that for the individual wheels and the struts (low and medium frequencies respectively) the noise can be determined from incoherent energy addition (the total noise is proportional to the number of gear components). On the other hand the addition of the high frequencies is considered to be impractical, thus a complexity factor is used to account for the high frequency noise generation. The complexity factor is also linked to measurable parameters in the aircraft design to allow noise prediction of

high frequencies feasible.

2.4.2 Computational techniques

Numerical investigations for low Reynolds numbers of roughly 200 have accurately predicted the Strouhal number and mean drag over a cylinder when compared to the existing experimental data [28, 29]. However at higher Reynolds numbers two-dimensional computations cannot accurately predict the drag and lift forces due to the increasingly dominant effect of three-dimensional flow fields [30, 31] although a two-dimensional setup would be possible to implement in a wind tunnel. Szepessy and Bearman [32] describe how the use of end plates on the edges of a circular cylinder can minimise the effect of three-dimensional flow in wind tunnel experiments.

Several computational methods are available to solve such flows, such as Direct Numerical Simulation (DNS), Large Eddy Simulation (LES) and Detached Eddy Simulation (DES). DNS does not use turbulence models but solves the time dependent Navier-Stokes equations and resolves all the relevant length scales of turbulence. Unfortunately this makes it too costly at relevant Reynolds numbers as very fine grids need to be used in order to capture the finest scales of motion. On the other hand LES is often computationally more cost effective than DNS. With LES, the large and medium eddies are captured whilst the small eddies, which are simpler, are modelled using a subgrid scale model [33]. The down side to LES is that it requires the eddies in the boundary layer to be resolved by the grid. This makes LES computationally prohibitive for most geometries when the boundary layers are turbulent [34]. A more interesting and cost effective approach is DES; this can be described as a hybrid using both large eddy simulation and Unsteady Reynolds Averaged Navier-Stokes [35]. The unsteady massively separated regions of the flow are treated using LES. Since the mechanisms of the flow such as vortex shedding involve length and time scales much larger than those of the boundary layer turbulence, the boundary layer modeling relies on the RANS equation without loss in the description [33]. The computational requirements for DES are similar to Unsteady RANS, but the accuracy of the complete flow field is potentially similar to LES. Reynolds-Averaging denotes averaging over a time interval which is very long relative to the maximum period of the turbulent velocity fluctuations, but shorter than the vortex shedding period [36]. Solving of Unsteady Reynolds Averaged Navier-Stokes (URANS) equations is a typical approach to simulating the unsteady flow around bluff bodies. The computing re-

quirements of this model are manageable up to high Reynolds numbers. It implies a separation of scales between coherent eddies, which will be resolved, and random eddies, which will be modeled [33]. Due to the Reynolds stresses that arise from the Reynolds averaging a turbulence model must be used. Shur *et al.* [37] state that modeling the flow over a cylinder with URANS results in a periodic unsteadiness and a two-dimensional solution with exaggerated vortex shedding rather then the more realistic chaotic three-dimensional unsteadiness. This behaviour is found also in the numerical investigation conducted by Mathelin *et al.* [38], who concluded that the Strouhal value is found to be much higher than that obtained in experiments and attribute this to the fact that three-dimensional modes present in experiments extract energy from the field, and lead to lower Reynolds stresses than in a purely two-dimensional configuration [30].

It is often not computationally feasible to resolve wave propagation from near-field sources to far field observers, so integral techniques such as the Ffowcs Williams-Hawking equation [14] are used to predict the acoustic signature at various locations using unsteady flow data from CFD calculations. The FW-H equation is an exact rearrangement of the Navier-Stokes equation that allows the prediction of acoustic signals at distant observer locations if the details of the source region are already known. For this reason the Navier-Stokes equations are still needed to solve the nonlinear and viscous effects [39].

Computational aeroacoustic studies of landing gears are computationally expensive due to the high resolution needed to accurately model the wave propagation through a computational domain. A typical minimum of 6 to 8 cells per wavelength are needed to resolve acoustic perturbations, increasing the spatial resolution needed due to smaller scales needed to solve the higher frequency pertubations. Lockard *et al.* [39] used a total of 13.3 million grid points for a simplified landing gear although the same author used half the number of grid points in a similar study [40]. Most of the time the major interest is in the far field noise rather than the near-field. It is necessary that the numerical scheme does not numerically disperse and dissipate the solution. Numerical dissipation will suppress the amplitude of acoustic fluctuations, while dispersion tends to spread out a local solution over a wider area. Low order interpolation schemes have a tendency to be highly dissipative and should therefore be avoided during aeroacoustic simulations [41]. High order numerical schemes are preferred to obtain the desired accuracy. Computational aeroacoustics (CAA) is computationally expensive. For landing gear applications, curved solid boundaries will result in highly stretched grid cells instead of uniform cells necessary for resolving isotropic wave propaga-

tion. Unstructured grids have an advantage over structured grids in terms of ease of production, however it is questionable if wave propagation is properly resolved along oblique cell boundaries.

Solid and permeable integration surfaces are two methods in which the noise is predicting using the FW-H equation. Souliez *et al.* [42] performed FW-H predictions of landing gear noise using the two methods and found solutions to vary in the near field but be nearly identical in the far field. Strong wakes passing through the permeable surfaces seem to contaminate the solution and therefore special care must be taken to position the permeable surface out of regions with strong vorticity.

2.5 A Review of Relevant Studies on Landing Gears

2.5.1 Noise sources

Several noise sources have been identified on a typical landing gear configuration. The wheels and struts are responsible for low frequency noise whilst the smaller details such as the hoses and dressings are responsible for the high frequency noise. This wide frequency spectrum makes testing of detailed scaled models important as the high frequencies are an important factor to the overall noise level as in shown [7].

Early experiments [1] performed on a simple landing gear scale model in an open-jet facility showed a haystack-shaped spectrum with a broad peak between a Strouhal number of 0.8 and 8 (based on the freestream velocity and wheel diameter). This peak depended on the dimension and configuration of the landing gear. A normalised spectrum is shown in figure 2.2 where in an attempt to identify the gear components that contribute substantially to the radiated noise, individual components were exposed to the flow. Although this was a coarse approach neglecting interaction effects the results nonetheless indicate which components are likely to be responsible for certain parts of the spectrum.

The noise generated by a landing gear is broadband in nature and normally does not exhibit any tonal noise. Some studies have shown tonal noise due to cavity resonance the causes of which are tube-type pins in various joints linking different

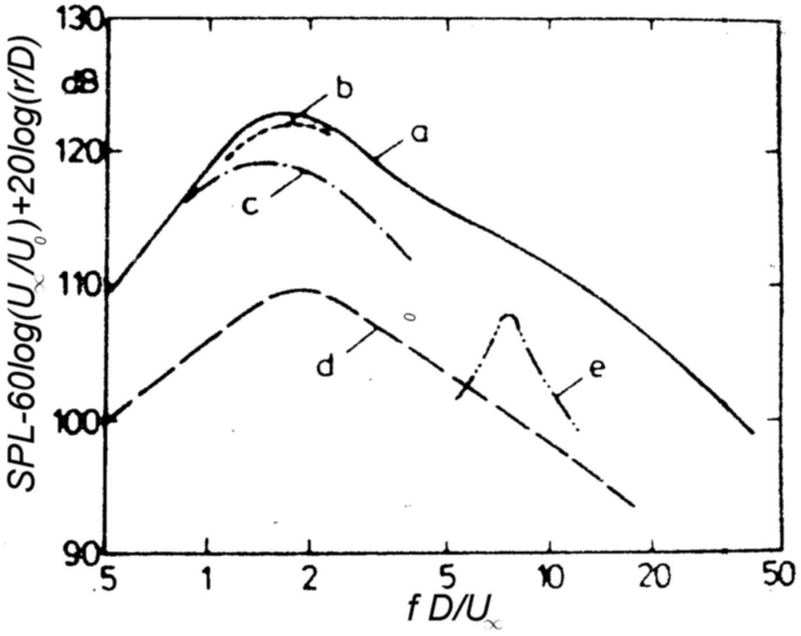

FIGURE 2.2: Normalised sideline spectra of nose gear model components a=complete configuration; b=side support struts; c=lower drag brace actuator; d=wheel; e=door ($U_\infty = 100\ m/s$.) [1]

gear components [43], as well as tyre treads [20]. Nonetheless it seems that this tonal noise is dependent on inflow velocity, turbulence and direction and so it is impossible to predict whether these will manifest themselves during the approach of an aircraft.

Flow interaction between different landing gear components can be a culprit in increasing the noise generated. The interaction between the wake produced by the upstream wheel when it collides with the wheel behind it seems to increase the noise directed towards the ground [16]. Dobrzynski *et al.* [44] conducted a study on the interaction of the flow between the nose landing gear and the main landing gear. The small changes to the nose landing gear configuration did not have much effect on the gear wake characteristics and no excess interaction noise that is of any practical relevance was detected.

2.5.1.1 Spectrum characteristics

Spectral data is often non-dimensionalised in order to compare data at different speeds and dimensions. This is done by converting frequency to a Strouhal number, hence normalising with freestream velocity and a characteristic length. To characterise the frequency domain, it is often decomposed into a low, mid and

high frequency range. There is no hard and fast rule to the limits of these ranges but for the purpose of this study low frequencies are below $f = 500\ Hz$, the mid frequency ranges lie between $f = 501\ Hz$ and $f = 5\ kHz$ and high frequencies are above $f = 5\ kHz$.

Scaling of the sound pressure level is achieved by adjusting the levels with a power scaling law. Scaling using a 6^{th} power of velocity was seen to collapse the data taken at different flow velocities [7]. This indicated the noise produced by the gear could have been associated with an acoustic dipole source (see equation (2.18)). However, it has been argued that for high frequency noise an estimate based on the quadrupole term is better suited to non-dimensionalise the spectra [22]. In the case of a non-compact surface, where the frequency is high or the body dimension is large, the surface contribution is comparable to that from turbulence quadrupoles for a non-compact body [45].

The above is valid for landing gears tested in isolation. The unsteady flow generated by the landing gear suffers interference with the airframe components when the landing gear is mounted to an aircraft. The noise is scattered at the doors in the vicinity of the undercarriage legs and wing trailing edge. Scaling with the 5^{th} power of velocity is deemed to be more appropriate for the landing gear configuration [46].

2.5.2 Noise directivity

Noise directivity is an important parameter as it illustrates the directional characteristics of a sound source. Typical nose landing gear configurations show a more pronounced directivity pattern than typical main landing gear configurations. The former radiates more noise to the side owing to its vertical orientation, whilst the main landing gear has a more uniformly distributed sound radiation with only a slight predominance to the side [1].

A study on a four-wheel bogie gear [7] revealed that at low Strouhal numbers the noise is almost omnidirectional whilst at higher Strouhal numbers a maximum is seen at the rear and forward arc. If the aerodynamic noise of the landing gear were dominated by large scale vortex shedding noise then it could be described by a simple dipole type source. Following this it is expected that the maximum noise levels should be perpendicular to the mean flow direction, which corresponds to a position under the gear. The measurements showed the opposite for the intermediate and high Strouhal numbers. As the scale of these Strouhal numbers

compares well with that of dressings which are responsible for high frequency noise it is thought that it is the local velocity which is responsible for this and not the freestream velocity. The fact that the local flow is oblique to the undisturbed inflow direction is one reason for this discrepancy, whilst another explanation is the interaction of turbulent wake flows with downstream gear components.

2.5.3 Noise reduction

Several methods to reduce noise generated by landing gears have been studied and tested. Dobrzynski *et al.* [47] presented several noise reduction improvements, they achieved this by installing fairings on the tow bar and axle, covering the steering column and the upper leg and applying a cap to the wheels and the steering actuator. The installation of these components showed a potential noise reduction of -2dB to -3dB (on the nose landing gear). The most effective devices for noise reduction were the fairing and the steering system cover giving a noise reduction of -2.7dB compared to the noise generated by the low noise configuration.

Most of the noise generated in the high frequency domain is caused by the small scale components, an effective way to reduce this is to cover most of these components behind a fairing. An unrealistic fairing setup showed a noise reduction potential of about 10dB but due to retractability of the landing gear makes this setup impossible to implement. A more realistic fairing setup showed a noise reduction potential of about 3dB [43].

The fairing can cause high speed flow to be deflected on to other components which are not covered by the fairing itself. As noise levels of landing gear components increase with the 6^{th} power of the locally incident flow velocity it is likely that the total power output of the landing gear is proportional to the spatially averaged 6^{th} power of flow velocity, $< U^6 >$ [27]. If the fairing covers a portion, p, of the landing gear components causing an increase in the flow over the remaining components by a factor, f, where $f =< U^6 >^{1/6} /U_0$ then the change in the sound power output of the gear is given by $\Delta dB = 10log_{10}(1-p)f^6$. Thus it is easy to see how the gain achieved by the fairing can easily be lost. Active flow control over the outer surface of the fairing will help in reducing the effect of the deflection of the flow.

2.6 A Review of the Aerodynamic Flow Around Cylinders

It is important to understand the direct implications and effects noise control devices have on the noise produced by flow around a landing gear configuration. It is clear that the flow around such intricate geometry is complex and too many design parameters exist to be able to pinpoint the direct effects of a control system such as suction and blowing around the fairing. The problem needs to be simplified to be able to understand the basic physics. The landing gear can be thought of as a series of cylinders, which is the reason for the proposed simplified model outlined in section 3.2. The aerodynamic flow around a circular cylinder must be considered as many flow regimes exist having different flow properties in terms of boundary layers, vortex shedding and resultant forces.

The main flow regimes are discussed in section 2.6.1 outlining the different types of flow at different Reynolds numbers whilst section 2.6.2 gives details of the effect the Reynolds number has on shedding frequency. Sections 2.6.3, 2.6.4 and 2.6.5 give examples of previous studies using different control methods in order to modify the vortex shedding frequency and the unsteady wake. It is important to note that some of these methods are conducted at lower Reynolds numbers than the ones of interest for this study. Nonetheless it is important to make note of these control methods as none of the cited authors ruled out the effectiveness of their methods at larger Reynolds numbers.

2.6.1 Flow regimes for a full cylinder in freestream

Flow around bluff bodies has been a subject of interest for many years and a vast amount of work has been done to fully understand the flow physics which in turn determines the aerodynamic performance of such bodies. Initial investigations were carried out by Vincenc Strouhal [48]and Theodore von Kármán [49] who first observed vortex shedding from a cylinder. Zdravkovich [50] presents a full and complete study investigating the related flow phenomena such as boundary layer separation, re-attachment, shear layers, vortex shedding just to mention a few. The canonical motion of the flow past a circular cylinder is relevant to numerous flows found in industrial applications (the flow past moving vehicles, aircraft components, buildings etc.).

For very low values of Re_d ($0 < Re_d < 4$) the flow is attached to the cylinder and

the streamlines are almost symmetrical around the cylinder. The velocity is so low that the inertia effects are extremely small. This regime of viscous flow is called Stokes flow. As Re_d is increased ($4 < Re_d < 40$) the flow separates at the back of the cylinder. This increase causes the formation of two stationary stable vortices (these remain behind the cylinder). Beyond the Re_d value of 40 the flow behind the cylinder becomes unstable. The two vortices that were behind the cylinder are shed alternately and flow downstream. The alternate shedding vortices form a Kármán vortex street. The Kármán vortex street starts to become turbulent at large Re_d numbers. The laminar boundary layer on the cylinder separates from the surface of the cylinder at nearly the top and bottom of the cylinder. This region corresponds to Re_d values of $1 \times 10^3 < Re_d < 3 \times 10^5$ and in this region the value of C_D is quasi constant. In the next regime the laminar boundary layer is still separated but now the free shear layer over the separated region transitions into a turbulent flow. This happens for Re_d numbers of $3 \times 10^5 < Re_d < 3 \times 10^6$. The flow now reattaches to the back face of the cylinder due to the turbulent nature of the flow, then separates again. The reattachment of the flow to the cylinder causes a thinner wake which in turn reduces the drag on the cylinder, this explains a sudden drop in C_D at the Re_d number of 300,000 (see figure2.3). At numbers larger then 3×10^6 the boundary layer turns fully turbulent and separates only towards the back of the cylinder. The turbulent boundary layer increases the skin friction which contributes to the increase again in C_D, but the biggest contribution comes from the fact that as the Re_d number increases further the separation point moves towards the top and bottom of the cylinder creating a fatter wake behind the cylinder which in turn increases C_D

2.6.2 Effect of Strouhal number with Reynolds number

The frequency with which the vortices are shed from the body can be made dimensionless with the flow velocity and the diameter of the circular body. This parameter depends only on the Reynolds number and is called the Strouhal number (2.21).

$$Str_d = \frac{fd}{U_\infty} \quad . \tag{2.21}$$

Applying blowing or suction may be interpreted as a decrease or increase, respectively, of an effective Reynolds number (related to an effective diameter). Fransson *et al.* [3] propose a relationship between the Strouhal number and the Reynolds

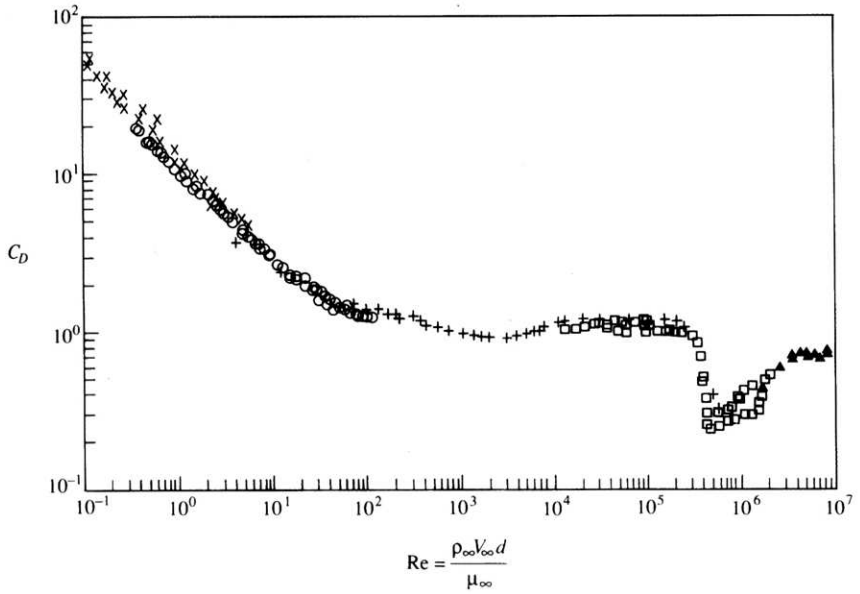

FIGURE 2.3: Variation of drag versus Reynolds number [2] .

Range of Reynolds Number	**Boundary Layer State**	**Details of the Flow**
$0 < Re_d < 4$	Laminar	Flow fully attached to the cylinder (Stokes flow)
$4 < Re_d < 40$	Laminar	Flow starts to separate from the back of the cylinder
$40 < Re_d < 1 \times 10^3$	Laminar	Flow behind the cylinder becomes unstable leading to the formation of the Karman vortex street.
$1 \times 10^3 < Re_d < 3 \times 10^5$	Laminar/Turbulent	The laminar boundary layer separates at the top and bottom of the cylinder resulting in a constant value of C_D
$3 \times 10^5 < Re_d < 3 \times 10^6$	Turbulent	The flow reattaches to the back of the cylinder which results in a sudden drop in C_D at Re_l of about 3×10^5
$Re_d > 3 \times 10^6$	Turbulent	The boundary layer becomes fully turbulent and C_D increases due to an increase in skin friction

TABLE 2.1: Summary of the flow regimes for a full cylinder in freestream

number, which is essentially a curve fit of huge amount of data collected from Norberg [51] and Zdravkovich [50]. They also formulated a relationship between the Strouhal number and a parameter Γ; this denotes a suction rate (negative value) or a blowing rate (positive value). Γ is defined as the ratio of the suction or blowing velocity and the freestream velocity. The plots for empirical equations derived for these relationships are shown in figures 2.4, 2.5 and 2.6.

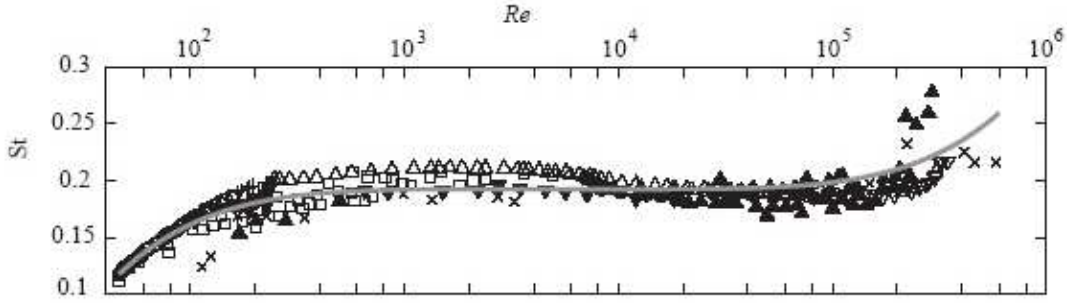

FIGURE 2.4: The effect of the Reynolds number on the Strouhal number [3] .

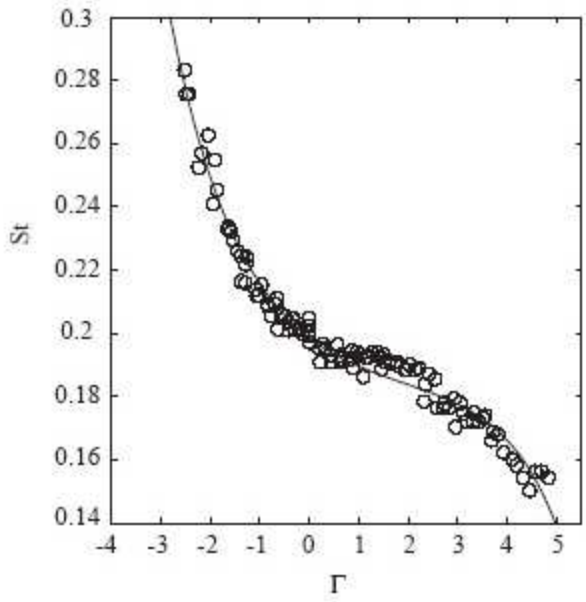

FIGURE 2.5: The effect of suction/blowing on the Strouhal number [3] .

2.6.3 Control of vortex shedding

A number of techniques have been developed to suppress vortex shedding or shift the shedding frequency at low Reynolds numbers (< 300). Berger [52] showed

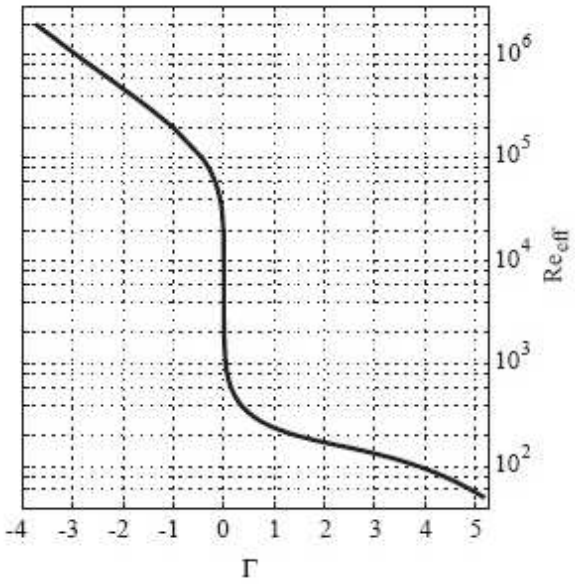

FIGURE 2.6: The effective Reynolds number vs. Γ [3] .

that one such method of control is to oscillate the cylinder in a rotary motion at a suitable frequency and amplitude. Homescu *et al.* [53] used optimal control to control the angular velocity of a rotating cylinder to suppress the Kármán vortex shedding in the wake. Wang *et al.* [54] as well as Masouka *et al.* [55] heated the cylinder which in turn changed the viscosity of the fluid close to the surface of the cylinder, thereby changing the effective Reynolds number. Another approach is to use feed back control, Roussopoulos [56] used a loudspeaker to acoustically induce actuation in a wind tunnel setup and also used a vibrating cylinder in a water channel. A numerical approach was investigated by Park *et al.* [57] where they utilized blowing and suction slots on the rear part of a cylinder. At larger Reynolds numbers different approaches to control the shedding could be attempted as cylinders with larger diameters may be used. Roshko [58] [59] modified the geometry of the cylinder setup in order to affect the vortex shedding. He achieved this by adding a splitter plate on the centerline just behind the cylinder demonstrating that with a suitable splitter plate length the flow behaviour can change from an alternating shedding mode to a symmetrical mode with two closed recirculation regions on either side of the plate. Takumaru and Dimotakis [60] performed experiments on a circular cylinder subjecting it to forced rotary oscillations. They showed a reduction in drag up to 80% at a Reynolds number of 15,000 for specific ranges of frequencies and amplitudes. These experiments have been confirmed by computational results, Shields and Leonard [61], and they also suggested that this kind of control could be even more efficient at higher Reynolds numbers. Plasma

actuation is a relatively new technology used to control the shedding frequency. Thomas *et al.* [62] conducted both aerodynamic and aeroacoustic experiments using plasma actuators around a circular cylinder at a Reynolds number of 33,000. An array of plasma actuators are capable of producing local tangential blowing on the surface of the cylinder, this has been shown to produce up to 90% drag reduction using steady blowing with two actuators on a cylinder in cross flow at a Reynolds number of 12,000 [63]. Both unsteady and steady actuation could be used showing that unsteady actuation is the most effective with total elimination of Karman shedding, a significant reduction in the turbulence levels in the wake and a reduction of 13.3dB in the near field sound pressure levels.

2.6.4 Porous surface using suction or blowing

A method which is more relevant to this study is to manipulate the flow by using suction or blowing through a porous surface as such a technology is easier to implement than some of the other methods mentioned previously. Pankhurst and Thwaites [64] carried out experiments on a porous cylinder using continuous suction as well as using suction together with a splitter plate positioned at different angles. They demonstrated that if the splitter plate is placed at an appropriate angle and if sufficient suction is applied, no separation occurs and the pressure distribution over the cylinder is extremely close to the potential flow solution. Further experiments were performed by Hurley and Thwaites [65] to investigate the boundary layer using the same setup. They found a good correlation with laminar boundary layer theory. Mathelin *et al.* [66] conducted experimental studies using continuous blowing through the entire surface of a circular cylinder. They used a cylinder with 30% porosity with an average pore diameter of $30\mu m$ achieved by using sintered stainless steel. They describe how blowing leads to the widening of the wake as well as a decrease in the Strouhal number. It is also shown and interesting to note for this study that the Strouhal number is linear with the blowing rate until saturation occurs. They also determined an analytical relation to provide an equivalent Reynolds number of the flow which has the same behaviour as the case with blowing. This is relevant as a flow submitted to blowing has the same characteristics in terms of instability as that of the flow at a lower Reynolds number. An alternative type of blowing was investigated by Glezer and Amitay [67]. They used synthetic jets at selected positions over the cylinder to provide a localised addition of momentum through the surface. This setup produced a delay in separation for both laminar and turbulent boundary layers. This

Method of Control	**Reynolds Number (Re_d)**	**Change in Drag Forces**	**Type of Approach**	**Author**
Oscillatory rotary motion of cylinder	77-300	N/A	Experimental	Berger [52]
Optimal control to control angular velocity of a rotating cylinder	60 - 1,000	-60%	Numerical	Homescu *et al.* [53]
Forced rotary oscillations to a circular cylinder	1.5×10^4	-80%	Experimental	Takumaru and Dimotakis [60]
Heating of cylinder to change the viscosity of the fluid	1×10^3	N/A	Experimental	Wang *et al.* [54]
Acoustic actuation using a loudspeaker close to cylinder	48 - 480	N/A	Experimental	Roussopoulos [56]
Blowing and suction slots on the rear part of the cylinder	100	N/A	Numerical	Park *et al.* [57]
Use of a splitter plate on the centerline behind the cylinder	1×10^4	-71%	Experimental	Roshko [58] [59]
Continuous blowing around a circular cylinder	3.9×10^3	$+37\%$	Numerical	Mathelin *et al.* [38]
Continuous blowing and suction around a circular cylinder	8.3×10^3	-70% (suction)	Experimental	Fransson *et al.* [3]
Plasma Actuators for Landing Gear Noise Control	8.3×10^3	-90% (Plasma Blowing)	Experimental	Thomas *et al.* [63]

TABLE 2.2: Summary of the various vortex shedding methods: $+ve$ values denote an increase in drag and $-ve$ values denote a decrease in drag.

delay in separation was attributed to the increased mixing in the boundary layer caused by the injection of the fluid.

Several studies have shown the effect of uniform suction and blowing over a circular cylinder. Fransson *et al.* [3] experimentally studied the flow around a circular cylinder for a Reynolds number of the order 10^4, where the boundary layer is still laminar. They show that strong enough suction moves the separation line to the rear part of the cylinder in a similar way as it does when the cylinder boundary layer becomes turbulent which in turn results in a narrower wake. This resulted in a reduction in C_D of up to 70% above a specific value of suction. They also showed that when blowing was applied the separation point moves to smaller angles and the drag is shown to increase linearly with an increase in the magnitude of blowing. They also show that the Strouhal number decreases with blowing whereas suction has the opposite effect. Mathelin *et al.* [38] performed a numerical study of blowing through the whole surface of a porous circular cylinder, showing a similar decrease in the vortex shedding frequency with an increase in the blowing as well as a strong increase in the pressure drag which leads to an increase in the overall drag. Both Fransson *et al.* [3] and Mathelin *et al.* [38] show that suction or blowing applied round the whole surface of a cylinder can effectively control the wake structure but this can prove to be difficult to put into practice in a majority of engineering applications. Suction and blowing through the surface of small bodies is difficult or even impossible to implement due to physical restrictions, an alternative solution is shrouding the small bodies with a larger bluff body, then using suction or blowing to control the wake emitted by the shrouding. This setup may have several engineering applications especially where the flow over small components or grouped components needs to be controlled, such as when a fairing is fitted in front of the landing gear components of a commercial aircraft in order to reduce the aero acoustic noise during takeoff and landing.

2.6.5 Splitter plates

Investigations by various authors have shown that the separation of flow from bluff bodies could be affected by placing a flat plate, splitter plate, behind the body along the center line parallel to the freestream flow. Roshko [59] modified the geometry of a cylinder setup by adding a splitter plate in its wake. The experiment was carried out at a Reynolds number of 1.45×10^4 at which a regular vortex street is shed from a stand alone circular cylinder. Roshko found that the vortex shedding otherwise present on a circular cylinder was suppressed with a

splitter plate length of $5D$. This also caused the pressure drag to be reduced by approximately 63%. A shorter splitter plate with a length of $1.14D$ did not suppress the vortex shedding, instead the splitter plate caused a reduction in the Strouhal number and an increase in the base pressure. Gerrard [68] focused on splitter lengths up to $2D$ measuring the frequency of the vortex shedding from a circular cylinder at a Reynolds number of 1.45×10^4. The shedding frequency decreased as the splitter length was increased to a length of $1D$ and then increased again as the splitter length was increased to $2D$. Apelt *et al.* [69] conducted further studies at Reynolds numbers from 1×10^4 to 5×10^4 investigating cylinders with splitter plates lengths of $5D - 7D$. They observed that, as described in Roshko's paper the vortex shedding was suppressed with splitter plates of lengths greater or equal to $5D$. They reported that the flow reattaches to the plate at approximately $5D$ downstream of the cylinder regardless of the splitter plate length with reversed flow upstream of the reattachment line. However they also report that a regular vortex street was observed at about $17D$ downstream from the cylinder. Experiments at Reynolds numbers from 10^6 to 10^7 were also conducted by Roshko [59] . The splitter plate length used was approximately $2.7D$. Roshko reported that the vortex shedding was suppressed although the decrease in the coefficient of drag was only 10%, much smaller than the reduction achieved at lower Reynolds Numbers.

Chapter 3

Research Methodology

This chapter discusses the methodology used in the research. Parameters that became apparent during the literature review are discussed to aid in formulating a research plan used in the investigation. The three models used during the research are discussed, highlighting their design and details of the experimental arraignments for the models are given.

3.1 Influential Parameters

The literature review highlighted a number of parameters that may have a influence on this present research. As discussed earlier this study focused on three different methods for landing gear noise reduction. Two of the methods focused on improving the performance of a fairing as a noise reducing device. The first was the use of a splitter plate in conjunction with the fairing and the second was the use of suction or blowing on the flow facing surface of the fairing. Before any of these technologies were investigated a number of parameters were chosen to investigate the performance of a fairing as a baseline configuration.

Fairings fitted to landing gears can be problematic due to the size and weight increase they incur. Also, landing gears have to be inspected and maintained regularly. Fairings tightly fitted to landing gear components make these operations labour intensive and time consuming. In light of these issues the fairing size and its distance from the components it was shielding were varied to determine the influence they have on the aerodynamics and acoustics of the set-up.

From literature the suction and blowing rates are seen to have an effect on the

effective Reynolds number hence influencing the separation points and the nature of the unsteady wake behind the bluff body. In addition to varying the flow rates the porous material used on the fairing was an important parameter which cannot be ignored. Flow through perforated material creates unwanted noise sources and thus needed to be considered as any noise reduction obtained using suction or blowing could have been eliminated by the introduction of this extra noise source.

As a natural progression from using splitter plates to reduce the fairing setup and the need to achieve noise reductions in the most compact way possible an alternative method was investigated which compromised using a splitter plate fitted behind a bluff body. Literature showed that the splitter plate length was a variable parameter which had an effect on the flow. The ratio of the splitter plate to a characteristic length of the bluff body was shown to affect the way in which the unsteady wake behaved [70]. Therefore, varying the splitter length aided in outlining guidelines for its implementation on a landing gear as it was desirable to have the smallest control device possible to achieve the best noise reductions.

3.2 Research Plan

The complex shape of a landing gear made the investigation of the physics of the flow using experimental and computational techniques diffcult. The literature review indicated that the computer resources needed to solve the flow and acoustics of a detailed landing gear were prohibitive. Moreover experimental techniques made the investigation of the flow field in enclosed areas (e.g. behind the fairing, between the torque link and the main strut) difficult. The interaction effects between the different landing gear components and a control device, such as a fairing, would have made distinguishing and interpreting the effect of such devices on the aeroacoustics complicated.

The first experiment proposed was to test a simplified fairing-strut configuration. This was done to simplify the geometry to remain true to a fairing which shields components, such as struts on a landing gear but to make the interrogation of the total field around the fairing-strut configuration possible. The fairing-strut configuration was used for both using a splitter plate with a fairing as well as using suction or blowing on the fairing. The low complexity of this configuration increased the signal to noise ratio between the various configurations and made it less costly to investigate the effect of fairing size and fairing-strut spacing. The

strategy to use a simplified configuration made it possible to conduct a computational study allowing a greater understanding of the flow field.

The second experiment proposed was to test a splitter plate fixed to the rear of a stand alone bluff body. The chosen bluff body had a H-beam cross section for reasons that will be discussed later on in this chapter. The splitter plate length was varied to understand the effects of this on the noise produced by the model.

It was not expected that the findings from the studies would be directly applicable to the landing gear at least in the sense of noise level reductions. The complex flow around landing gear components together with interaction effects and inflow conditions would not allow the direct comparison of the results obtained by the proposed experiments. However, the experiments would aid in design guidelines to outline the sensitivity of the various parameters as well as the control devices being proposed. If the findings are considered on a local scale, it would be expected to find localised noise reductions and hence noise reductions on a landing gear as a whole.

The rest of the chapter is dedicated to the design of the models as well as the experimental arrangements and test apparatus used during the course of these studies.

3.3 Design of Experiment

3.3.1 The fairing-strut with splitter plate

The complexity of the flow around a landing gear makes a fundamental study of the technology being discussed difficult. As explained in section 3.2 a simple geometry was used instead to examine the flow characteristics and to highlight different parameters that may be used to improve its performance when used on the landing gear. The simplified model consisted of a thin walled half cylindrical shell shielding a circular cylinder shown in figure 3.1. The shape of the fairing was cylindrical in shape due to its known aerodynamic shape and its close association with the actual fairings used on a landing gear (i.e. the articulation link fairing). In practice the fairing would shield landing gear components which are generally made up of various cylindrical struts. To mimic this effect during the experiments a circular strut was placed aft of the fairing. The smooth circular struts used in the experiments were void of small scale details, characteristic of landing gear

components. After lessons learnt from the set-up employing the circular cylinder a cylinder with a H-beam cross section was used as it has a richer noise signature.

As discussed earlier the size of the fairing with respect to the components it was shielding was deemed to be an important parameter. To avoid changing the diameter of the fairing hence minimising blockage effects during the experiments the diameter of the struts was varied. Four different circular strut diameters (D_{strut}) were used; $D_{strut}/D_{shell} = 0.67$, 0.76, 0.86 and 0.93. Another parameter investigated was the separation distance between the shell and the strut. The distance between the center of the shell and the strut center was varied between $1/4 < x_c/D_{shell} < 2/3$ (see figure 3.2). Table 3.1 specifies the dimensions of the different configurations.

Parameter	Value for Experiments	Remarks
D_{Shell} (mm)	$150mm$	Shell Diameter
D_{Strut}/D_{Shell}	$0.67, 0.76, 0.86, 0.93$	Strut Diameter
L_{model} (mm)	$500mm$	Length of model
x_c/D_{Shell}	$1/4, 2/5, 1/2, 2/3$	Strut center distance from shell center
t_f (mm)	$2mm$	The thickness of the trailing edge
$Re_{D_{Shell}}$	$1.75 \times 10^5 - 4.0 \times 10^5$	Range of Reynolds number based on the shell diameter

TABLE 3.1: Main design parameters of the simplified wind tunnel model.

The control device was a splitter plate which was positioned between the shell and the strut in the $x - z$ plane at $y = 0$. The splitter plate consists of a rigid steel plate, which was secured to prevent vibrations caused by flow perturbations. The origin of the coordinate system was centered about the shell center and the mid-span of the model. The x-coordinate was in the streamwise direction, the y-coordinate was in the lateral direction and the z-coordinate was in the spanwise direction.

Aerodynamic considerations

Wind tunnel blockage effects, the aspect ratio of the model, and Reynolds number effects are key to the quality of the experimental results. This implies that the wind tunnel model must be designed giving priority to these key effects.

Reynolds number effects: -

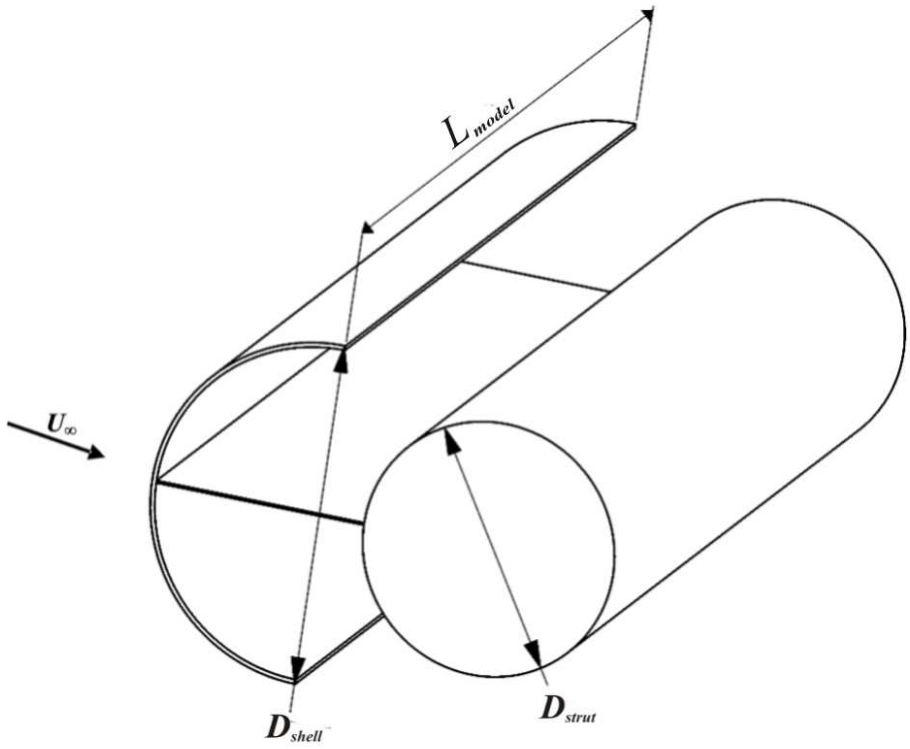

FIGURE 3.1: Schematic of simplified model in *Splt* configuration.

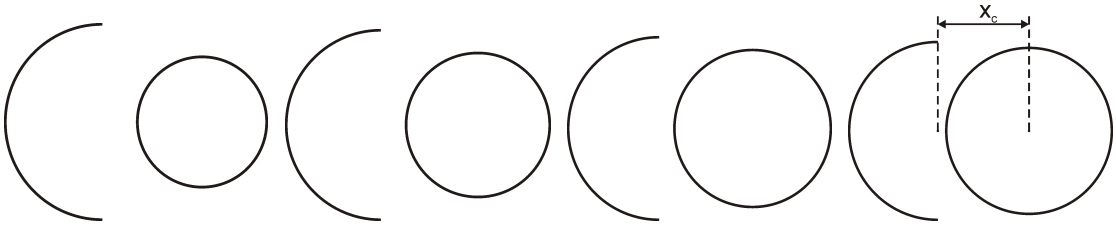

(a) $D_{strut}/D_{shell} = 0.67$. (b) $D_{strut}/D_{shell} = 0.76$. (c) $D_{strut}/D_{shell} = 0.86$. (d) $D_{strut}/D_{shell} = 0.93$.

FIGURE 3.2: Schematics of the four different cylinder configurations.

In flight conditions the Reynolds number based on the dimension of the fairing ranges between $1 \times 10^6 - 4 \times 10^6$. If these Reynolds numbers were to be replicated in the wind tunnels available this would mean that the diameter of the shell (which represents the fairing) would have needed to be approximately $0.360m$ to achieve the minimum Reynolds number of 1×10^6. This diameter was too large and was not adequate, the reasons for which will be discussed later. At these large Reynolds numbers the boundary layer flow would have been turbulent. As discussed in section 2.6.1 the flow regime would have had an effect on the drag as well as the shedding frequency so it was important that the tests were done in the same flow regime as the in flight conditions. For practical reasons the maximum Reynolds number (based on the diameter of the shell, $Re_{D_{shell}}$) for the model was of the

order 10^5. From the literature review it was seen that there was a drop in drag for a circular cylinder at a Reynolds number of about 300,000 which indicated a transition to turbulence in the boundary layer. This was still well below the in flight conditions but a tripping device (e.g a roughness strip) was used to ensure that the boundary layer transitions to a turbulent one. The roughness strips consisted of $10mm$ wide 120 grit carborundum strips placed on the fairing at $\theta = \pm 45°$. In addition to this point, one must note that the shell is half a cylinder. This means that the separation point was fixed at the apex and hence the Reynolds number effects will be diminished.

Blockage effect: -

As the wind tunnel test section was of a finite size, it imposed different conditions to the flow field. The interaction of the flow between the model, its wake and the wind tunnel wall would have caused an increase in the dynamic pressure and therefore, the velocity field would have been different to a model placed in free field. The blockage effect was simply the model projected frontal area to the tunnel cross sectional area. A blockage ratio for a two-dimensional setup of up to 6% was found to be acceptable without any large pressure distribution variations and nearly no appreciable changes in the Strouhal number [71]. Larger blockage ratios would have resulted in uncorrectable flow measurements. The blockage ratio dictated a physical constraint on the size of the model. To ensure a blockage ratio of 6% or less in the $3' \times 2'$ tunnel the diameter of the outer shell would have needed to be $0.054m$. This diameter was too small and posed a problem as the Reynolds numbers achieved would have been too small. To be able to accommodate the Reynolds number restriction a shell diameter of $0.15m$ had to be used. The blockage ratio in the $3' \times 2'$ tunnel would be 14%, whilst the ratio in the $7' \times 5'$ would be 2.5%. Even if the blockage in the smaller tunnel was more than the acceptable value the nature of the tests was to compare different configurations and did not need to be compared to similar experiments. During the course of the experiments the blockage ratio was not changed as the diameter of the fairing was kept constant.

Aspect Ratio: -

The experiments were be carried out in the critical regime using an aspect ratio of $L/D_{shell} = 4.0$ and roughening strips to trip the boundary layer. The aspect

ratio was important to obtain a nominal two-dimensional flow configuration. Previous experiments conducted in this regime used an aspect ratio of 5 and yielded acceptable experimental results [72].

3.3.2 The fairing-strut with suction and blowing

A brief description of the design of the simplified wind tunnel model, figure 3.3 with suction or blowing is given in this section. The model had to meet a number of design criteria:

- The size of the model was restricted by the size of the smallest tunnel but the diameter of the shell had to be large enough to ensure a suitable Reynolds number.
- The trailing edge of the shell had to be as thin as possible to increase the frequency of the trailing edge noise. The bluff body noise was expected to be in the low to mid frequency range and hence by designing the model in a way to allow the trailing edge noise to be in the higher frequency range would allow easier analysis of the results.
- Stiffness of the model was important as unwanted vibrations could cause additional noise and would have affected the flow around it.
- The flow distribution through the perforations had to be as uniform as possible along the length of the model.
- The noise generated by the suction/blowing had to be as low as possible.

The shell was a 20 mm thick hollow half cylinder. The excessive thickness was due to the internal chambers needed for the suction/blowing system. The central part of the shell (figure 3.4) was made up of eight individual chambers. These split up the settling chamber to achieve a more uniform flow distribution. Each chamber was fed by independent pipes which were linked up with the pump. The pipes were uniformly perforated which was not ideal. The flow through each orifice of the pipe was going to be different due to the varying pressure drop in the pipe after each orifice. It would have been ideal to vary the diameter of each orifice to allow the same mass flow rate through each hole. This kind of optimisation was not possible as each suction or blowing flow rate would require a different hole

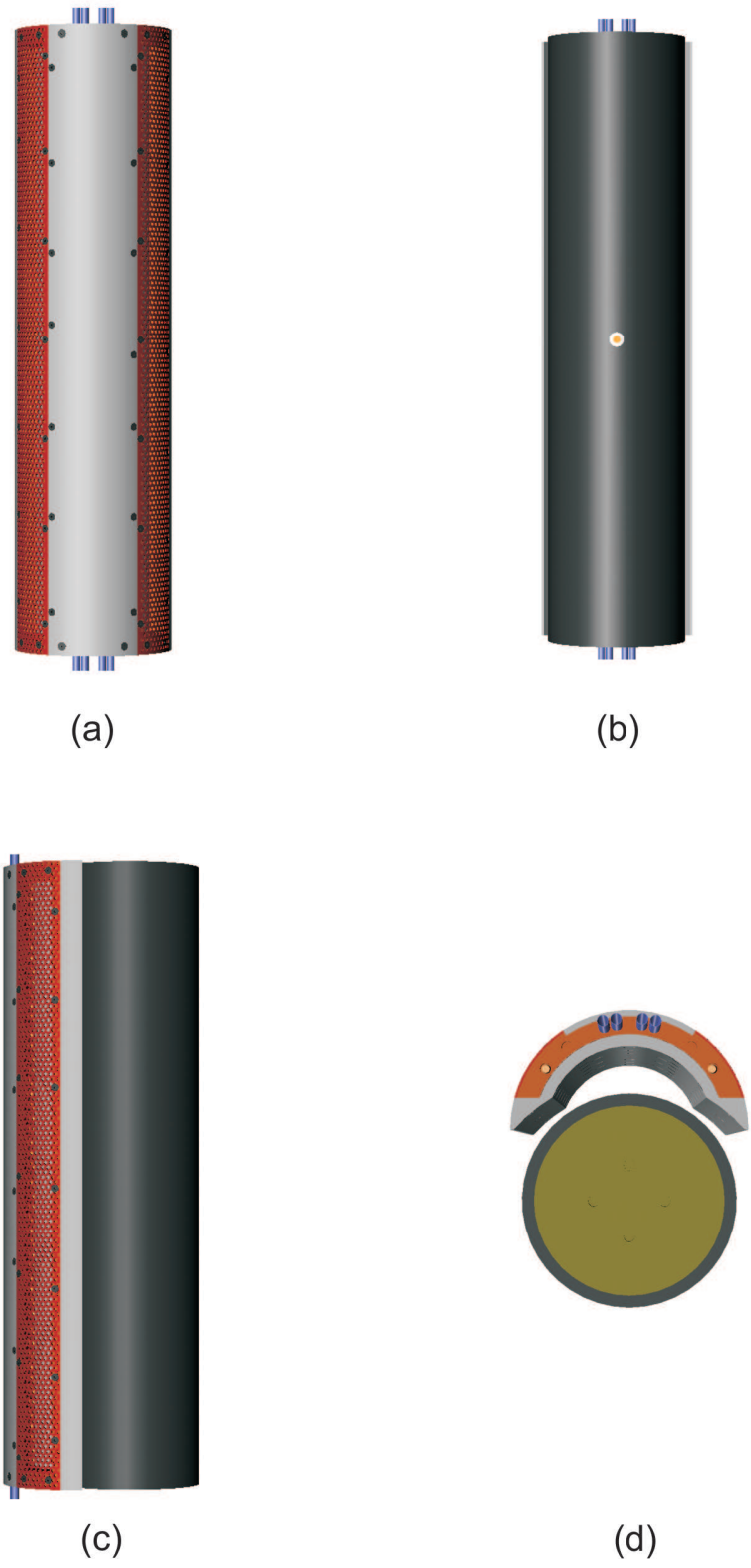

FIGURE 3.3: Views of the simplified wind tunnel model using suction or blowing. (a) front (b) back (c) left and (d) top.

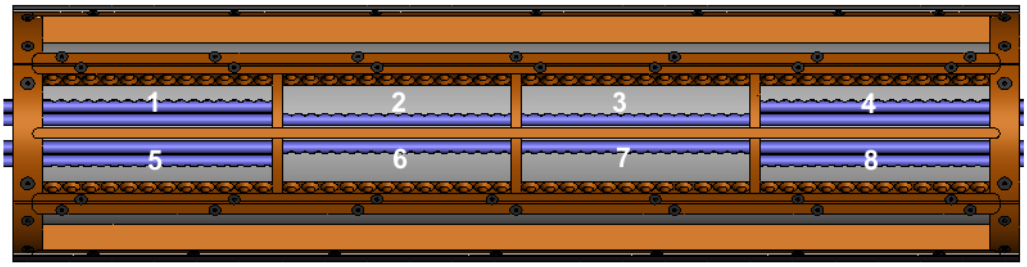

FIGURE 3.4: Detail showing the eight independent chambers.

diameter distribution. Changing the pipes for each flow rate was not an option as this would have caused a lot of down time during testing.

Directly opposite each pipe a number of ports fed the chambers which sat directly below the porous material (figure 3.5). The ports were chamfered to avoid sharp corners which would otherwise generate noise. For practical reasons the porous surface through which suction/blowing was applied cannot cover the whole surface of the shell as the shell would have to be made thicker to accommodate the settling chambers. The chosen position of the porous surface was located towards the trailing edge of the shell as it was believed that most of the noise generated is created in this area due to higher velocities, secondly the flow control would be most effective towards the separation point. A summary of the model dimensions are listed in table 3.2.

Parameter	Value for Experiments	Remarks
D_{Shell} (mm)	$127mm$	Shell Diameter
D_{Strut} (mm)	$114mm$	Strut approx 90% of the shell diameter
L_{model} (mm)	$500mm$	Length of model
t_f (mm)	$2mm$	The thickness of the trailing edge
σ (%)	31%, 30%	Porosity of the perforated and sintered plates respectively
$Re_{D_{Shell}}$	$1.75 \times 10^5 - 3.5 \times 10^5$	Range of Reynolds number based on the shell diameter

TABLE 3.2: Main design parameters of the simplified wind tunnel model with suction or blowing.

Acoustic Considerations: -

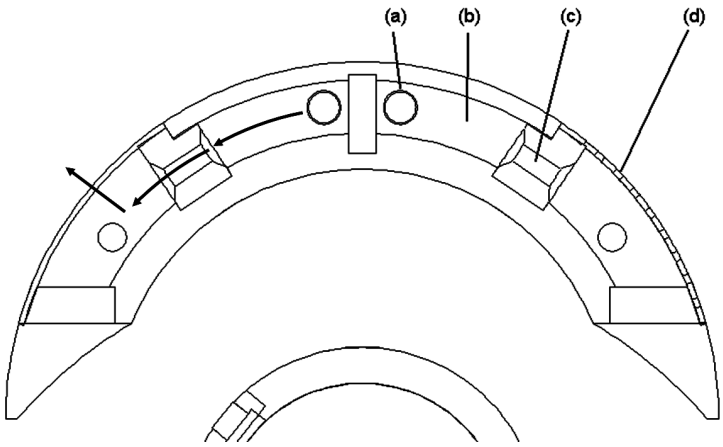

FIGURE 3.5: A view of the layout inside the model. (a) chamber pipe (b) settling chamber (c) chamber ports (d)perforates.

The main problem was the noise generated by the suction/blowing system. The flow through the entire system would have generated noise and this needed to be reduced as much as possible. A compressor pump provided the necessary suction and blowing rates. The pumps inherently generated noise, which traveled through the pipes that fed the model. The noise generated was broadband in nature, so a plenum chamber was introduced between the pump and the model to absorb noise before it reached the model in the tunnel (see figure 3.6).

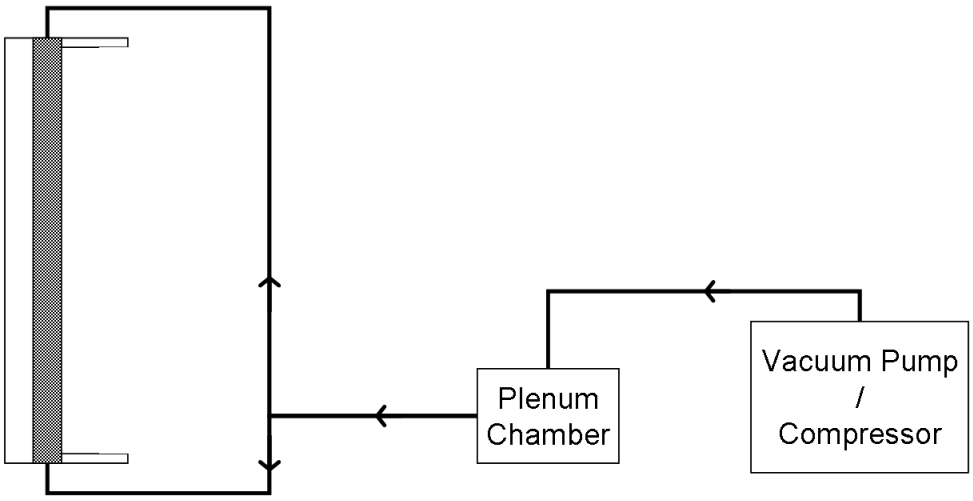

FIGURE 3.6: Schematic representation of the wind tunnel model.

The plenum chamber (see figure 3.7), was made up of a chamber with a large volume and a large cross section between two smaller ducts which were located

at opposite ends and were offset to minimize the direct transmission of sound. The inside of the plenum chamber was lined with sound absorbing material that absorbed a large amount of the sound energy as it was reflected around the internal walls of the chamber.

The suppression of noise inside the internal chamber of the fairing and the flow through the perforates was critical. Ideally the ducts inside the model would be large in diameter to reduce the velocity of the flow as sound intensity scales with the velocity of the flow. Although this would have been ideal, the thickness of the shell restricted the size of the ducts.

Flow rate requirements

Preliminary calculations had to be done to determine the pump requirements needed to achieve the desired flow rates. The pressures within the model plenum chambers were assumed to be constant. The external pressure distribution around the shell varied with angular position. The inviscid pressure distribution around a circular cylinder is given by:

$$C_p = 1 - 4sin^2\theta \tag{3.1}$$

As the flow around the shell was expected to be turbulent in nature the peak negative pressure would have been less than that for the inviscid case. ESDU 81039 [73] provided a semi-empirical method for estimating the pressure loss through perforated materials. The pressure loss across a perforated plate was given by:

$$\Delta p = \frac{1}{2}\rho_i V_i^2 K_i, \tag{3.2}$$

where the subscript i refers to the injected fluid and K_i is a constant dependent on the porosity of the material and the ratio of the thickness of the plate to the orifice diameter (t/d_{perf}).

The injected fluid was based on the pressure difference between the plenum pressure and the pressure on the external surface of the perforated plate. A non-dimensional relationship for the pressure difference can be written as:

$$\frac{\Delta p}{\frac{1}{2}\rho_\infty U_\infty^2} = (1 - 4sin^2\theta) - C_{p,plenum} \tag{3.3}$$

Using the two relationships shown in equations 3.2 and 3.3 a ratio between the freestream velocity and the injected velocity can be derived:

$$\frac{V_i}{U_\infty} = \sqrt{\frac{(1 - 4sin^2\theta) - C_{p_{plenum}}}{K_i}} \tag{3.4}$$

The angular position of the plenum was from 39° to 60°. Using the inviscid pressure distribution, given in equation 3.1, the Cp at 60° was -2. If the pressure coefficient in the plenum was less then -2 then reverse flow will occur through the perforated case. This is valid for suction as the pressure within the chamber had to be below atmospheric. To ensure that suction occurs along the whole of the surface a sufficiently low pressure had to be ensured.

Two types of permeable materials were used in the tests. The first was a $1mm$ perforated plate with a porosity $\sigma = 31\%$ while the second was a sintered bronze metal plate with a porosity of $\sigma = 30\%$ and a thickness of $2mm$. Sintering is a process where the raw powder material is subjected to heat and pressure which bond the metal particles together. The result is a porous material with a very small pore size ($12\mu\ m$). The pressure loss across the plate is higher than that for the perforated plate, which results in less variation in the transpiration velocity along the length of the plate.

An estimate of the required flow rates through the pump was made using the perforated plate at a freestream velocity of 40m/s. From the relation given in ESDU 81039 [73], K_i=18.43. The limiting case was when the coefficient of pressure inside the plenum had a pressure equivalent to $C_p = -2$, which corresponded to a gauge pressure of $1960N/m^2$. To calculate the mass flux through the perforated plate, the average transpiration velocity was needed:

$$\left(\frac{V_i}{U_\infty}\right) = \frac{\int_{\theta_1}^{\theta_2} \frac{V_i}{U_\infty} d\theta}{[\theta_2 - \theta_1]} = 0.18 \tag{3.5}$$

The limits of the integration used are 39° to 60° which corresponded to the angular limits of the plenum chamber. The mass flow rate was given by:

$$Q_m = \rho V_i A \tag{3.6}$$

where A was the open area. The suction and blowing coefficient were defined by:

$$C_\mu = \frac{Q_m V_i}{\frac{1}{2}\rho_\infty V_\infty^2} S = 2\left(\frac{V_i}{V_\infty}\right)^2 \left(\frac{A}{S}\right) \tag{3.7}$$

where S is the frontal area of the shell, which was equal to $0.0635m^2$ and A was the open area, which was equal to $6.3 \times 10^{-3}m^2$

Using these values and equation 3.7 the suction coefficient was calculated at 6.4×10^{-3}. This corresponded to a mass flow rate of $0.0454Kg/s$

For blowing, a positive pressure coefficient always existed in the plenum and therefore the reverse flow consideration was not relevant.

3.3.3 Pump

The pump used was a variable speed side channel blower $G200e$ by Rietschle. The pump was capable of delivering a maximum flow rate of $0.078kg/s$ at $170mbar$. Both the flow rate and the pressure were larger than the minimum requirements calculated above. This additional pressure was needed to achieve a suitable range of mass flow rates and to overcome the additional pressure required when the sintered plates were used.

The specifications of the pump state that the pump noise is 63dB(A) at a distance of 1m and at an operating frequency of 50Hz.

3.3.4 Plenum chamber

As mentioned earlier, a plenum chamber could effectively attenuate noise produced by the pump. Wells [74] derived a model to predict the transmission loss TL inside a lined plenum chamber. The attenuation of the lined plenum was given by the following equation:

$$TL = -10log\left[S_E\left(\frac{1-\alpha}{\alpha S_W} + \frac{cos\beta}{2\pi d^2}\right)\right], \tag{3.8}$$

where TL was the transmission loss in dB, S_E was the plenum exit area, S_W was the total plenum wall area, α was the sound absorbing coefficient of the lining material, d was the distance between the inlet and the outlet of the chamber and β was the angle between the inlet and the outlet of the plenum chamber. A

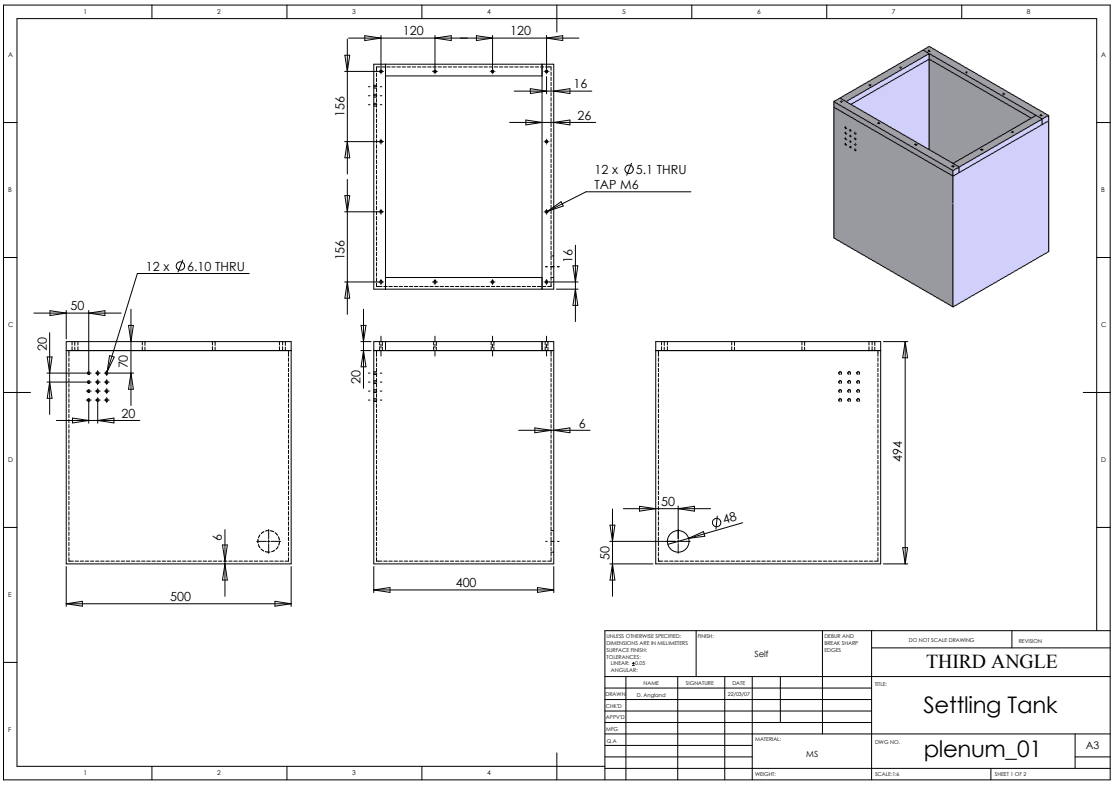

FIGURE 3.7: Drawing of plenum chamber

$0.5m \times 0.5m \times 0.4m$ plenum box was designed and was lined with $25.4mm$ of open celled polyurethane 3.7.

The plenum was also used to minimize the pressure loss in the piping used to supply the model. The model inlet pipes had an internal diameter of $4mm$ which would result in large losses if this pipe diameter was to be maintained all the way up to the pump. Instead a $38.1mm$ pipe connected the plenum to the pump while the plenum was placed as close as possible to the model. Eight $6mm$ pipes then connected the plenum to the model. This configuration decreased the pressure losses and maximized the mass flow rates.

3.3.4.1 H-beam with splitter plate

The use of splitter plates with the fairing strut configuration led to the idea of splitter plates being used as a control device for a bluff body without using a fairing. The advantage was that, as described earlier, a fairing added extra weight to a landing gear and also led to complications during the retraction of the landing gear. What was proposed was to place a splitter plate behind a bluff body, in

the same way that splitter plates were used for the control of vortex shedding. The argument discussed earlier with regards to using a simplified representative case of landing gear components applied. A simple geometry was used instead to examine the flow phenomena and to highlight different parameters that may be used to improve its performance when used on the landing gear. A bluff body with an H-beam cross section, (see figure 3.8) was used. This cross-section profile was used as it produces noise over a broad range of the frequency spectrum as opposed to a simple circular cylinder with noise over a much narrower frequency range.

Three different splitter plate lengths were positioned in the midplane behind the H-beam. The lengths used where $L/W = 1$, $L/W = 2$ and $L/W = 3$ (L, being the length of the splitter plate). The splitter plates were fastened securely to avoid any structural vibrations which would influence the results. The origin of the coordinate system was centered about the H-beam cross section and the mid-span of the model. The x-coordinate was in the streamwise direction, the y-coordinate was in the lateral direction and the z-coordinate was in the spanwise direction.

Parameter	Value for Experiments	Remarks
$W\ (mm)$	$100mm$	Width of H-Beam
L/W	$1, 2, 3$	Length of splitter plates
$L_{model}\ (mm)$	$500mm$	Length of model

TABLE 3.3: Main design parameters of the H-beam with splitter plate model

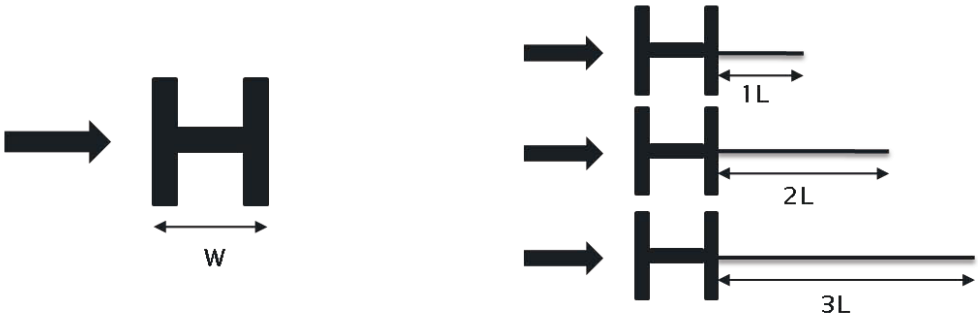

FIGURE 3.8: Schematics of H-Beam model fitted with splitter plates.

3.3.5 Experimental setup

Three different facilities were used to conduct the aerodynamic and acoustic measurements. The $3' \times 2'$ wind tunnel was used for flow measurements, the $7' \times 5'$ tunnel was used for acoustic measurements including on surface microphones and

microphone array measurements. Force measurements were also performed using an overhead balance fitted in the tunnel. An open-jet anechoic facility was used to perform tests using free field microphones.

3.3.5.1 $3' \times 2'$ wind tunnel

The $3' \times 2'$ wind tunnel was a closed jet, open circuit suction tunnel. The tunnel test section measures $0.6m \times 0.9m \times 2.4m$ and had perspex windows along its vertical walls and optical access on its ceiling panels. The size of the tunnel together with its favorable optical access made the tunnel easy to use and allowed varied measurement techniques to be used including hot wire and PIV. As the tunnel was a suction type, the static pressure within the tunnel was lower than atmospheric pressure and therefore care was taken to ensure minimal leaks in the tunnel. Another disadvantage of the tunnel was that it was noisy, which made accurate acoustic measurements impractical. For this reason, this tunnel was only used for aerodynamic and preliminary acoustic measurement.

In the commissioning of the tunnel, the flow direction was tested using woollen tufts and showed satisfactory results [75]. A turbulence level of 0.2% was reported in [76] for tunnel speeds between $15m/s$ and $30m/s$. The average thickness of the boundary layer was reported to be about $20mm$ [77] at the location of the model.

Flow velocity was set by a manual frequency controller varying the fan rotational speed. The velocity in the test section was measured with a pitot tube located upstream of the model. This was connected to a Furness Controls FC012 digital micro manometer with a range of $199 \pm 0.5\% mmH_2O$. An analogue to digital converter was used to acquire the readings on computer. The readings could then be corrected for changes in atmospheric temperature and pressure.

In order to obtain a two-dimensional flow in the $3' \times 2'$ wind tunnel the model had to span the height of the test section. In order to obtain valid results the model was placed in the core of the flow without interaction with the boundary layers that develop on the tunnel walls. End plates were used, the size of which were based on a study by Gerrard [78]. The model was placed on the longitudinal center. The width normal to this center line was $7D_{Shell}$ and the distance from the center line of the shell to the trailing edge and leading edge of the plates is $4.5D_{Shell}$ and $3.5D_{Shell}$ respectively. The leading edges of $10mm$ thick plates were rounded and roughness strips of 80 grit Carborundum were placed $50mm$ from the leading edge. The roughening strips This treatment ensured that the boundary

layer would not separate. The thickness of the boundary layer at the end plate's leading edge location was approximately $20mm$, while the end plates were located $40mm$ from the tunnel floor and ceiling keeping them clear of any interaction with the tunnel's developing boundary layer. The problem with having an end plate located on the top part of the model was that this would have blocked optical access which was necessary for PIV measurements. To circumvent this problem the end plates where fabricated out of Perspex.

The origin of the coordinate system was centered about the shell center and the mid-span of the model. The x-coordinate was in the streamwise direction, the y-coordinate was in the lateral direction and the z-coordinate was in the spanwise direction.

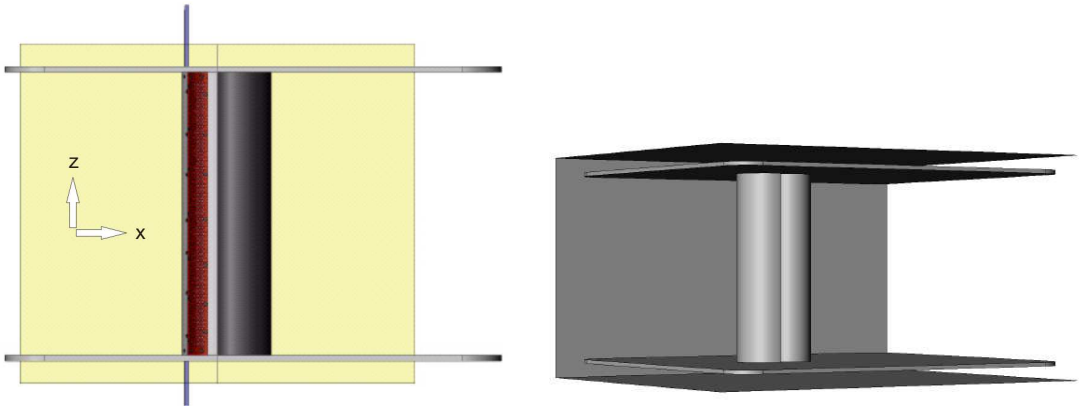

(a) side view (b) angled view

FIGURE 3.9: The model set up in the $3' \times 2'$ wind tunnel.

3.3.5.2 $7' \times 5'$ wind tunnel

The wind tunnel was a closed circuit tunnel with a high speed test section measuring $2.1 \times 1.7\ m$. The maximum flow speed capability was $U_\infty = 45\ m/s$ which limited the maximum Reynolds number to $Re_{D_{shell}} = 4 \times 10^5$. The reported turbulence level was less than $Tu = 0.1$ when the tunnel was commissioned [79]. The first set of turning vanes after the test section produce a distinct tone at a frequency of 1000 Hz at a velocity of $U_\infty = 30\ m/s$ depending on atmospheric conditions and model blockage.

The model was suspended horizontally in the middle of the test section between two end plates using ceiling mounted struts to support the model. The set up is shown in figure 3.10. The end plates measured 500 mm by 300 mm with a rounded leading edge and tapered trailing edge. The endplates were much smaller than the

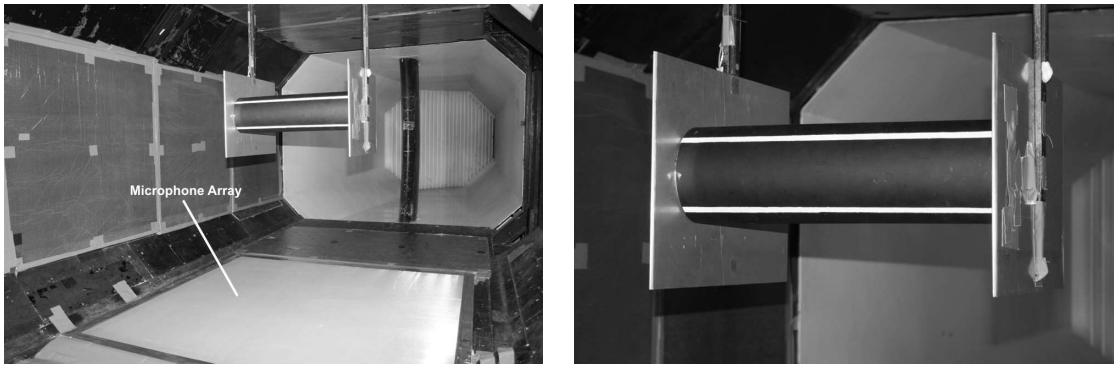

(a) Microphone array placement (b) Suspension of model

FIGURE 3.10: The model set up in the $7' \times 5'$ wind tunnel.

ones used in the $3' \times 2'$ experiments as the larger endplates would interfere with the microphone array measurements. The large end plates would prevent the free propagation of sound to the microphones located at the edge of the array. Oil flow was performed to ensure that the two-dimensionality of the flow was acceptable. The model blockage ratio was 2.5%, based on the frontal area of the model over the cross sectional area of the test section.

The coordinate system used was similar to that of the $3' \times 2'$ tunnel. The flow speed was measured by a pitot-static tube located upstream from the model. The dynamic pressure was measured by a Setra Model 239 pressure transducer with a range of 1.25×10^3 Pa with a quoted accuracy of 0.14%.

3.3.5.3 Open-jet anechoic facility

Farfield microphone measurements were performed in an anechoic chamber equipped with an open-jet nozzle. The anechoic chamber measured $9.15\ m \times 9.15\ m \times 7.32\ m$ with glass-fibre wedges covering the walls, the floor and the ceiling giving a lower threshold free field frequency of 80 Hz. The open-jet set-up consisted of a nozzle connected to a high pressure source through a series of silencers [80]. A 10:1 contraction ratio nozzle with a rectangular exit of $0.35\ m \times 0.5\ m$ $(width \times height)$ was used in the tests, delivering a maximum freestream velocity of $U_\infty = 45\ m/s$ for about 30 seconds. A maximum speed of 40 m/s was used in these experiments.

The model was suspended horizontally on rigid struts which were bolted to the floor of the chamber. Two end plates measuring $500\ mm \times 850\ mm$ were flush mounted to the sides of the nozzle to prevent the wake from spreading in the spanwise direction. The span of the model had to be reduced to 350 mm due to

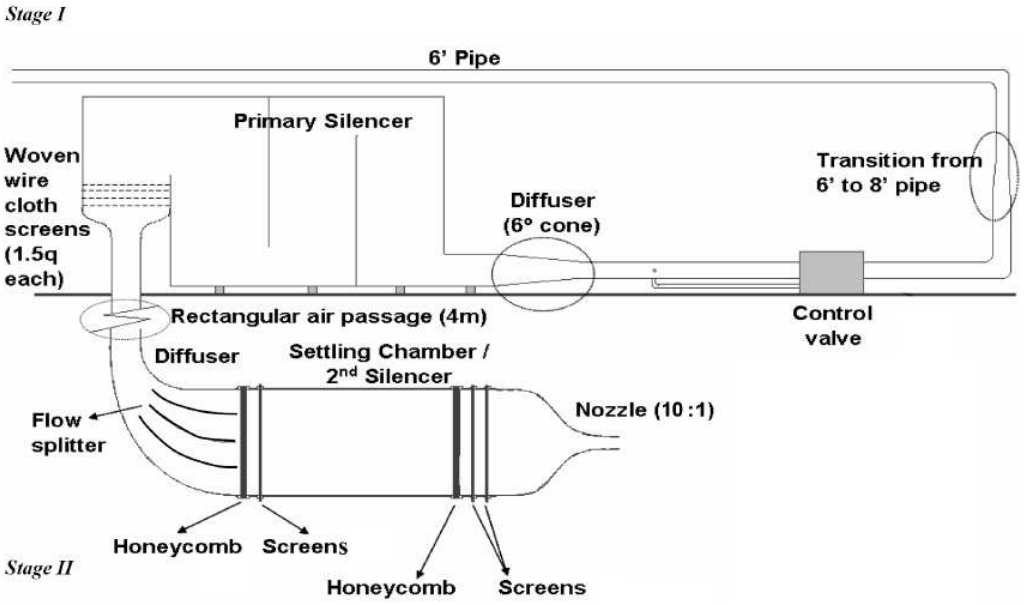

FIGURE 3.11: Schematic of open-jet facility

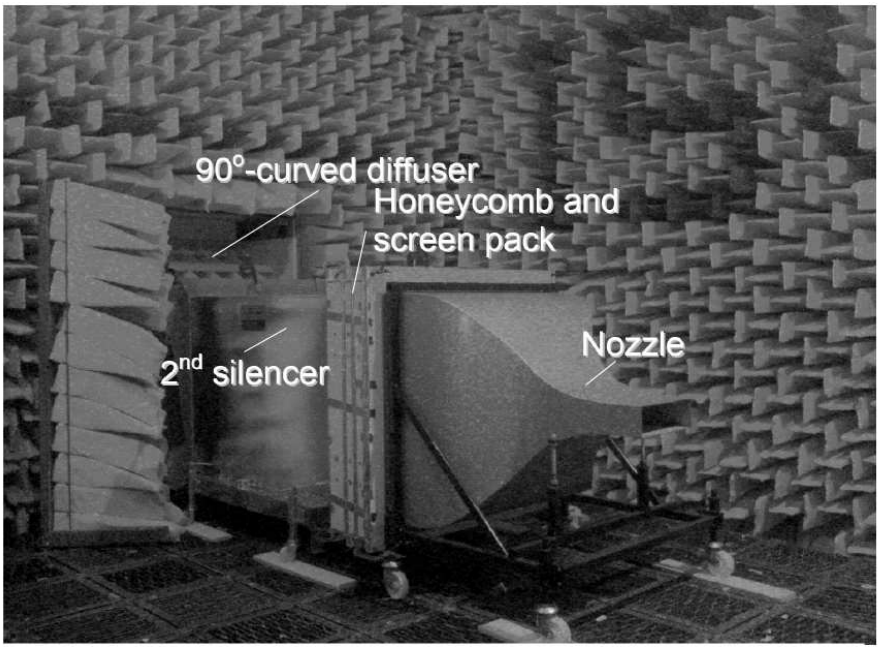

FIGURE 3.12: Nozzle and the 2^{nd} silencer inside the anechoic chamber

the size restriction of the nozzle. Two holes were cut into the endplates to fit the model between the endplates. The resulting gaps were sealed using aluminium tape to ensure that air leakage did not occur. The coordinate system is similar to the one used in the other tunnels. The x-coordinate was in the streamwise direction, the y-coordinate was in the lateral direction and the z-coordinate was in the spanwise direction. The freestream speed was controlled by a pitot static tube

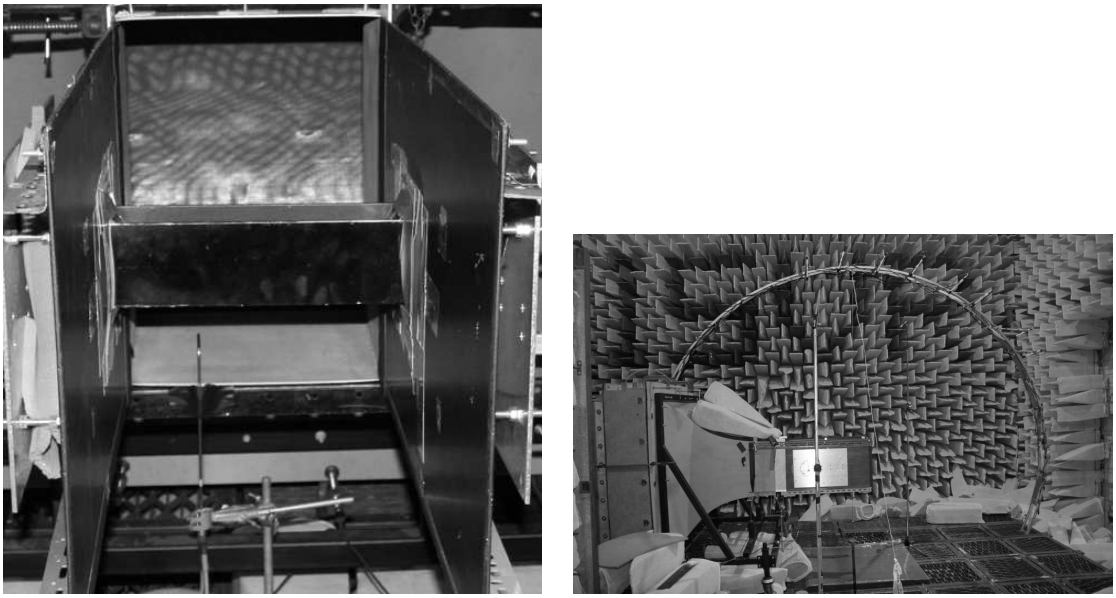

(a) Suspension of model (b) Placement of microphone arc

FIGURE 3.13: The model set up in the anechoic open-jet tunnel.

which was located at the nozzle exit. The dynamic pressure was measured by a Comark C9551 pressure meter with a range of 14000 Pa with an accuracy of 0.2%. This equates to a maximum uncertainty in the freestream velocity of ± 0.125 %.

	$3' \times 2'$ wind tunnel	$7' \times 5'$ wind tunnel	Open-jet anechoic facility
Oil flow	✓		
Hotwire	✓		
PIV	✓		
Force balance		✓	
Unsteady Pressure	✓		
On-surface microphone	✓	✓	✓
Freefield microphone			✓
Microphone array		✓	

TABLE 3.4: Testing facilities and apparatus matrix.

3.4 Testing Apparatus

3.4.1 Oil flow visualisation

A liquid suspension of titanium dioxide, paraffin and oleic acid was applied to the surfaces of the model. The liquid is transported along the surface streaklines and when dry leaves a time-averaged flow pattern. The streakline pattern was photographed with the model in the tunnel so as not to disturb the flow pattern.

3.4.2 Hotwire

Hotwire anemometry was used to investigate the unsteady flow field downstream of the model. The probe was a 2.5 μm diameter platinum-plated tungsten single wire sensor. The hot wire probe was attached to a traversing rod to allow the position of the probe to be changed precisely. The device was connected to a constant-temperature bridge circuit which in turn was linked to a data acquisition computer via an analogue to digital converter.

Calibration of the hotwire probe was done by using a calibrated pitot tube as a reference. The system was calibrated several times during a single experiment to compensate the drift in the measurements. The probe was aligned in the z direction, making it sensitive for capturing the x and y velocity components. The power spectral density (PSD) of the velocity signal $u(t)$ was obtained, by measuring the energy contained in each frequency band by using:

$$PSD(u(t)) = \frac{|FFT(|u(t)|)|^2}{n}. \tag{3.9}$$

The hotwire data was sampled at $f_{sample} = 10,000\ Hz$ using a block size of $n = 8192$ and averaged over 50 blocks, giving a resolution of 1.22 Hz. The frequencies in the PSD plots were non-dimensionalised using

$$Str_{shell} = \frac{fD_{shell}}{U_\infty} \tag{3.10}$$

Uncertainty: -

The uncertainties for the hotwire measurements were categorised as fixed and variable errors [81]. The fixed error was introduced due to the accuracy of the

pitot-static tube, which was used to calibrate the hot wire as well as the calibration process itself. This resulted in an error of $0.32m/s$ at $30m/s$. The variable error was estimated by comparing the mean values over the acquired blocks used during one measurement set. The average standard deviation at $30m/s$ was of $0.07m/s$. To combine the two errors the root-sum-square was applied to yield a total uncertainty in the velocity measurements of $0.33m/s$ at $30m/s$ or 1.1% of the freestream velocity. This was valid for the regions outside the reversed wake and the shear layers where the velocities measured by a single hot wire were not reflected accurately. The hot wire was only used to qualitatively compare the energy spectra in the wake with a resolution of $\Delta f = 1.22Hz$.

3.4.3 Particle image velocimetry

Particle image velocimetry (PIV) was used to gain an insight into the flow around the model and the wake directly behind it. The PIV images were acquired using a Dantec Dynamics system with an 80C60 HiSense CCD camera with a pixel resolution of 1280×1024 pixels and a New Wave Gemini $120mJ$ Nd:YAG dual laser system. A Dantec Flowmap system was used to acquire and process the data. The camera was mounted on the roof of the tunnel on a sliding traverse focusing perpendicular to the laser sheet in the $x - y$ plane located at the spanwise center of the model. A 60 mm lens was used to focus in onto the plane of interest, giving an image size of 100 $mm \times 125$ mm.

Three traverse positions in the streamwise direction were performed to visualize the areas of interest while overlapping the neighboring image by 15 mm. Measurements were performed at 30 m/s using the pitot tube to measure the freestream velocity. At each position 500 image pairs were recorded. The time per recording image pair was kept constant at 0.5 seconds and the time between pulses was varied depending on the freestream velocity.

The images were post-processed using adaptive correlation with 3 refinement steps ending with an interrogation area size of 32×32 pixels using 75% overlap. Where needed, range and peak validation were used to remove erroneous vectors. The mean velocity field was obtained by averaging over the 500 instantaneous vector maps.

Uncertainty: -

The accuracy of the instantaneous velocity field was estimated using the following

relationship [82]:-

$$\epsilon_u = \frac{S_f \eta p_c}{\Delta t} \tag{3.11}$$

S_f represented the scale factor which was fixed for all the tests. The correlation peak p_c was typically 0.1. The CCD resolution η was determined by the hardware and was fixed and Δt was the time between the laser pulses.

Using this relationship the maximum error in the velocity was of $0.4m/s$. Using error analysis for multi-sample experiments as described by Moffat [81], the uncertainty in the time averaged vector was $0.02m/s$ or 0.06% of the freestream velocity.

3.4.4 Force Balance

The $7' \times 5'$ wind tunnel contained a three-component balance with a weigh-beam design with stepper motor driven weights. Only the drag forces were recorded during the experiments. The reference area used in the calculation of the coefficient of drag was 0.075 m^2 (the diameter of the shell multiplied by the span of the model). Tare corrections were made to the measurements to remove the contribution from the endplates and the struts. The drag force data was averaged over three runs and the repeatability for C_d was within 1.7%.

Uncertainty: -

The free stream values of temperature, static pressure and velocity were averaged from the values at the beginning and the end of each run. The average variations between the start and the end of the run were $\pm 0.3\ ^\circ C$ for temperature, $\pm 0.1\ mmH_2O$ for pressure and $\pm 0.01\ m/s$ for velocity. The resulting uncertainty for the drag forces was 3%.

3.4.5 Unsteady pressure transducers

Pressure transducers were used to acquire the pressure distribution around the strut. Twenty positions were recorded between $\theta = 9^\circ$ and 180° using five pressure sensors. The strut was rotated four times during each configuration giving pressure sensor data every 9°. The sensors used were 2.4 mm diameter Kulite type XCQ-093 sensors with a range of 0.35 bar and a natural frequency of 150 kHz. They are

powered by an 8 channel VISHAY model 2150 strain gauge amplifier. Analogue to digital conversion was performed using a National Instruments PXI-4472 24 bit data acquisition card, controlled by a PC using LabView software. To convert the output voltage to pressure units, a calibration was performed using a Druck DPI 601-F pressure calibrator for each individual Kulite transducer, assuming a linear relationship between voltage and pressure.

The pressures were presented as the normalised pressure coefficient:

$$C_p = \frac{p - p_s}{\frac{1}{2}\rho {U_\infty}^2} \tag{3.12}$$

where p_s was the static pressure inside the tunnel and ρ was calculated from the barometer and temperature readings using the ideal gas law.

To minimize the influence of signal drifting of the signal, a zero run was performed before each measurement, which was subtracted from the experimental measurements before conversion the pressures were converted to C_p values. The data was sampled at $f_{sample} = 10k\ Hz$ with a block size of $n = 8192$ and averaged over 100 blocks, giving a resolution of $\Delta f = 1.22\ Hz$.

Uncertainty

The fixed error for the unsteady pressure measurements was comprised of the error of the calibrator and the pressure transducers themselves. The calibrator used had a quoted accuracy of $\pm 0.05\%$ while the Kulites had a quoted accuracy of 0.1%. The combined error adds up to $C_p = \pm 0.07\%$ at a freestream velocity of $30m/s$.

By comparing the average values of the 100 blocks the variable error was calculated. The average standard deviation at $U_\infty = 30m/s$ was equal to 0.0054. The total uncertainty at $U_\infty = 30m/s$ calculated using the root-sum-square was of $Cp = \pm 0.07\%$.

3.4.6 Microphones

On-surface microphones: -

The microphones used for on-surface acoustic data were Panasonic omnidirectional back electret condenser cartridges, type WM-61A. The electret microphones were packaged in 6 mm cartridges and powered by a preamplifier which was built in-house. The frequency response range of the microphones was 20 Hz to $20k\ Hz$,

a sensitivity of $-44 \pm 5\ dB$ and signal to noise ratio greater than 58 dB. The frequency response curve supplied by the manufacturer showed that response was constant over the frequency range of interest.

A microphone was flush mounted to the strut, at $\theta = 180°$. The data was sampled at $f_{sample} = 48k\ Hz$ with a block size of $n = 16384$ and averaged over 100 blocks, giving a resolution of $\Delta f = 2.93\ Hz$.

Freefield microphones: -

Freefield acoustic data were acquired using Behringer ECM8000 omnidirectional electret microphones. These are powered by using DIGIMAX FS preamplifiers by Presonus. This setup had a frequency response range of 15 Hz to $20k\ Hz$.

A total of 11 microphones were suspended on an arc above the model. The arc was offset by 700 mm from the $x - z$ plane. Metal tubes protruded from the arc to align the microphones at $z = 0$ in the $x - y$ plane. The angular positions of the microphones spanned from 56° to 166° in the $x - z$ plane, these are summarised in table 3.5. The angles are defined from the front of the model in the clockwise direction, where 90° is directly above the model. To be able to compare the data between the microphones the distance was corrected to a distance of 2 m. This is done by using the linear scaling law of acoustic pressure with distance. The data was sampled at $f_{sample} = 44.1k\ Hz$ with a block size of $n = 8192$ and averaged over 100 blocks, giving a resolution of $\Delta f = 5.38\ Hz$.

Microphone number	Angle in x-z plane (°)	Distance from model center (mm)
1	56	1800
2	76	1730
3	90	1820
4	101	1830
5	110	1980
6	120	2050
7	130	2170
8	139	2200
9	150	2300
10	156	2340
11	166	2420

TABLE 3.5: Position of free field microphones relative to the model center.

Both sets of microphones were calibrated using a B&K pistonphone which is calibrated to give a pure tone of 94 dB at 995 Hz. From the calibration values the raw data in volts was converted to instantaneous sound pressure and converted to SPL using

$$SPL = 20log\frac{|FFT(|\acute{p}(t)|)|^2}{np_{ref}} \tag{3.13}$$

where p_{ref} is the reference pressure and is equal to $2 \times 10^5\ Pa$.

Uncertainty

The microphone levels are compared between different configurations and hence the fixed error is constant. The pistonphone used to calibrate the microphones had an accuracy of $\pm 0.3dB$. An additional source of error was introduced as the Panasonic electret microphones did not have a perfect fit inside the calibrator. A flat response was assumed over the frequency range of interest. This assumption was deemed good enough after the sample of the electret microphones were tested along side a 1/2" B&K microphone giving a coherence of 1 after being exposed to white noise.

The variable error was estimated by comparing the values of the acquired blocks. The error added up to 0.6 dB for both sets of microphones, approximately constant up to the maximum frequency of interest.

3.4.7 Microphone array

A phased microphone array was used to localize noise sources on the model. The 1.2 m array consisted of 112 microphones which were recessed by 12.7 mm behind a tensioned acoustically transparent cloth. The microphones used were 6 mm Panasonic omnidirectional back electret condenser cartridges (WM-61A), with a frequency response of 20 Hz to $20k$ Hz. The electret microphones were preamplified using purpose built preamplifiers with adjustable gain. The signals were acquired using National Instruments PXI-4472 data acquisition cards. The microphones were calibrated against a 1/2" B&K microphone. Both microphones were placed in proximity to each other and subjected to white noise. The coherence between the two microphones was approximately 1. The signals of the microphones used in the array were corrected for magnitude and phase. Due to the large data file sizes generated when using all 112 microphones, and the large computing requirements needed to process the data, the sampling frequency was set to $f_{sample} = 48k\ Hz$, block size $n = 4096$ and the data was averaged over 60 blocks. An in-house beamforming code written by Fenech [83] was used.

The scan plane used for these results was the $x-z$ plane at $y = 0$. The microphone

array was therefore placed underneath the model on the tunnel floor. 1/3-octave band averaged plots were calculated from 32 Hz to 20k Hz. The resolution of the array below 2k Hz was poor and was not capable of accurately localizing noise sources although the sound pressure levels from plots below this frequency could still be used. Several 1/3-octave frequency spectra presented in this work were obtained by integrating the beamforming plots. This was done by summing the beamforming levels over the model area for each 1/3-octave frequency band. The absolute levels of these plots were not physical, however the difference in the levels was significant.

Uncertainty

The microphone array data was used to compare different configurations and not for absolute levels, making fixed errors irrelevant. The variable error was calculated by comparing two runs using the same configurations. The maximum error for the beamforming plot was 1.3 dB, taken at various points in the scan plane and at different frequencies.

Chapter 4

Experimental Results for Fairing-Strut with Splitter Plate

Aerodynamics and acoustics of the fairing (shell)-strut configuration using a splitter plate as a control device are discussed in this chapter. The flowfield around the model is discussed by presenting the time-averaged flow features. Following the research on the mean flow behaviour, the influence the strut diameter, strut location and splitter plate have on the vortex shedding and the overall noise level are presented. Finally the aerodynamic and acoustic results for the fairing-H-beam configuration are discussed.

4.1 Time-averaged Flow Features

4.1.1 On-surface Flow

4.1.1.1 Effect of strut diameter

An oil flow visualisation was carried out as explained in section 3.4.1 and will be discussed to start building up a clear picture of the flow physics around the model. The oil flow was done on two of the configurations, $D_{strut}/D_{shell} = 0.67$ and $D_{strut}/D_{shell} = 0.93$. The surface of the model was kept as clean as possible but due to holes used for the on-surface microphones some distortion appeared, therefore flow visualisation on the strut should be interpreted with care.

Oil flow visualisation pictures of the rear of the strut are shown in figure 4.1. The

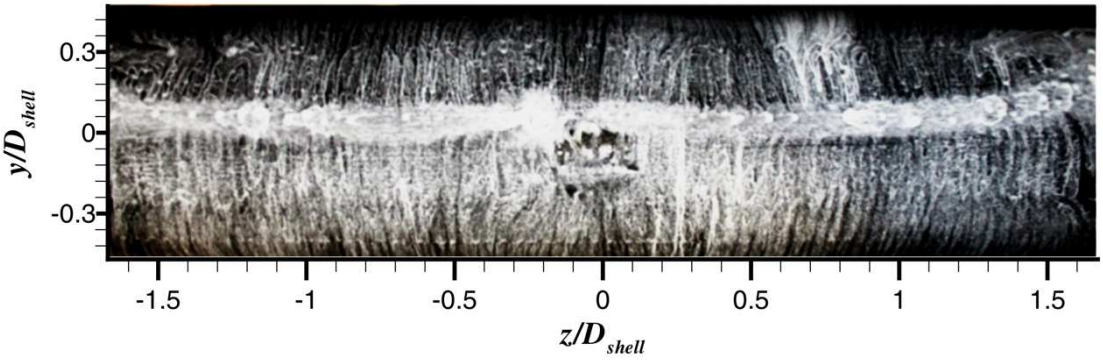

FIGURE 4.1: Oil flow visualisation on the rear of the strut in the $D_{strut}/D_{shell} = 0.93$ case. Flow out of page.

views reveal broadly two-dimensional flow behaviour over the model. This was discussed in section 3.3.5 which highlighted the importance of appropriate sized end plates to achieve nominal two-dimensional flow. However, some spanwise directed streaklines are visible close to the ends of the model which is caused by junction flow phenomena (horseshoe vortex).

Figures 4.2 and 4.3 show detailed visualisations of the oil flow patterns on the $D_{strut}/D_{shell} = 0.67$ and $D_{strut}/D_{shell} = 0.93$ cases respectively. In both cases the flow separated at the trailing edge of the shell and was reasonably uniform in the spanwise direction. Neither the presence of the strut nor its size had an effect on the separation location which was important when comparing the two cases to each other. The flow pattern on the rear of the strut for both cases (see figures 4.2c and 4.3c) showed two-dimensional streaklines, uniform in the spanswise direction. A strong vortex shedding mechanism with reversed flow velocities on the rear of the strut could explain this pattern.

The difference between the two cases were seen when the side view of the strut was inspected (see figures 4.2b and 4.3b). In both images an impingement or reattachment line was observed along the entire span of the model. This reattachment indicated that the flow which separated off the trailing edge of the shell impinged on the strut. To either side of the reattachment point the time-averaged streaklines indicated the flow flowed in opposite directions. Upstream of the impingement point the flow direction was inside the shell-strut cavity while downstream of the impingement line the flow moved to the rear of the strut. The oil flow pattern to the upstream of the impingement line differs between the two cases. The streaklines downstream of the impingement line for the $D_{strut}/D_{shell} = 0.93$ case were better defined. The streaklines stopped resulting in a darker line along the span

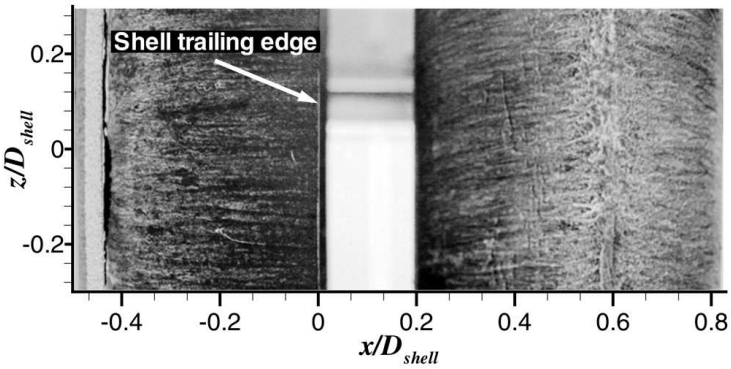

(a) Side view of the shell. Flow from left to right.

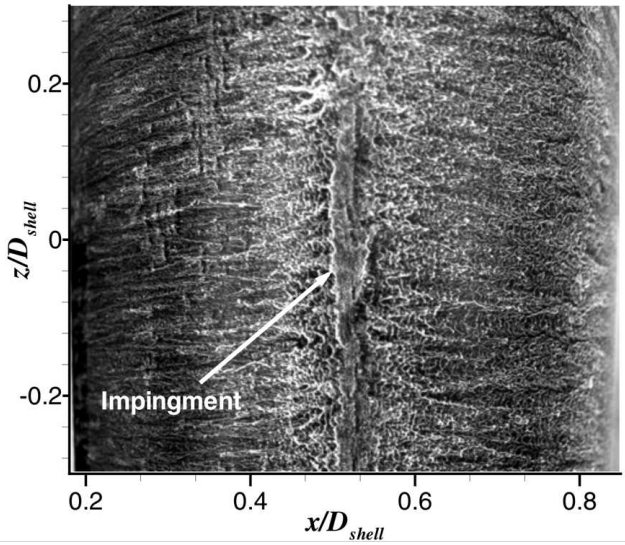

(b) Side view of the strut. Flow from left to right.

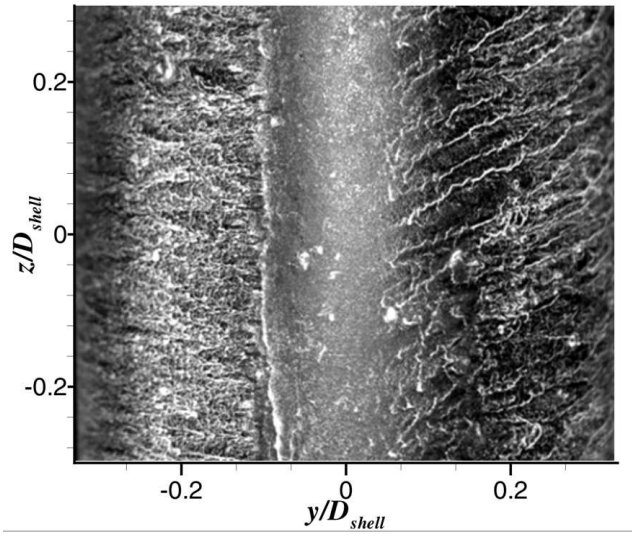

(c) Rear view of the strut. Flow out of page.

FIGURE 4.2: Oil flow visualisation of $D_{strut}/D_{shell} = 0.67$ case. $U_\infty = 30\ m/s$.

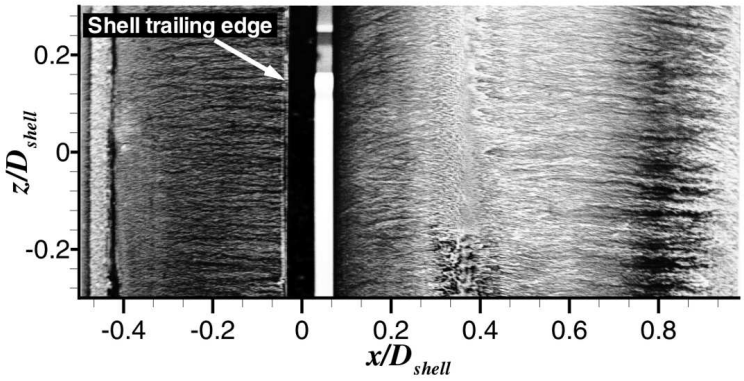

(a) Side view of the shell. Flow from left to right.

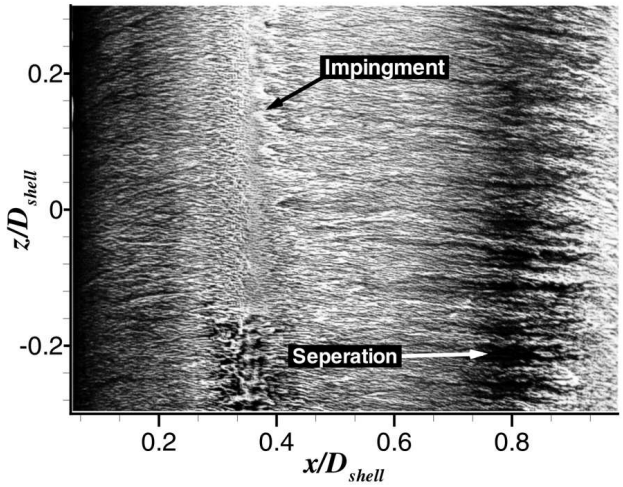

(b) Side view of the strut. Flow from left to right.

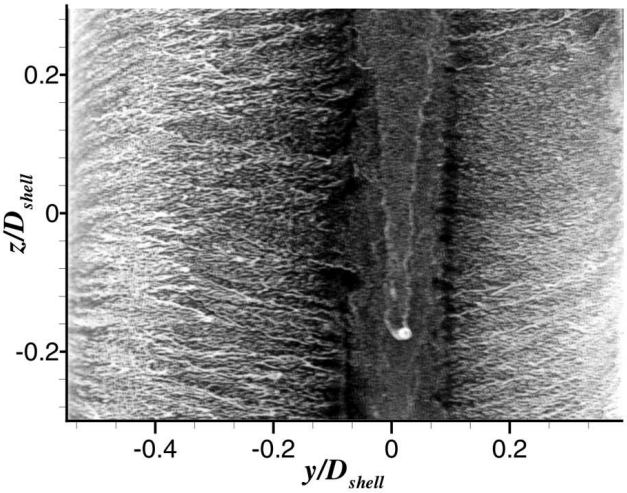

(c) Rear view of the strut. Flow out of page.

FIGURE 4.3: Oil flow visualisation of $D_{strut}/D_{shell} = 0.93$ case. $U_\infty = 30\ m/s$.

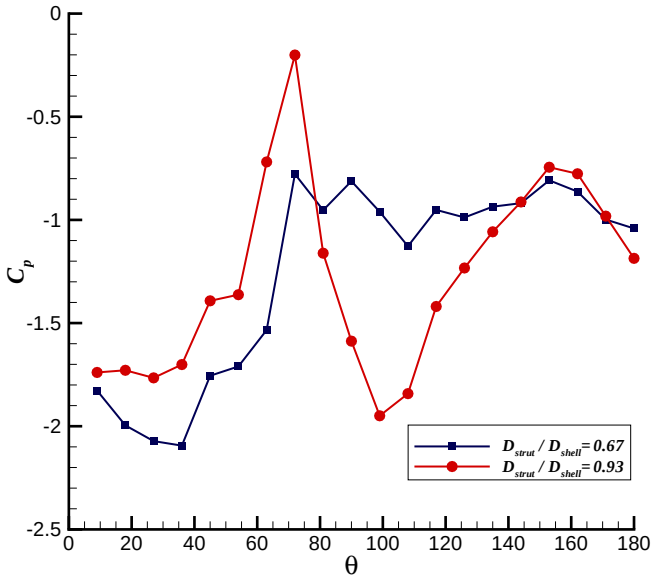

FIGURE 4.4: Pressure distribution around the strut. $x_c/D_{shell} = 1/2$. $U_\infty = 30\ m/s$.

of the strut which was believed to be the point at which flow separated to then produce the vortex shedding described earlier. This pattern was not seen for the $D_{strut}/D_{shell} = 0.67$ case.

Pressure measurements around the strut were recorded in order to understand the flow physics over the strut and what effect the strut diameter had on the overall flow. From the oil flow visualisations it was determined that the flow around the different sized struts behaved differently. Figure 4.4 shows the pressure distributions around the struts of the $D_{strut}/D_{shell} = 0.67$ and $D_{strut}/D_{shell} = 0.93$ cases. In both cases the struts were located at $x_c/D_{shell} = 1/2$.

The $D_{strut}/D_{shell} = 0.67$ pressure distribution shows low C_p values in the shell strut cavity region which increases to a value of $C_p = -0.8$ at $\theta = 72°$. This point corresponded approximately to the location described previously where the shear layer coming off the shell impinged on the strut. Between $\theta = 72°$ and $\theta = 153°$ C_p did not vary considerably although it dipped at $\theta = 108°$. The pressure distribution for the strut in the $D_{strut}/D_{shell} = 0.93$ case showed that the flow around the strut differed to that of the smaller strut. The distribution in the cavity region was similar to that of the $D_{strut}/D_{shell} = 0.67$ case which showed that the shear layer impinged on the strut at approximately $\theta = 72°$. The C_p dropped sharply to a value of $C_p = -1.95$ at $\theta = 100°$. This location corresponded to

the approximate location where the streaklines present after the impingement line stopped in the oil flow images. This sharp drop indicated that higher velocity flow was present in that region when compared to the smaller strut.

4.1.1.2 Effects of strut location

This section deals with the effects the strut location has on the time averaged on-surface flow. Again the two cases $D_{strut}/D_{shell} = 0.67$ and $D_{strut}/D_{shell} = 0.93$ were used to highlight the difference each using three strut locations. The strut for the $D_{strut}/D_{shell} = 0.67$ case was positioned at $x_c/D_{shell} = 1/4$, 2/5 and 1/2 whilst the $D_{strut}/D_{shell} = 0.93$ case used $x_c/D_{shell} = 2/5$, 1/2 and 2/3 for the strut location. It was not possible to position the larger strut closer to the shell due to physical constraints, nonetheless the three locations used showed a trend and some conclusions could be drawn from them.

Pressure distributions around the strut for the $D_{strut}/D_{shell} = 0.67$ case were taken at three different strut locations, $x_c/D_{shell} = 1/4$, 2/5 and 1/2 (see figure 4.5a). The pressures around all three cases did not vary greatly between $\theta = 0°$ and $\theta = 45°$, inside the cavity region. The strut locations $x_c/D_{shell} = 2/5$, 1/2 showed that the flow separating off the shell impinged on the strut. This position varied between the two strut locations, the further away the strut was situated the closer the impingement line was to the front of the strut. The $x_c/D_{shell} = 1/4$ case did not manifest a clear impingement line but instead showed lower C_p values up to $\theta = 108°$ when compared to the other two strut locations. It was believed that due to the closer proximity of the strut to the shell the shear layer off the shell did not impinge on the strut, hence the strut was in the shell's wake. The $x_c/D_{shell} = 1/4$ case also exhibited the lowest base pressure with a difference of $\Delta C_p = 0.36$ when compared to $x_c/D_{shell} = 1/2$.

The pressure distributions around the strut for the $D_{strut}/D_{shell} = 0.93$ are shown in figure 4.5b. The pressure around the strut in the cavity region for the $x_c/D_{shell} = 2/5$ case showed lower C_p values when compared to the other two strut locations. Unlike the $D_{strut}/D_{shell} = 0.67$ case the location where the shear layer impinged on the strut was approximately at $\theta = 72°$ for all three configurations, not varying with the strut location. This result was not conclusive as the resolution of the pressure points was not adequate to locate the exact point of impingement although the location of the strut in this case had less of an effect on this position. The $x_c/D_{shell} = 2/3$ case showed the highest base pressure when compared to

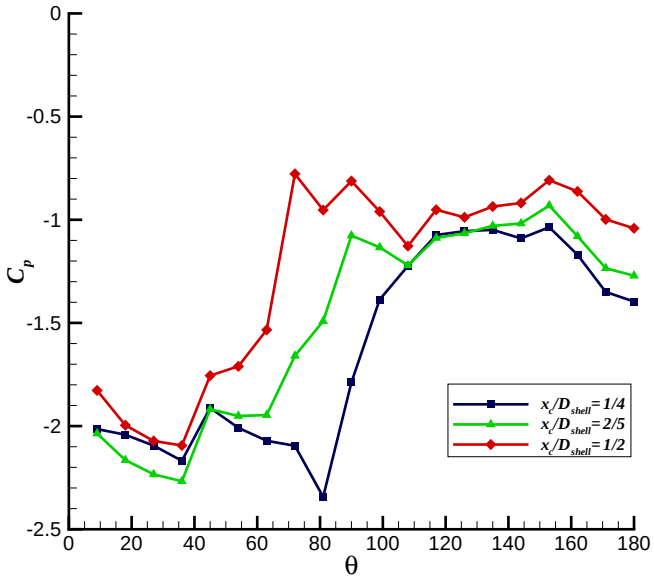

(a) $D_{strut}/D_{shell} = 0.67$.

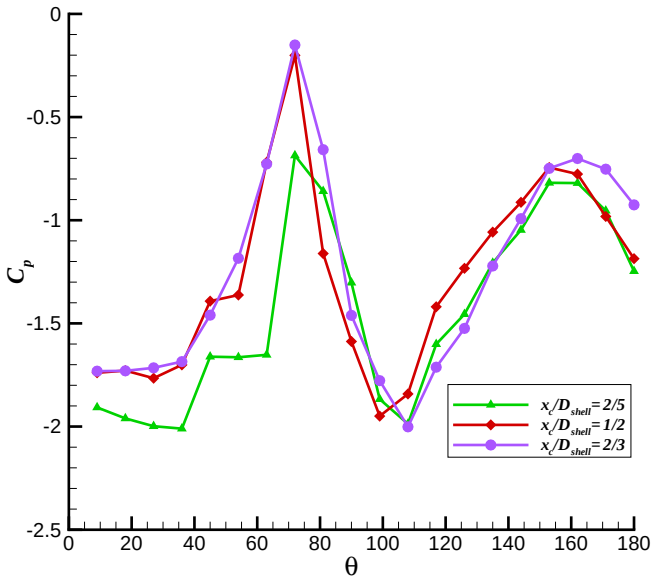

(b) $D_{strut}/D_{shell} = 0.93$.

FIGURE 4.5: Pressure distribution around the strut. $U_\infty = 30\ m/s$.

the other two strut locations with an increase of $\Delta C_p = 0.3$ when compared to $x_c/D_{shell} = 2/5$ which had the lowest base pressure.

4.1.1.3 Effect of splitter plate

The effect of introducing a splitter plate between the shell and the strut is presented in this section. The on-surface flow is discussed for the the $D_{strut}/D_{shell} = 0.67$ and $D_{strut}/D_{shell} = 0.93$ cases both fitted with a splitter plate denoted by the abbreviation *Splt*. In both cases the location of the strut was fixed at $x_c/D_{shell} = 1/2$.

Figures 4.6 and 4.7 show detailed visualisations of the oil flow patterns on the $D_{strut}/D_{shell} = 0.67Splt$ and $D_{strut}/D_{shell} = 0.93Splt$ configurations respectively. In both cases the flow separated at the trailing edge of the shell and were uniform in the spanwise direction. Neither the presence of the strut nor its size had an effect on the separation location which was important when comparing the two cases to each other.

The flow around the strut showed different behaviours for the two configurations being investigated. Figure 4.6b shows the side view oil flow pattern on the $D_{strut}/D_{shell} = 0.67Splt$ strut. The pattern does not reveal a flow impingement line as was apparent in the $NoSplt$ configuration. The flow pattern between $x/D_{shell} = 0.2$ and 0.4 was not well defined and was devoid of streaklines. A possible explanation was that the velocity of the flow in the cavity region was greatly reduced due to the splitter plate. The streaklines between $x/D_{shell} = 0.2$ and 0.87 showed that the flow in this region was moving in the upstream direction indicating that the flow was recirculating in this region. This hypothesis was strengthened when the rear of the strut was analysed showing that two symmetric recirculation regions on either side of the strut were present. The downward direction of the streaklines was thought to be due to the low recirculating velocity making the oil more susceptible to gravity.

Figure 4.7b shows the side view oil flow pattern on the strut for the $D_{strut}/D_{shell} = 0.93Splt$ configuration. Two clear separation lines were present on either side of an impingement line. The impingement line was located further upstream when compared to the $NoSplt$ configuration. As was described previously there was no clear oil flow pattern within the cavity region due to the presence of the splitter plate. The separation line upstream of the impingement line indicated the presence of a recirculation bubble between the separated shear layers off the shell and

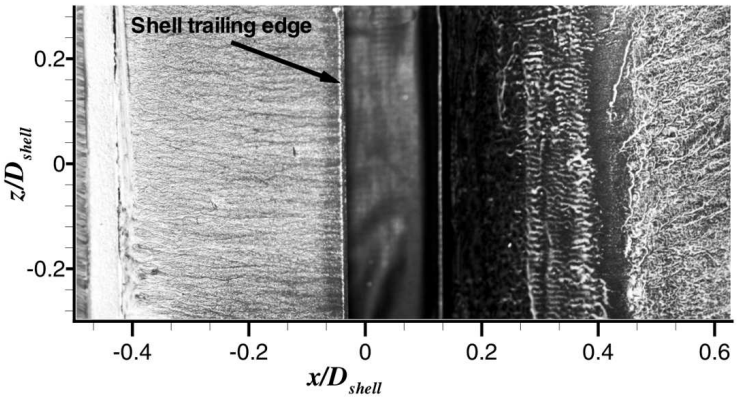

(a) side view of the shell. Flow from left to right.

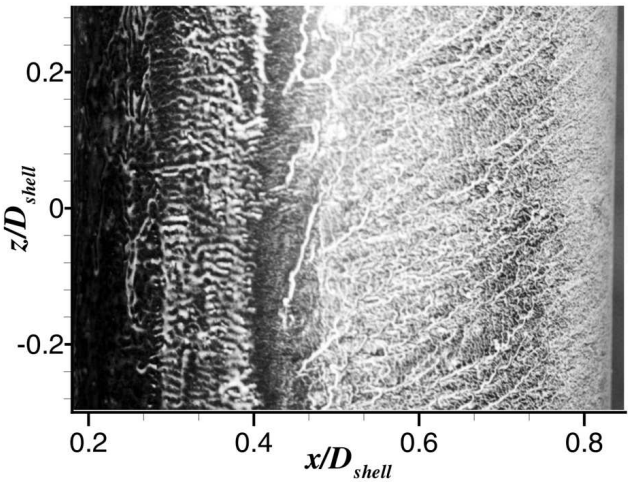

(b) Side view of the strut. Flow from left to right.

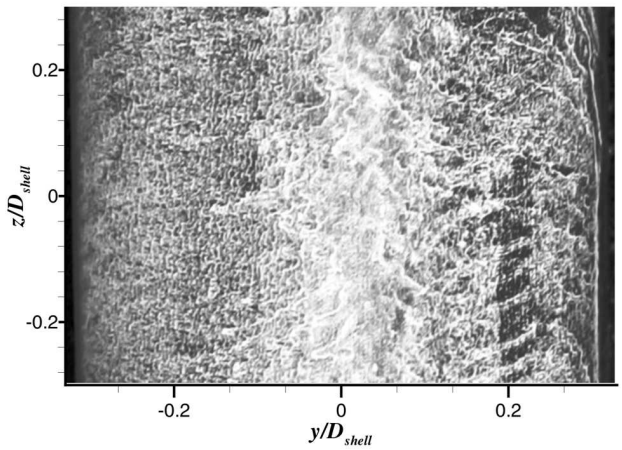

(c) Rear view of the strut. Flow out of page.

FIGURE 4.6: Oil flow visualisation of $D_{strut}/D_{shell} = 0.67 Splt$ configuration. $U_\infty = 30\ m/s$.

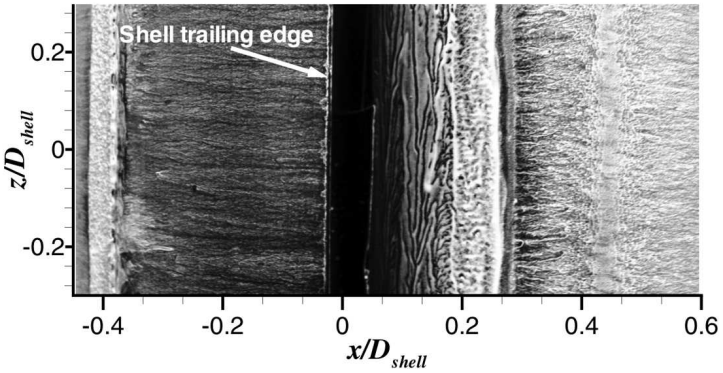

(a) side view of the shell. Flow from left to right.

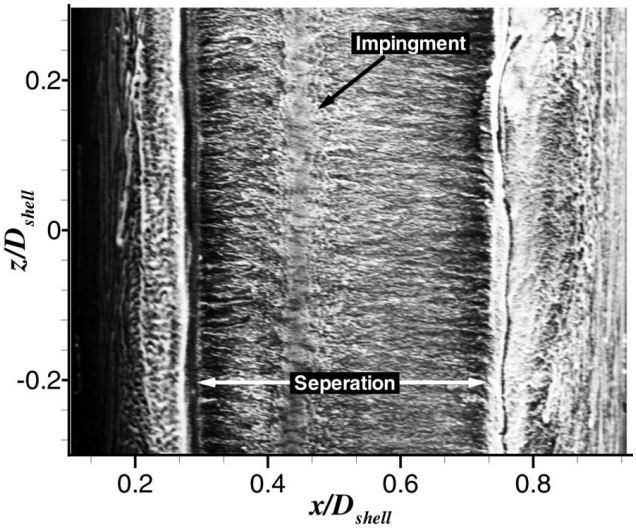

(b) Side view of the strut. Flow from left to right.

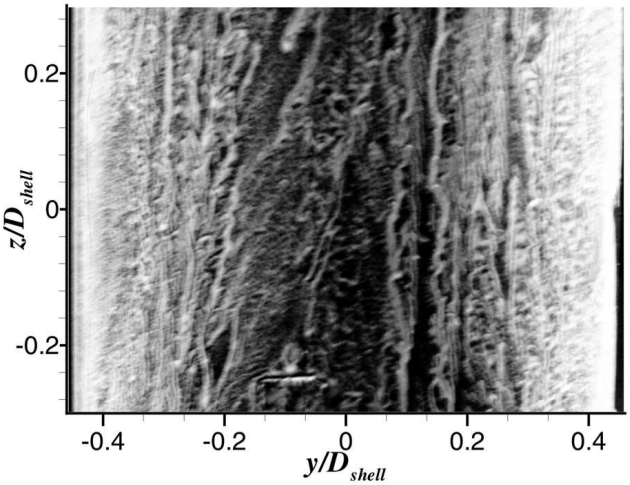

(c) Rear view of the strut. Flow out of page.

FIGURE 4.7: Oil flow visualisation of $D_{strut}/D_{shell} = 0.93Splt$ configuration. $U_\infty = 30\ m/s$.

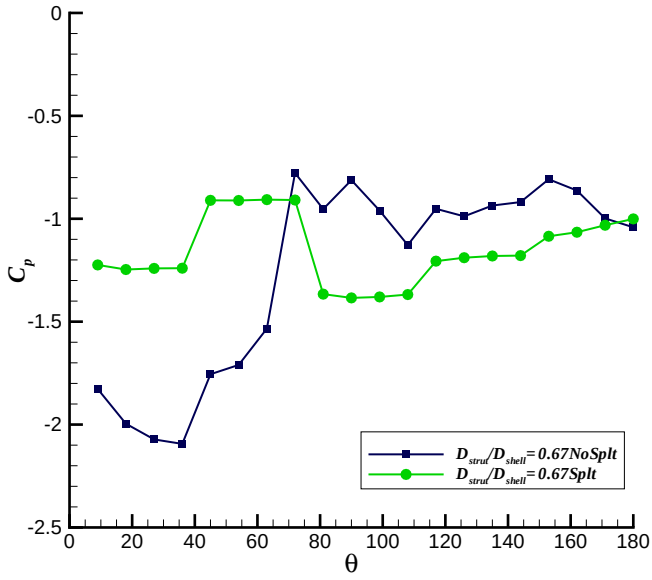

(a) $D_{strut}/D_{shell} = 0.67$.

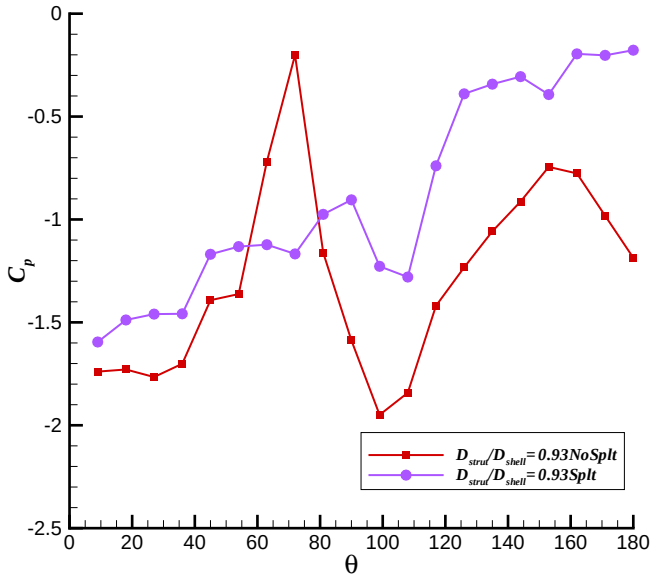

(b) $D_{strut}/D_{shell} = 0.93$.

FIGURE 4.8: Pressure distribution around the strut. $U_\infty = 30\ m/s$.

the strut. The strong separation line downstream of the impingement line and the chaotic non-symmetrical flow structure observed on the rear of the strut (see figure 4.7c) were thought to be caused by a near wake with low velocities without spanwise coherence. Again the low velocities present caused the oil to accumulate and dribble down due to gravity.

Figure 4.8 compares the pressure distributions around the strut for the *NoSplt* and the *Splt* configurations. The splitter plate in the $D_{strut}/D_{shell} = 0.67$ configuration showed higher C_p values around the strut in the cavity region. As was seen in the oil flow visualisation the recirculation velocities inside the cavity were reduced due to the splitter plate blocking the interaction of the shear layers in the cavity. Interestingly the C_p values in the cavity region for the $D_{strut}/D_{shell} = 0.93$ did not differ in the same way when the splitter plate was used. Whereas the shear layer impinged on the strut in the *Nosplt* configuration, showing up as a higher value of C_p at $\theta = 72°$, for the *Splt* configuration the shear layer attached to the strut at $\theta = 81°$ and then separated at $\theta = 108°$. The base pressure was for the *Splt* case which resulted in a difference of the base pressure of $\Delta C_p = 1$.

4.1.2 Off-surface Flow

4.1.2.1 Effect of strut diameter

The time averaged velocity contours using PIV are shown in figure 4.9. These measurements were taken in the $x - y$ plane at $z/D_{shell} = 0$.

From the time averaged contours the differences between the two smaller struts and the two larger ones could be seen. Aft of the shell trailing edge the thin high gradient shear layer impinged on to the struts. The streamlines showed that the flow upstream of the impingement point recirculated inside the strut shell cavity for all four cases. Figure 4.10a shows velocity profiles for the four cases extracted from the PIV data at a streamwise location of $x/D_{shell} = 0.7$. This location corresponds to a position just aft of the point where the flow impinges on the struts. The velocity flow aft of the impingement point in the vicinity of the strut for the $D_{strut}/D_{shell} = 0.86$ and $D_{strut}/D_{shell} = 0.93$ are higher than that of the the two smaller strut cases. This ties in with the hypothesis made in sections 4.1.1.1 which indicated that the flow was accelerated further round the two larger struts. It was also apparent that the deflected velocities in the lateral direction were higher with an increase of 8% in the maximum velocity for the

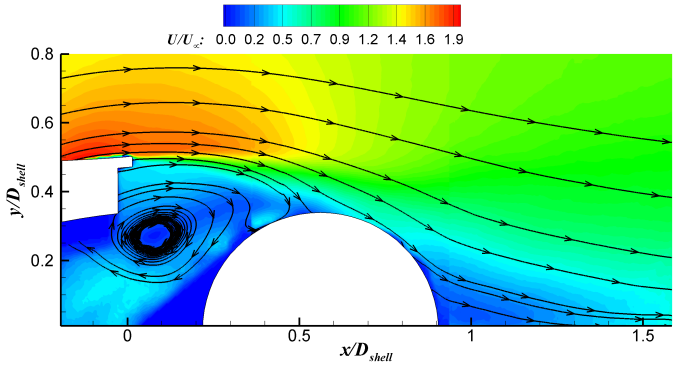

(a) $D_{strut}/D_{shell} = 0.67$.

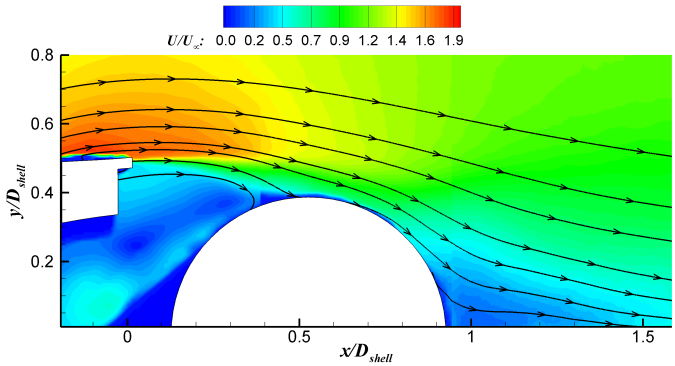

(b) $D_{strut}/D_{shell} = 0.76$.

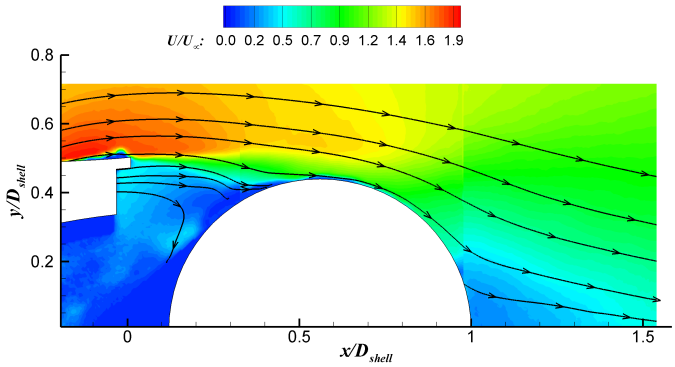

(c) $D_{strut}/D_{shell} = 0.86$.

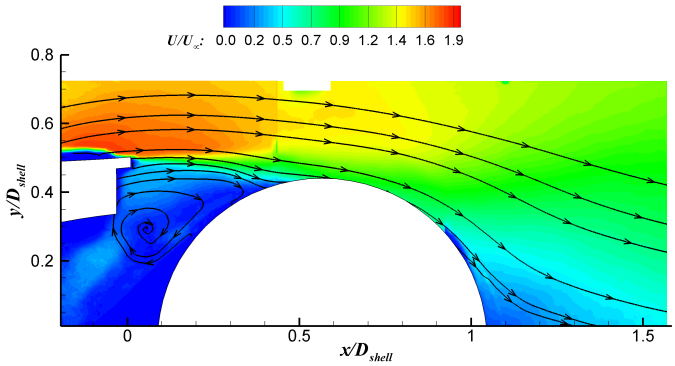

(d) $D_{strut}/D_{shell} = 0.93$.

FIGURE 4.9: Time-averaged velocity contours and streamlines. $U_\infty = 30\ m/s$. Flow from left to right.

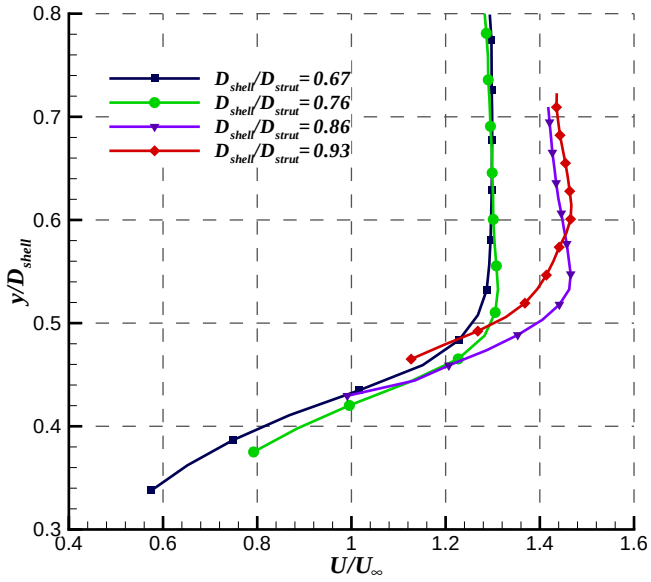

(a) $x/D_{shell} = 0.7$.

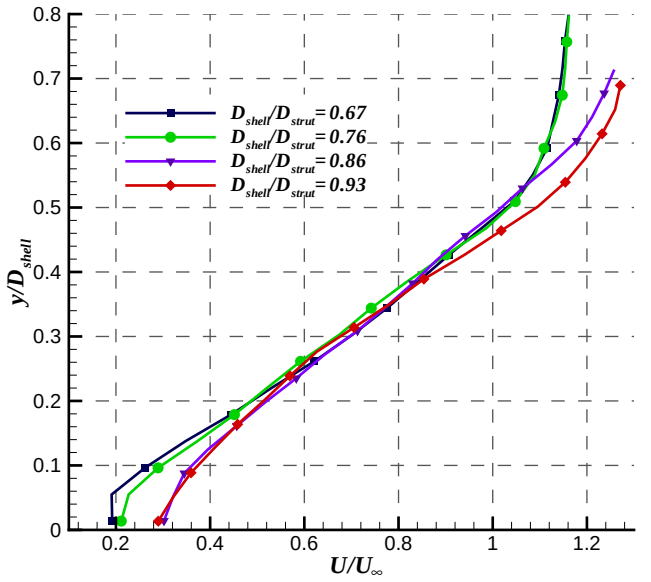

(b) $x/D_{shell} = 1.2$.

FIGURE 4.10: Non-dimensional velocity profiles from PIV data at two different x/D_{shell} positions and $z/D_{shell} = 0$. $U_\infty = 30\ m/s$.

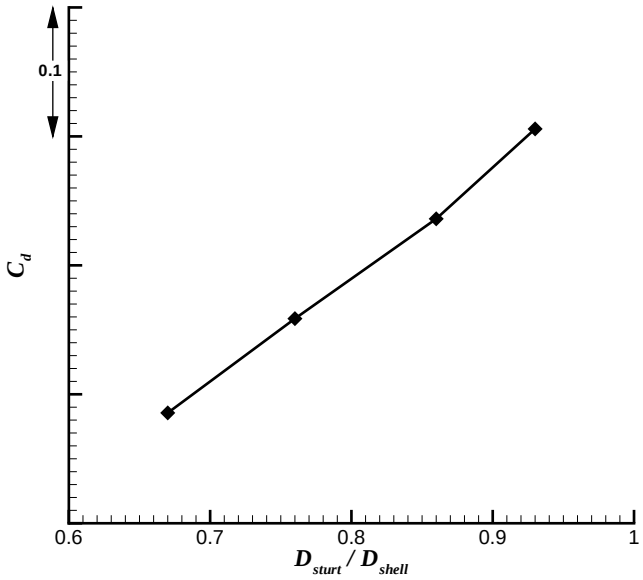

(a) Coefficient of drag for different strut diameters. C_d vs D_{strut}/D_{shell}

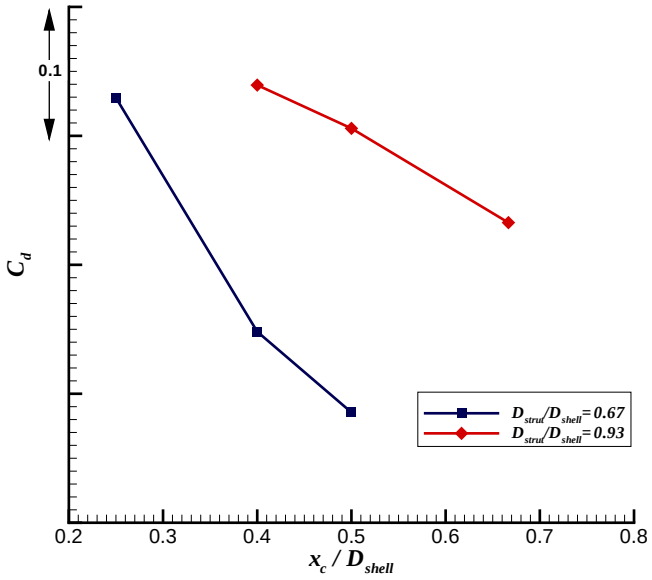

(b) Coefficient of drag for different strut locations. C_d vs x_c/D_{shell}.

FIGURE 4.11: Coefficient of drag. $U_\infty = 40\ m/s$.

$D_{strut}/D_{shell} = 0.86$ and $D_{strut}/D_{shell} = 0.93$ cases.

Velocity profile data in the wake of the four cases are shown in figure 4.10b. At $y/D_{shell} = 0$ the velocities for the two smaller struts are 50% less than those of the other two cases. The $D_{strut}/D_{shell} = 0.86$ and $D_{strut}/D_{shell} = 0.93$ cases showed wider wakes with the larger strut case having the widest wake.

Figure 4.11a shows the mean coefficients of drag, C_d for the different struts. The drag increased as the strut diameter increased. The drag increased by $\Delta C_d = 0.24$ between the smallest and the largest strut. This increase in drag was attributed to the lower base pressure behind the strut for $D_{strut}/D_{shell} = 0.93$ configuration and the wider wake produced by the model.

4.1.2.2 Effect of strut location

From the results discussed in section 4.1.1.2 the effect of the strut location on the off-surface flow can be deduced. The pressure distribution showed that the flow around the strut did not vary with strut location except for the $D_{strut}/D_{shell} = 0.67$ case when the strut was located at $x_c/D_{shell} = 1/4$. At this position the pressure distribution around the strut showed that the flow off the shell did not impinge on the strut and that the strut was entirely in the wake of the shell.

From the drag measurements for the $D_{strut}/D_{shell} = 0.67$ case (see figure 4.11b), $x_c/D_{shell} = 1/4$ resulted in the largest drag with a drag increase of 18% when compared to the $x_c/D_{shell} = 2/5$ case. The difference between $x_c/D_{shell} = 0.4$ and $x_c/D_{shell} = 0.5$ was less with a drag reduction of 9%.

The mean drag for the $D_{strut}/D_{shell} = 0.93$ case showed similar behaviour to the $D_{strut}/D_{shell} = 0.67$ case where the drag decreased by 12% as the strut was positioned further away from the shell(see figure 4.11b).

4.1.2.3 Effect of splitter plate

The time averaged velocity contours of the four cases, $D_{strut}/D_{shell} = 0.67Splt$, $0.76Splt$, $0.86Splt$ and $0.93Splt$ with the splitter plate fitted between the shell and strut are shown in figure 4.12. The *Splt* configurations, when compared to those in figure 4.9 showed the effect of the splitter plate on the overall flow around the model. In the first two configurations, $D_{strut}/D_{shell} = 0.67Splt$ and $0.76Splt$, the shear layer aft of the trailing edge did not interact with the strut. Furthermore

the presence of the splitter plate did not allow the shear layers to roll-up inside the cavity. The $D_{strut}/D_{shell} = 0.86Splt$ and $0.93Splt$ configurations showed a different flow structure. The shear layer attached to the strut but the overall effect was still different to the $NoSplt$ case as no apparent oscillatory flow featured within the cavity. As the shear layers did not roll-up in the cavity and therefore did not accelerate the flow further around the shell the local velocity of the flow at the trailing edge of the shell was reduced when the splitter plate was introduced.

Velocity profiles plotted at $x_c/D_{Shell} = 0.7$ presented in figure 4.13 shows that even if the deflected velocity at the trailing edge of the shell was reduced with the introduction of the splitter plate the velocity at $x/D_{Shell} = 0.7$, $y/D_{Shell} = 0.8$ was $\Delta U/U_\infty = 0.12$ greater for the $D_{strut}/D_{shell} = 0.67Splt$ when compared to the $NoSplt$ configuration. In the case of the $D_{strut}/D_{shell} = 0.93Splt$ the velocities were similar in magnitude to those of the $NoSplt$ configurations. For the $D_{strut}/D_{shell} = 0.67Splt$ and $0.76Splt$ configurations the wake width increased in comparison to the $Nosplt$ configurations. This increase in width was attributed to the shear layers not diffusing and not impinging on the strut and hence widening the wake as this convected downstream. In the case of the $D_{strut}/D_{shell} = 0.93Splt$ configuration the wake was narrower than that for the $NoSplt$ configurations. The attachment and subsequently the separation of the flow off the rear of the strut reduced the width of the wake.

The dimensions of the strut and its distance from the shell were shown to affect the mean drag. Figure 4.14a shows the mean drag versus the strut diameter when the splitter plate was used and figure 4.14b shows the mean drag versus the strut location for $D_{strut}/D_{shell} = 0.93Splt$. The mean drag for the $D_{strut}/D_{shell} = 0.67Splt$ and $0.76Splt$ cases were 24% and 7%, respectively, larger than their respective $Nosplt$ configurations. The displacement of the shear layer from the strut caused the strut to be entirely in the wake of the shell leading to lower pressures around the back face of the strut, thus increasing the pressure drag. The drag was decreased by a maximum $\Delta C_d = 0.5$ when the splitter plate was used on the $D_{strut}/D_{shell} = 0.86Splt$ and $0.93Splt$. As was the case for the $Nosplt$ configurations the $Splt$ configurations showed the same trend when the strut was located further away from the shell, i.e. the mean drag decreased (see figure 4.14b).

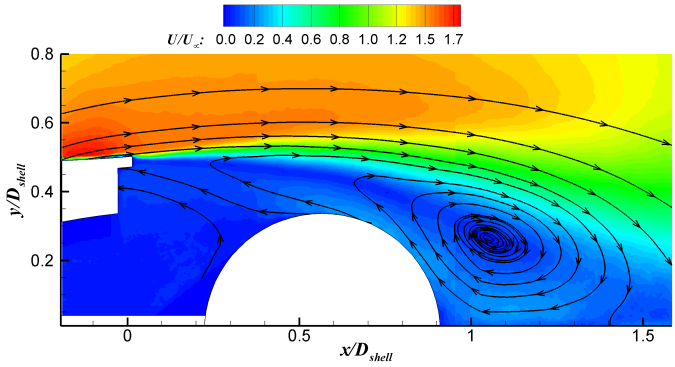

(a) $D_{strut}/D_{shell} = 0.67 Splt$

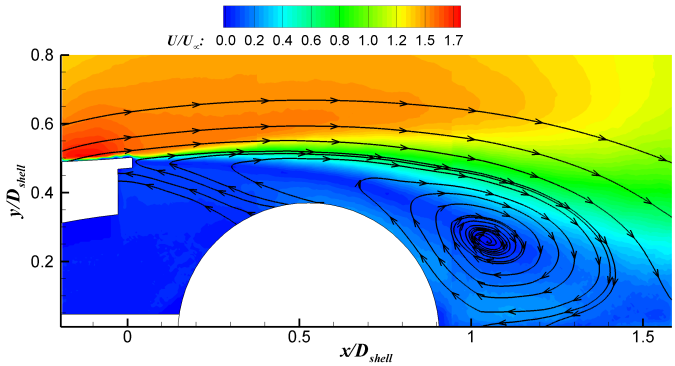

(b) $D_{strut}/D_{shell} = 0.76 Splt$

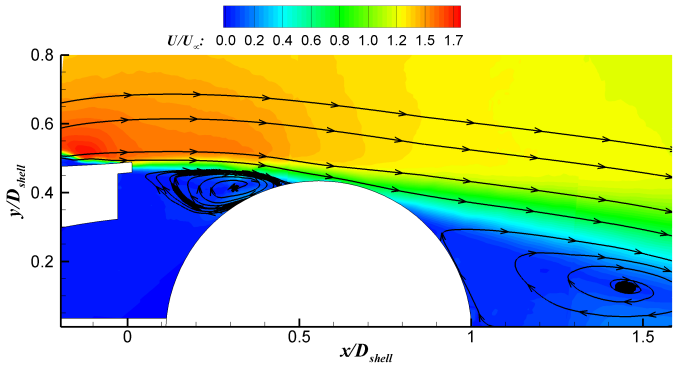

(c) $D_{strut}/D_{shell} = 0.86 Splt$

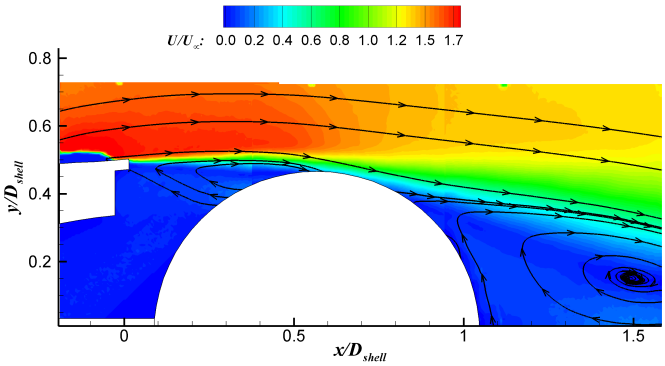

(d) $D_{strut}/D_{shell} = 0.93 Splt$

FIGURE 4.12: Time-averaged velocity contours and streamlines. $U_\infty = 30\ m/s$. Flow from left to right.

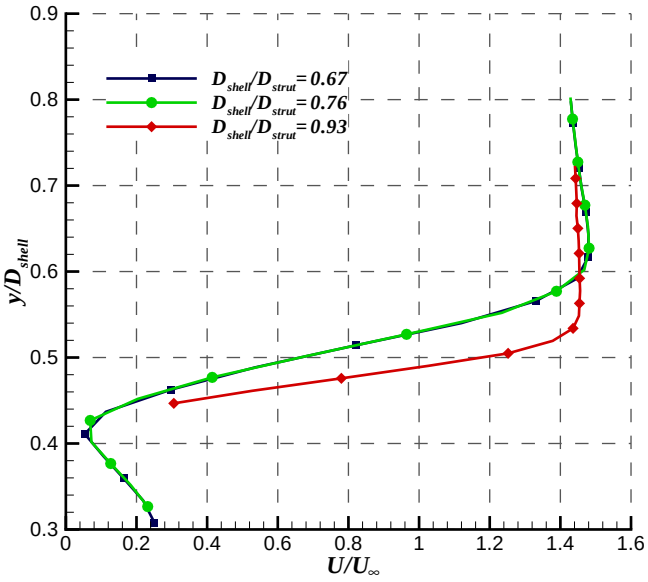

(a) $x/D_{shell} = 0.7$.

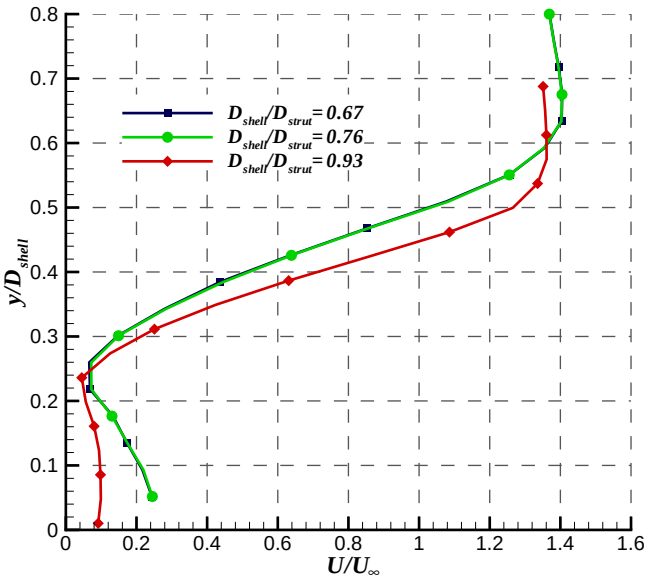

(b) $x/D_{shell} = 1.2$.

FIGURE 4.13: Non-dimensional velocity profiles from PIV data at two different x/D_{shell} positions and $z/D_{shell} = 0$. *Splt* configurations. $U_\infty = 30\ m/s$.

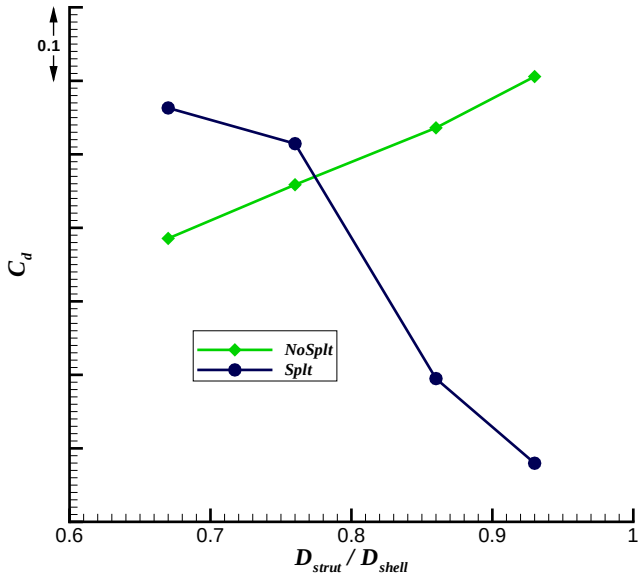

(a) Coefficient of drag, C_d vs strut diameter.

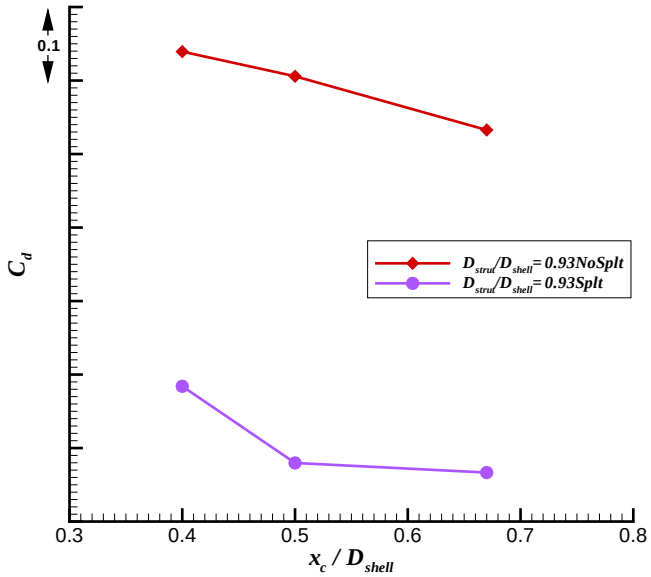

(b) Coefficient of drag, C_d vs strut diameter. $D_{strut}/D_{shell} = 0.93$. $x_c/D_{shell} = 1/2$

FIGURE 4.14: Comparison of drag forces. $U_\infty = 40\ m/s$.

4.2 Vortex Shedding

In the previous section the time averaged results were presented and showed the overall mean flow around the model. Although this information was useful to highlight the differences between the uses of the different struts sizes, strut locations and the use of the splitter plate it did not include the unsteady aerodynamics which was important to understand how the model generated aerodynamic noise.

4.2.1 Effect of strut diameter

In order to understand how the flow was behaving instantaneous vorticity maps were studied. It could be argued that the images presented in figures 4.15 and 4.16 are not representative of the flow field as they are composed of two image planes taken at different points n times. The figures are used to aid in explaining what the author observed over the course of the study both in the experiments, using a smoke wand and in the computational work.

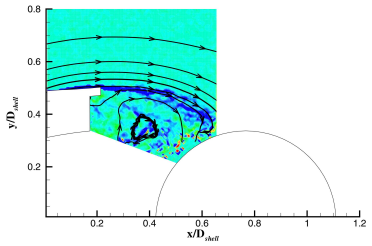

(a) Position 1 at $t = t_1$.

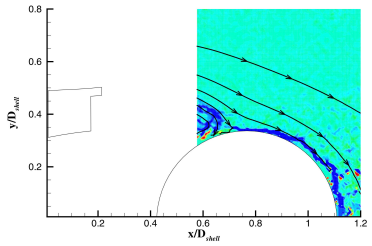

(b) Position 2 at $t = t_1$.

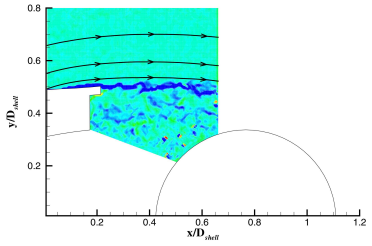

(c) Position 1 at $t = t_2$.

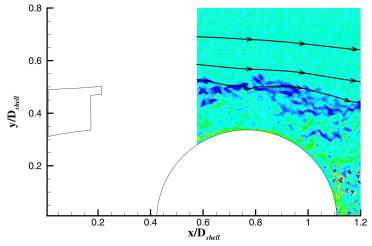

(d) Position 2 at $t = t_2$.

FIGURE 4.15: Instantaneous vorticity contours and streamlines $D_{strut}/D_{shell} = 0.67$. $U_\infty = 30\ m/s$. Flow from left to right.

Figures 4.15 and 4.16 shows two pairs of images displaying the flow at two different arbitrary points in time, $t = t_1$ and $t = t_2$. At t_1 the shear layer aft of the fairing's

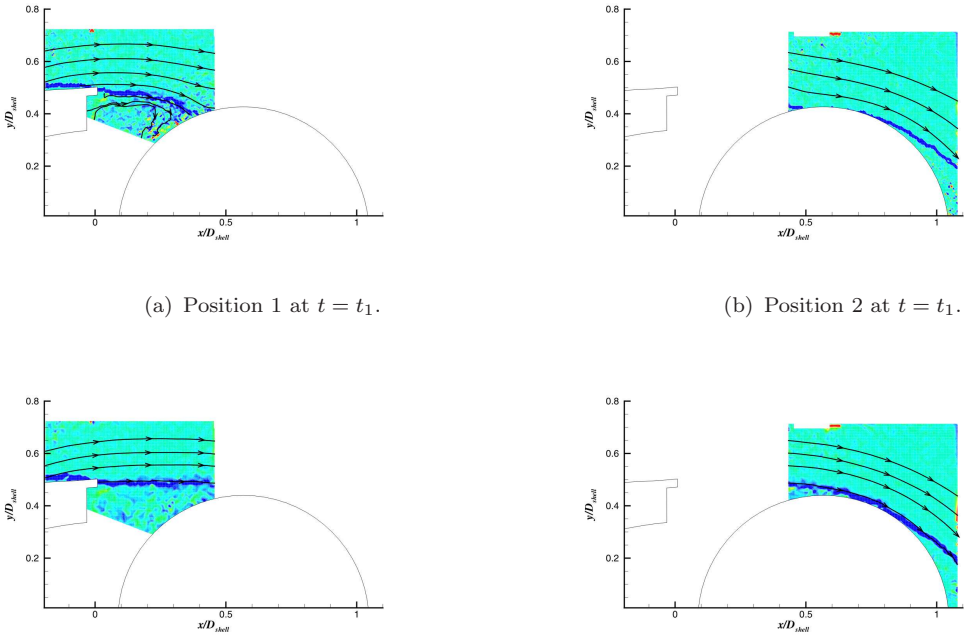

(a) Position 1 at $t = t_1$.

(b) Position 2 at $t = t_1$.

(c) Position 1 at $t = t_2$.

(d) Position 2 at $t = t_2$.

FIGURE 4.16: Instantaneous vorticity contours and streamlines. $D_{strut}/D_{shell} = 0.93$. $U_\infty = 30\ m/s$. Flow from left to right.

trailing edge impinged onto the downstream strut. The open cavity between the shell and the strut allowed the interaction between the two opposing shear layers causing the shear layer to roll-up within the shell-strut cavity. The roll-up of the shear layer inside the cavity cut off the circulation to the rear of the strut which caused the flow to remain attached around the rear face of the strut. At this stage the recirculating flow continued to grow, fed by the circulation from its connected shear layer, until it was strong enough to draw the other shear layer into the cavity. The approach of the oppositely-signed vorticity cut off the circulation to the first vortex which ceased to increase in strength. At $t = t_2$ the weakening first vortex inside the cavity was expelled out of the cavity which caused the shear layer not to remain attached to the strut but instead convect downstream where it developed into a vortex as the shear layers of opposite vorticity present behind the strut interacted.

For $D_{strut}/D_{shell} = 0.93$ the shear layer at $t = t_2$ was closer to the strut than in the $D_{strut}/D_{shell} = 0.67$ which affected the local flow around the strut. The proximity of the shear layer to the strut explained the increase in the velocity of the flow downstream of the impingement point.

Vorticity magnitude contours from the DES simulation for the $D_{strut}/D_{shell} = 0.93$

configuration are shown in figure 4.17. The contours clearly showed the behaviour of the vortex inside the cavity as previously described and also demonstrated that the formation of the vortex inside the cavity developed out of phase with the formation of the vortex aft of the strut.

Turbulence statistics in the form of standard deviation of velocity in the y-direction are shown in figure 4.18 for the $D_{strut}/D_{shell} = 0.67$ and $D_{strut}/D_{shell} = 0.93$ cases. The two opposing shear layers at the rear of the strut interacted and rolled up to result in high amplitude velocity fluctuation in the y-direction peaking at the centerline of the wake ($y/D_{shell} = 0$). There were marginal differences in the maxima between the two cases but what emerged was that the formation of the vortex shedding was independent of the size of the strut although its frequency and magnitude were affected.

Spectral analysis was performed on the signal recorded by the hotwire probe positioned outside the wake. In figure 4.19a the power spectral density was plotted against the non dimensional frequency $Str_{D_{shell}}$ for the four different struts at $x/D_{shell} = 1$, $y/D_{shell} = 1.3$ and $z/D_{shell} = 0$. The spectral shapes were similar for the four different cases with more energy in frequencies near the shedding frequency. These spectral peaks were associated with vortex shedding behind the model, the center frequency of this peak scaled linearly with the freestream velocity which confirmed the hypothesized nature of the fluctuation. The set of spectra can be paired up between the two smaller struts and the two larger ones. The two larger strut cases showed higher energy levels before and after the spectral peak. The shedding Strouhal number decreased from $Str_{D_{shell}} = 0.26$ to $Str_{D_{shell}} = 0.22$ with an increase in the strut diameter (see figure 4.19b). Roshko [70] defines the non-dimensional frequency to be a function of wake width, frequency and the wake velocity related to the base pressure. Using this analogy the shedding frequency would in fact decrease with an increase in the width of the wake as was seen in these results.

The effect of the vortex shedding on the aerodynamic noise was investigated using the on-surface microphones and the freefield measurement measured in the anechoic facility. The spectra presented in figure 4.20a show distinct peaks at Strouhal numbers approximately equal to those discussed above, these also scaled with velocity. The difference in the $Str_{D_{shell}}$ opposed to the dominant frequency of the velocity fluctuations from the hotwire measurements was attributed to the larger blockage in the $3' \times 2'$ wind tunnel and to the change in the aspect ratio of the model. The measured spectra were 20 dB above the background noise of the

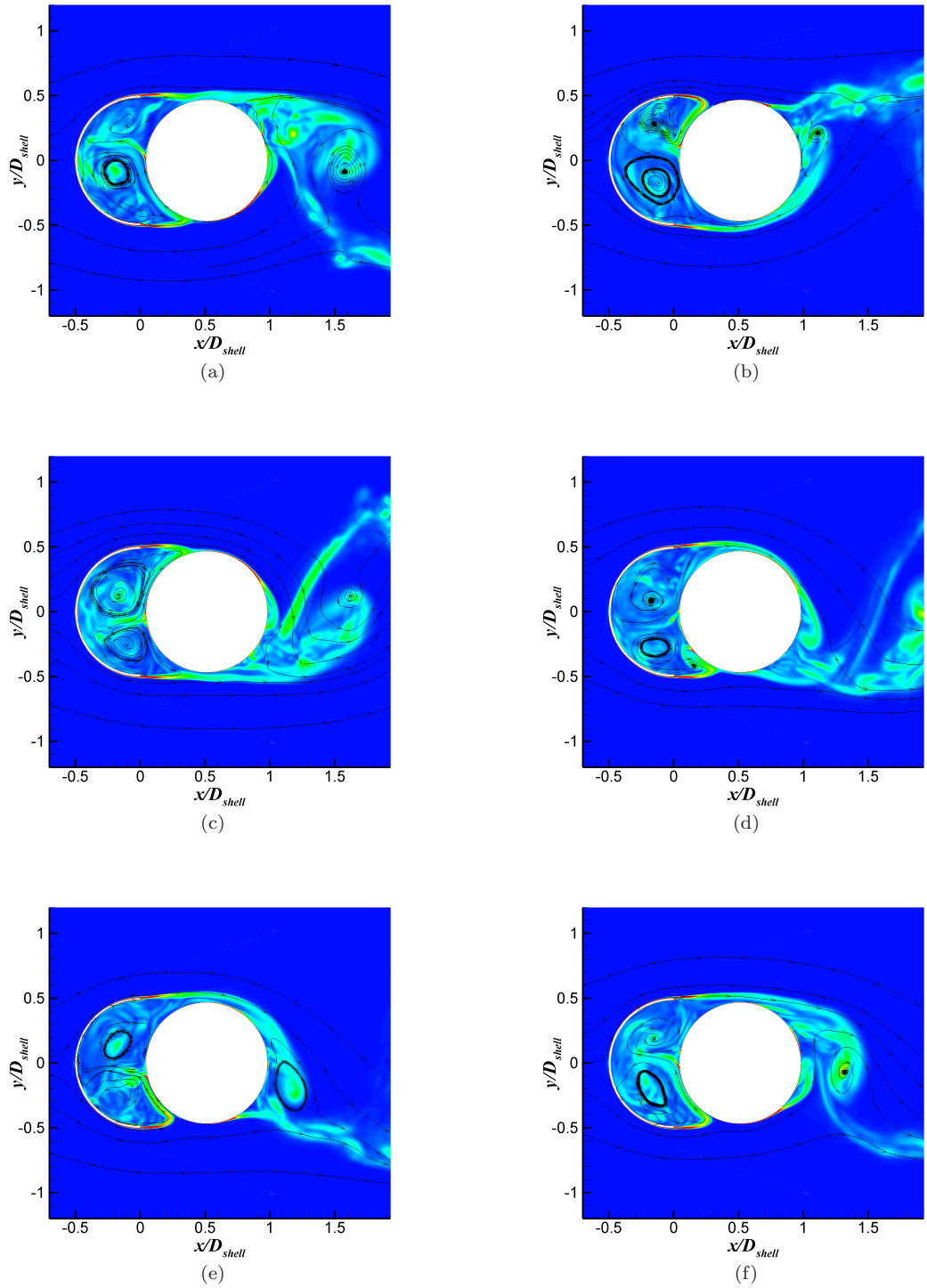

FIGURE 4.17: Instantaneous vorticity contours and streamlines. $D_{strut}/D_{shell} = 0.93$ (DES). $\Delta t = 2.25 \times 10^{-3}$ between images. $U_\infty = 40\ m/s$. Flow from left to right.

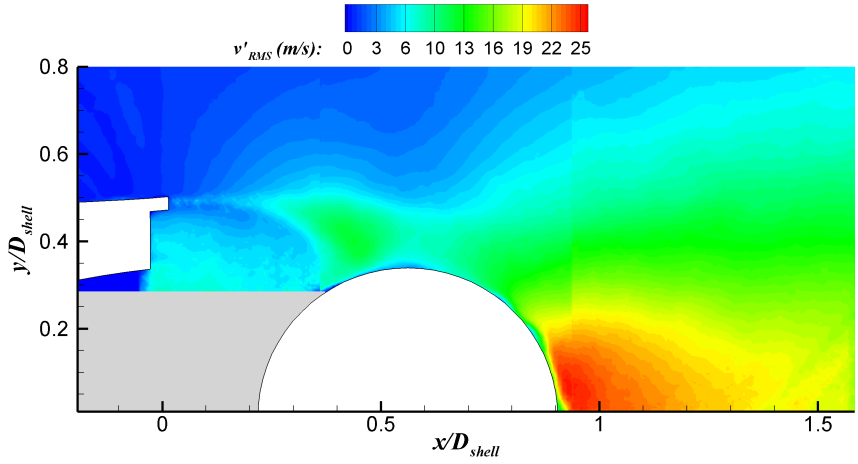

(a) $D_{strut}/D_{shell} = 0.67$.

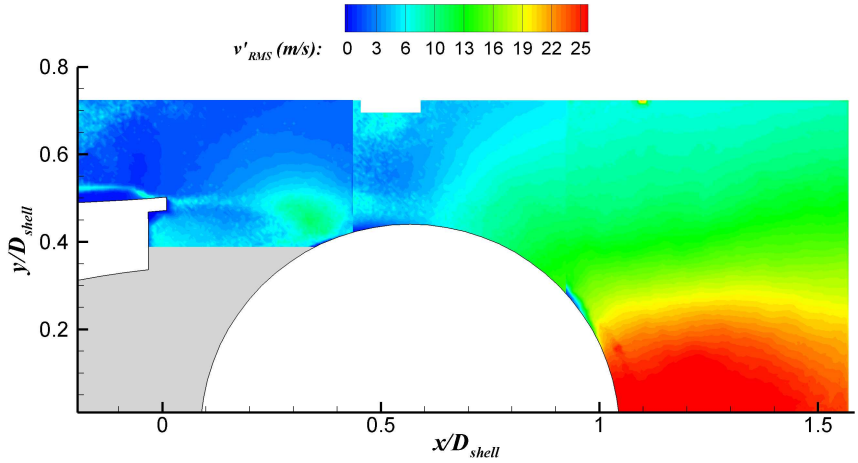

(b) $D_{strut}/D_{shell} = 0.93$.

FIGURE 4.18: Standard deviation of velocity in the y-direction. $U_\infty = 30\ m/s$. Flow from left to right.

empty chamber across the entire frequency range.

Consistent with the anechoic freefield measurements were the noise spectra of the on-surface microphone shown in figure 4.20b. The distinct peaks present in the spectra were at the double the frequency of their respective cases. The doubling of the frequency was believed to be due to the position of the microphone at the rear of the strut where it was subjected to the alternating shedding from both sides of the model. The difference in levels between the cases was caused by the difference in the local flow over the microphones.

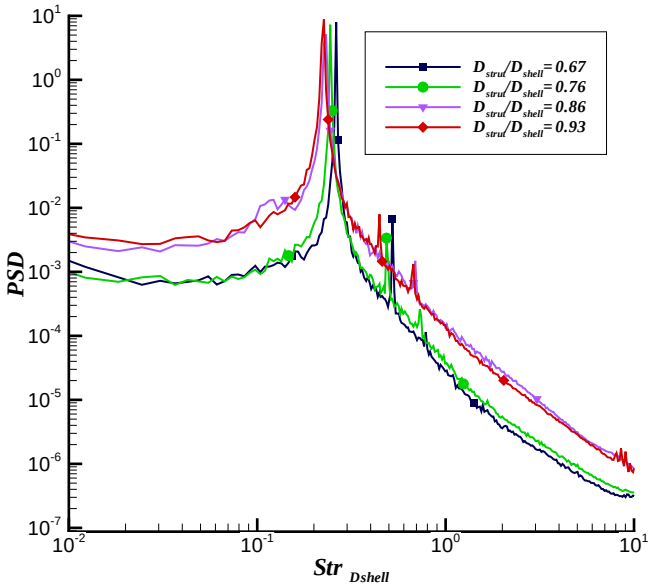

(a) Frequency spectra (PSD). $U_\infty = 30m/s$. $(x/D_{Shell} = 1, y/D_{shell} = 1.33, z/D_{shell} = 0.)$

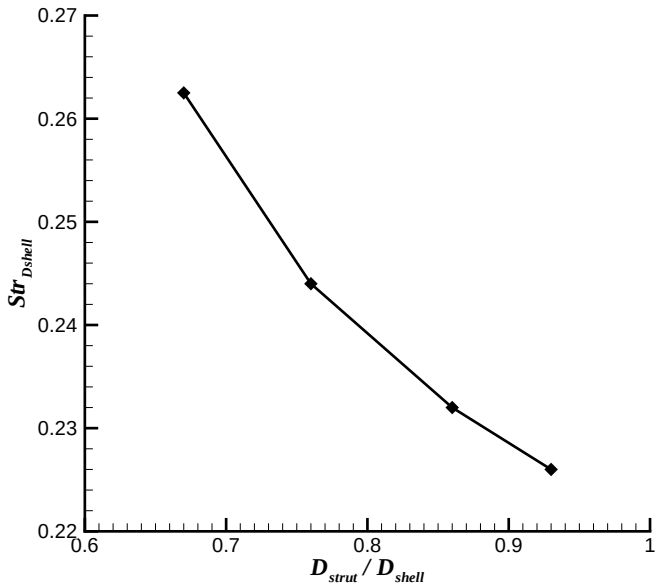

(b) $Str_{D_{shell}} vs D_{strut}$.

FIGURE 4.19: Frequency spectra (PSD) measured using hotwire and Strouhal number comparisons

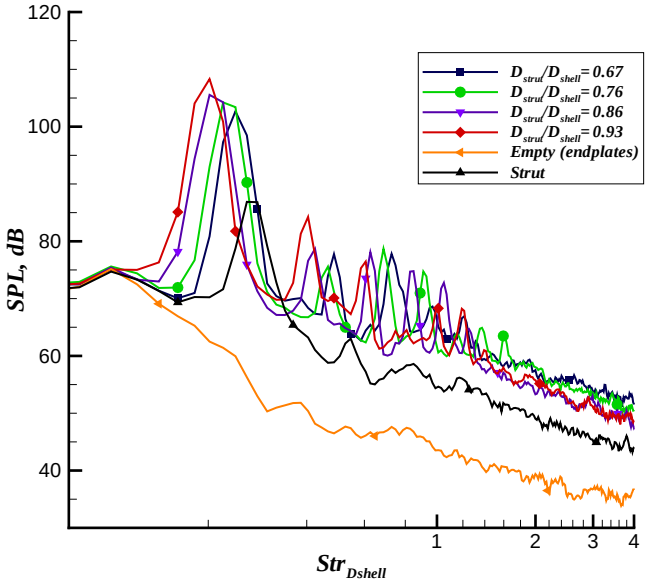

(a) Freefield acoustics measured in the anechoic chamber (averaged over microphone 1-8, $d = 2\ m$).

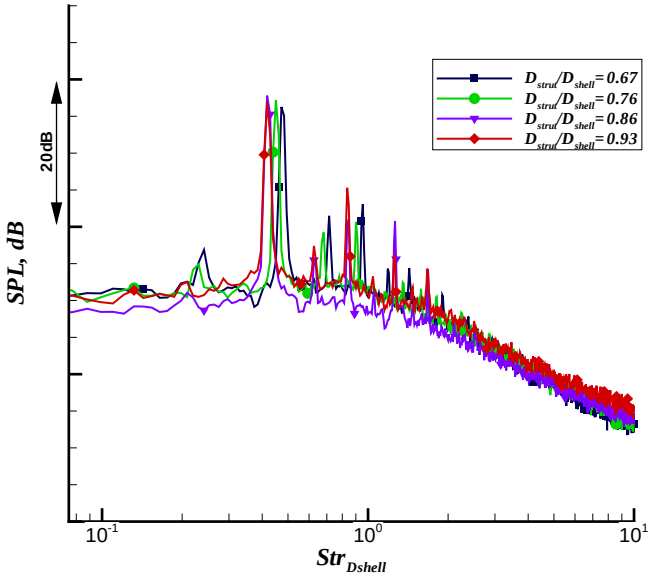

(b) On-surface microphone measurement on the rear of the strut located at $\theta = 180°$.

FIGURE 4.20: Acoustic measurements for effect of strut diameter. $U_\infty = 40m/s$.

4.2.2 Effect of strut location

The spectral shape measured at $x/D_{shell} = 1$, $y/D_{shell} = 1.3$ and $z/D_{shell} = 0$ for $D_{strut}/D_{shell} = 0.67$ shown in figure 4.21a are similar to those discussed earlier in section 4.2.1, a strong peak was centered around the shedding frequency. The strut located at $x_c/D_{shell} = 1/4$ had a shedding frequency of $Str_{D_{shell}} = 0.2$, which was less than those for the other two locations. This was also observed in the freefield microphone measurements shown in figure 4.22a. Apart from the strut location affecting the shedding frequency it did not affect the noise produced by the model as there were no significant changes in the SPL levels of the dominant peak. The hotwire measurements $D_{strut}/D_{shell} = 0.93$ case seen in figure 4.21b showed that the shedding frequency decreased with an increase in x_c/D_{shell}. This shift was not seen for the freefield microphone measurements, possibly caused by the change in the aspect ratio of the model due to the size restriction of the open-jet nozzle.

4.2.3 Effect of splitter plate

Vorticity magnitude contours from the DES simulation for the $D_{strut}/D_{shell} = 0.93$ configuration with the splitter plate are shown in figure 4.23. As opposed to the vorticity magnitude contours for the $Nosplt$ configuration, figure 4.17, the presence of the splitter plate blocked the interaction between the separated shear layers aft of the trailing edges of the shell. As a result no alternating vortex occurred in the cavity and instead the shear layers impinged on the strut with no noticeable change in the location of impingement. The contours also showed that the separation point on the rear of the strut remained constant and that the separated flow developed in a less distinct form of shedding when compared to the $NoSplt$ configuration, as noted for supercritical cylinder flow [50].

Standard velocity deviations in the y-direction for the $D_{strut}/D_{shell} = 0.67Splt$ and $0.93Splt$ configurations are shown in figure 4.24. The respective $Nosplt$ configurations exhibited higher RMS velocities (see figure 4.18) in the proximity of the strut, when compared to the $Splt$ configuration. In the case of the $Nosplt$ configurations the unsteadiness was concentrated around the strut with the highest velocity fluctuations just aft of the strut. In the $Splt$ configuration the unsteadiness moved further downstream and away from the model for the two cases. The amplitude of the velocity fluctuations in the $D_{shell}/D_{strut} = 0.93Splt$ were 50% lower than those of the smaller strut with the maxima at $y/D_{shell} = 0$ further downstream of the strut.

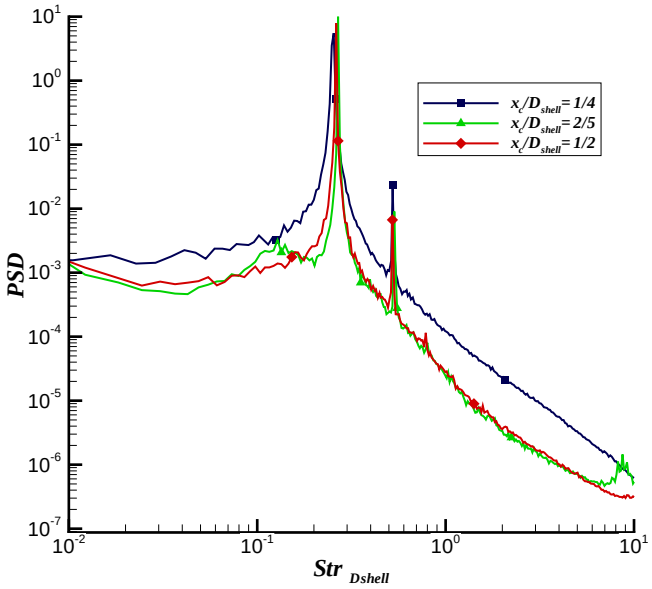

(a) $D_{strut}/D_{shell} = 0.67$.

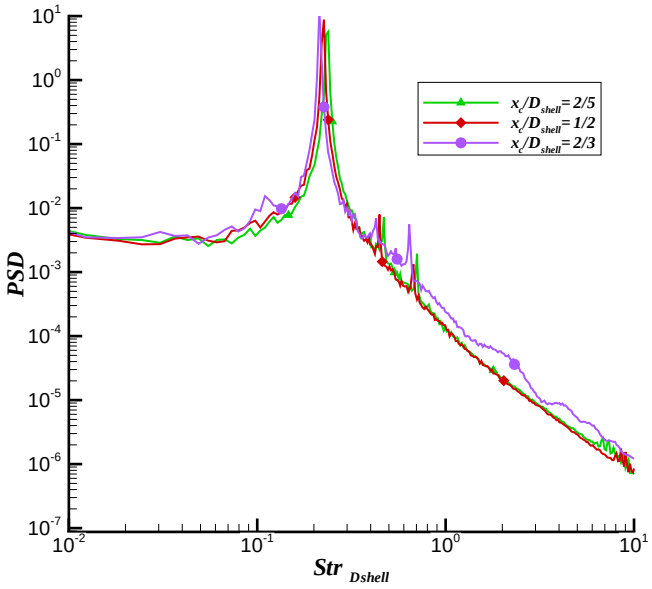

(b) $D_{strut}/D_{shell} = 0.93$.

FIGURE 4.21: Frequency spectra (PSD) measured using hotwire. $U_\infty = 30\, m/s$. $(x/D_{Shell} = 1,\ y/D_{shell} = 1.33,\ z/D_{shell} = 0.)$

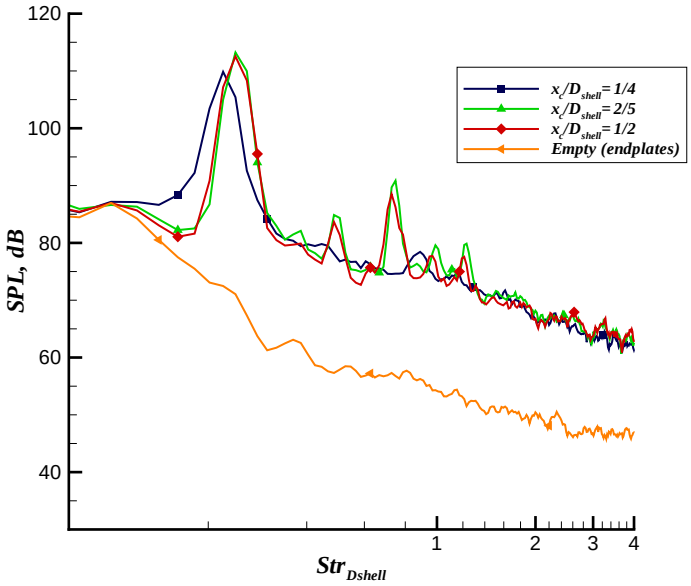

(a) $D_{strut}/D_{shell} = 0.67$.

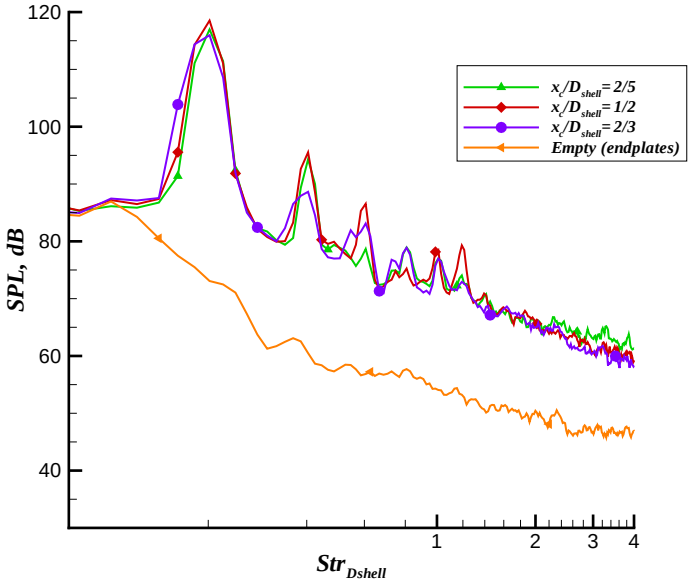

(b) $D_{strut}/D_{shell} = 0.93$.

FIGURE 4.22: Freefield acoustics measured in the anechoic chamber (averaged over microphone 1-8, $d = 2\ m$). Effect of strut location. $U_\infty = 40m/s$.

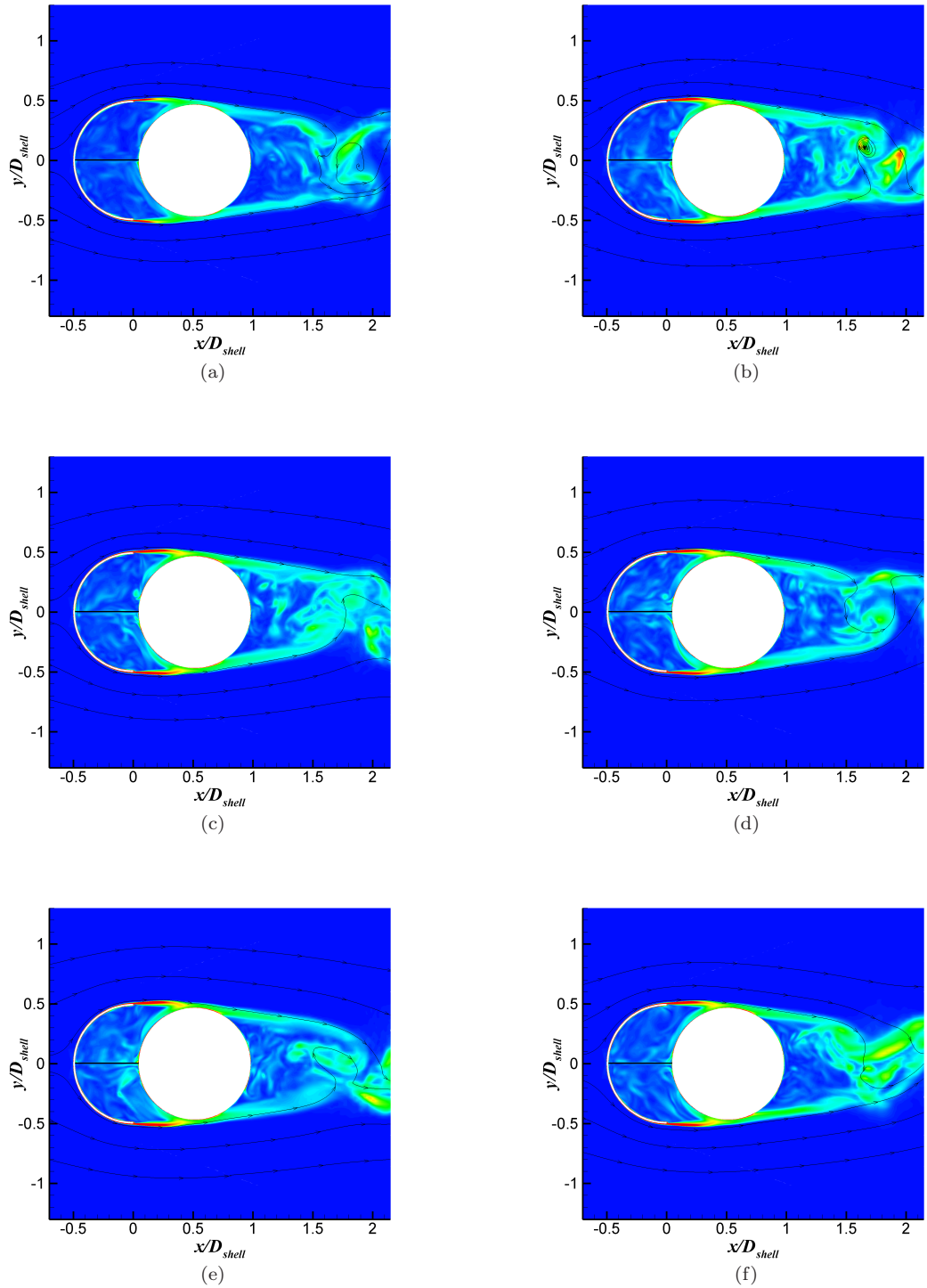

FIGURE 4.23: Instantaneous vorticity contours and streamlines. $D_{strut}/D_{shell} = 0.93$ (DES). $\Delta t = 2.25 \times 10^{-3}$ between images. $U_\infty = 40\ m/s$. Flow from left to right.

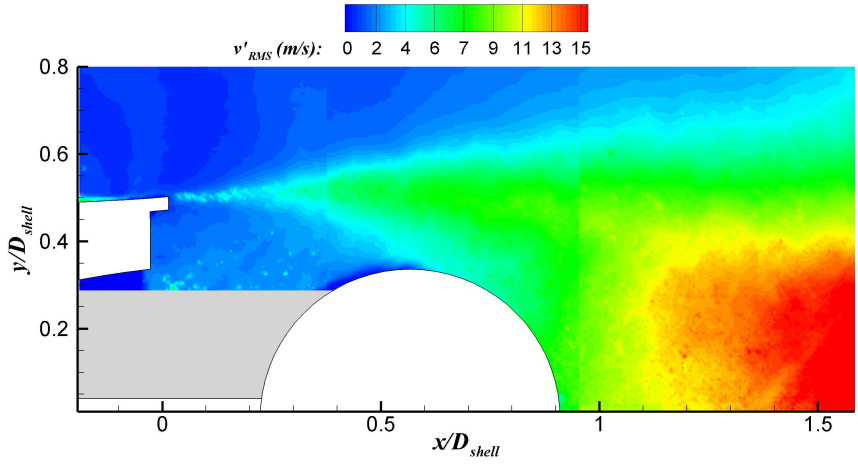

(a) $D_{strut}/D_{shell} = 0.67Splt.$

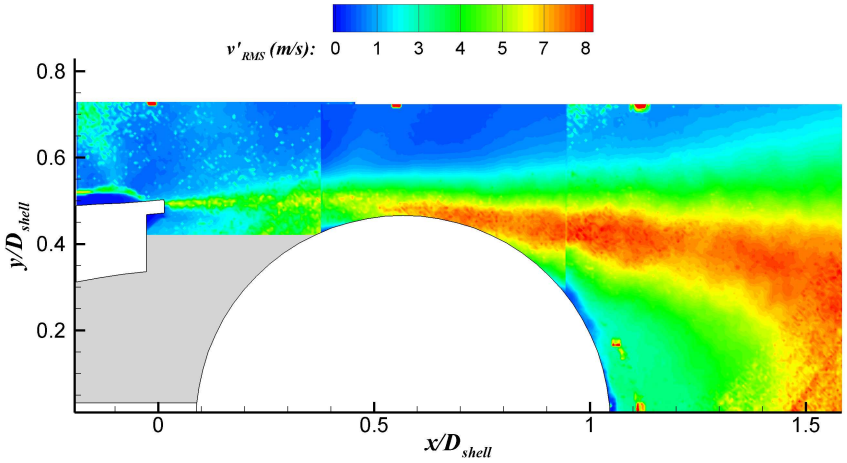

(b) $D_{strut}/D_{shell} = 0.93Splt.$

FIGURE 4.24: Standard deviation of velocity in y-direction. $U_\infty = 30m/s$. Flow from left to right.

Figure 4.25 displays the hotwire measurements for the $D_{strut}/D_{shell} = 0.67Splt$ and $0.93Splt$ configurations. As was previously seen, when the splitter plate was introduced the two smaller strut cases exhibited different flow physics from those with the larger struts. This was also seen in the measured hotwire spectra. The spectral levels for the $0.67Splt$ showed an increase in the PSD levels up to $Str_{D_{Shell}} = 0.2$, when compared to the $Nosplt$ configuration. It was possible that this increase was due to the fact that a wider wake is created by the shear layers aft of the trailing edge of the shell not impinging on the downstream strut. The shear layer did not break down, entraining the wake further downstream while still spreading. The shedding frequencies remained relatively unchanged although the strength of the shedding peak was reduced by nearly two orders of magnitude (see figure 4.25a).

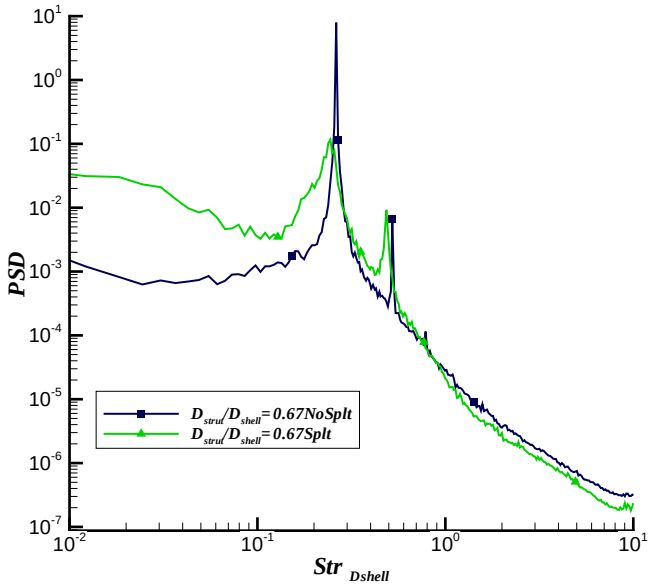

(a) $D_{strut}/D_{shell} = 0.67Splt.$

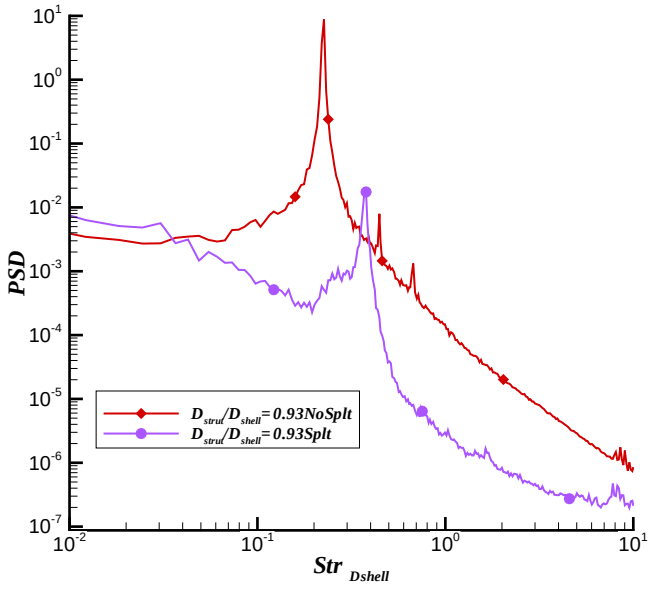

(b) $D_{strut}/D_{shell} = 0.93Splt.$

FIGURE 4.25: Frequency spectra (PSD) measured using hotwire. $U_\infty = 30m/s$. $(x/D_{Shell} = 1,\ y/D_{shell} = 1.33,\ z/D_{shell} = 0.)$

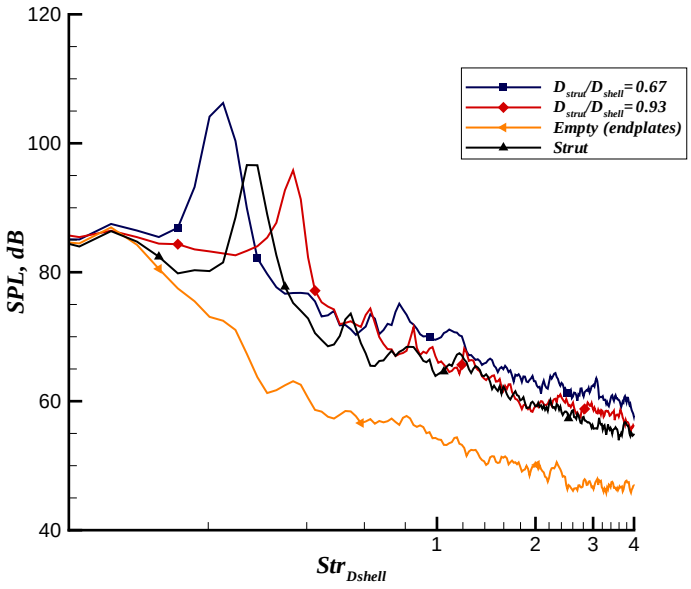

(a) Freefield acoustics measured in the anechoic chamber (averaged over microphone 1-8, $d = 2\ m$).

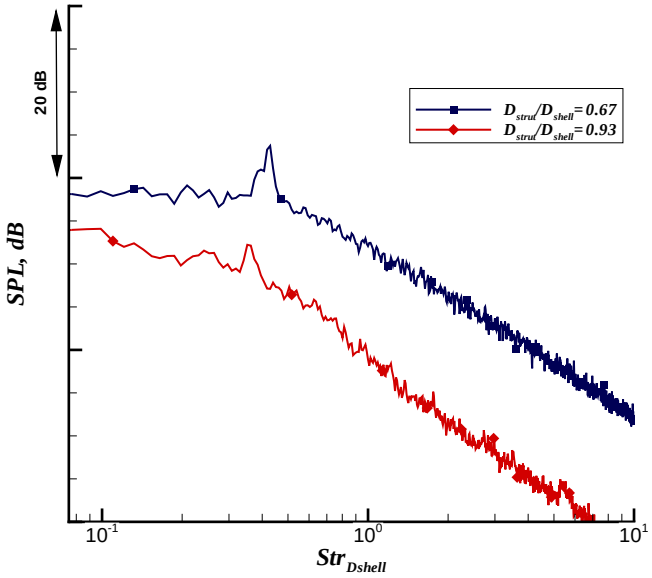

(b) On-surface microphone measurement on the rear of the strut located at $\theta = 180°$.

FIGURE 4.26: Acoustic measurements for effect of splitter plate. $U_\infty = 40m/s$.

A peak at $Str_{D_{shell}} = 0.37$ was present for the $D_{strut}/D_{shell} = 0.93Splt$ configuration (see figure 4.25b). The strong shedding peak at $Str_{D_{shell}} = 0.22$ created in the $Nosplt$ case was eliminated when the splitter plate was used. As shown before, the shear layers attached to the downstream strut and separated towards the back face of the strut which subsequently had an effect on the shedding frequency.

For the effect of the splitter plate on the acoustics, figure 4.26 presents the noise generated by the $D_{strut}/D_{shell} = 0.67Splt$ and $0.93Splt$ configurations measured by the freefield microphones and the on-surface microphones.

The freefield data revealed the same trend as was seen in the hotwire measurements. The $D_{strut}/D_{shell} = 0.67Splt$ case showed a distinct peak at approximately the shedding frequency viewed earlier, the difference was again attributed to the blockage in the $3' \times 2'$ tunnel where the hotwire measurements were taken. The on-surface microphone showed a peak at $Str_{D_{shell}} = 0.42$, doubling the frequency observed by the freefield microphone. As explained earlier the location of the microphone was at $\theta = 180°$ on the strut and hence the microphone was subjected to the alternate shedding from both sides of the model. For $D_{strut}/D_{shell} = 0.93Splt$ the dominant peak was 10 dB lower than the magnitude of the peak of the smaller strut. The on-surface microphone located at $\theta = 180°$ on the strut shown in figure 4.20b did not reveal the doubling in the frequency of the dominant peak. The oil flow pattern showed a chaotic pattern on the rear of the strut which indicated that the shear layers were breaking down in a shedding wake downstream of the strut, hence the microphone was not subjected to alternating shedding as seen for $D_{strut}/D_{shell} = 0.67Splt$.

4.2.4 Reynolds number effect

The effect of the Reynolds number on the flow around two-dimensional bodies is often compared to cylinder flow which is well documented [50] and was discussed in section 2.6. The maximum Reynolds number based on the diameter of the shell achieved was $Re_{D_{shell}} = 4 \times 10^5$. This was limited by the maximum velocity of 40 m/s achieved in the testing facilities. The in-flight Reynolds number would be approximately twice that tested and in the case of a cylinder in the supercritical regime. The Reynolds number achieved means that the flow tested was in the proximity of the critical Reynolds number and hence necessitated a sensitivity study on the Reynolds number effects.

4.2.4.1 Shell with strut

The half-cylindrical shell had a fixed trailing edge and from the oil flow visualisation showed a fixed separation point at the trailing edge at different freestream velocities ($U_\infty = 20\ m/s$ and $U_\infty = 30\ m/s$). Even if this was the case it was still not certain how the unsteady flow and the noise would be affected with a change in the Reynolds number. Figure 4.27 shows the energy spectra measured by the hotwire and the noise measured with the freefield microphones in the anechoic chamber at different freestream velocities.

The data showed that the flow over the model was insensitive to the change in the Reynolds number. The distinct shedding peak scaled with velocity in both the aerodynamic and the acoustic results, increasing in amplitude with an increase in freestream velocity. Although the model was insensitive to Reynolds number over the tested range, it was expected that the shedding phenomenon will become less distinct for high Reynolds numbers ($Re_{D_{shell}} > 10^6$) as is the case for supercritical cylinder flow [50].

4.3 Broadband Noise

The noise of the model was shown to be dominated by vortex shedding at lower frequencies and the size of the strut, its location and the splitter plate were shown to have an effect on the frequency and the magnitude of the shedding. In engineering applications it is also important to achieve broadband reductions to make the technology attractive for use on the aircraft. The next section will deal with the effect of the strut size, strut location and the effect of the splitter plate on the broadband noise.

4.3.1 Effect of strut diameter

The ΔSPL levels for the four different strut diameters are displayed in figure 4.28. The baseline configuration used was the isolated strut with its diameter equal to the one used for the $D_{strut}/D_{shell} = 0.93$ case. All four cases showed higher noise levels than the strut over the entire frequency range. This result does not invalidate the use of fairings as noise reduction devices as the strut was clean and did not have any hoses, dressings and other small details which would otherwise make it noisier.

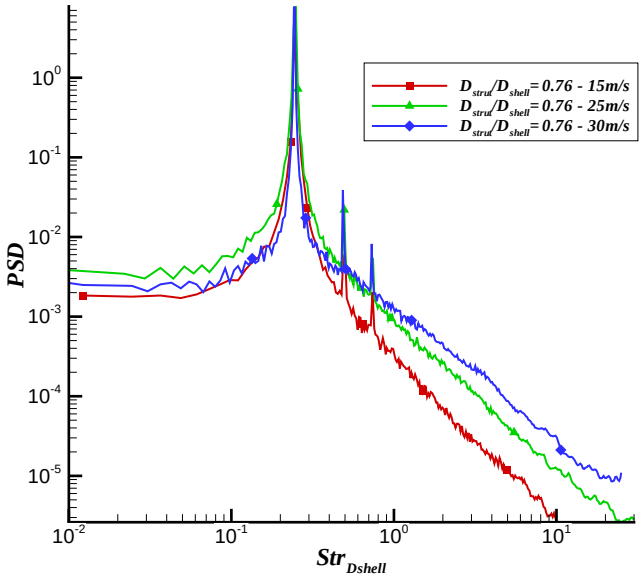

(a) Frequency spectra (PSD) measured using hotwire. $U_\infty = 30m/s$. $(x/D_{Shell} = 1,\ y/D_{shell} = 1.33,\ z/D_{shell} = 0.)$

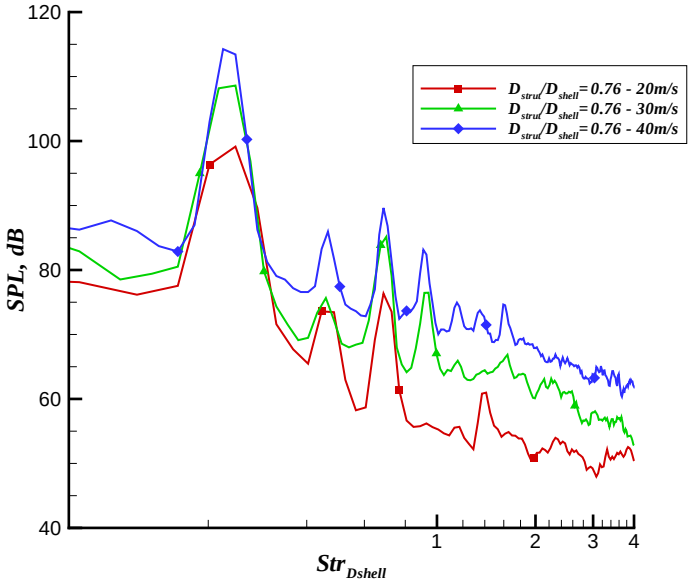

(b) Freefield acoustics measured in the anechoic chamber (averaged over microphone 1-8, $d = 2\ m$).

FIGURE 4.27: Hotwire and freefield microphone measurements for $D_{strut}/D_{shell} = 0.76$.

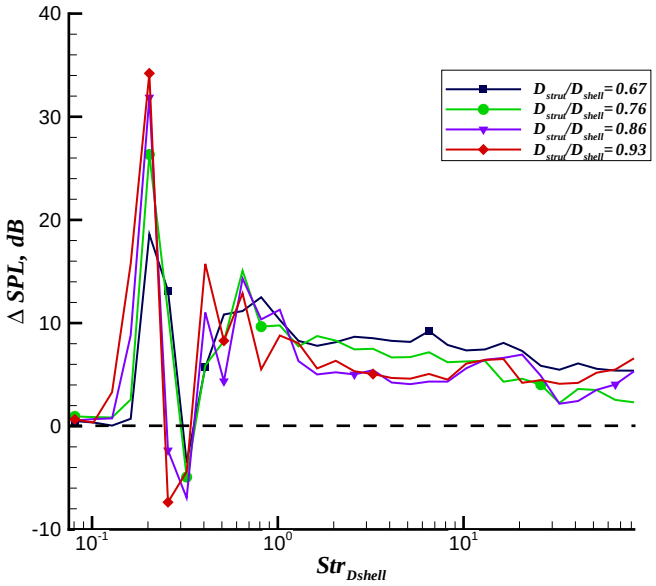

FIGURE 4.28: ΔSPL of 1/3 octave band averaged freefield spectra for effect of strut diameter, (strut used as a baseline). $U_\infty = 40\ m/s$.

The differences in the noise levels of the shedding peak for the different cases were already discussed in section 4.2.1 with the smallest strut having the lowest SPL level. At higher frequencies ($Str_{D_{shell}} = 1.3$) the cases $D_{strut}/D_{shell} = 0.86$ and $D_{strut}/D_{shell} = 0.93$ had noise levels $4dB$ lower than the smaller struts up to $Str_{D_{shell}} = 11$.

4.3.2 Effect of strut location

The effect of the strut location on the noise produced by the different cases is displayed in figure 4.29. For the $D_{strut}/D_{shell} = 0.67$ case the strut location $x_c/D_{shell} = 1/4$ was used as the baseline. The cases $x_c/D_{shell} = 2/5$ and $1/2$ showed higher noise levels than the baseline case over the entire frequency range. This demonstrated that the smaller the separation distance between the shell and the strut for the $D_{strut}/D_{shell} = 0.67$ the lower the noise produced by the model. From the time-averaged flow the strut in the $D_{strut}/D_{shell} = 0.67$, $x_c/D_{shell} = 1/4$ case was in the wake of the shell and the separated flow off the shell did not impinge on the strut. This would result in a reduction of the unsteady pressure perturbations around the strut and could explain the lower noise generated at this strut location.

The $D_{strut}/D_{shell} = 0.93$ case showed a different picture as seen in figure 4.29b. The baseline used was the strut with the same diameter as was used in the $D_{strut}/D_{shell} = 0.93$ case. Here the loudest strut location was $x_c/D_{shell} = 2/5$ from $Str_{D_{shell}} = 1$ all the way up to the higher frequencies. In this case the increase in separation distance produced noise levels approximately $3dB$ lower.

4.3.3 Effect of splitter plate

The splitter plate was shown to be effective in reducing the strength of the shedding tone by as much as $15dB$. The splitter plate also showed to reduce the broadband noise displayed in figure 4.30a. The figure shows the ΔSPL levels for the $D_{strut}/D_{shell} = 0.67Splt$ and the $D_{strut}/D_{shell} = 0.93Splt$ configurations which are compared to their respective $NoSplt$ configurations. Both configurations showed a noise reduction of approximately $5dB$ above $Str_{D_{shell}} = 1$. Figure 4.30b compares the narrow band spectra measured by the freefield microphones for the $D_{strut}/D_{shell} = 0.67Splt$ and $0.93Splt$ configurations. The configuration with the larger strut showed lower absolute levels when compared to the smaller strut. The results shown in figure 4.24 show that the flow around the models was different with the $D_{strut}/D_{shell} = 0.93Splt$ having lower levels of fluctuating velocities in the vicinity of the strut.

Source localisation was performed using the microphone array. Beamforming plots at $Str_{D_{shell}} = 9.4$ for the $D_{strut}/D_{shell} = 0.93$ without and with the splitter plate are shown in figures 4.31a and 4.32a respectively. Meaningful beamforming results at low Strouhal numbers were not possible and hence it was not possible to localize at the dominant tonal frequencies. The parallel horizontal lines in the figure represent the end-plates while the two rectangular blocks represent the shell and the cylindrical strut. The flow is from left to right. The comparison between the two plots shows that in the $Nosplt$ configuration a dominant noise source is located towards the leading edge of the strut.

Using the CFD simulation the magnitude of the on-surface dipole term is shown on the shell and the strut together with the vorticity magnitude contours at $z/D_{shell} = 0$ in figures 4.31b and 4.32b. The magnitude of the dipole term in the FWH equation is proportional to the Root Mean Square (RMS) of the on-surface pressure fluctuations with time,

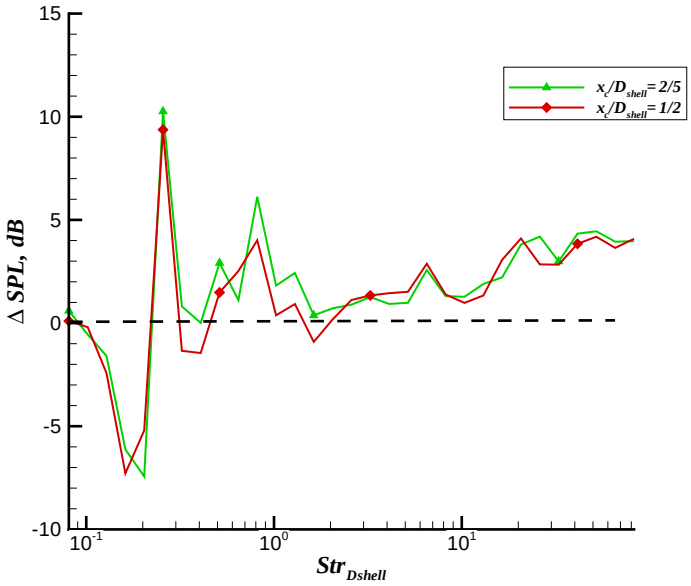

(a) $D_{strut}/D_{shell} = 0.67$

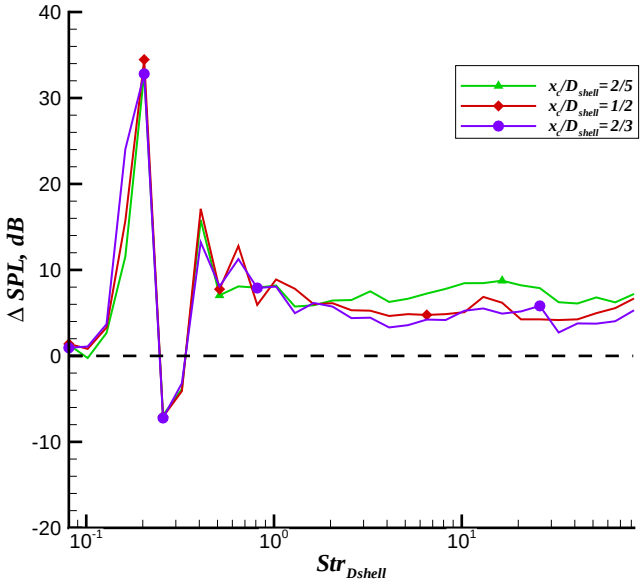

(b) $D_{strut}/D_{shell} = 0.93$

FIGURE 4.29: ΔSPL of 1/3 octave band averaged freefield spectra for effect of strut location, ($x_c/D_{shell} = 1/4$ used as basline for (a), strut used as a baseline for (b)). $U_\infty = 40\ m/s$.

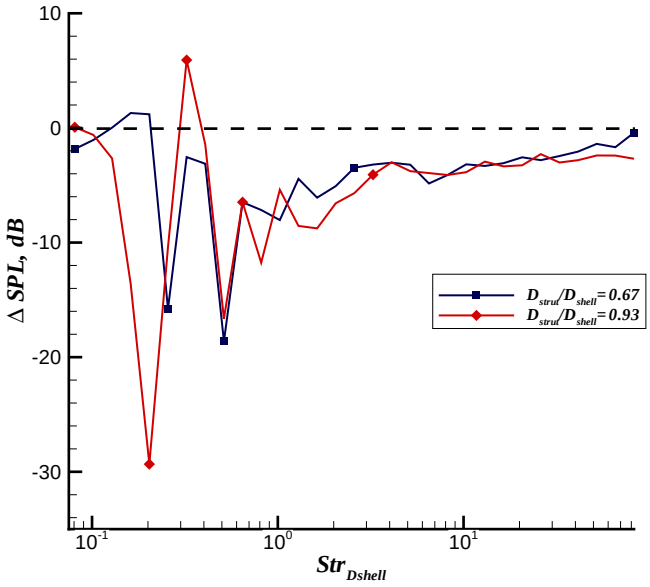

(a) ΔSPL of 1/3 octave band averaged freefield spectra (baseline=$Nosplt$).

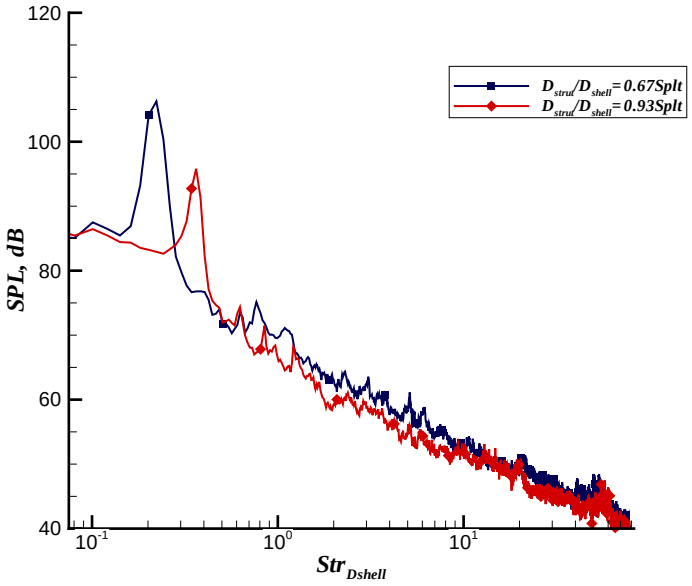

(b) Freefield acoustics measured in the anechoic chamber (averaged over microphone 1-8, $d = 2\ m$).

FIGURE 4.30: Acoustic measurements for effect of splitter plate. $U_\infty = 40m/s$.

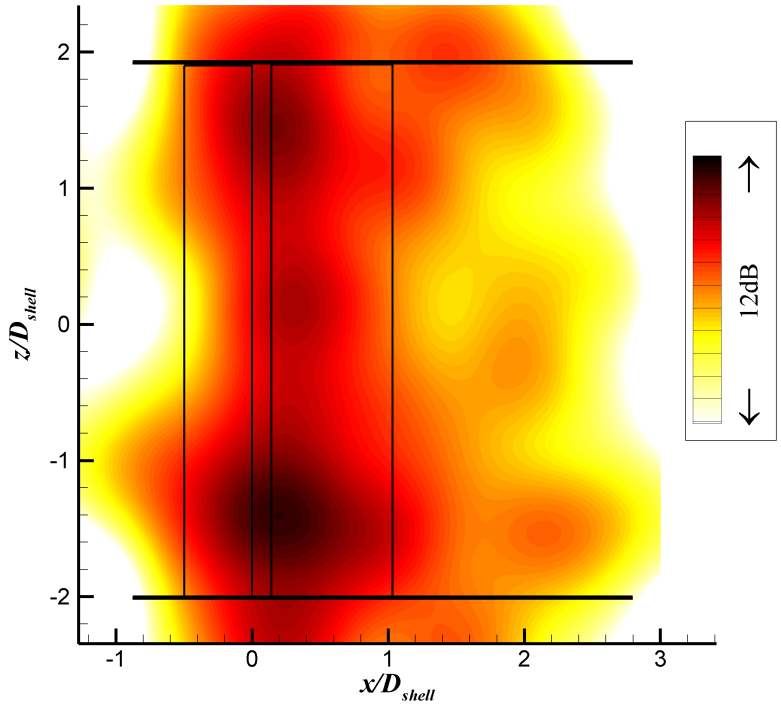

(a) Beamforming plot at $Str_{D_{shell}} = 9.4$.

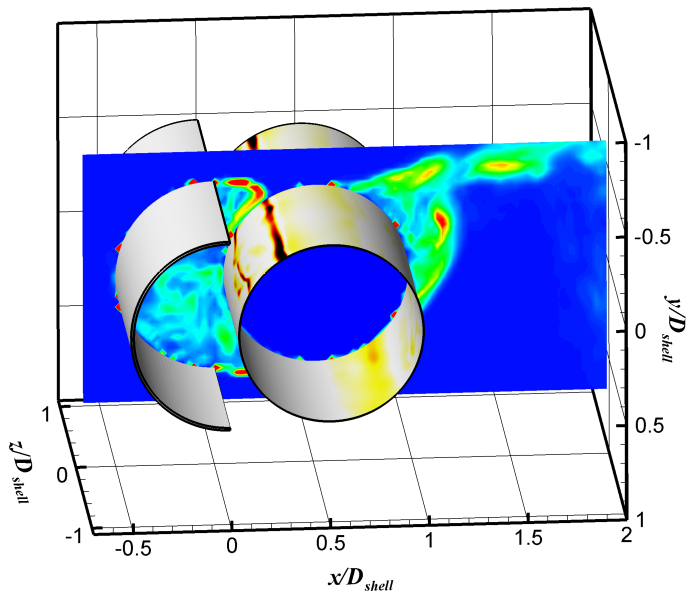

(b) Magnitude of on-surface dipole source term and vorticity magnitude contour plot at $z/D_{shell} = 0$. (DES)

FIGURE 4.31: $D_{strut}/D_{shell} = 0.93 Nosplt$. $U_\infty = 40\ m/s$. Flow from left to right.

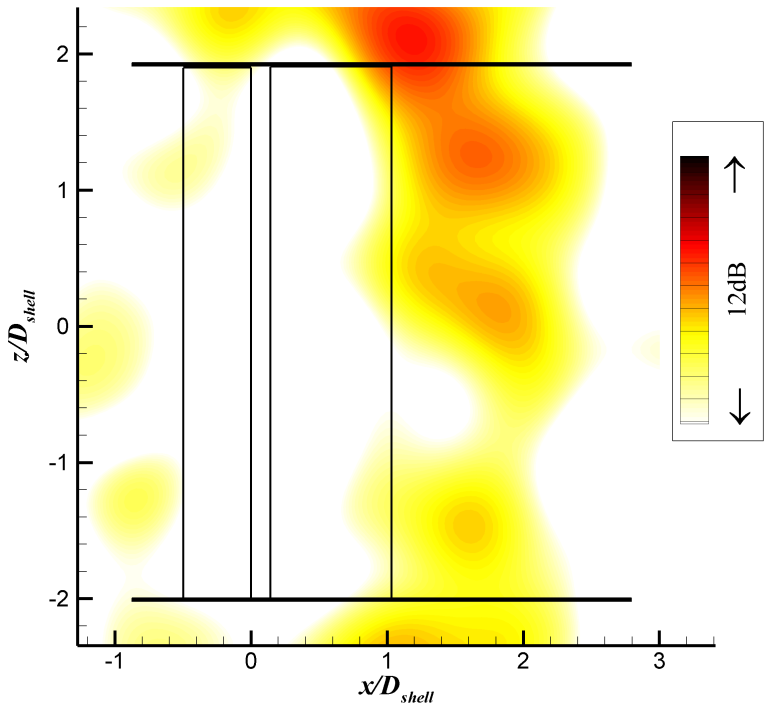

(a) Beamforming plot at $Str_{D_{shell}} = 9.4$.

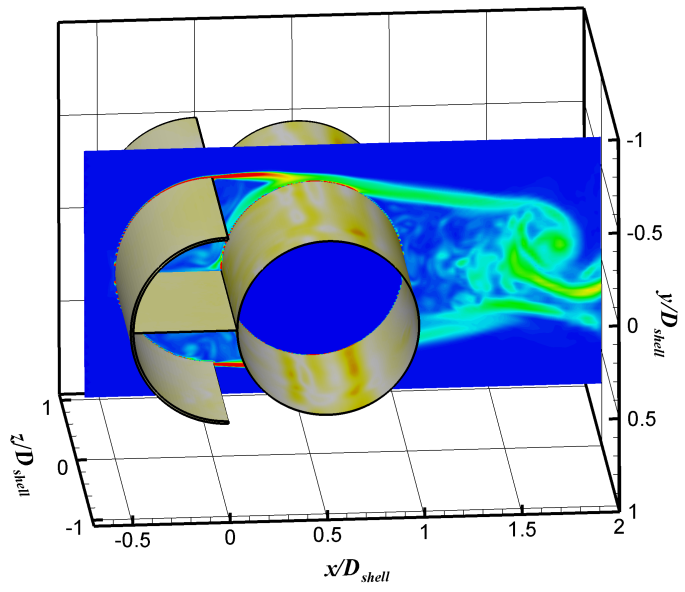

(b) Magnitude of on-surface dipole source term and vorticity magnitude contour plot at $z/D_{shell} = 0$. (DES)

FIGURE 4.32: $D_{strut}/D_{shell} = 0.93 splt$. $U_\infty = 40\ m/s$. Flow from left to right.

$$\sqrt{\frac{1}{T_2 - T_1}\int_{T_1}^{T_2}\left(\frac{\partial p'}{\partial t}\right)^2 dt}. \tag{4.1}$$

The highest acoustic source on the strut of the *Nosplt* configuration was where the shear layer aft of the shell's trailing edge impinged on the strut. The unsteady pressure perturbations from the shear layer layer interacted with the strut and were radiated as sound. The beamforming plots and the CFD simulations confirm that the presence of the splitter plate reduces the acoustic source on the strut as it reduces the pressure perturbations caused by the separated shear layer. Instead an off surface noise source is distinguishable at approximately $x/D_{shell} = 1.5$ which corresponds to the location of the formation of the vortex shedding as shown in the CFD plot.

4.4 Fairing with H-beam

The following section deals with replacing the strut used so far with an H-beam. From the results discussed so far the strut was dominated by shedding at low frequencies and was relatively quiet at higher frequencies. On landing gears, the components the fairings would be shielding have small scale details (i.e. hoses) that would make the struts louder then if they were clean. The H-beam was chosen as it features sharp edges, which is true for components on the landing gear, such as the articulation links.

4.4.1 Time-averaged flow features

The time averaged velocity contours using PIV are shown in figure 4.33. These measurements were taken in the $x - y$ plane at $z/D_{shell} = 0$.

The configuration without the splitter plate shows a thin high gradient shear layer aft of the shell trailing edge. The shear layer diffuses aft of the H-beam shortening the length of the wake downstream of the model. For the configuration with the splitter plate the same high gradient shear layer is observed aft of the shell trailing edge but due to the presence of the splitter plate the shear layer is displaced further away from the H-beam. More importantly it moves the shear layer away from the sharp edge of the H-beam at $x/D_{shell} = 0.95$, which was potentially a source of noise. Due to the shear layer not diffusing so readily as in the case of

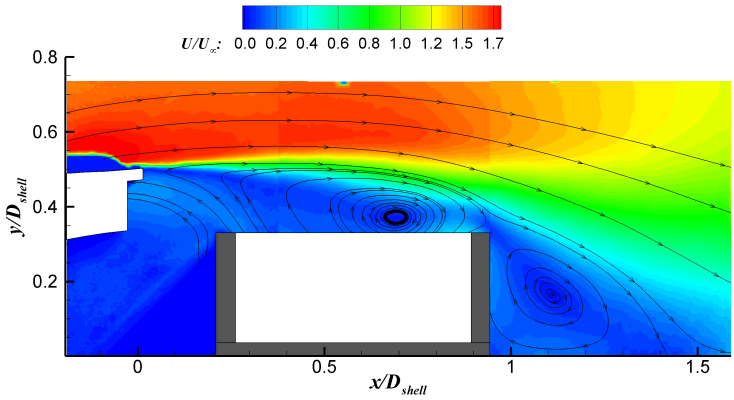

(a) Shell+H-beam.

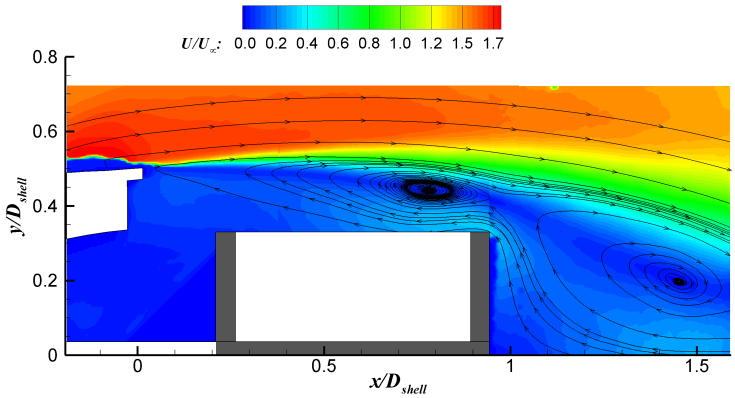

(b) Shell+H-beam with splitter plate.

FIGURE 4.33: Time-averaged velocity contours and streamlines. $U_\infty = 30\ m/s$. Flow from left to right.

the *Nosplt* configuration the wake is extended further downstream as well as the higher velocity deflected flow.

4.4.2 Vortex shedding

Turbulence statistics in the form of standard deviation of velocity in the y-direction are shown in figure 4.34 for both the *Splt* and *Nosplt* configurations. Similar to what was shown in section 4.2.3 the splitter plate affected the velocity fluctuations. The maximum at $y/D_{shell} = 0$ moved further downstream and away from the rear of the H-beam in the case of the *Splt* configuration. Moreover the amplitude of the velocity fluctuations was 50% less than the values obtained for the *Nosplt* configuration.

To investigate the spectral content of the unsteadiness, the results obtained from

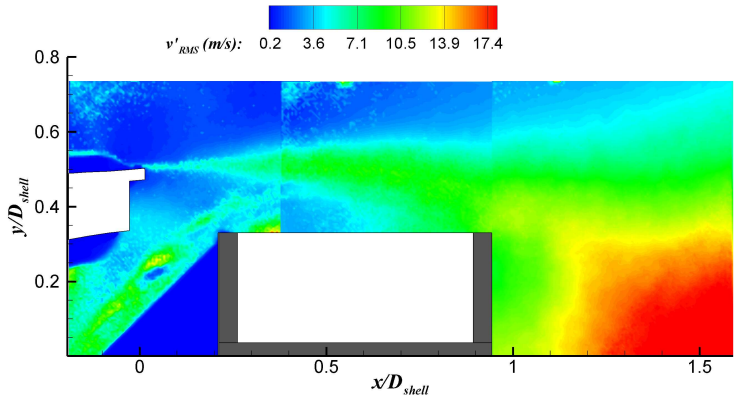

(a) Shell+H-beam.

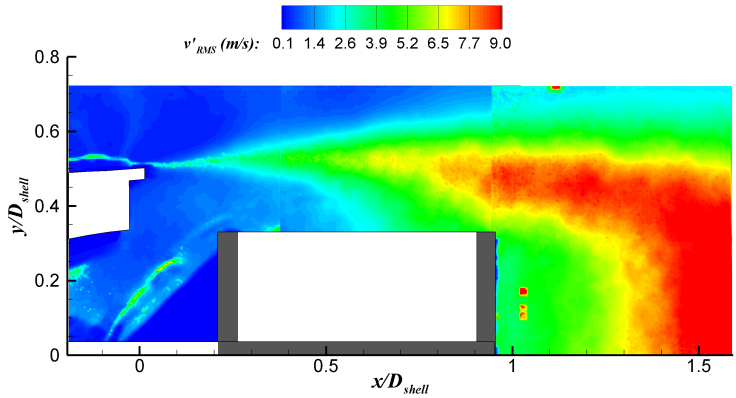

(b) Shell+H-beam with splitter plate.

FIGURE 4.34: Standard deviation of velocity in the y-direction. $U_\infty = 30\ m/s$. Flow from left to right.

the hotwire measurements are presented in figure 4.35a. Three configurations were tested, the isolated H-beam, and the shell with the H-beam in the *Nosplt* and *Splt* configuration. The isolated H-beam was dominated by a shedding peak at $Str_{D_{shell}} = 0.21$ that scaled with velocity, the second peak at the $Str_{D_{shell}} = 0.42$ was thought to be the harmonic of the first peak, this also scaled with velocity. Both the *Nosplt* and *Splt* configuration were dominated by a shedding peak at $Str_{D_{shell}} = 0.27$. This frequency was approximately equal to that seen in the $D_{strut}/D_{shell} = 0.67$ case where the diameter of the strut was equal to length and width of the H-beam. This lead to the conclusion that in this case the shell was responsible for the large scale vortex shedding, independent of the shielded object.

The levels of aerodynamic noise produced by the models are shown in figure 4.35 using freefield microphones in the anechoic chamber. The isolated H-beam showed two dominant spectral peaks at $Str_{D_{shell}} = 0.19$ and $Str_{D_{shell}} = 1.2$ that scaled with velocity. The peak at $Str_{D_{shell}} = 1.2$ was not picked up with the hotwire

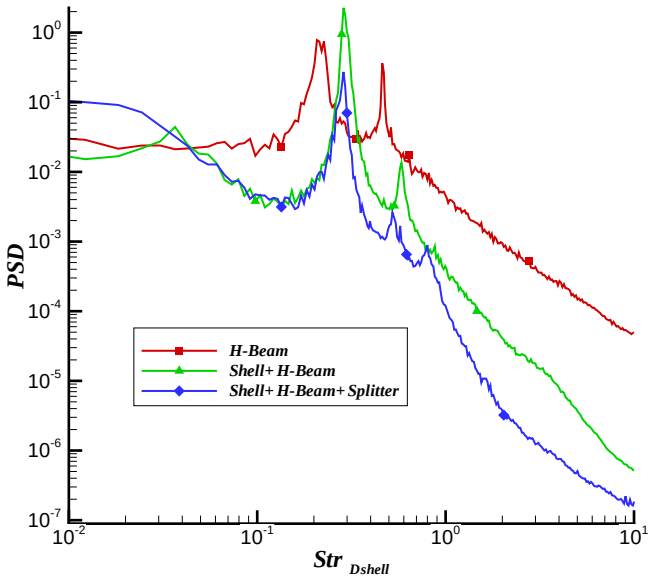

(a) Frequency spectra (PSD) measured using hotwire. $U_\infty = 30m/s$. ($x/D_{Shell} = 1$, $y/D_{shell} = 1.33$, $z/D_{shell} = 0$.)

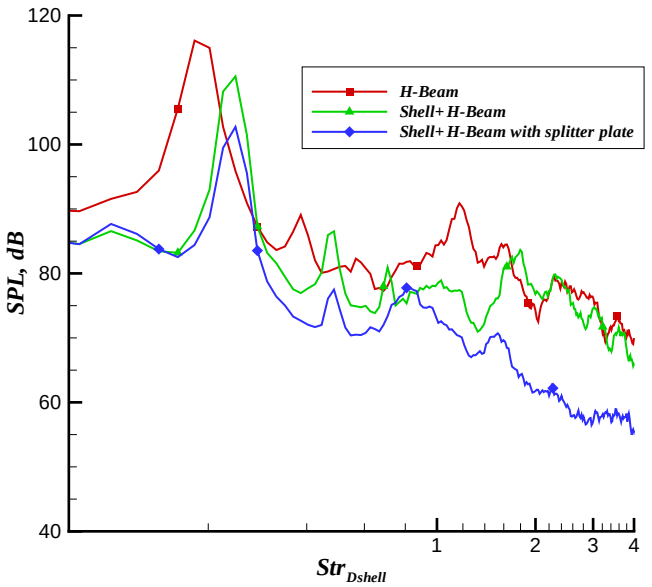

(b) Freefield acoustics measured in the anechoic chamber (averaged over microphone 1-8, $d = 2\ m$). $U_\infty = 40m/s$.

FIGURE 4.35: Hotwire and freefield microphone measurements.

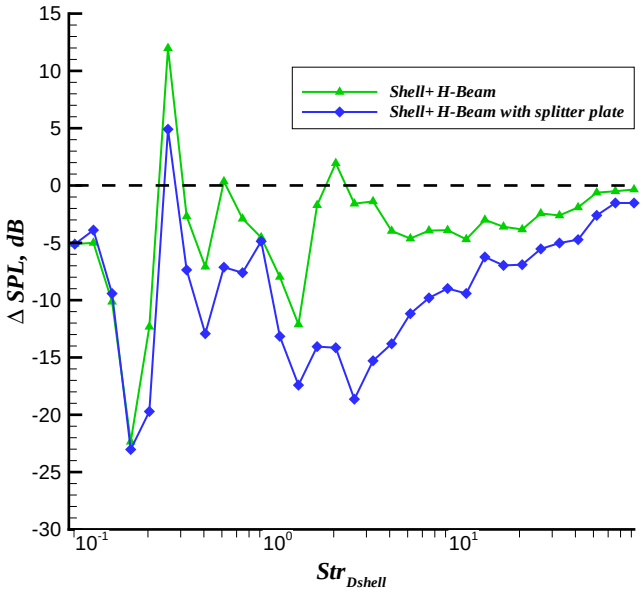

FIGURE 4.36: ΔSPL for shell+H-beam in $Nosplt$ and $Splt$ configurations (isolated H-beam is used as a baseline). $U_\infty = 40\ m/s$.

shown in figure 4.35a. The reason for this was that noise responsible for this peak was located on the model, possibly the H-beam cavity as this did not show up in the wake spectra. Similar to hotwire measurements the $Nosplt$ and $Splt$ configurations showed a spectral peak at $Str_{D_{shell}} = 0.24$, the difference in the Strouhal number was attributed to the blockage in the $3' \times 2'$ tunnel. The peak for the $Splt$ configuration was 8 dB lower then that of the $Nosplt$ configuration while the peak at $Str_{D_{shell}} = 1.2$ was attenuated.

4.4.3 Broadband noise

Finally the overall reductions achieved by using the splitter plate on the shell shielding the H-beam are discussed. Figure 4.36 displays the ΔSPL levels for the different configurations, the baseline configuration is the isolated H-beam. Shielding the H-beam with the shell showed an effective way of reducing the broadband noise, with approximately 4 dB reduction between $Str_{D_{shell}} = 4$ and 26. Larger noise reductions were seen in the $Splt$ configuration. A reduction of more than 10 dB was seen between $Str_{D_{shell}} = 1$ and 10 which then reduced to approximately 5 dB between $Str_{D_{shell}} = 12$ and 42.

4.5 Summary

Experiments with a fairing-strut model have been performed to investigate the effect the strut diameter and the strut location have on the noise generated by the model. As a means of passive noise control, a splitter plate placed between the shell and the strut, was used. Both aerodynamics and the related acoustics were studied employing two different wind tunnels and an open-jet anechoic chamber facility.

Four different sizes of struts were used to investigate the possibility of reducing the size of the shell with respect to the strut. The strut location was kept constant at $x_c/D_{shell} = 1/2$. An increase in the strut diameter increases the deflected velocities. The wake width was also affected, the larger struts resulted in wider wakes. The increase in the width of the wake together with the larger strut having a lower base pressure affected the mean drag measurements. The drag increased with an increase in the strut diameter with the largest strut being $\Delta C_d = 0.24$ higher than the smallest strut tested. The hotwire measurements revealed that the wake was dominated by vortex shedding. The frequency of the shedding varied as a consequence of the change in the strut diameter. The shedding frequency decreased with an increase in the strut diameter, decreasing from $Str_{D_{shell}} = 0.26$ for the smallest strut to $Str_{D_{shell}} = 0.22$ for the largest strut. The acoustic measurements were consistent with the aerodynamic results, with the vortex shedding manifesting itself as a spectral peak. The absolute noise level of the smaller struts was approximately 10 dB less than the larger struts although the larger struts showed a 4 dB reduction between $Str_{D_{shell}} = 1.3$ and 11.

The effect of the strut location on the aerodynamics and the acoustics was also investigated. Two different strut diameters were used for this investigation, varying the respective strut locations for each case. The first, $D_{strut}/D_{shell} = 0.67$ showed small or no effects for two of the strut locations for both the aerodynamic and the acoustic results. The freefield measurements also revealed that the strut in the location $x_c/D_{shell} = 1/4$ generated 4 dB less noise. The second case, $D_{strut}/D_{shell} = 0.93$ showed an opposite effect with a decrease in noise of approximately 3 dB for the struts located further away from the shell.

The splitter plate modified the flow around the model. Again the $D_{strut}/D_{shell} = 0.67$ and 0.93 cases were used as they showed very different flow features when the splitter plate was used. For the $D_{strut}/D_{shell} = 0.67Splt$ cases the splitter plate blocked the interaction of the shear layers which separated off the shell.

This resulted in an increase of 10% in the deflected velocity and the widening of the wake. As a consequence of this the drag increased by 24% when compared to the $Nosplt$ configuration. The low frequency noise was dominated by a vortex shedding peak at the same frequency as for the $Nosplt$ configuration but was 12 dB less. The $D_{strut}/D_{shell} = 0.93Splt$ showed a narrowing of the wake and a reduction in the drag of $\Delta C_d = 0.5$ when compared to the $Nosplt$ configuration. The $D_{strut}/D_{shell} = 0.93Splt$ case suppressed the vortex shedding experienced when the splitter plate was not used. Another peak was observed which was 15 dB lower than the peak of the uncontrolled configuration. Both the $D_{strut}/D_{shell} = 0.67Splt$ and the $0.93Splt$ showed broadband reductions with the larger strut resulting to be the quieter.

Finally the circular strut was replaced by an H-beam. Freefield acoustic measurements revealed that the isolated H-beam had two spectral peaks at $Str_{D_{shell}} = 0.18$ and 1.2. By shielding the H-beam with the shell the peak at $Str_{D_{shell}} = 0.18$ shifted to 0.24, similar to the frequencies seen for the shell shielding the strut. Shielding the H-beam also resulted in a broadband reduction of 4 dB between $Str_{D_{shell}} = 4$ and 26. The addition of the splitter plate reduced the broadband noise further, more than 10 dB between $Str_{D_{shell}} = 1$ and 10 and approximately 5 dB between $Str_{D_{shell}} = 12$ and 42.

Chapter 5

Experimental Results for Fairing-Strut with Suction or Blowing

This chapter will discuss another method which was employed to reduce the noise generated by the fairing-strut configuration which was introduced in chapter 4. As described in section 3.3.2 flow control was applied to the surface of the fairing through which suction and blowing at different flow rates were applied. The flow around the model was similar to the one discussed in chapter 4 and only the effects of the flow control will be presented in this chapter. Two types of porous materials were investigated, a perforated ($Perf$) and sintered ($Sint$) plate. Firstly, the results of the effect the porous materials had on the noise generated by the model will be discussed. This will be followed by the effects of suction and blowing. The notation for the flow rates is a positive volume flow rate for blowing and a negative volume flow rate for suction.

5.1 Effect of the Porous Material

The two porous materials used in the investigation were a perforated plate and a sintered plate, details of which were listed in section 3.3.2. This section will concentrate on the noise generated by the flow through the porous material and will quantify and justify the use of the sintered plate throughout the investigation. The strut dimension used was $D_{strut}/D_{shell} = 0.9$ and the separation distance between the shell and the strut was $x_c/D_{shell} = 1/2$.

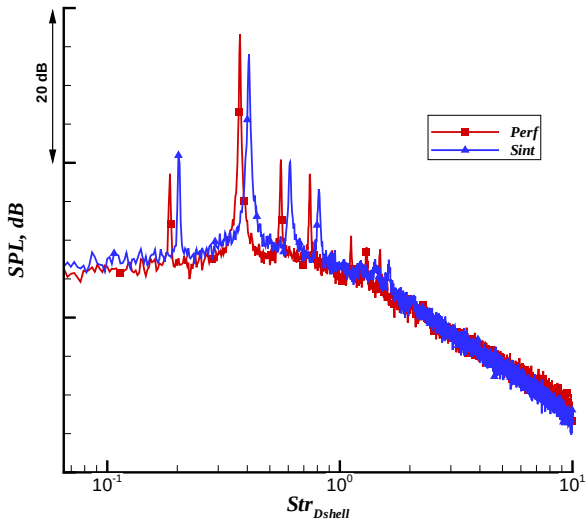

(a) On-surface microphone measurement on the rear of the strut located at $\theta = 180°$.

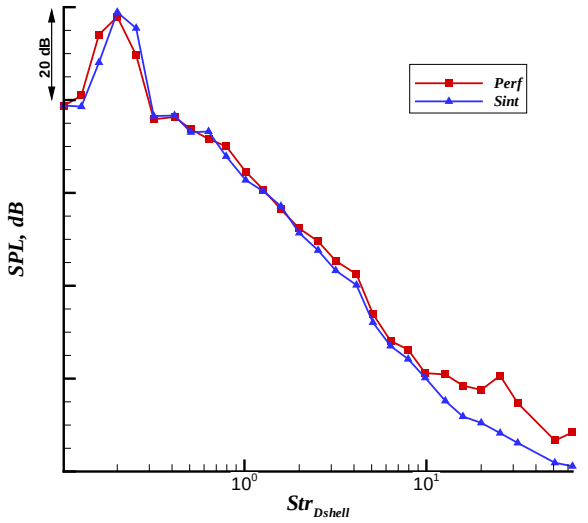

(b) Integrated 1/3 octave band averaged beamforming plots ($x/D_{shell} = \pm 2$, $z/D_{shell} \pm 2$) .

FIGURE 5.1: Measured acoustics, comparing the noise due to porous materials. $U_\infty = 40\ m/s$.

Figure 5.1 shows the noise levels obtained from the microphone array measurements and from an on-surface microphone located at $\theta = 180°$, the rear of the strut. The flow control was off and the freestream velocity was $U_\infty = 40\ m/s$. The on-surface microphone shows a clear peak at $Str_{D_{shell}} = 0.2$ for the $Sint$ case and a peak at $Str_{D_{shell}} = 0.18$ for the $Perf$ case. The peaks at double these frequencies seen in the plot were due to the microphone measuring the alternating

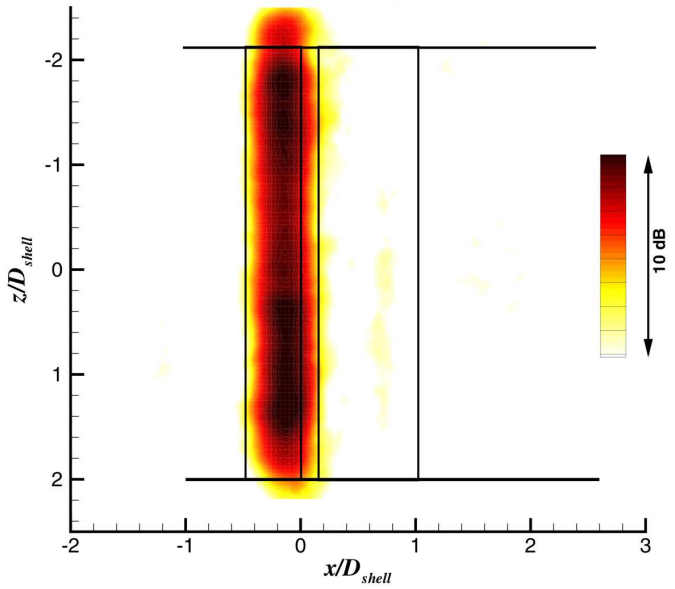

FIGURE 5.2: Beamforming plot at $Str_{D_{shell}} = 20$ for the $Perf$ case. $Q = 0\ m^3/s$, $U_\infty = 40\ m/s$.

shedding from either side of the model. These were attributed to vortex shedding behind the model as the flow was expected to be similar to the flow discussed in the chapter 4. Figure 5.1b shows the 1/3 Octave band averaged spectra obtained from integrated microphone array beamforming plots as explained in section 3.4.7. Consistent with the on-surface microphone the vortex shedding peaks appear at the same Strouhal numbers. Above $Str_{D_{shell}} = 10$ the $Perf$ case showed increased noise levels when compared to the $Sint$ case which did not show any high frequency noise sources.

Source localisation was performed using the microphone array to identify the high frequency noise source seen in figure 5.1. Figure 5.2 shows the beamforming plot centered at $Str_{D_{shell}} = 20$ for the shell fitted with the perforated plate. A noise source generated by the perforated plate showed that the high frequency noise observed was originating from the perforate holes. These observations feed the hypothesis that the high frequency peak was related to flow resonance of the perforate. Grazing flow past edges is known to create an edge tone type noise [84, 85]. By comparing $U_\infty = 40\ m/s$, $U_\infty = 30\ m/s$ and $U_\infty = 20\ m/s$ data sets the spectral peak was seen to scale with velocity centered about $Str_{D_{shell}} = 25$, shown in figure 5.3. From the spectra it appears that the phenomenon was not purely tonal, which can be explained by the varying velocity magnitude around the shell.

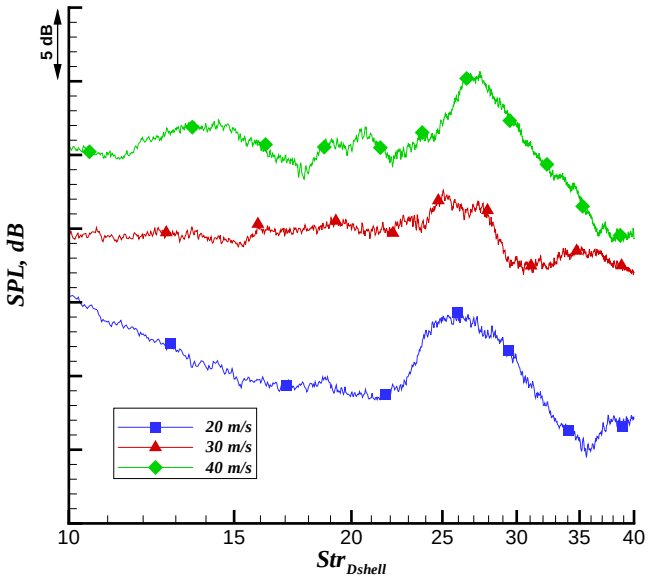

FIGURE 5.3: High frequency noise for $Perf$ at varying freestream velocities. Floor microphone located at $x/D_{shell} = 0$, $y/D_{shell} = 5.9$ and $z/D_{shell} = 0$. $Q = 0\ m^3/s$.

Another contributor to the broadband feature was the fluctuation originated from the turbulent boundary layer passing over the perforated sheet which was known to create broadband type noise [86].

The noise of the blowing system was measured with wind off, $U_\infty = 0\ m/s$ and was compared to a case where the flow control system was turned off to estimate the system noise as shown in figure 5.4. The results were averaged over one-third octave bands and subtracted to determine the change in sound pressure level due to the flow control system. The blowing system noise was apparent for both the $Perf$ and the $Sint$ cases although the $Sint$ case was approximately 20 dB quieter, the flow rates were identical in both cases.

Two test cases were compared in figure 5.5 at different freestream velocities, one with the perforated plate and the other with the sintered metal plate. In both cases the blowing flow rate was $Q = 9 \times 10^{-3}\ m^3/s$ and the configuration of the model was identical. The test cases were compared to a hard walled case. As was seen in figure 5.4 the $Perf$ case showed higher noise levels than the $Sint$ case, true for all the freestream velocities. However additional noise created by the blowing system became less with an increase in the freestream velocities. This was due to the hard walled case noise increasing with the freestream velocity, becoming

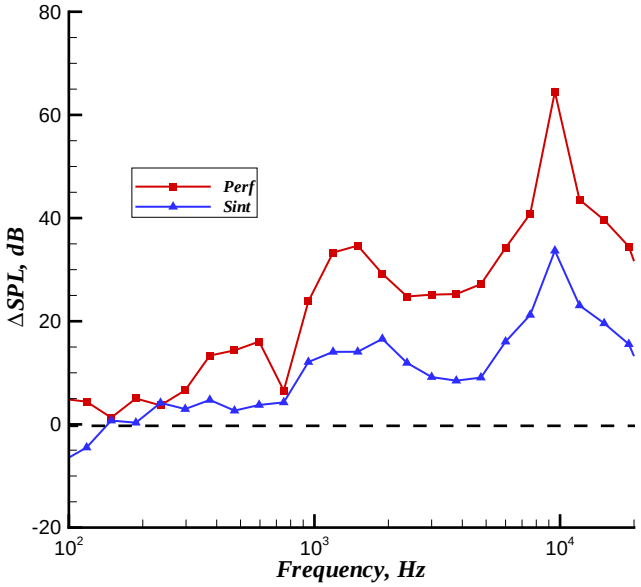

FIGURE 5.4: Comparison of integrated 1/3 octave band averaged beamforming plots for $Perf$ and $Sint$. $Q = 9 \times 10^{-3}\ m^3/s$, $U_\infty = 0\ m/s$.

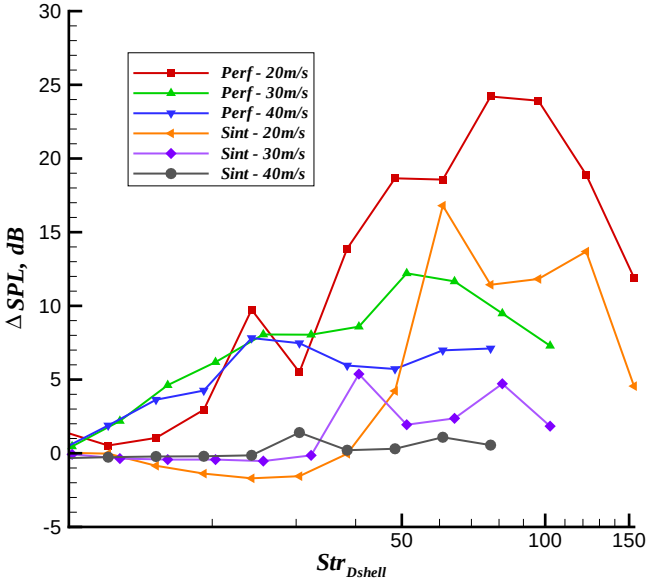

FIGURE 5.5: Comparison of integrated 1/3 octave band averaged beamforming plots for $Perf$ and $Sint$ at varying freestream velocities. Hard wall case used as a baseline. $Q = 9 \times 10^{-3}\ m^3/s$.

more broadband in nature and therefore the additional noise at higher frequencies becoming less significant. For the *Sint* case at $U_\infty = 40\ m/s$ the noise generated by the blowing system did not exceed the noise created by the hard wall case.

From the results presented so far the noise generated by the injected flow through the sintered metal plate was less prominent, making it a more attractive option.

5.2 Effect of Suction

This section will investigate the effect suction had on the noise generated by the model. In section 2.6.4, discussed literature showed the effect suction had on the flow around a circular cylinder. From this information the influence of suction on the flow around the model being investigated may be deduced. Suction on the surface of a circular cylinder in flow moved the separation point further towards the rear of the cylinder, narrowing the wake and increasing the shedding frequency [3]. However the effect of suction on the present model was thought to be less significant. In section 4.1.1.1 the separation point was shown to be fixed at the trailing edge of the shell and did not vary with Reynolds number. Even if the suction would increase the effective Reynolds number at the trailing edge of the shell the separation point will remain unchanged.

The on-surface microphones located at $\theta = 180°$ shown in figure 5.10 showed that the shedding frequency did not vary with suction applied through the sintered metal plate, remaining fixed at $Str_{D_{shell}} = 0.2$. In figure 5.7, the flow rate is kept constant and three different freestream velocities are compared. The shedding frequency scaled with velocity resulting in the shedding peak remaining unchanged at $Str_{D_{shell}} = 0.2$. These results fed the hypothesis that the separation point remained fixed at the trailing edge of the shell and hence did not vary the separation distance between the separated shear layers which in turn would have had an effect on the shedding frequency.

The ΔSPL at $U_\infty = 20\ m/s$ with varying suction flow rates is shown in figures 5.8- 5.10. Three different model configurations were tested to investigate the effect the strut diameter and its location had on the generation of sound when suction was applied to the shell. All three configurations used the sintered metal plate. Common to all three configurations was a noise reduction observed between $Str_{D_{shell}} = 5.7$ and $Str_{D_{shell}} = 35.7$ peaking at $Str_{D_{shell}} = 20$ with the reduction increasing with an increase in the suction flow rate. The ΔSPL levels for the shell

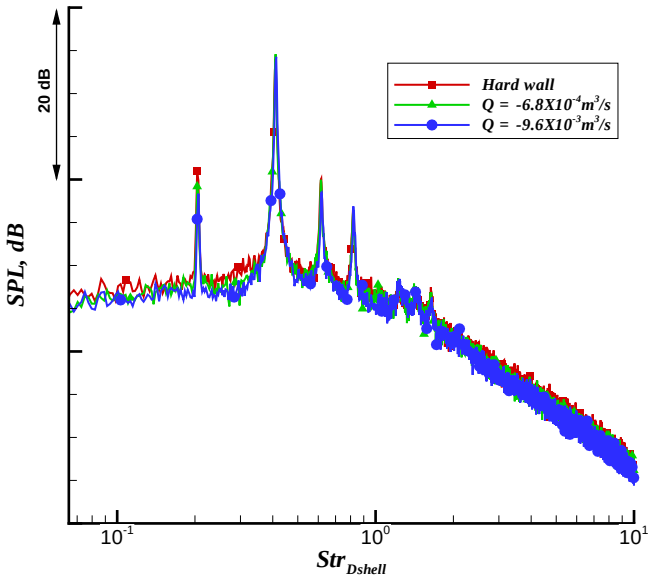

FIGURE 5.6: On-surface microphone measurement on the rear of the strut located at $\theta = 180°$. *Sint* case with suction. $U_\infty = 40\ m/s$.

without a downstream strut is shown in figure 5.11. An increase in suction flow rates resulted in increased noise reductions. The reductions were observed at the same frequencies as was seen for the configuration with the strut. This indicated that the self noise of the shell was reduced by applying suction to the surface of the shell. In the configuration where the strut was located at $x_c/D_{shell} = 1/2$, the noise reduction was less pronounced. As shown in section 4.3.2 the noise generated by the configuration is greater the further downstream the strut is located. Figure 5.12 shows the effect of the Reynolds number on the maximum reduction obtained at $Str_{D_{Shell}} = 15$. The curves are all at a constant flow rate of $Q = -9.6 \times 10^{-3}\ m^3/s$. The peak reduction decreases with an increase in the free stream velocity. The effect of suction becomes less pronounced indicating that larger suction rates were required to obtain reductions at higher Reynolds number. The C_p as defined in equation 5.1 is valid for a circular cylinder with some dependency on the Reynolds number for the separated region.

$$C_p = \frac{p - p_\infty}{\frac{1}{2}\rho_\infty U_\infty^2}. \tag{5.1}$$

As the freestream velocity increased the pressure difference in the numerator of equation (5.1) also increased. As the atmospheric pressure was constant the low

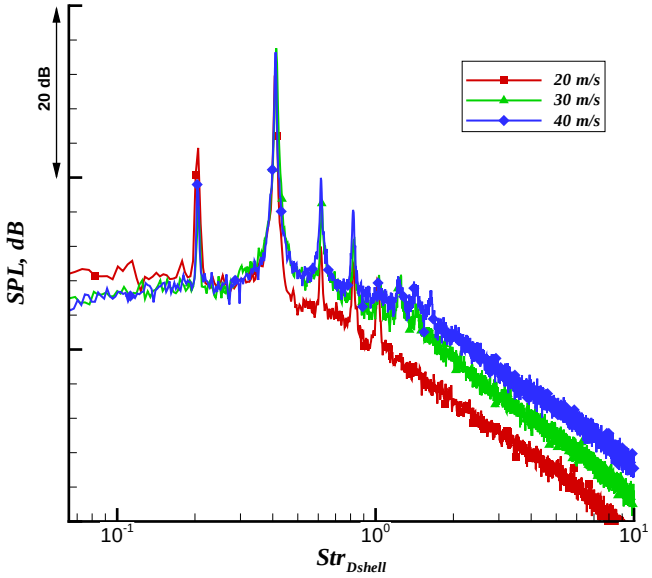

(a) $Q = -6.9 \times 10^{-4}\ m^3/s$.

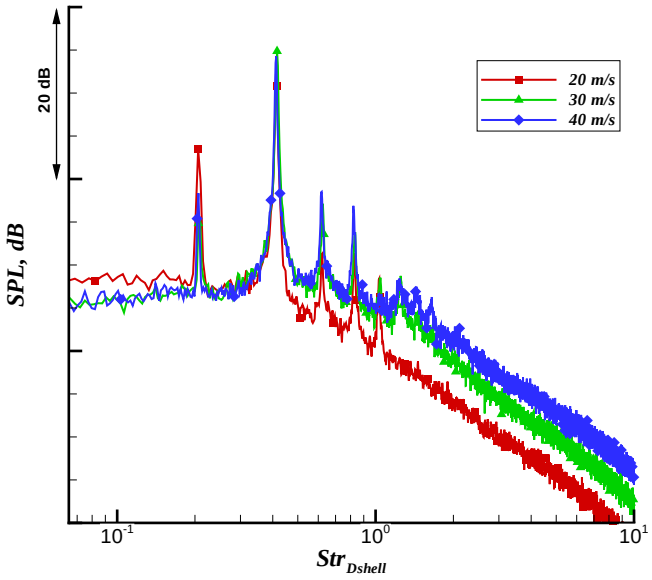

(b) $Q = -9.6 \times 10^{-3}\ m^3/s$.

FIGURE 5.7: On-surface microphone measurement on the rear of the strut located at $\theta = 180°$. *Sint* case with suction. $U_\infty = 40\ m/s$.

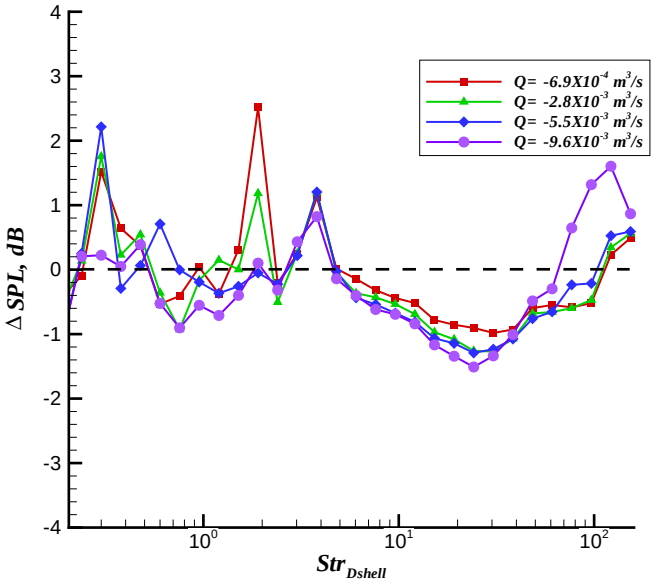

FIGURE 5.8: ΔSPL of integrated 1/3 octave band averaged beamforming plots for varying suction flow rates. $D_{strut}/D_{shell} = 0.9$, $x_c/D_{shell} = 1/2$ configuration. $U_\infty = 20\ m/s$.

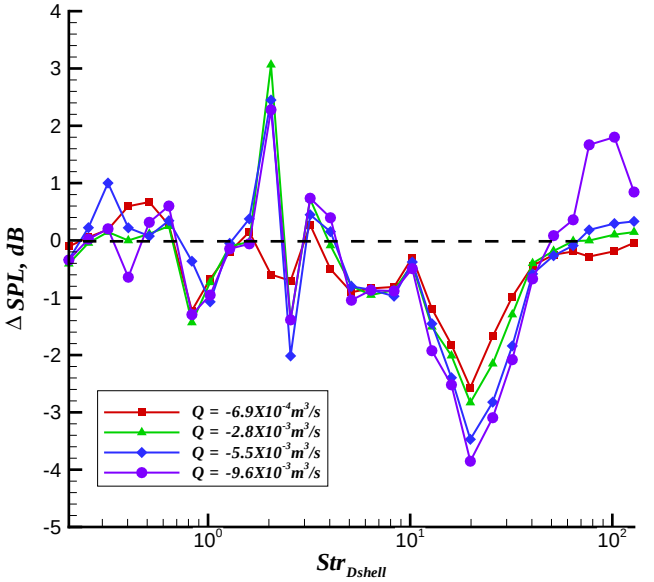

FIGURE 5.9: ΔSPL of integrated 1/3 octave band averaged beamforming plots for varying suction flow rates. $D_{strut}/D_{shell} = 0.9$, $x_c/D_{shell} = 1/4$ configuration. $U_\infty = 20\ m/s$.

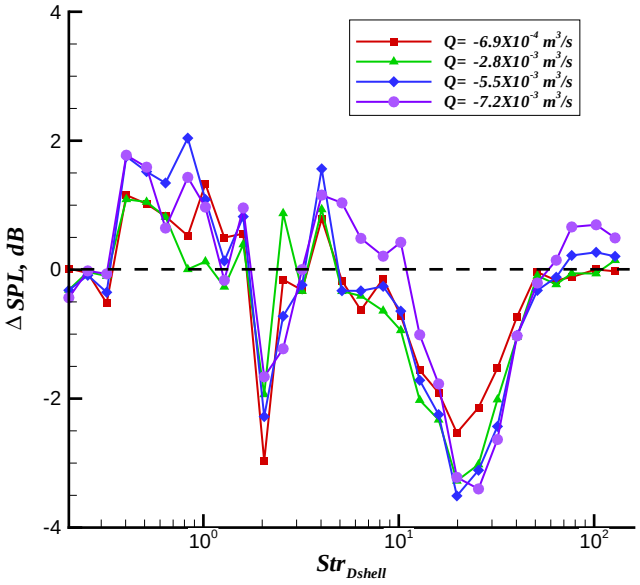

FIGURE 5.10: ΔSPL of integrated 1/3 octave band averaged beamforming plots for varying suction flow rates. $D_{strut}/D_{shell} = 0.78$, $x_c/D_{shell} = 1/4$ configuration. $U_\infty = 20\ m/s$.

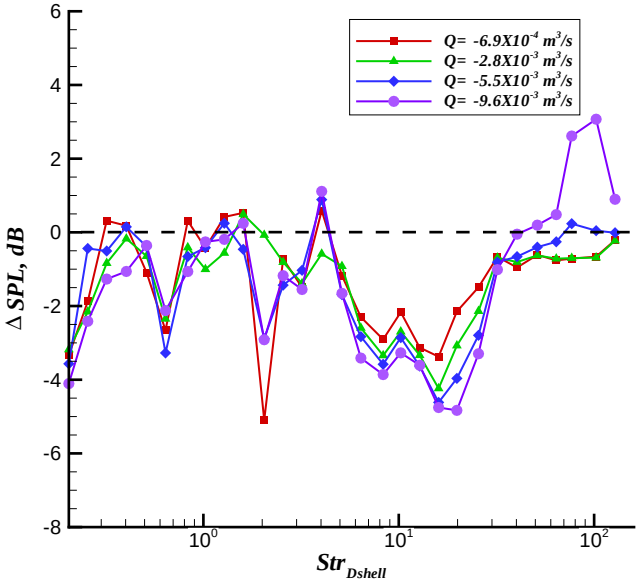

FIGURE 5.11: ΔSPL of integrated 1/3 octave band averaged beamforming plots for varying suction flow rates. Isolated shell configuration. $U_\infty = 20\ m/s$.

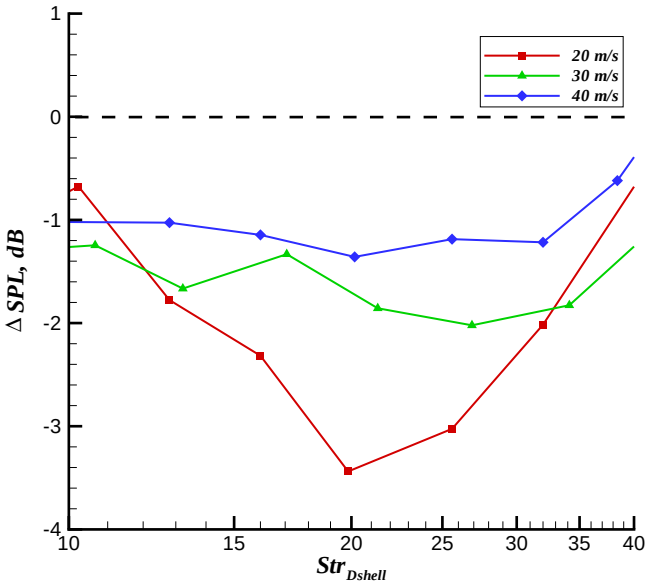

FIGURE 5.12: ΔSPL of integrated 1/3 octave band averaged beamforming plots for varying freestream velocities. $D_{strut}/D_{shell} = 0.9$, $x_c/D_{shell} = 1/4$ configuration. $Q = -9.6 \times 10^{-3}\ m^3/s$.

pressure over the shell decreased as the freestream velocity increased. This decreased the pressure differential across the sintered metal plate, scaling with U_∞^2. This could lead to large amounts of suction flow rates being required for in flight conditions where the local freestream velocities around the landing gear are about 80 m/s.

5.3 Effect of Blowing

This next section will discuss the effect blowing had on the sound generated by the model. Blowing on the surface of a circular cylinder was shown to increase the shedding frequency by blowing normal to the surface of a cylinder [3,66]. The blowing promoted earlier separation compared to an uncontrolled case; this increased the distance between the separated shear layers hence reducing the frequency of the shedding. This also led to an increase in the mean drag.

Blowing at different flow rates was applied through the sintered metal and resulted in the shedding frequency being modified. Figure 5.13 shows the data measured by the on-surface microphone located at $\theta = 180°$, the rear of the strut. The

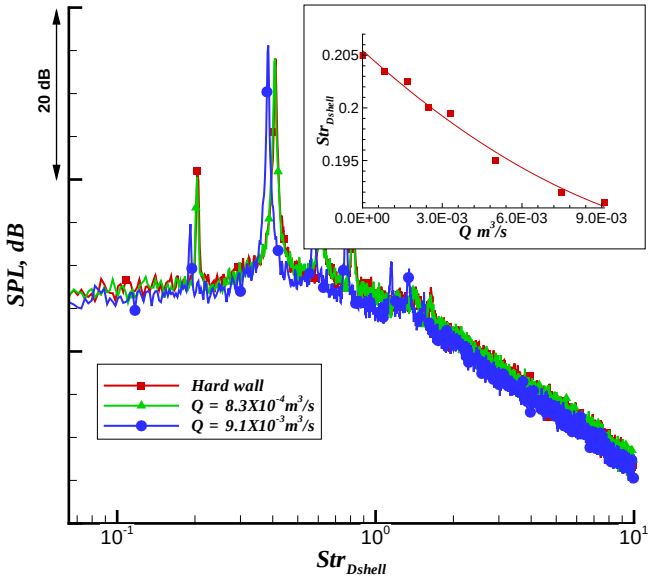

FIGURE 5.13: On-surface microphone measurement on the rear of the strut located at $\theta = 180°$. *Sint* case with blowing. $U_\infty = 40\ m/s$.

hard walled case had a shedding peak at $Str_{D_{shell}} = 0.2$ which decreased with increasing blowing flow rates. This behaviour was similar to what was seen for normal blowing on a circular cylinder [3]. The decrease in the Strouhal number indicated that the flow separated before the trailing edge of the shell, displacing the shear layers further away from each other which resulted in a decrease in the shedding frequency [70].

The ΔSPL levels with varying blowing flow rates are shown in figures 5.14- 5.17. Similar to suction cases, three different model configurations were tested. For all the three configurations as well as the isolated shell in figure 5.17 noise reductions were observed between $Str_{D_{shell}} = 10$ and $Str_{D_{shell}} = 40$ peaking at $Str_{D_{shell}} = 25$. The greatest reductions were observed for the two configurations where the strut was located at $x_c/D_{shell} = 1/4$. Similar to what was seen when suction was applied, the isolated shell showed noise reductions in the same frequency range as for the configurations with the strut. Similar to the suction case when the strut was located further downstream the reduction in noise decreased.

Figure 5.18 shows the effect the Reynolds number had on the noise reductions obtained using blowing. The peak reductions decrease with an increase in the freestream velocity. This would indicate that at higher Reynolds numbers larger blowing flow rates were required to achieve more significant noise reductions.

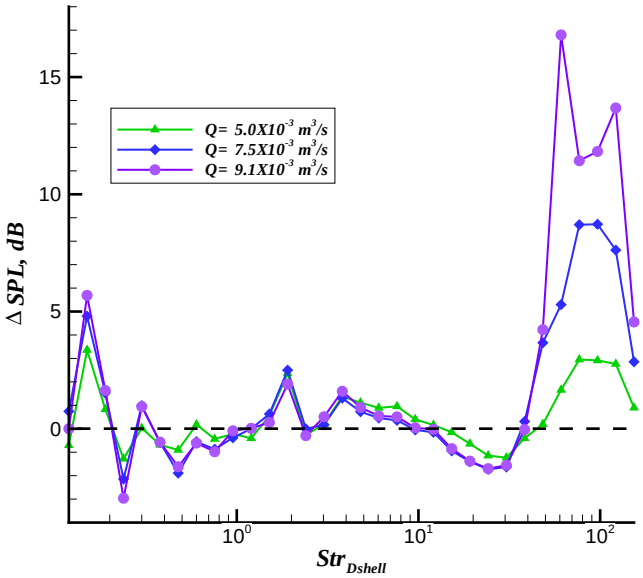

FIGURE 5.14: ΔSPL of integrated 1/3 octave band averaged beamforming plots for varying blowing flow rates. $D_{strut}/D_{shell} = 0.90$, $x_c/D_{shell} = 1/2$ configuration. $U_\infty = 20\ m/s$.

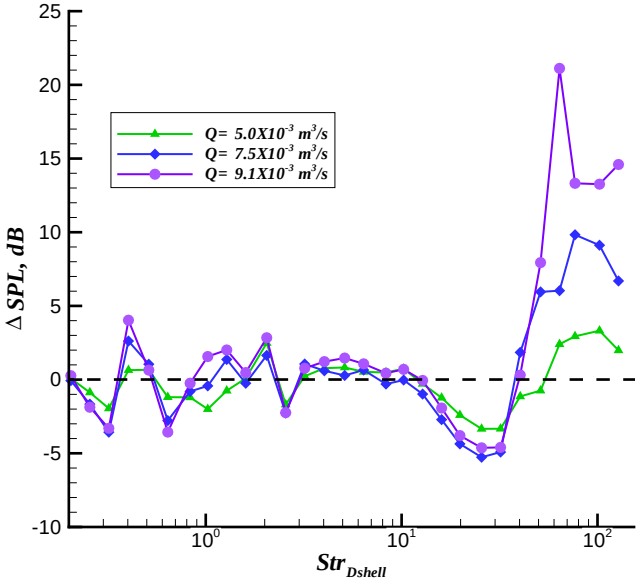

FIGURE 5.15: ΔSPL of integrated 1/3 octave band averaged beamforming plots for varying blowing flow rates. $D_{strut}/D_{shell} = 0.90$, $x_c/D_{shell} = 1/4$ configuration. $U_\infty = 20\ m/s$.

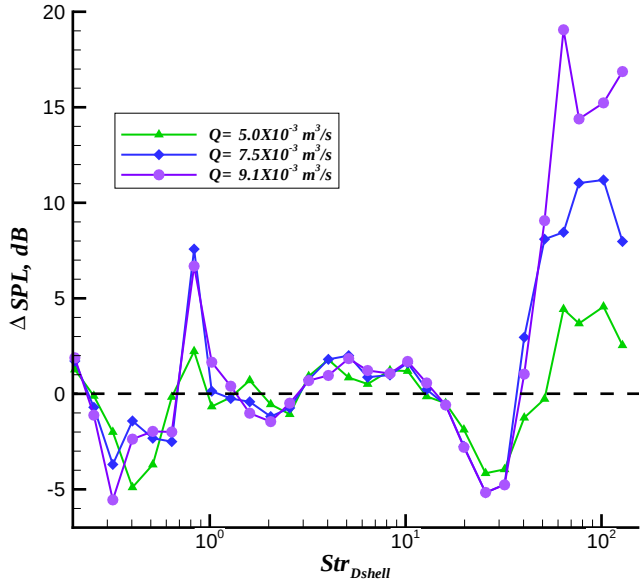

FIGURE 5.16: ΔSPL of integrated 1/3 octave band averaged beamforming plots for varying blowing flow rates. $D_{strut}/D_{shell} = 0.78$, $x_c/D_{shell} = 1/4$ configuration. $U_\infty = 20\ m/s$.

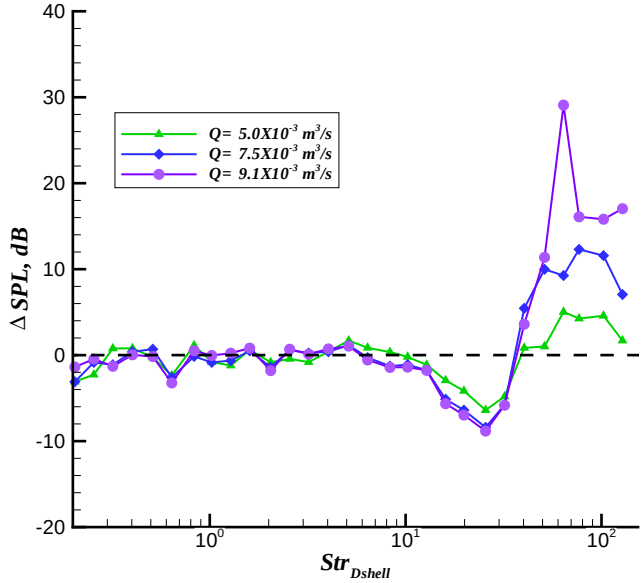

FIGURE 5.17: ΔSPL of integrated 1/3 octave band averaged beamforming plots for varying blowing flow rates. Isolated shell configuration. $U_\infty = 20\ m/s$.

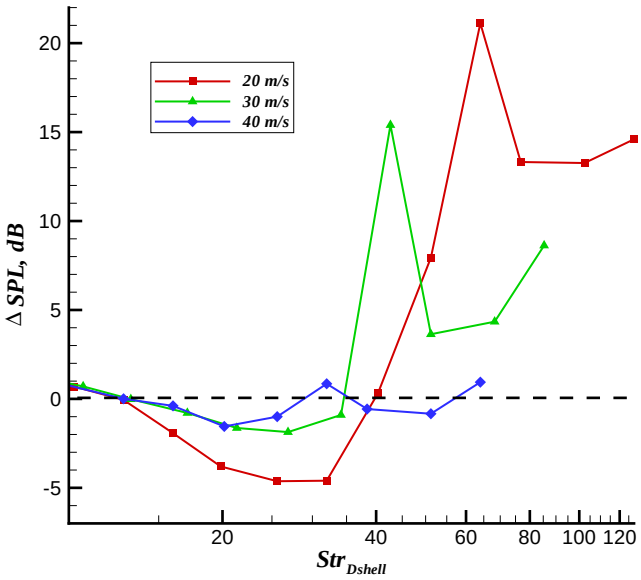

FIGURE 5.18: ΔSPL of integrated 1/3 octave band averaged beamforming plots for varying freestream velocities. $D_{strut}/D_{shell} = 0.9$, $x_c/D_{shell} = 1/4$ configuration. $Q = 9.1 \times 10^{-3}\ m^3/s$.

5.4 Summary

Experiments were conducted to investigate applying suction or blowing to the surface of the shell to reduce the noise produced by the shell-strut configuration. Acoustics measurements were performed using on-surface microphones and a microphone array.

Two porous materials were investigated, a perforated plate and a sintered metal plate. With no flow applied the perforated plate increased the noise produced by the model at high frequencies, above $Str_{D_{shell}} = 10$ when compared to the sintered metal plate. This was thought to be caused by a turbulent boundary layer passing over the perforated sheet. The perforated sheet also shows noise levels increased by as much as 20 dB when blowing and suction system were used and compared to the sintered metal case. Due to the increased noise levels seen for the perforated case the sintered metal was used to present the results for the effect of suction and blowing.

Suction did not have an effect on the shedding frequency, whilst the shedding frequency decreased with an increase in blowing flow rates. In the case of suction the separation remained fixed at the trailing edge of the shell. Blowing caused

the flow on the shell to separate earlier and hence decrease the frequency of the shedding.

Both suction and blowing showed noise reductions of as much as 5 dB between $Str_{D_{shell}} = 5.7$ and $Str_{D_{shell}} = 35$ for suction and $Str_{D_{shell}} = 10$ and $Str_{D_{shell}} = 40$ for blowing at $U_\infty = 20\ m/s$. For both suction and blowing the peak reductions were reduced with an increase in the Reynolds number, reducing the reduction to about 1 dB which is at the limit of the accuracy of the system. In the case of blowing the frequency range over which the reduction was observed was also reduced with an increase in the Reynolds number.

Chapter 6

Experimental Results for H-Beam with Splitter Plate

Using a splitter plate on a bluff body without a fairing was investigated in this chapter. Chapter 4 presented the results of a fairing shielding a bluff body and using a splitter plate as a passive noise reduction device. This proved to be effective at attenuating broadband noise, but fairings have a disadvantage when used on landing gears. The weight penalty, the increased complexity required to retract the landing gear and the shielding of landing gear components which need to be inspected and maintained regularly make the fairing less attractive. Past research has shown that splitter plates mounted behind bluff bodies were effective at suppressing vortex shedding and displacing the shedding process away from the bluff body surface [69], which was desirable for the reduction of noise. In this work, a H-beam was selected as a test case and three different splitter plate lengths were used. Aerodynamic and acoustic measurements were performed to investigate the effect of the splitter plate on the noise generated by the model.

6.1 Time-averaged Flow features

The time-averaged velocity contours using PIV are shown in figure 6.1. Four configurations were tested, the isolated H-beam, $L/W = 0$, and the H-beam with the splitter plate lengths, $L/W = 1$, $L/W = 2$ and $L/W = 3$. These measurements were taken in the $x - y$ plane at $z/D_{shell} = 0$.

The time-averaged flow for the isolated H-beam showed a thin shear layer with

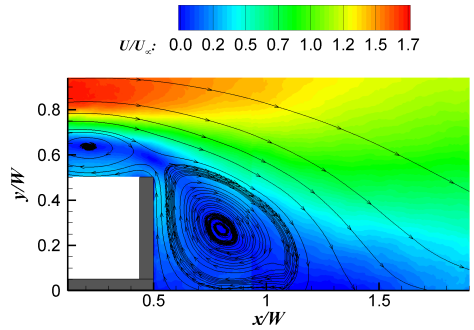

(a) $L/W = 0$.

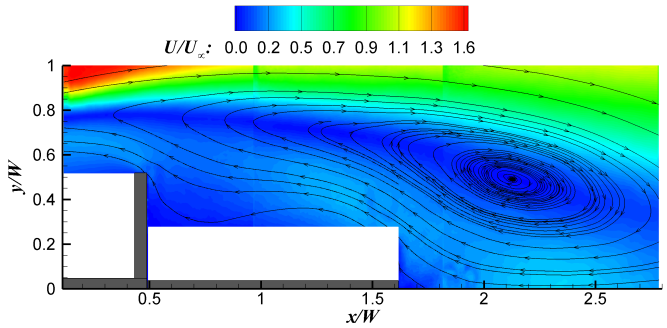

(b) $L/W = 1$.

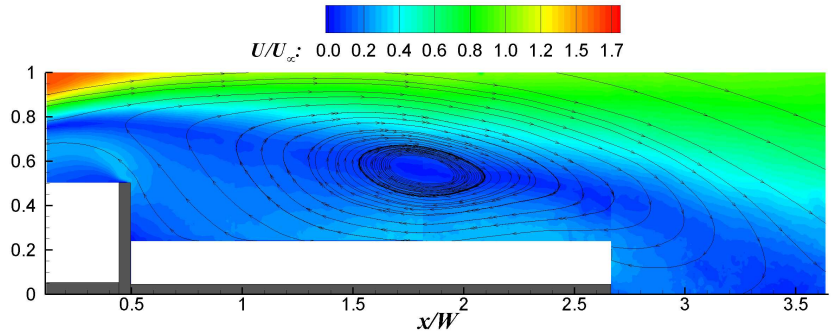

(c) $L/W = 2$.

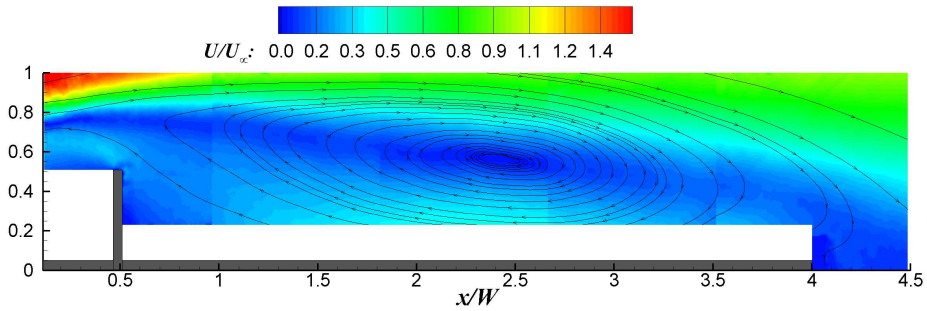

(d) $L/W = 3$.

FIGURE 6.1: Time-averaged velocity contours and streamlines. $U_\infty = 30\ m/s$. Flow from left to right.

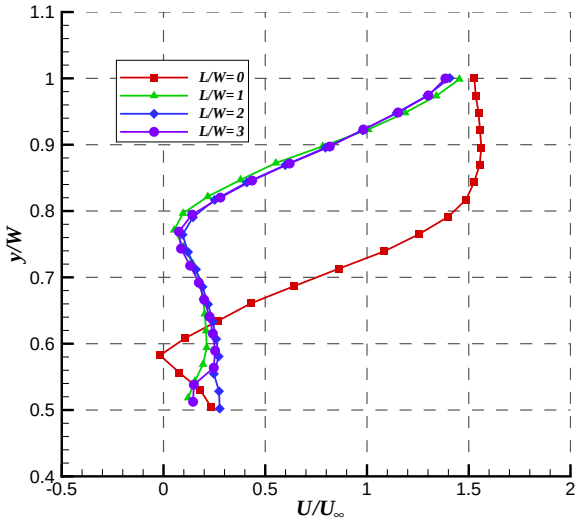

(a) $x/W = 0.5$.

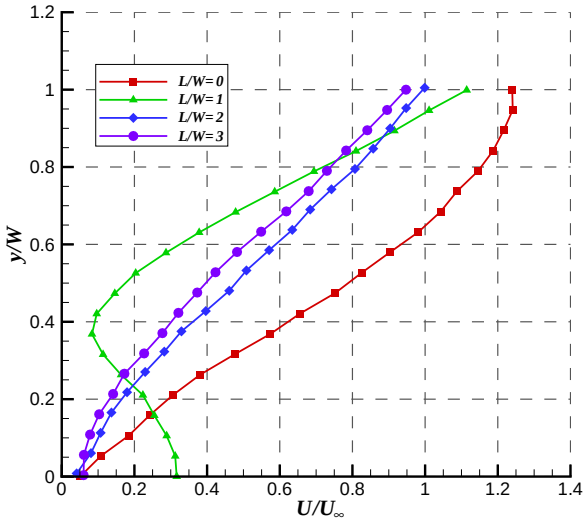

(b) $x/W = 1.0$.

FIGURE 6.2: Non-dimensional velocity profiles from PIV data at two different x/W positions and $z/D_{shell} = 0$. $U_\infty = 30\ m/s$.

high velocity gradient at $x/W = 0$, $y/W = 1.7$. Velocity contours over the front of the H-beam were not available however it was safe to assume that the flow separated off the front of the H-beam, similar to the way flow would separate off the edges of a flat plate placed normal to the flow.

For the $L/W = 1$, $L/W = 2$ and $L/W = 3$ configurations the flow was believed to separate off the front of the H-beam, similar to that seen for $L/W = 0$. Therefore

the splitter plates did not influence the separation point, this was dictated entirely by the sharp edges at the leading edges of the H-beam. The presence of the splitter plate aft of the H-beam impeded the shear layer from diffusing, instead the shear layer was deflected further away from the H-beam. Non-dimensional velocity profiles extracted from the PIV data at $x/W = 0.5$ are shown in figure 6.2a. This streamwise location corresponds to the rear edge of the H-beam. The shear layer was deflected by approximately $\Delta y/W = 0.2$ further away in the lateral direction for the splitter plate configurations when compared to the $L/W = 0$ configuration but at this location no variation was observed between the splitter plate configurations. Figure 6.2b shows the non-dimensional velocity profiles in the wake for all four configurations. The profiles were measured at a streamwise location of $x/W = 1$ downstream of the rear of the H-beam for $L/W = 0$ and of $x/W = 1$ downstream from the trailing edge of the splitter plate for the $L/W = 1$, $L/W = 2$ and $L/W = 3$. For $L/W = 0$, the low velocity region of the wake is shorter and narrower than for the splitter plate configurations. The splitter plates caused the deflected shear layers to spread in the y-direction which led to widening of the wake. The $L/W = 1$ case showed a different flow structure in the wake to the other two splitter plate configurations $L/W = 2$ and $L/W = 3$. From the time-averaged streamlines shown in figure 6.1 a recirculation region was seen downstream of the trailing edge of the splitter plate for $L/W = 1$ while the longer splitter plates showed a recirculation region over the splitter plate. Experiments for a circular cylinder with splitter plates of varying lengths showed that the longer splitter plates had reversed flow region over the splitter plates while for the shorter splitter the reversed flow extended beyond the splitter plate and into the wake [69]. This is also evident in the velocity profiles shown in figure 6.2b, the configurations $L/W = 2$ and $L/W = 3$ showed similar profiles.

The variations in the drag coefficient C_d with splitter length are shown for the H-beam in figure 6.3. An increase in splitter length resulted in a reduction in the mean drag. The largest drop of $C_d = 0.7$ was seen between $L/W = 0$ and $L/W = 3$.

6.2 Vortex Shedding

Turbulence statistics in the form of standard deviation of velocity in the y-direction are shown in figure 6.4 for the $L/W = 0$, $L/W = 1$ and $L/W = 2$ configurations. For the $L/W = 0$ configuration, the two opposing shear layers interact and roll-

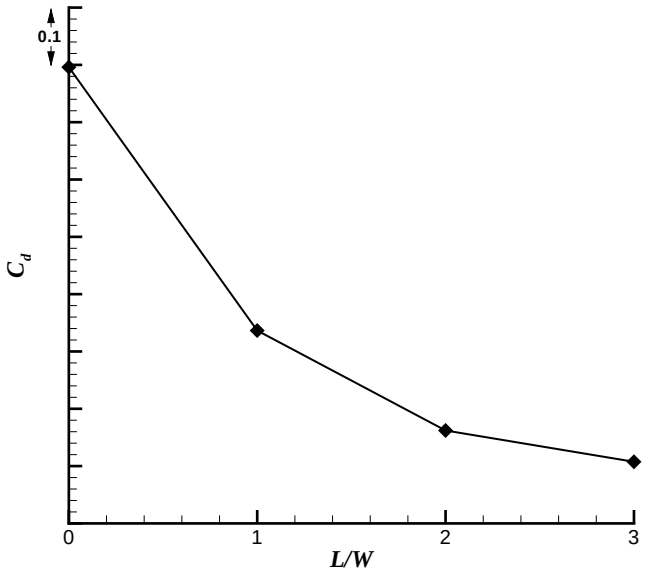

FIGURE 6.3: Coefficient of drag for different splitter plate lengths. C_d vs L/W. $U_\infty = 40\ m/s$.

up to result in high amplitude transverse velocity fluctuations peaking on the centerline of the wake ($y/W = 0$). The effect of splitter plate was seen in the standard deviation of velocity in the y-direction for the $L/W = 1$ and $L/W = 2$ configurations and as was seen in the time-averaged flow there was a difference in the flow between the two configurations. For the $L/W = 1$ configuration the splitter plate blocked the interaction between the shear layers on either side of the model until aft of the trailing edge of the splitter plate. This resulted in the velocity fluctuation being displaced further downstream of the H-beam and the amplitude of the maximum was reduced by 40% when compared to $L/W = 0$. The $L/W = 2$ configuration showed the amplitude of the velocity fluctuation maximum was also reduced by 40%, but in this configuration the maximum was located closer to the trailing edge of the splitter plate. The use of the splitter plate had an important effect on the velocity fluctuation around the sharp edge at the rear of the H-beam ($x/W = 0.5$, $y/W = 0.5$). Figure 6.5 shows the standard deviation of velocity in the y-direction just above the sharp edge. At $x/W = 0.5$ and $y/W = 0.5$ the velocity fluctuation was 77% and 67% less than the $L/W = 0$ configuration, for the $L/W = 1$ and the $L/W = 2$ respectively. This was an important result coupled with the reduction in the local velocity at this location (figure 6.2) for the generation of sound. Sound generated from dipole and quadrupole sources close to a sharp edge follows a scaling law of U_∞^5. In the absence of a sharp edge the

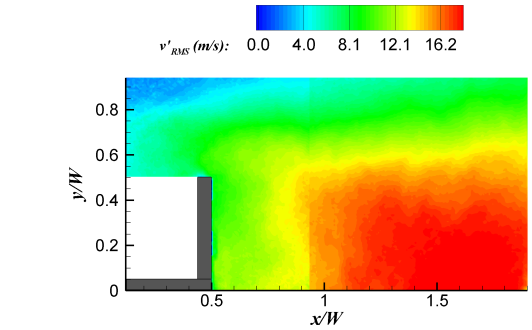

(a) $L/W = 0$.

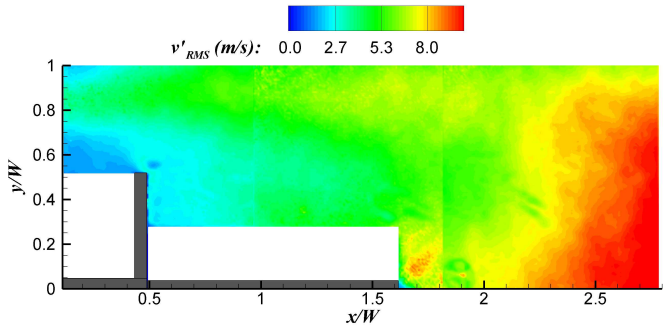

(b) $L/W = 1$.

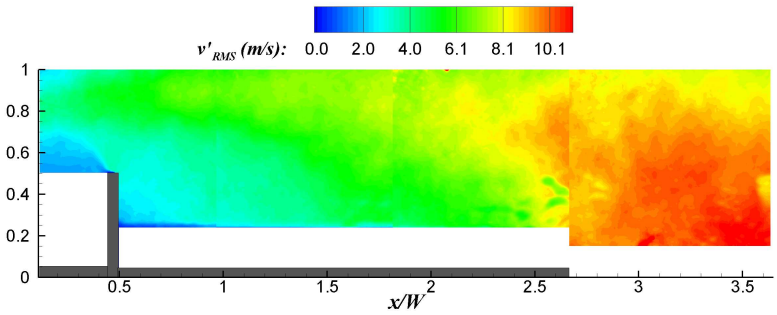

(c) $L/W = 2$.

FIGURE 6.4: Standard deviation of velocity in the y-direction. $U_\infty = 30\ m/s$. Flow from left to right.

sources radiate proportional to U_∞^6 and U_∞^8 respectively [45].

Spectral analysis was performed on the signal recorded by the hotwire probe. Figure 6.6 shows the hotwire measurements at $\Delta x/W = 1.5$ from rear of the respective models and at two lateral positions $y/W = 0$ and $y/W = 2$.

The spectra are characterised by large scale velocity fluctuations associated with vortex shedding. Distinct peaks arise at different frequencies depending on the length of the splitter plate. The peak for the isolated H-beam, $L/W = 0$, was

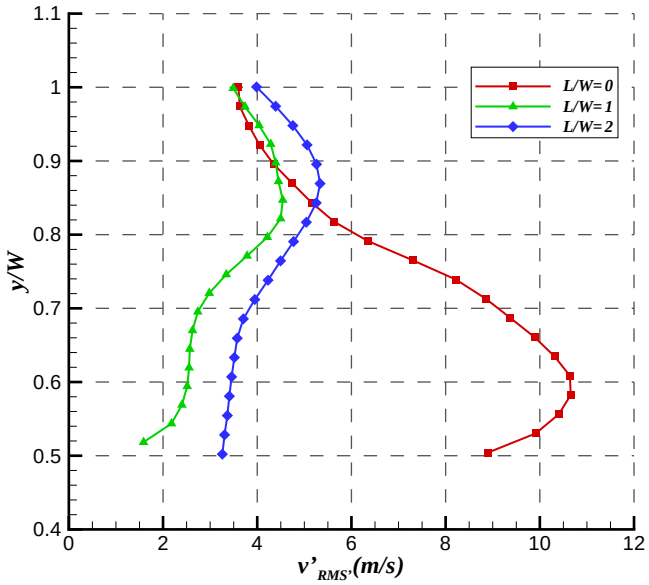

FIGURE 6.5: Profiles of the standard deviation in the y-direction from PIV data ($x/W = 0.5$, $z/D_{shell} = 0$). $U_\infty = 30\ m/s$.

at $Str_W = 0.3$ at $y/W = 0$ and $Str_W = 0.15$ at $y/W = 2$. The doubling of the frequency at $y/W = 0$ was thought to be the effect of the vortices being shed from both sides of the H-beam. Similar Strouhal numbers were reported for flat plates normal to the flow [69], this is possibly due to the similar way in which the flow separated off the sharp edges at the leading edge of the H-beam resulting in a comparable separation distance between the shear layers. The splitter plates progressively modified the shedding in the wake. With an increase in L/W, the shedding frequency decreased, agreeing with the observations for a flat plate with splitter plates [69].

The aerodynamic noise was investigated using on-surface microphones and freefield microphones. Figure 6.7 displays the on-surface microphone data, where the microphone was located at $y/W = 0$,$z/W = 0$ at the rear of the H-beam. The isolated H-beam, $L/W = 0$, showed a dominant spectral peak at $Str_W = 0.28$ similar to the hotwire measurements measured at $y/W = 0$. The splitter plate configurations showed the same reduction in the shedding frequency shown for the hotwire data. The shedding for $L/W = 3$ configuration did not feature as this was below $Str_W = 0.05$, which corresponds to $f = 20\ Hz$ (the lowest audible frequency) based on W and the freestream velocity. The SPLs for the on-surface microphone were dominated by the local flow over the microphones.

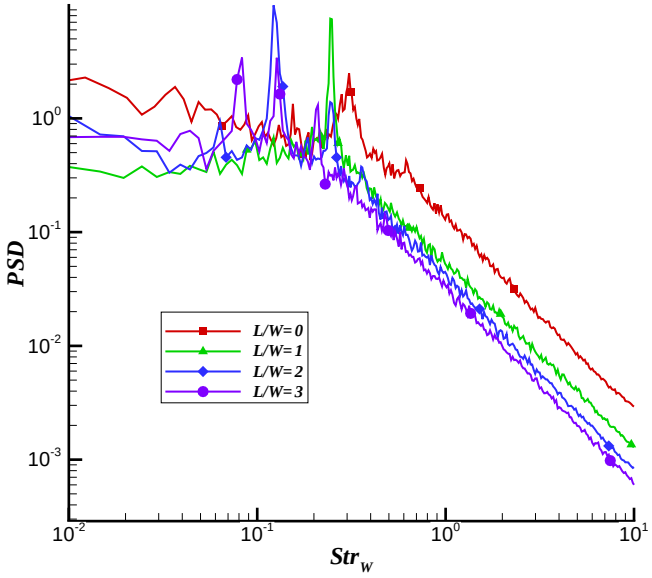

(a) $x/W = 1.5$ aft of model,$y/W = 0$ and $z/W = 0$.

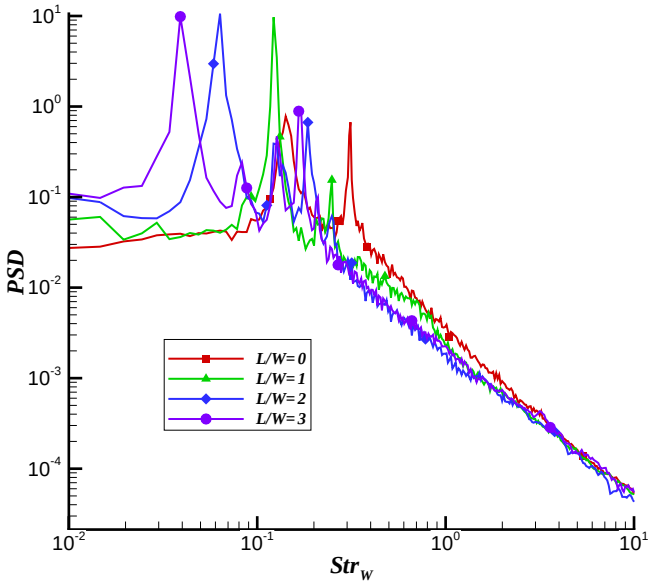

(b) $x/W = 1.5$ aft of model,$y/W = 2$ and $z/W = 0$.

FIGURE 6.6: Frequency spectra (PSD). $U_\infty = 25\ m/s$

The freefield microphone measurements are shown in figure 6.8a and 6.8b which correspond to two microphones at angular positions $\theta = 90°$ and $\theta = 120°$ respectively. The $L/W = 0$ configurations showed two peaks at $Str_W = 0.12$ and $Str_W = 0.78$ for both the freefield microphones, these scaled with velocity. The peak at $Str_W = 0.78$ was not picked up with the hotwire shown in figure 6.6. A

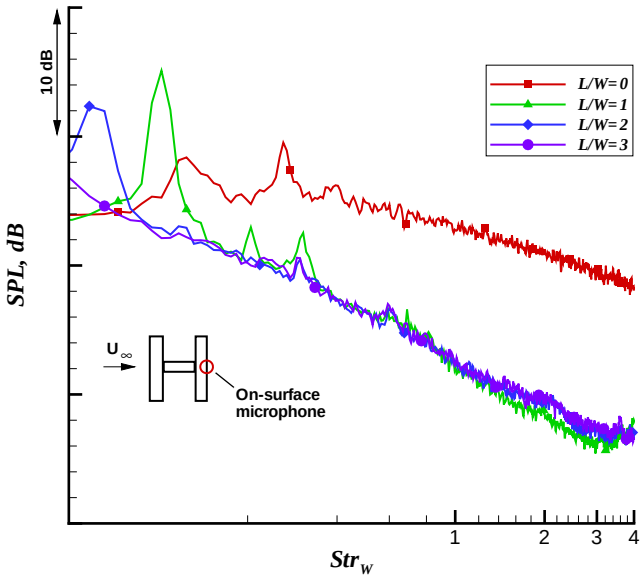

FIGURE 6.7: On-surface microphone. $U_\infty = 40\ m/s$.

possible reason for this was that noise source responsible for this peak was located on the model as this did not show up in the wake spectra.

Distinct peaks were not observed for the splitter plate configurations. For the freefield microphone at $\theta = 90°$ the peaks present for the $L/W = 0$ configurations were completely suppressed. The freefield microphone at $\theta = 120°$ showed that the splitter plate configurations had higher SPLs at frequencies lower than $Str_W = 0.1$ but still did not manifest distinct peak. This increase in level was seen in all the microphones located at an angular position larger than $\theta = 90°$. From the standard deviation contours shown in figure 6.4 the maximum velocity fluctuations, caused by the shedding wake, for the $L/W = 0$ configuration were in the proximity of the H-beam causing the sound at the shedding frequency to be radiated as would be expected by a dipole source. In the case of the splitter plate configurations the wake started to shed downstream of the H-beam and hence the shedding perturbations around the H-beam were reduced causing the peak associated with shedding to be suppressed.

6.3 Broadband Noise

The overall noise reductions achieved by using splitter plates at the rear of a H-beam are discussed.

Figure 6.9 displays ΔSPL for the different configurations for two freefield microphones at different angular positions, $\theta = 90°$ and $\theta = 120°$, the baseline configuration was the isolated H-beam. At $\theta = 90°$ all three splitter lengths showed broadband reductions across the entire frequency range, but did not show variations in the sound pressure levels between $Str_W = 0.05$ and $Str_W = 21$ when compared to each other. Above $Str_W = 21$ the $L/W = 2$ configuration was $\Delta 3\ dB$ quieter than the $L/W = 3$, which showed the least reduction above this Strouhal number when compared to the $L/W = 0$ configuration. The noise source localisation maps measured with the microphone array did not pick up any noise sources at these frequencies and therefore makes it difficult to come to a conclusion as to why the $L/W = 2$ configuration had lower noise levels above $Str_W = 21$. The results from the freefield microphone located at $\theta = 120°$ resulted in the three spitter plate configurations showing an increase of 20 dB for frequencies below $Str_W = 0.1$. This observation was discussed in the section 6.2. Above $Str_W = 0.1$ the broadband noise reductions were observed even if the ΔSpl levels were approximately 5 dB higher between $Str_W = 0.5$ and $Str_W = 3.5$ when compared to the results at $\theta = 90°$. This confirmed the hypothesis that the splitter plate configurations radiated more noise towards the rearward arc of the model. It is difficult to determine, but a possible explanation was that this was due to the scattering of noise from the trailing edge of the splitter plate due to the unsteadiness being concentrated in that region.

6.4 Summary

Experiments were conducted to investigate the potential of using a splitter plate placed at the rear of a bluff body as a means of noise reduction. The bluff body profile used was a H-beam. This featured sharp edges which was true for components on the landing gear, such as the articulation link. Three different splitter plate lengths were used as the literature review revealed that the splitter plate length had an influence on the near wake characteristics. Both aerodynamic and the related acoustics were studied employing two different wind tunnels and an open-jet anechoic chamber facility.

The application of the splitter plates had an effect on the wake, deflecting the shear layers in the lateral direction and impeding the vortex shedding until aft of the trailing edge of the splitter plates. The splitter plates also modified the drag and the shedding frequency, both decreasing with an increase in the splitter length. The largest drop of $\Delta C_d = 0.7$ was seen between $L/W = 0$ and $L/W = 3$.

The velocity fluctuations in the y-direction at the trailing edge of the H-beam were reduced by as much as 77% when the splitter plate was used translating into noise reductions over the entire frequency range. The freefield microphones did not reveal spectral peaks associated with vortex shedding; these were suppressed due to the maximum unsteadiness being displaced away from the solid surface of the H-beam and hence the sound radiated at these frequencies was greatly reduced. The reduction obtained with the splitter plate configurations was reduced in the rearward arc possibly due to the scattering of sound off the trailing edge of the splitter plates.

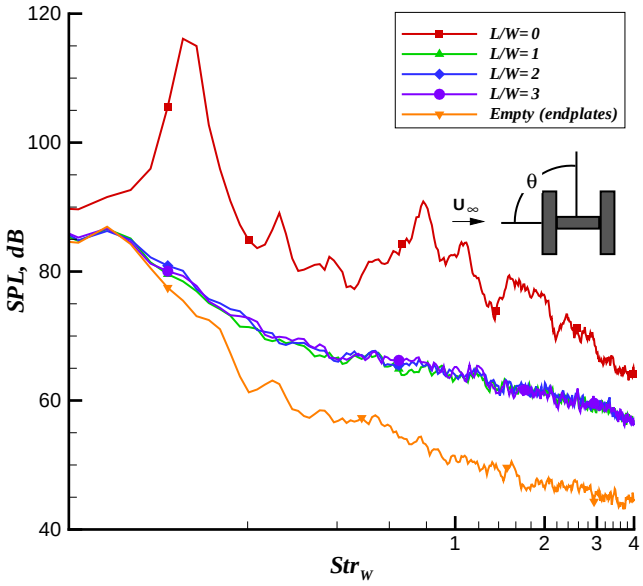

(a) Freefield microphone located at $\theta = 90°$.

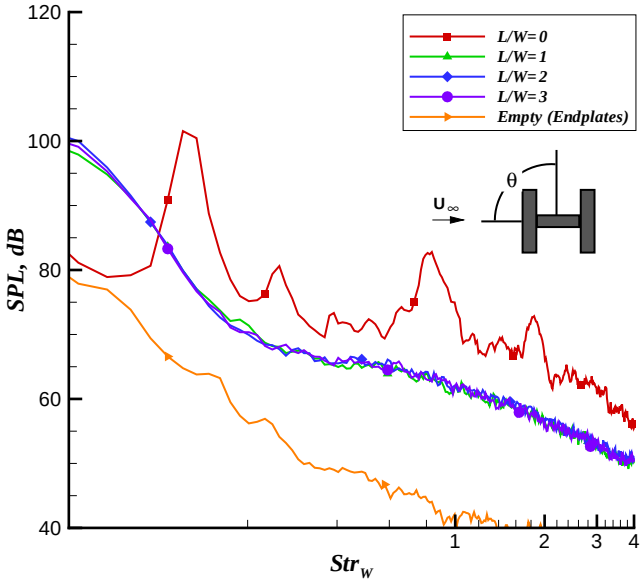

(b) Freefield microphone located at $\theta = 120°$.

FIGURE 6.8: Freefield microphone spectra measured in the anechoic chamber. $U_\infty = 40\ m/s$.

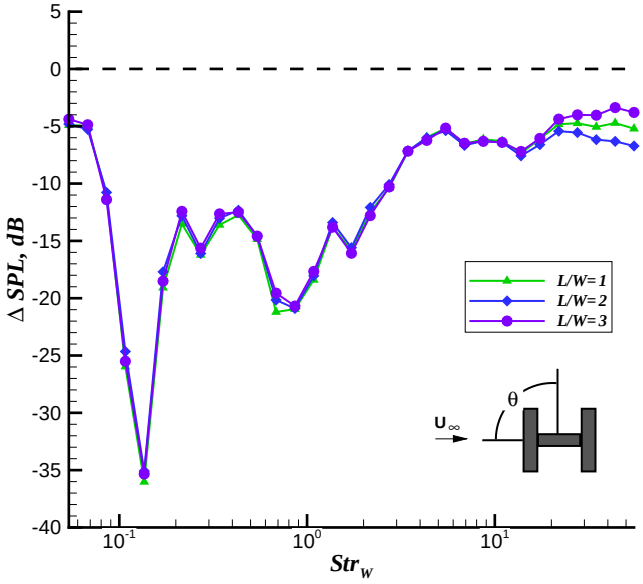

(a) Freefield microphone located at $\theta = 90°$.

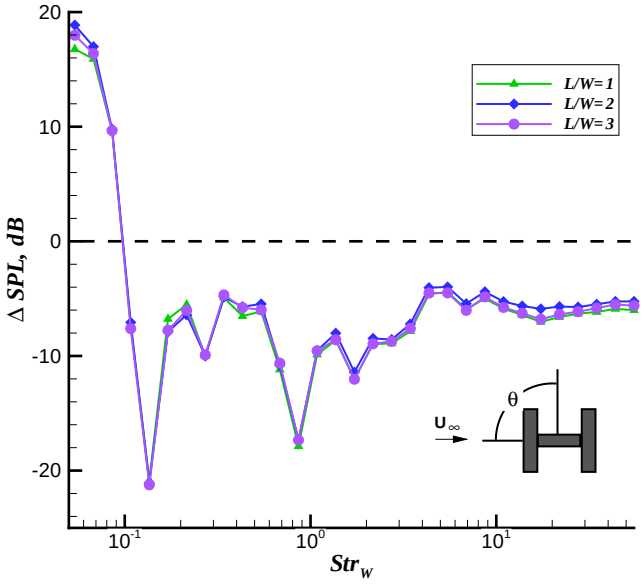

(b) Freefield microphone located at $\theta = 120°$.

FIGURE 6.9: ΔSPL for H-beam with splitter plates. $L/W = 0$ used as baseline. $U_\infty = 40\ m/s$.

Chapter 7

Conclusions and Recommendations

The main aim of this study was to investigate noise reduction techniques for bluff body noise. Three methods were investigated, using a splitter plate on a fairing-strut configuration, applying flow control to the surface of a fairing and fitting a splitter plate behind an isolated bluff body. The complex flow around landing gear necessitated the studies to be more fundamental to enable a better understanding of the noise generating mechanisms. Conclusions that may be drawn for each method are presented, followed by recommendations as to how they may be applied to landing gears.

7.1 Fairing-Strut with Splitter Plate

Wind tunnel tests of fairing-strut configurations were conducted to investigate the effect the strut diameter and the strut location have on the noise generated by the configuration. As a means of passive noise control, a splitter plate placed between the shell and the strut was used. Both aerodynamic and acoustic measurements were performed employing two different wind tunnels and a open-jet anechoic chamber.

7.1.1 Effect of strut diameter

- Time-averaged flow

An increase in the strut diameter increases the deflected velocities. The width of the wake was also affected, the larger struts resulted in wider wakes. The increase in the width of the wake together with the larger strut having a lower base pressure affected the mean drag measurements. The drag increased with an increase in the strut diameter with the largest strut having $\Delta C_d = 0.24$ higher than the smallest strut tested.

- Vortex shedding

  The hotwire measurements revealed that the wake was dominated by vortex shedding. The frequency of the shedding varied as a consequence of the change in the strut diameter. The shedding frequency decreased with an increase in the strut diameter, decreasing from $Str_{D_{shell}} = 0.26$ for the smallest strut to $Str_{D_{shell}} = 0.22$ for the largest strut.

- Acoustics

  The acoustic measurements were consistent with the aerodynamic results, with the vortex shedding manifesting itself as a spectral peak. The absolute noise level of the spectral peak associated with the vortex shedding was approximately 10 dB less for the smaller strut when compared to the larger strut. Although the smaller struts showed lower noise levels at the shedding frequency the larger struts showed a 4 dB broadband reduction between $Str_{D_{shell}} = 1.3$ and 11.

7.1.2 Effect of strut location

- Vortex shedding

  The $D_{strut}/D_{shell} = 0.67$ case showed small or no effects for two of the strut locations for both the aerodynamic and the acoustic results. However the strut location which was closest to the shell, $x_c/D_{shell} = 1/4$ showed a reduction in the shedding frequency of $Str_{D_{shell}} = 0.02$ when compared to the other two locations.

- Acoustics

  The freefield measurements revealed for the $D_{strut}/D_{shell} = 0.67$ case that the noise level for a strut in the location $x_c/D_{shell} = 1/4$ was 4 dB less when compared to the struts positioned further away from the shell. The $D_{strut}/D_{shell} = 0.93$ case showed an opposite effect with a decrease in noise of approximately 3 dB for the struts located further away from the shell.

7.1.3 Effect of splitter plate

- Time-averaged flow features

  For the $D_{strut}/D_{shell} = 0.67Splt$ case the splitter plate blocked the interaction of the shear layers which separated off the shell. This resulted in an increase of 10% in the deflected velocity and the widening of the wake. As a consequence of this the drag increased by 24% when compared to the $Nosplt$ configuration. The $D_{strut}/D_{shell} = 0.93Splt$ case showed a narrowing of the wake and a reduction in drag of $\Delta C_d = 0.5$ when compared to the $Nosplt$ configuration.

- Vortex shedding and acoustics

  For $D_{strut}/D_{shell} = 0.67Splt$ configuration the low frequency noise was dominated by a vortex shedding peak at the same frequency as for the $Nosplt$ configuration but was 12 dB less. The $D_{strut}/D_{shell} = 0.93Splt$ case suppressed the vortex shedding experienced when the splitter plate was not used. Another peak was observed which was 15 dB lower than the peak of the uncontrolled configuration. Both the $D_{strut}/D_{shell} = 0.67Splt$ and the $0.93Splt$ showed broadband reductions with the latter being the most effective at reducing noise.

7.1.4 Fairing with H-beam

The circular strut was replaced by an H-beam. Freefield acoustic measurements revealed that the isolated H-beam had two spectral peaks at $Str_{D_{shell}} = 0.18$ and 1.2. By shielding the H-beam with the shell the peak at $Str_{D_{shell}} = 0.18$ shifted to 0.24, similar to the frequencies seen for the shell shielding the strut. Shielding the H-beam also resulted in a broadband reduction of 4 dB between $Str_{D_{shell}} = 4$ and 26. The addition of the splitter plate reduced the broadband noise further, more than 10 dB between $Str_{D_{shell}} = 1$ and 10 and approximately 5 dB between $Str_{D_{shell}} = 12$ and 42.

7.2 Fairing-Strut with Suction or Blowing

7.2.1 Effect of porous material

Two porous materials were investigated, a perforated plate and a sintered metal plate. With no flow rates applied the perforated plate increased the noise produced by the model at high frequencies, above $Str_{D_{shell}} = 10$ when compared to the sintered metal plate. This was thought to be caused by a turbulent boundary layer passing over the perforated sheet. The perforated sheet also showed noise levels increased by as much as 20 dB when the blowing and suction system were used and compared to the sintered metal case. Due to the increased noise levels seen for the perforated case the sintered metal was used to generate the results for the effect of suction and blowing.

7.2.2 Effect of suction and blowing

Suction did not have an effect on the shedding frequency, whilst the shedding frequency decreased with an increase in blowing flow rates. In the case of suction the separation remained fixed at the trailing edge of the shell. Blowing caused the flow on the shell to separate earlier and hence decrease the frequency of shedding.

Both suction and blowing showed reductions of as much as 5 dB between $Str_{D_{shell}} = 5.7$ and $Str_{D_{shell}} = 35$ for suction and $Str_{D_{shell}} = 10$ and $Str_{D_{shell}} = 40$ for blowing at $U_\infty = 20\ m/s$. For both suction and blowing the peak reductions were reduced with an increase in the Reynolds number, reducing the reduction to about 1 dB which is at the limit of the accuracy of the system.

7.3 H-Beam with Splitter Plate

The application of the splitter plates had an effect on the wake, deflecting the shear layers in the lateral direction and impeding the formation of vortex shedding until aft of the trailing edge of the splitter plates. The splitter plates also modified the drag and the shedding frequency, both decreasing with an increase in the splitter length. The largest drop of $\Delta C_d = 0.7$ was seen between $L/W = 0$ and $L/W = 3$.

The velocity fluctuations in the y-direction at the trailing edge of the H-beam were reduced by as much as 77% when the splitter plate was used, translating into

noise reductions over the entire frequency range. The freefield microphones did not reveal spectral peaks associated with vortex shedding, these were suppressed due to the maximum unsteadiness being displaced away from the solid surface of the H-beam and hence the sound radiated at these frequencies was greatly reduced. The reduction obtained with the splitter plate configurations was reduced in the rearward arc possibly due to the scattering of sound off the trailing edge of the splitter plates.

7.4 Recommendations

The recommendations for the application of the technologies investigated in the study on landing gear are highlighted followed by recommendations for future work.

7.4.1 Application on landing gears

The section summarises how the findings from the discussed studies could be applied to the landing gear and its fairing. As the investigations were fundamental studies care should be taken in applying the findings directly to the landing gear. Certain flow features are considered to be specific to the model geometry.

- Fairing size and location

  The efficiency of the fairing may be increased by using fairings which are not much larger then the component they are shielding. Small differences in the noise levels were seen when the ratio of the fairing diameter to the strut diameter was varied. Weight saving and easier landing gear retractability are advantages of having smaller fairings.

  Fairings have the disadvantage of making routine maintenance and landing gear inspections difficult. The findings showed that the variation in noise levels was small when the fairing-strut separation distance was varied. This could allow the fairings to be placed further away from the shielded components and thus improve accessibility. These recommendations are valid when the component being shielded is cylindrical in cross section.

- Splitter plate.

Splitter plates were shown to be effective in reducing the broadband noise both when fitted to the fairing and when used behind a bluff body.

Potentially the splitter plates may be used coupled to small, localised fairings on the landing gear. Examples of these locations could include the articulation link, drag arm, bogie beam and main strut. This could reduce the noise generated by these individual components which would have an effect on the global noise generated by the landing gear. Nonetheless care must be taken as the interaction of the deflected flow onto downstream components may cancel out the reductions achieved by using the splitter plate.

Findings have shown that splitter plates located behind bluff bodies of relatively short length have the potential to reduce broadband noise. Short splitter plates would not have a significant effect on added weight and could be small enough to make landing gear retraction possible. Splitter plates placed behind individual components such as the main strut and the bogie beam would be recommended.

- Flow Control

  The flow control reduced the self noise of the fairing which was desirable. The largest reduction was seen at low Reynolds numbers as the flow rates required to achieve similar reductions at high Reynolds numbers were large. Flow control placed towards the trailing edge of the fairings seemed to be effective although the flow rates required in flight conditions would need to be high, requiring a lot of energy from the aircraft systems.

7.4.2 Future work

- The splitter plate was only used on a single bluff body. Applying this to bluff bodies in tandem would be beneficial. The wake of the upstream bluff body interacts with the downstream body causing an increase in the generation of noise. Splitter plates placed between the tandem bluff bodies, behind the downstream bluff body or a combination of both could be possible configurations.

- As the study was restricted to generic models, future work would comprise performing aerodynamic and acoustic tests of the different technologies on the landing gear.

Appendix A

Numerical Models

A.1 Governing Equations

The unsteady, compressible Navier-Stokes equations were used to solve the flow. For a turbulent flow the instantaneous value of velocity, density etc is equal to the sum of the ensemble-averaged component and the fluctuating component, $u_i = \bar{u}_i + u_i'$. In addition to the velocity and pressure fluctuations, the density and temperature fluctuations must also be accounted for when the medium is a compressible fluid. The Favre-averaged Navier-Stokes equations for variable density flow were used and are given in equations A.1-A.3.

$$\frac{\partial \bar{\rho}}{\partial t} + \frac{\partial \bar{\rho}\bar{u}_i}{\partial x_i} = 0. \tag{A.1}$$

$$\frac{\partial \bar{\rho}\bar{u}_i}{\partial t} + \frac{\partial \bar{\rho}\bar{u}_i\bar{u}_j}{\partial x_j} = -\frac{\partial \bar{p}}{\partial x_i} + \frac{\partial}{\partial x_j}\left(-\overline{\rho u_i' u_j'} + \bar{\tau}_{ij}\right). \tag{A.2}$$

$$\begin{aligned}\frac{\partial \bar{\rho}\bar{E}}{\partial t} + \frac{\partial}{\partial t}\left(\left(\bar{\rho}\bar{E} + \bar{p}\right)\bar{u}_j\right) &= -\frac{\partial}{\partial x_j}\left(\bar{q}_j + \overline{\rho u_j' e'}\right) \\ + \frac{\partial}{\partial x_j}\left(\bar{u}_i\left(\bar{\tau}_{ij} - \overline{\rho u_i' u_j'}\right)\right) &+ \frac{\partial}{\partial x_j}\left(\overline{\tau_{ij} u_i'} + \frac{1}{2}\overline{\rho u_j' u_i' u_i'}\right).\end{aligned} \tag{A.3}$$

The unresolved turbulent fluctuations in the velocity and specific internal energy are given by u_i' and e' respectively. The two additional terms compared to the instantaneous Navier-Stokes equations are $\overline{\rho u_i' u_j'}$ and $\overline{\rho u_j' e'}$, the Reynolds stress

tensor and the turbulent heat flux respectively. The heat flux vector is given by equationA.4:

$$\bar{q}_j = -\left(\frac{\mu}{Pr} + \frac{\mu_t}{Pr_t}\right) c_p \frac{\partial \bar{T}}{\partial x_j}, \tag{A.4}$$

where Pr_t is the turbulent Prandtl number which defines the ratio of viscous diffusion to thermal diffusion and μ_t is the turbulent viscosity.

The Favre-averaged total energy is given in equation A.5.

$$\bar{\rho}\bar{E} = \bar{\rho}\left(\bar{e} + \frac{1}{2}\bar{u}_i\bar{u}_i\right) + \frac{1}{2}\overline{\rho u_i' u_i'}. \tag{A.5}$$

The Favre-averaged specific energy is denoted by $\bar{e}$. The Boussinesq assumption was employed to relate the Reynolds stresses to the mean velocity gradient resulting in the following viscous stress tensor.

$$\bar{\tau}_{ij} = (\mu + \mu_t)\left[\left(\frac{\partial \bar{u}_j}{\partial x_i} + \frac{\partial \bar{u}_i}{\partial x_j}\right) - \frac{2}{3}\frac{\partial \bar{u}_k}{\partial x_k}\delta_{ij}\right], \tag{A.6}$$

The terms $\overline{\tau_{ij}u_i'}$ and $\overline{\rho u_j' u_i' u_i'}$ in equation A.3 which correspond to the molecular diffusion and the turbulent transport of the turbulent kinetic energy were ignored [87]. The turbulent fluctuation terms in the total energy equation A.5 were ignored. Also the viscous terms involving fluctuating terms were also ignored in the stress tensor.

A.2 Solver

The solver was a cell-centered, finite volume commercial CFD code, Fluent. The governing equations were solved using a pressure-velocity correction approach. To enforce mass conservation and to obtain the pressure field the pressure-velocity algorithm used was SIMPLE. The pressure, energy and density discretisation schemes used were second order upwind, while the momentum and modified turbulent viscosity discretisation schemes used central differencing. The time scheme was an implicit second-order time scheme with dual time stepping.

The computations were performed on a Linux cluster hence allowing the solution to be computed in parallel on a different nodes. The grid was partitioned into

equal size subdomains.

A.3 Turbulence Model

A Detached-Eddy simulation (DES) model was employed as a turulence model. This approach combined RANS modeling with LES for applications in which classical LES is not affordable (e.g. high-Re external aerodynamics simulations). The DES model is based on the one-equation Spalart-Allmaras (SA) turbulence model with a modified length scale.

The SA model is a one equation model which solves the transport equation for the modified turbulent viscosity, $\tilde{\nu}$. The transport equation is defined by,

$$\frac{\partial \tilde{\nu}}{\partial t} + \nabla \cdot (\tilde{\nu}\mathbf{V}) = c_{b_1}\tilde{S}\tilde{\nu} + \frac{1}{\sigma}\left[\nabla \cdot ((\nu + \tilde{\nu})\nabla\tilde{\nu}) + c_{b_2}(\nabla\tilde{\nu}) \cdot (\nabla\tilde{\nu})\right] - c_{w_1} f_w \cdot \left(\frac{\tilde{\nu}}{d}\right)^2. \tag{A.7}$$

$$\nu_t = \tilde{\nu} f_{v_1}. \tag{A.8}$$

The modified turbulent viscosity, $\tilde{\nu}$ is related to the eddy viscosity, ν_t by equation A.8.

The vorticity/strain relationship [88] was used for the production term S. This was done to take into account the effect of the mean strain on the turbulence production. The modified production term is given by equation A.9

$$S \equiv |\Omega_{ij}| + C_{prod} min\left(0, |S_{ij}| - |\Omega_{ij}|\right), \tag{A.9}$$

where $|\Omega_{ij}|$ is the magnitude of vorticity, $|S_{ij}|$ is the magnitude of the strain tensor and $C_{prod} = 2$.

From equation A.7 the wall destruction term is proportional to $(\tilde{\nu})^2$. When the destruction term is equal to the production term the eddy viscosity is proportional to $\hat{S}d_2$, where $\hat{S}$ is the strain rate. In large-eddy simulations (LES) a sub-grid model is used to solve the turbulent stresses that are not directly resolved. In the Smagorinski sub-grid scale model the eddy viscosity is proportional to $\hat{S}\Delta^2$,

where $\Delta = max\,(\Delta x, \Delta y, \Delta z)$. By using the distance to the nearest wall in the SA model ($\hat{d}$) instead of Δ then the SA model can be coupled to the LES model and replace the Smagorinski sub-grid model. The length scale ($\hat{d}$) in equation A.7 is replaced by a modified length scale ($\tilde{d}$).

$$\tilde{d} = min\left(\hat{d}, C_{DES}\Delta\right) \tag{A.10}$$

where C_{DES} is a constant.

When the distance to the nearest wall is smaller than $C_{DES}\Delta$ the turbulence model will use the SA model to compute the flow while if greater, the LES model is used.

A.4 Computational grid

A three-dimensional structured grid was used for the CFD solution. The geometry used was the fairing-strut configuration to investigate the effect of the splitter plate. The strut used in the computation had a diameter of $D_{strut}/D_{shell} = 0.93$ at a streamwise location of $x/D_{shell} = 1/2$. A C-mesh type grid was used with the domain extending a minimum of $20D_{shell}$ from the model [89]. The span of the computational model was $2D_{shell}$. The reduction in spanwise length was done to improve the quality and number of spanwise cells, crucial in providing adequate resolution in a DES computation. The value of $2D_{shell}$ was chosen based on previous DES computational studies on circular cylinders at similar Reynolds numbers [90].

The grid consisted of 5.4×10^6 structured cells and 50 blocks. The viscous RANS region for the attached boundary layer had a first wall cell spacing of $y^+ = 1$ and a stretching ratio of 1.2 [91] with at least the first 15 cells in the boundary layer. To reduce the number of grid cells patching was used. A fine cubic cell grid was maintained around the solid walls and in the downstream wake region as these contain all the turbulence and vorticity generated by the solid body. The outer region used a coarser grid in all three directions which helped to reduce the grid count. Figures of the grid are illustrated in figures A.1-A.4.

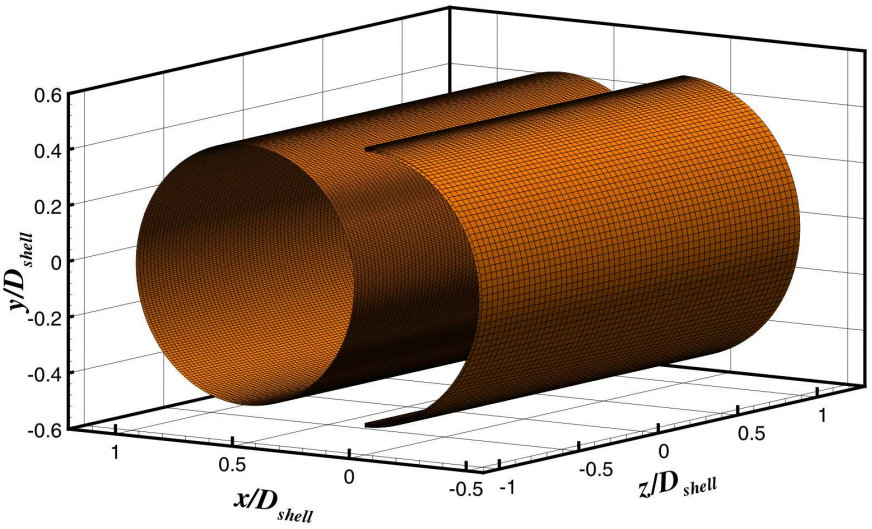

FIGURE A.1: On-surface grid around the model

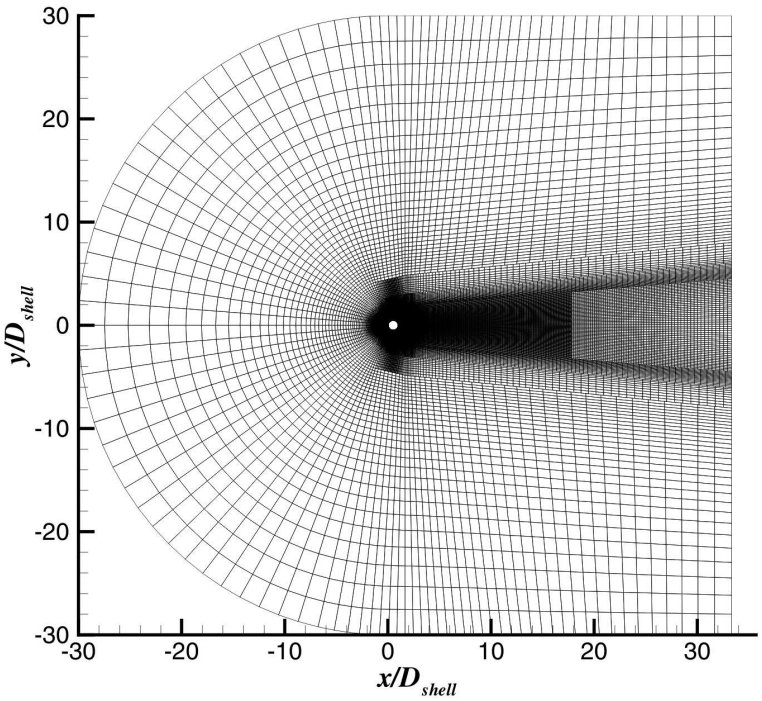

FIGURE A.2: Overview of a slice through the grid.

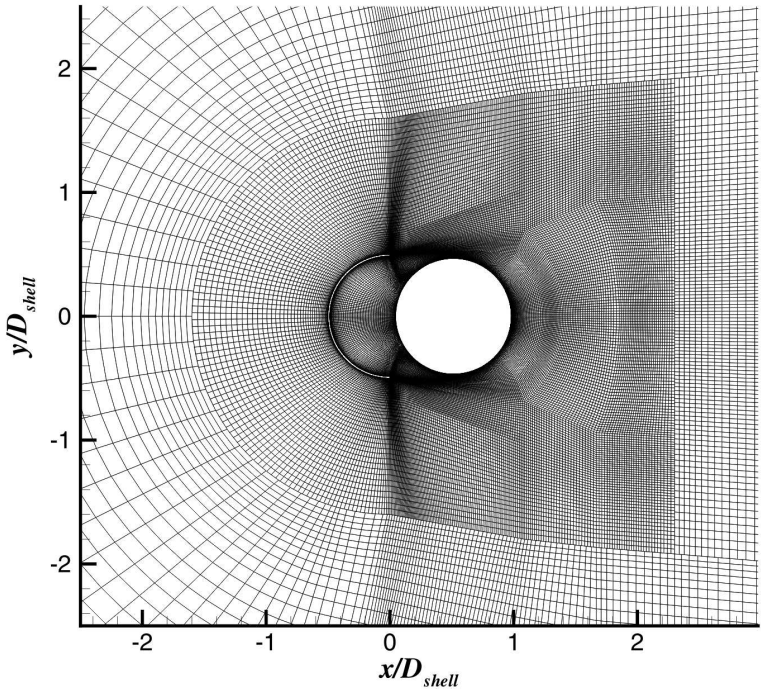

FIGURE A.3: Detail of the patched grid.

A.5 Boundary Conditions

Pressure farfield boundary condition

The pressure farfield boundary condition was a non-reflective boundary based on the introduction of the Riemann invariants for a one-dimensional flow normal to the boundary [92]. There are two Riemann invariants that correspond to the incoming and outgoing waves.

$$R_\infty = u_{n_\infty} + \frac{2a_\infty}{\gamma - 1}, \tag{A.11}$$

and

$$R_i = u_{n_i} - \frac{2a_i}{\gamma - 1}, \tag{A.12}$$

where u_n is the velocity normal to the boundary, a is the local speed of sound and γ is the specific heat ratio for an ideal gas. The subscript ∞ refers to the conditions

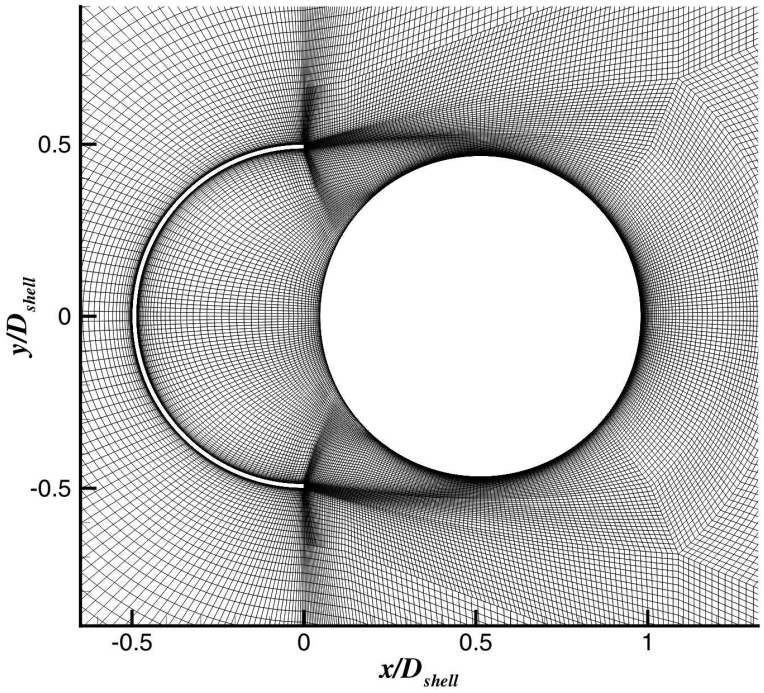

FIGURE A.4: Detail of the grid around the model

being applied at infinity and i refers to the condition in the cell adjacent to the boundary face. Equations 2.13 and 2.14 may be added and subtracted to obtain the following two relationships:

$$u_n = \frac{1}{2}\left(R_i + R_\infty\right), \tag{A.13}$$

$$a = \frac{\gamma - 1}{4}\left(R_i - R_\infty\right), \tag{A.14}$$

where u_n and a are the values applied on the boundary. At a face through which flow exits, the tangential velocity components and entropy are extrapolated from the interior whilst at an inflow face, these are specified as having free-stream values. Using the values for the velocity normal to the boundary, the speed of sound, the tangential velocity components, and entropy the values of density, velocity, temperature, and pressure at the boundary face can be calculated.

The spanwise computational extents were modelled using periodic boundary conditions. A pressure drop is allowed to occur across the translationally periodic

boundaries, enabling the modeling of "fully-developed" periodic flows [92]. The wall boundary condition was a non-slip boundary condition while the density was calculated using the ideal gas law. The positions of the boundary conditions are sketched in figureA.5

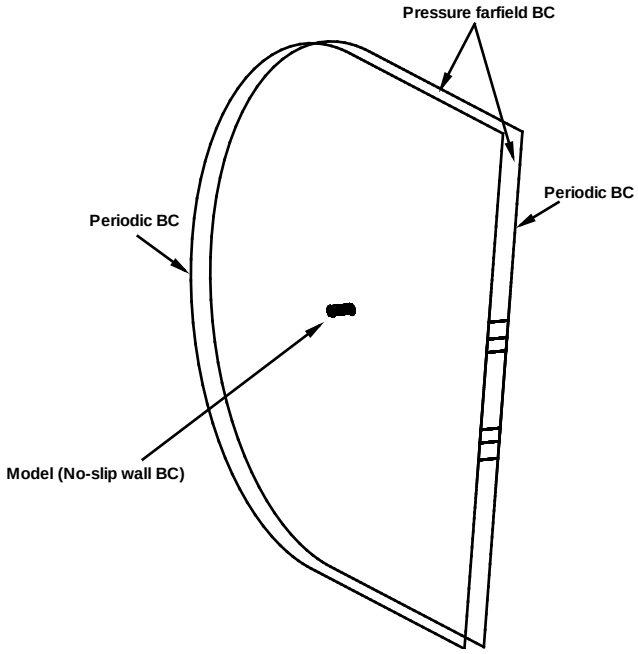

FIGURE A.5: Sketch of boundary conditions

A.6 Convergence Criteria

A physical time step of 2.5×10^{-5} s which corresponds to a sampling frequency of $40k$ Hz was used. Based on this the highest frequency resolved was $20k$ Hz according to the Nyquist criteria. The timestep corresponded to a non-dimensional timestep of 6.7^{-3}, normalised with inflow velocity and the fairing diameter. About 700 timesteps per shedding period were employed, well above the suggested value of 500 suggested by Rumsey [89] for circular cylinders. The solution was run for 70 time units before time-averaging and acoustic data was acquired. This ensured that the values of drag and lift were stable and the residuals fell by three-four orders of magnitude and levelled off.

A.7 Validation

The validation process of the three-dimensional grid used in the investigation was conducted by performing a grid convergence study on three two-dimensional grids of different grid densities. Once results and flow physics of the two-dimensional grids were demonstrated to be grid independent the grid of a medium grid density was extruded to construct the three-dimensional grid. The results of the three-dimensional grid were validated further by comparing the computational aerodynamic and acoustic results with experimental results.

A.7.1 Two-dimensional grid convergence study

The two-dimensional grids were solved using an Unsteady Reynolds Averaged Navier Stokes (URANS) code in order to solve the unsteady nature of of the flow physics around the model geometry being investigated.

The turbulence models considered to solve the turbulent fluctuations in the two-dimensional calculations were linear viscosity models. These models are based on the statistics at a single point where the Reynolds Stresses are determined using the Boussinesq approximation, which is used to compute the Reynolds stress tensor as a product of an eddy viscosity and the mean strain-rate tensor. The four turbulent models were the Spalart-Allmares (SA) one equation model, the two equation model $k-\varepsilon$ and $k-\omega$ model, and the shear stress transport (SST) two equation $k-\omega$ model of Menter.

The Spalart-Allmaras turbulence model is a one equation model which directly solves a differential equation for eddy viscosity at a point in the flow field. It was designed to perform well in wall bounded, attached flow but is known to be over dissipative. The $k-\varepsilon$ model solves two equations for the turbulent kinetic energy k and the rate at which turbulent energy is dissipated to smaller eddies ε. This is a very robust model for a large variety of flows, however it performs poorly when faced with separation, it has a tendency to predict the onset of separation too late and to under predict the amount of separation, it is often also inadequate for adverse pressure gradients. The $k-\omega$ model solves the turbulent kinetic energy k and ω the frequency of the large eddies (specific dissipation rate). The model performs well close to the walls in boundary layer flows, particularly under strong adverse pressure gradients. However it is sensitive to the free stream value of ω. The Shear Stress Transport turbulence model is a blend of both the $k-\varepsilon$ model

and the $k-\omega$ model. This model functions by solving the turbulent-frequency model near the wall and the model in the bulk of the flow making the model perform well in non-equilibrium boundary layer regions, however it fares poorly when predicting the flow recovery following reattachment. Previous research on bluff bodies at a similar Reynolds number has shown the SST $k-\omega$ model yields computational results which conform with experimental results [36]. The SST $k-\omega$ model was used as the turbulence model for the two-dimensional grids.

A grid convergence study was carried out to determine whether the grid was fine enough to capture the flow physics and to ensure that the solution of the computation was grid independent. The $D_{strut}/D_{shell} = 0.93 Osplt$ configuration was used and three grids, coarse, medium and fine grids were constructed. The two-dimensional grids were constructed as described in section A.4 and the grid spacing details are summarised in Table A.1.

	Total No. of Cells	No. of cells around shell	No. of cells around cylinder
Coarse	26,432	113	197
Medium	73,356	226	395
Fine	156,874	452	789

TABLE A.1: Details of two-dimensional grids.

The number of cells on each edge around the strut and the shell were doubled per refinement step resulting in $26,432$, $73,356$ and $156,874$ for the coarse, medium and fine grids respectively. A patched grid for the two-dimensional grids was used to reduce the eventual grid size of the three-dimensional grid with more and finer grid cells around the solid walls and the near wake.

Previous studies on cylinder flow suggest that to ensure adequate temporal resolution 300 time steps per shedding cycle are necessary [36]. Based on the shedding frequency from the experimental observations a time step size of $\Delta t = 5 \times 10^{-5}$ was used. The sub iterations per time step were fixed at 20 as it was sufficient for the residuals to drop by three orders of magnitude per time step.

Iterative convergence is assessed using the non dimensional time

$$t_D = \frac{tU_\infty}{D_{shell}}. \tag{A.15}$$

The physical meaning of equation A.15 is the number of characteristic lengths i.e. shell diameter, that travel through the computational domain. In order to achieve

iterative convergence (dynamic steady state) the computation was run to allow the characteristic length to travel once through plus an additional 20 non dimensional time steps resulting in $t_D \approx 60$.

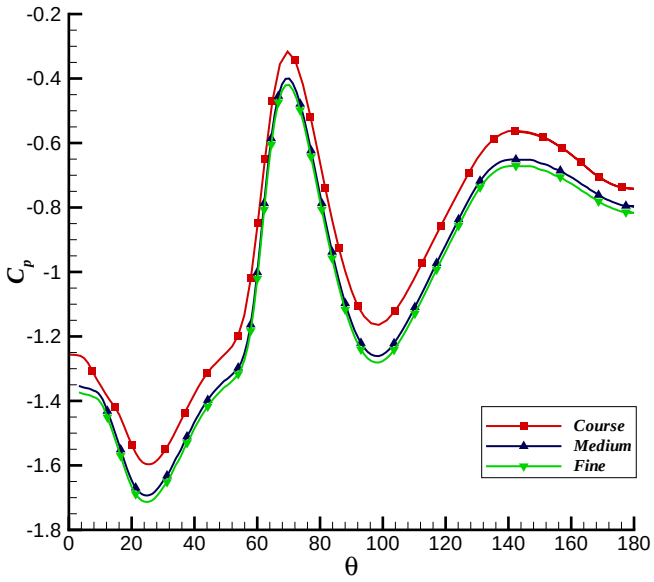

FIGURE A.6: Grid convergence; Time-averaged pressure distribution around the strut for the two-dimensional grids.

Time averaged pressure distributions were monitored around the strut shown in figure A.6. The grid refinement from the coarse grid yielded a variation of approximately 7% in the base pressure of the strut when compared to the medium grid. The variation between the medium and fine grids was approximately 1.5%. The flow physics was consistent for all three grids indicating that the CFD solution was not grid dependent. The variations in the qualitative solutions of the grid would have warranted a finer grid to achieve a better two-dimensional CFD solution, however this exercise was carried out as a grid stability study for the three-dimensional grid and hence a finer grid would have resulted in being computationally expensive.

A.7.2 Three-dimensional grid validation

The next section deals with comparisons between the experimental and the three-dimensional DES results in order to validate the numerical simulations.

The pressure distributions around the strut for the *Splt* and *Nosplt* configurations

are shown in figures A.7 and A.8. For the *Splt* configuration the impingement and separation locations agreed well between the experimental and numerical results however $\Delta C_p \approx 0.72$ was observed at the separation point at $\theta = 100°$. A possible explanation for this is the dissipative nature of the computational model as well as that the strut, around which the pressure distribution was compared, is in the separated wake of the shell. The experimental results of *Nosplt* configuration did not compare as well with the numerical results. The reattachment and separation locations were under predicted by $\Delta\theta \approx 5°$. Although the numerical solution over-predicted the value of C_p for both configurations the numerical simulation was deemed to have adequately captured the physical flow.

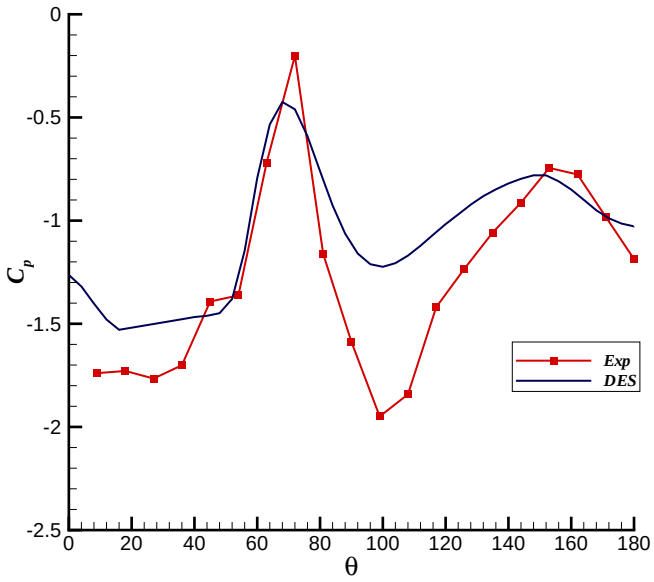

FIGURE A.7: Comparison of experimental and computational distribution around the strut. *Nosplt* configuration.

The coefficient of drag, C_D was compared and for the *Nosplt* configuration yielded a $\Delta C_D = 0.01$ whilst the *Splt* configuration yielded a larger discrepancy of $\Delta C_D = 0.029$. The comparison between the pressure distributions showed that there was a larger difference in the base pressure of the strut for the *Splt* configuration which was thought to have led to the larger difference in the coefficient of drag.

Figure A.9 shows the acoustic spectra obtained from the numerical simulations for both the *Nosplt* and *Splt* configurations. The results were dominated by the shedding wake which is what was demonstrated in the experimental tests. The frequencies at which the shedding peak occurred agreed well with the experimental

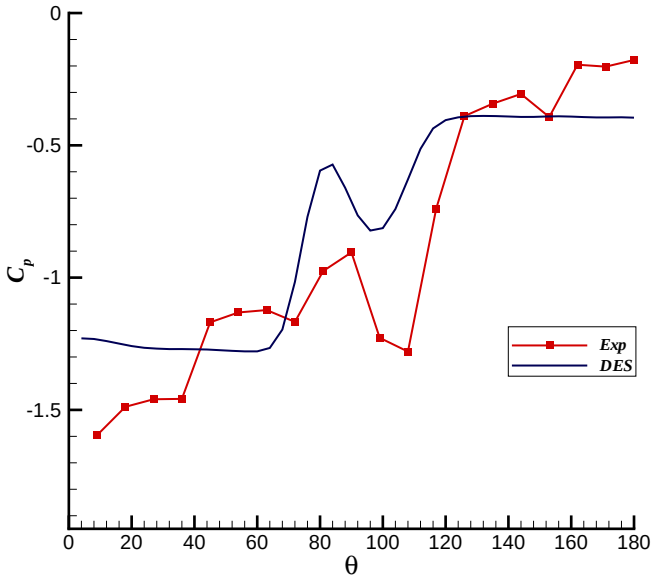

FIGURE A.8: Comparison of experimental and computational distribution around the strut. *Splt* configuration.

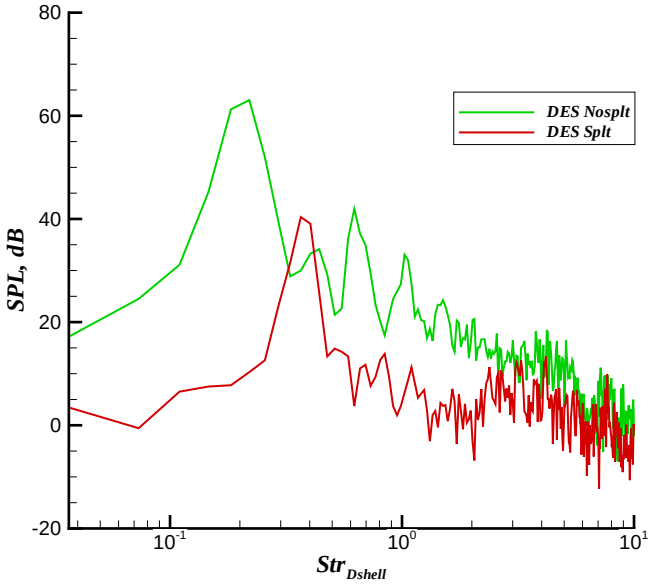

FIGURE A.9: Farfield acoustic computational results. $\theta = 90°$ and $r = 100m$. $U_\infty = 40m/s$.

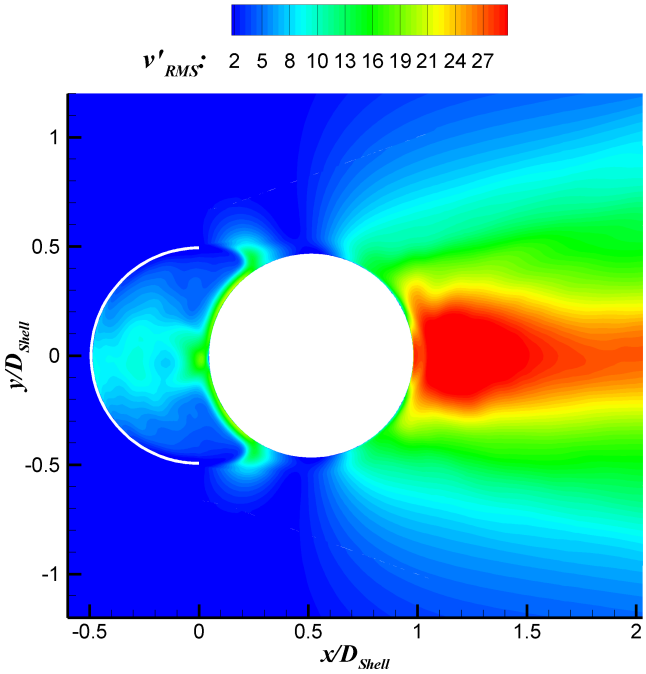

(a) *NoSplt.*

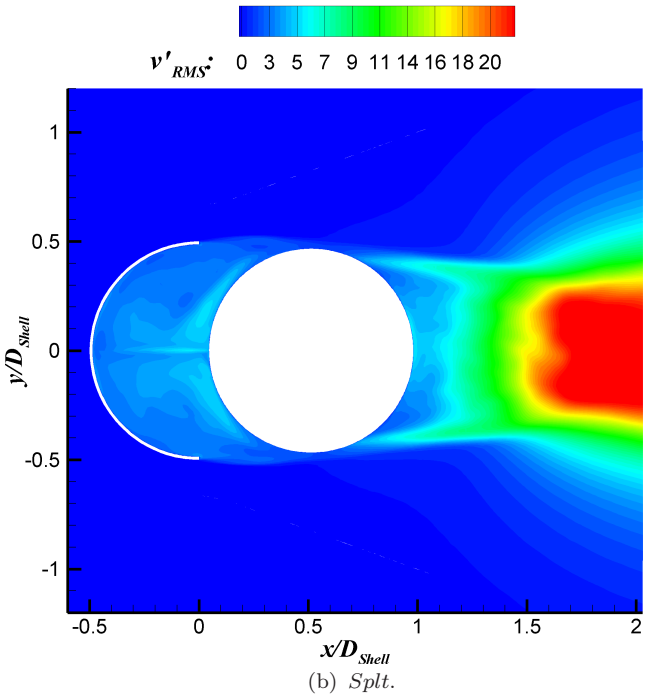

(b) *Splt.*

FIGURE A.10: Standard deviation of velocity in the y-direction. $U_\infty = 40\ m/s$. Flow from left to right.

results.

Figure A.10 shows the standard deviation of the velocity in the y-direction computed from the numerical simulation. The figure may be compared to figures 4.18b and 4.24b for the *Nosplt* and the *Splt* configurations respectively. As was observed experimentally the maxima were just aft of the strut in the *Nosplt* configuration but were displaced further downstream from the strut when the splitter plate was used.

Appendix B

Technical Drawings of Fairing-Strut Model

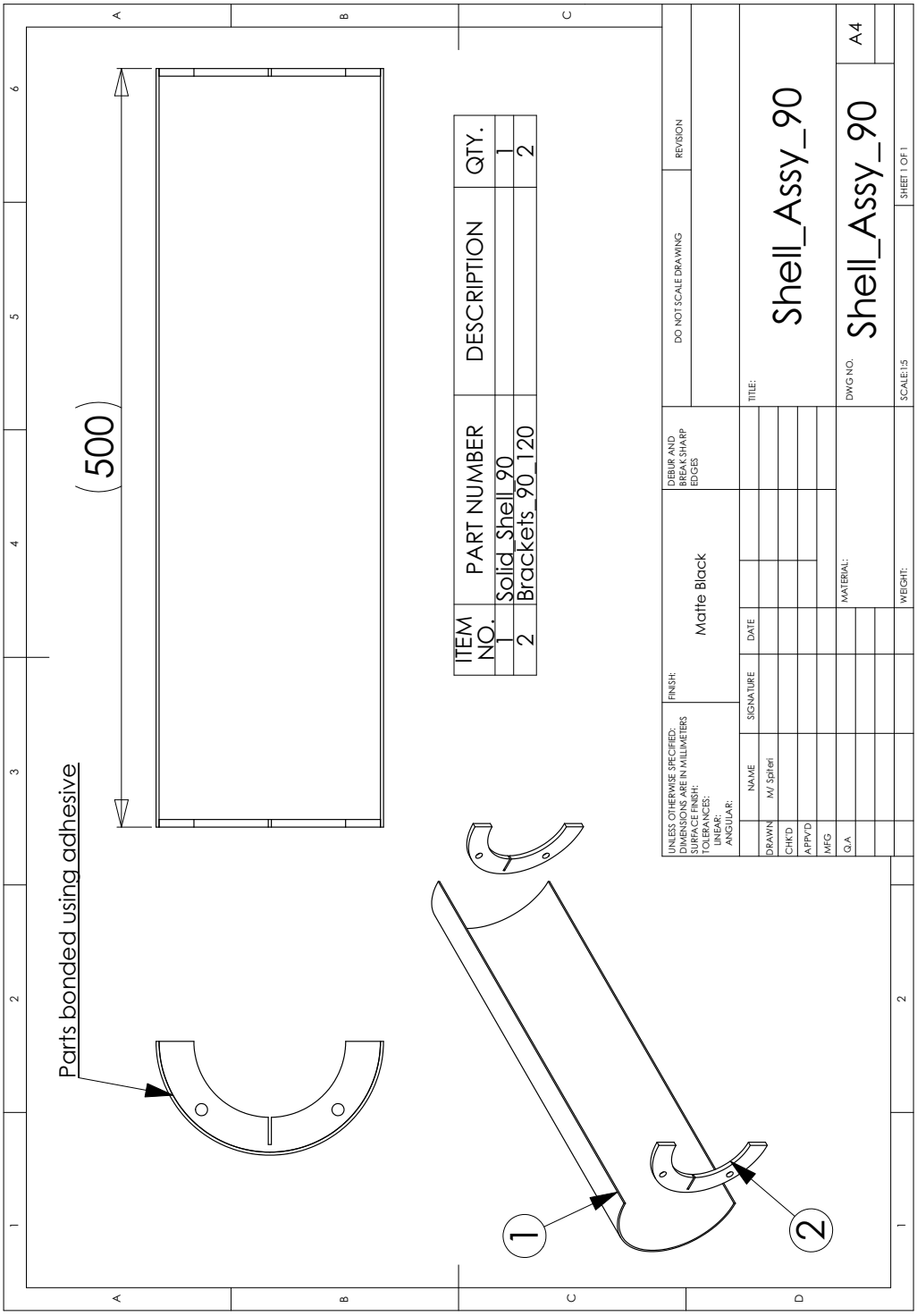
Parts bonded using adhesive
500
ITEM NO.
PART NUMBER
DESCRIPTION
QTY.
1
Solid_Shell_90
1
2
Brackets_90_120
2
1
2
DO NOT SCALE DRAWING
REVISION
TITLE:
Shell_Assy_90
UNLESS OTHERWISE SPECIFIED:
DIMENSIONS ARE IN MILLIMETERS
SURFACE FINISH:
TOLERANCES:
LINEAR:
ANGULAR:
FINISH:
Matte Black
DEBUR AND BREAK SHARP EDGES
NAME
SIGNATURE
DATE
DRAWN
M. Spiteri
CHK'D
APPV'D
MFG
Q.A
MATERIAL:
DWG NO.
Shell_Assy_90
A4
WEIGHT:
SCALE:1:5
SHEET 1 OF 1

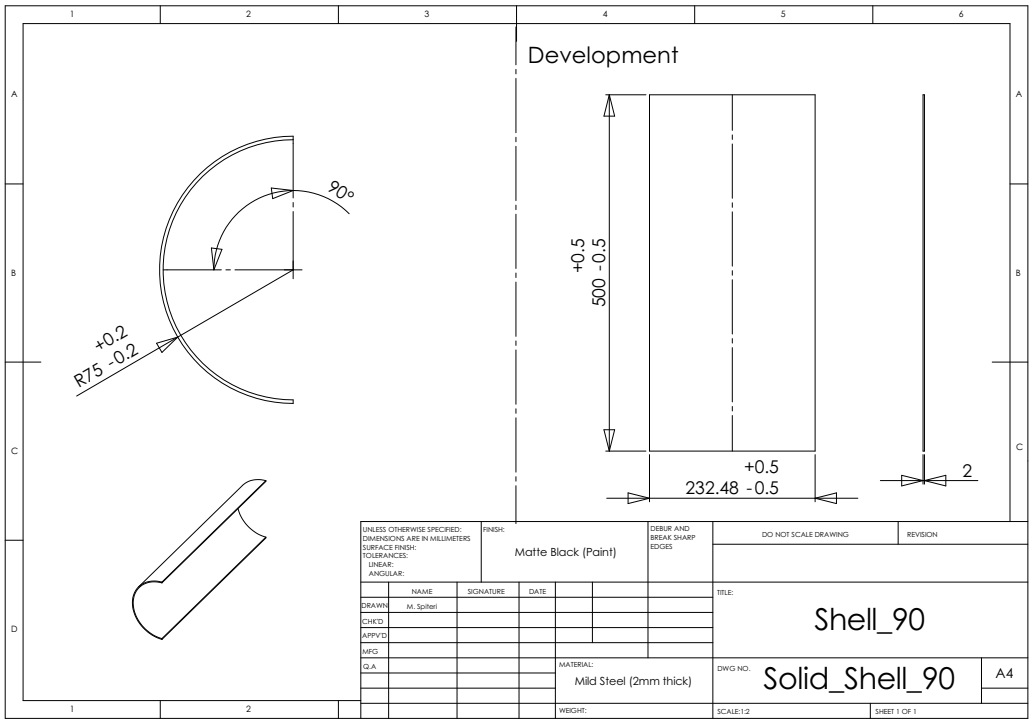
Development
90°
+0.2
R75 -0.2
+0.5
500 -0.5
+0.5
232.48 -0.5
2
UNLESS OTHERWISE SPECIFIED:
DIMENSIONS ARE IN MILLIMETERS
SURFACE FINISH:
TOLERANCES:
LINEAR:
ANGULAR:
FINISH:
Matte Black (Paint)
DEBUR AND BREAK SHARP EDGES
DO NOT SCALE DRAWING
REVISION
NAME
SIGNATURE
DATE
DRAWN
M. Spiteri
CHK'D
APP'V'D
MFG
Q.A
MATERIAL:
Mild Steel (2mm thick)
WEIGHT:
TITLE:
Shell_90
DWG NO.
Solid_Shell_90
A4
SCALE:1:2
SHEET 1 OF 1

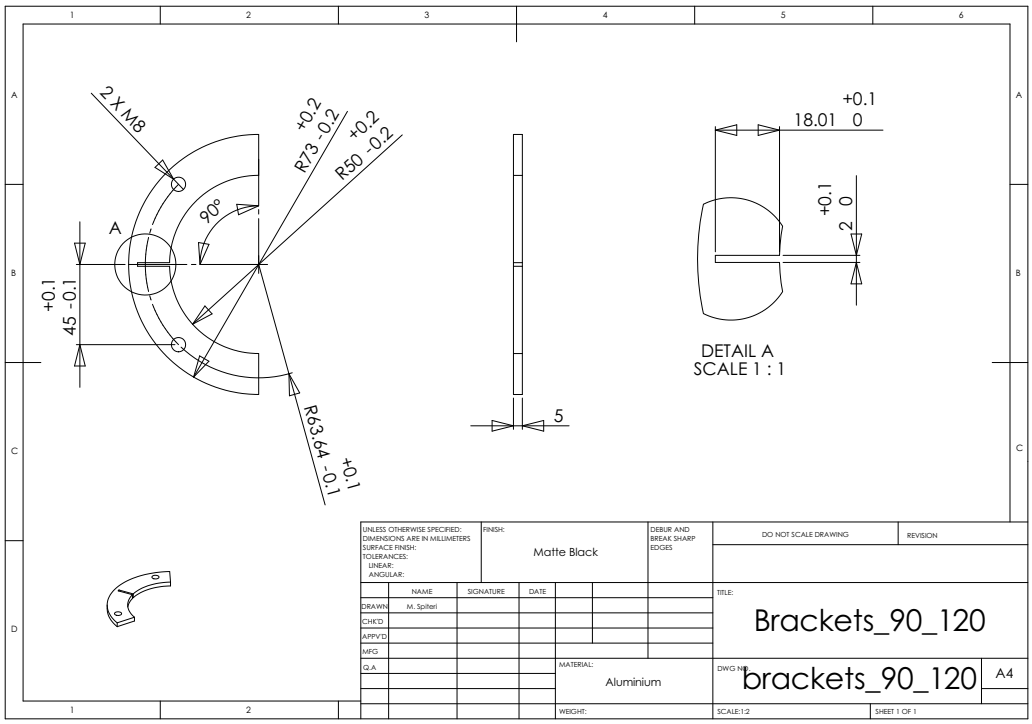
2 X M8
+0.2
R73 -0.2
+0.2
R50 -0.2
90°
A
+0.1
45 -0.1
R63.64 +0.1 -0.1
5
+0.1
18.01 0
+0.1
2 0
DETAIL A
SCALE 1 : 1
UNLESS OTHERWISE SPECIFIED:
DIMENSIONS ARE IN MILLIMETERS
SURFACE FINISH:
TOLERANCES:
LINEAR:
ANGULAR:
FINISH:
Matte Black
DEBUR AND BREAK SHARP EDGES
DO NOT SCALE DRAWING
REVISION
NAME
SIGNATURE
DATE
DRAWN
M. Spiteri
CHK'D
APP'V'D
MFG
Q.A
MATERIAL:
Aluminium
WEIGHT:
TITLE:
Brackets_90_120
DWG NO.
brackets_90_120
A4
SCALE:1:2
SHEET 1 OF 1

Appendix C

Technical Drawings of Fairing with Flow Control

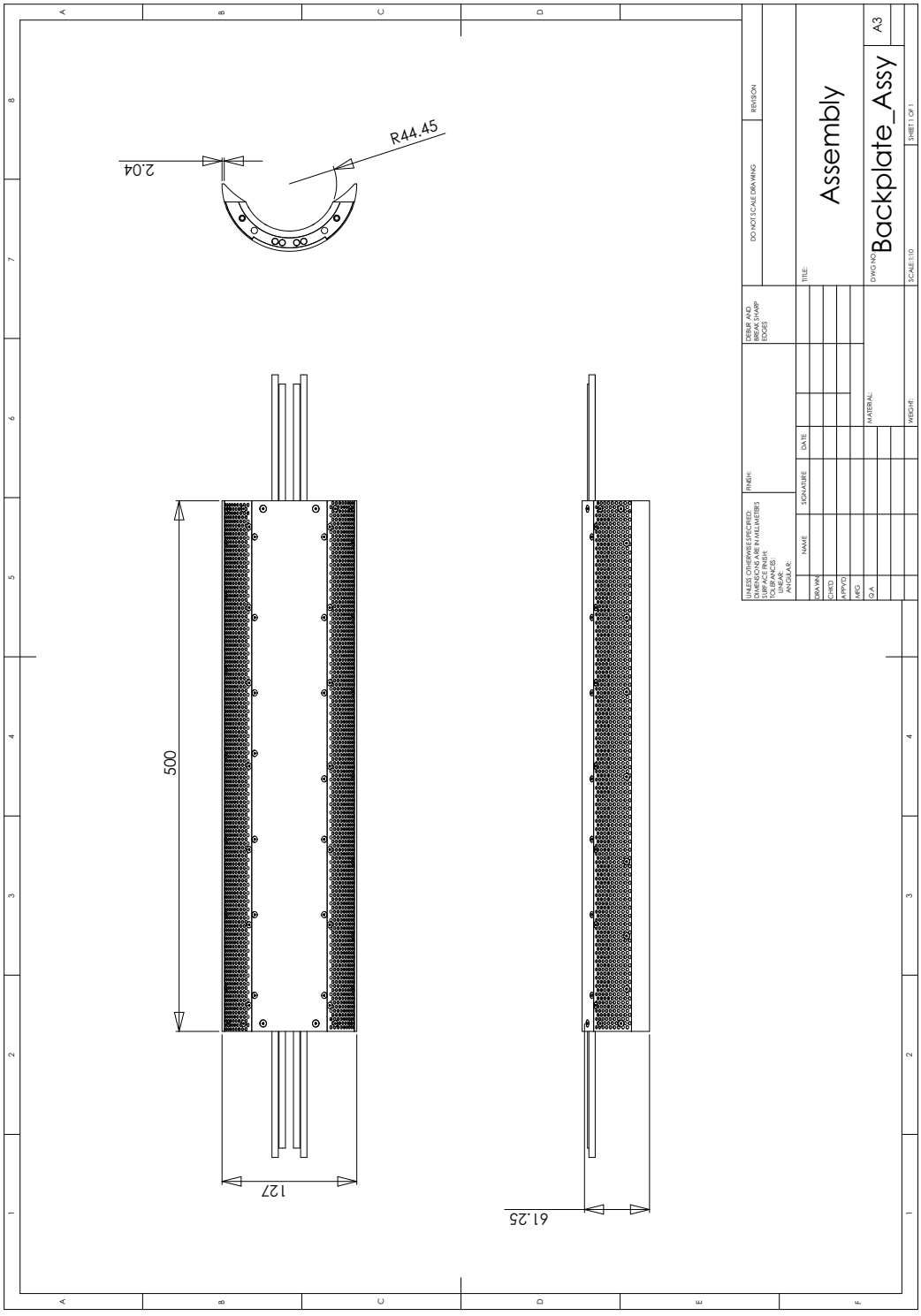
R44.45
2.04
500
127
61.25
Assembly
Backplate_Assy
A3
DO NOT SCALE DRAWING
REVISION
DEBUR AND BREAK SHARP EDGES
FINISH:
MATERIAL:
WEIGHT:
SCALE:1:10
SHEET 1 OF 1
DWG NO
TITLE:
UNLESS OTHERWISE SPECIFIED:
DIMENSIONS ARE IN MILLIMETERS
SURFACE FINISH:
TOLERANCES:
LINEAR:
ANGULAR:
NAME
SIGNATURE
DATE
DRAWN
CHK'D
APP'D
MFG
Q.A.

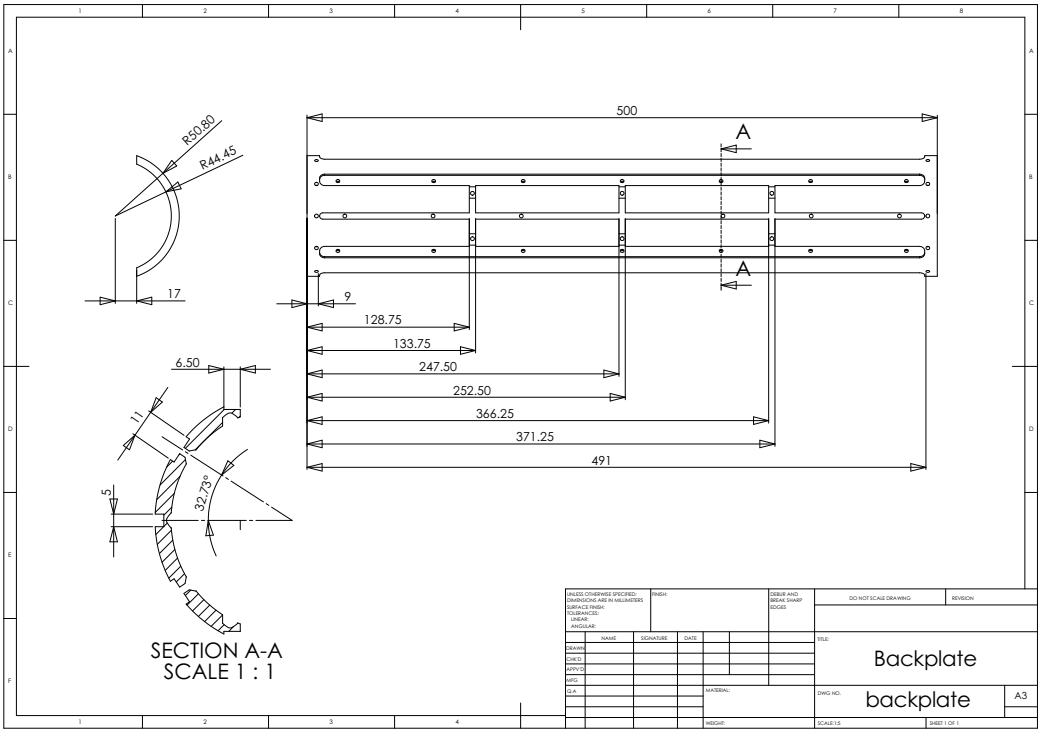
R50.80
R44.45
17
500
A
A
9
128.75
133.75
247.50
252.50
366.25
371.25
491
6.50
11
5
32.73°
SECTION A-A
SCALE 1 : 1
Backplate
backplate
A3

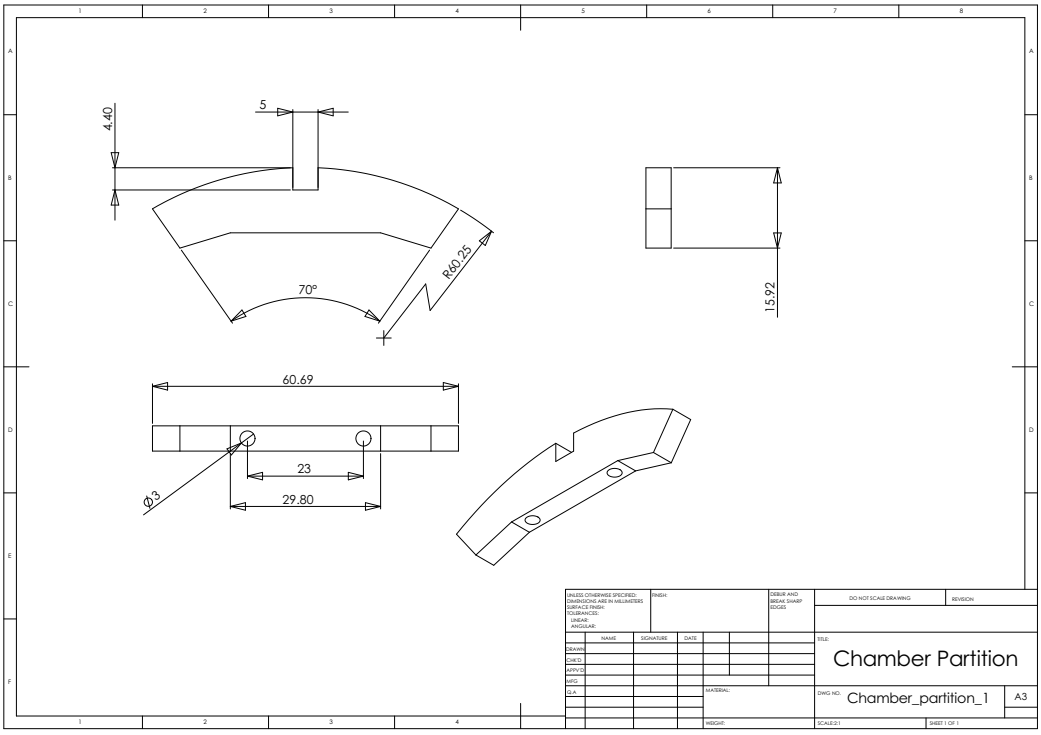
4.40
5
70°
R60.25
15.92
60.69
23
29.80
Ø3
Chamber Partition
Chamber_partition_1
A3

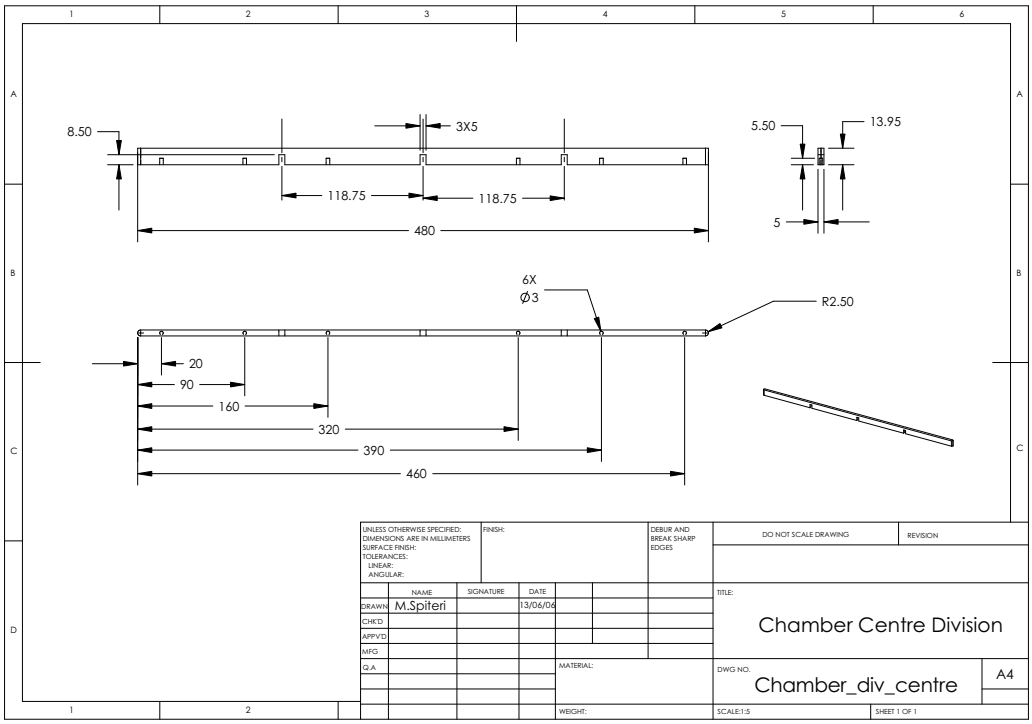
8.50
3X5
118.75
118.75
480
5.50
13.95
5
6X
Ø3
R2.50
20
90
160
320
390
460
UNLESS OTHERWISE SPECIFIED:
DIMENSIONS ARE IN MILLIMETERS
SURFACE FINISH:
TOLERANCES:
LINEAR:
ANGULAR:
FINISH:
DEBUR AND BREAK SHARP EDGES
DO NOT SCALE DRAWING
REVISION
NAME
SIGNATURE
DATE
DRAWN
M.Spiteri
13/06/06
CHK'D
APP'VD
MFG
Q.A
MATERIAL:
WEIGHT:
TITLE:
Chamber Centre Division
DWG NO.
Chamber_div_centre
A4
SCALE:1:5
SHEET 1 OF 1

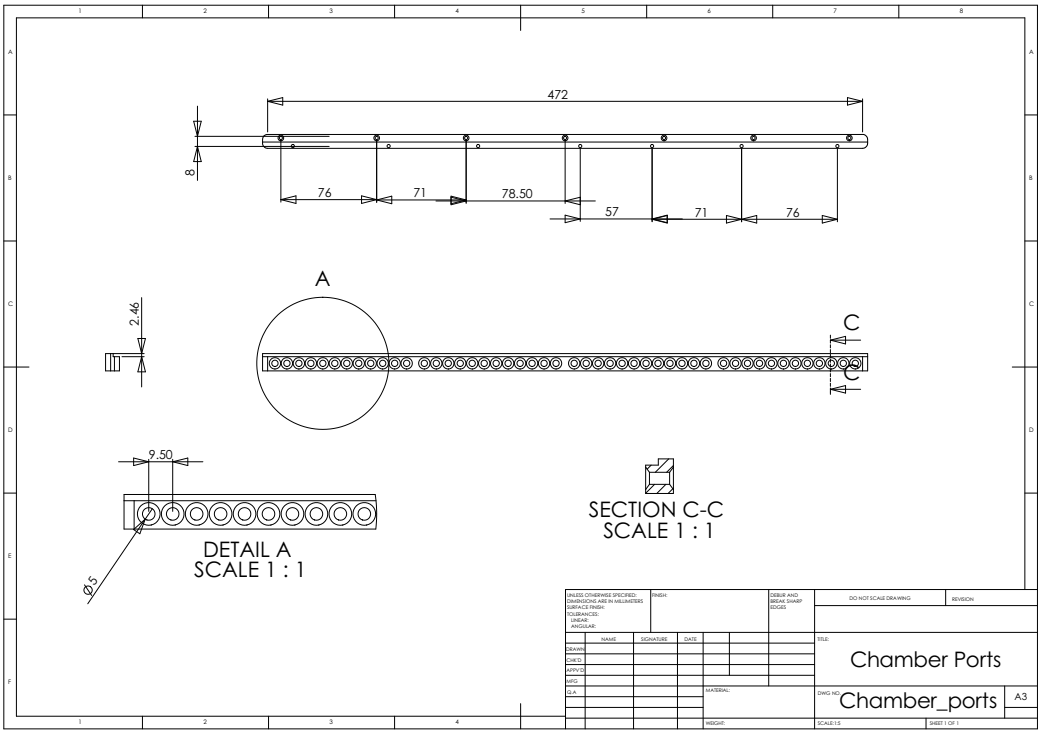
472
8
76
71
78.50
57
71
76
A
2.46
C
C
9.50
Ø5
DETAIL A
SCALE 1 : 1
SECTION C-C
SCALE 1 : 1
UNLESS OTHERWISE SPECIFIED:
DIMENSIONS ARE IN MILLIMETERS
SURFACE FINISH:
TOLERANCES:
LINEAR:
ANGULAR:
FINISH:
DEBUR AND BREAK SHARP EDGES
DO NOT SCALE DRAWING
REVISION
NAME
SIGNATURE
DATE
DRAWN
CHK'D
APP'VD
MFG
Q.A
MATERIAL:
WEIGHT:
TITLE:
Chamber Ports
DWG NO.
Chamber_ports
A3
SCALE:1:5
SHEET 1 OF 1

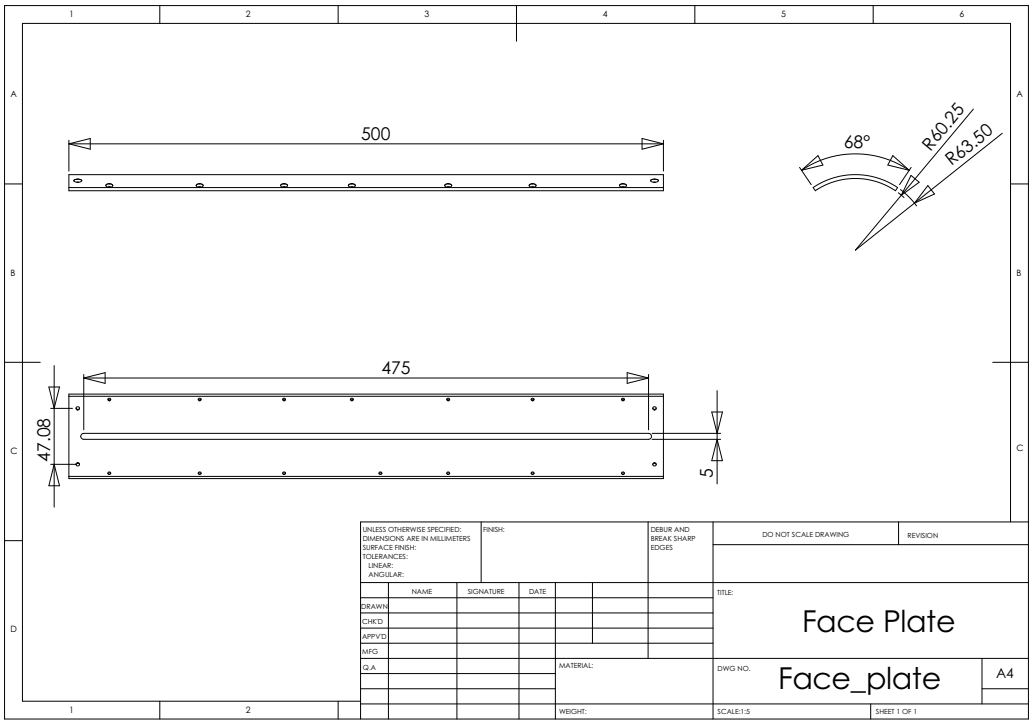
500
68°
R60.25
R63.50
475
47.08
5
UNLESS OTHERWISE SPECIFIED:
DIMENSIONS ARE IN MILLIMETERS
SURFACE FINISH:
TOLERANCES:
LINEAR:
ANGULAR:
FINISH:
DEBUR AND BREAK SHARP EDGES
DO NOT SCALE DRAWING
REVISION
NAME
SIGNATURE
DATE
DRAWN
CHK'D
APP'V'D
MFG
Q.A
MATERIAL:
WEIGHT:
TITLE:
Face Plate
DWG NO.
Face_plate
A4
SCALE:1:5
SHEET 1 OF 1

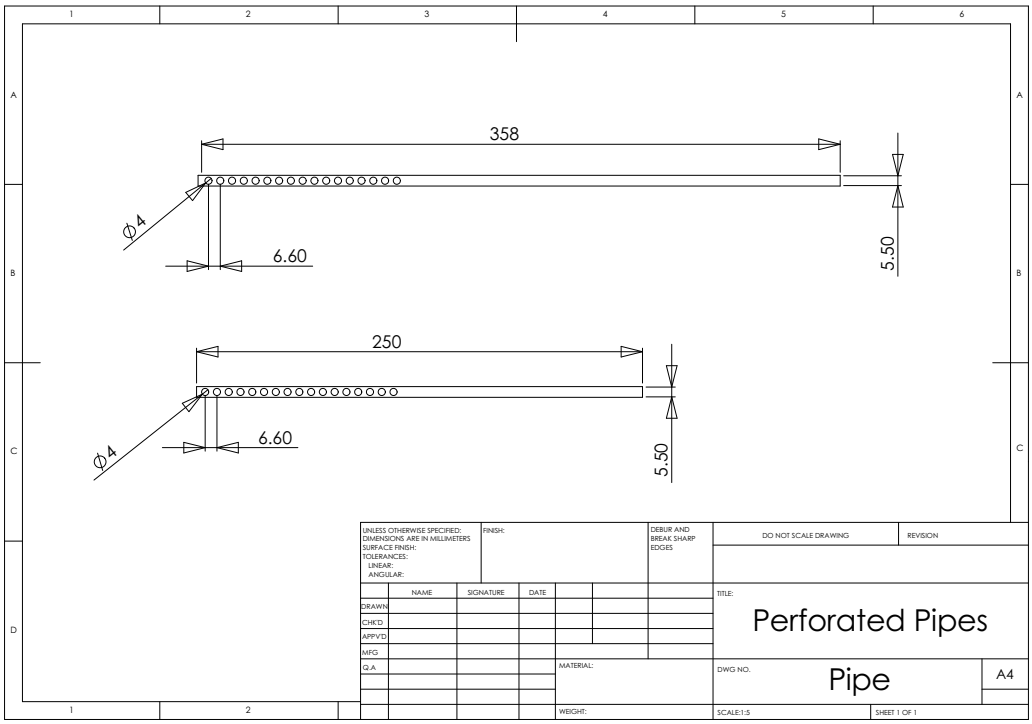
358
Ø4
6.60
5.50
250
Ø4
6.60
5.50
UNLESS OTHERWISE SPECIFIED:
DIMENSIONS ARE IN MILLIMETERS
SURFACE FINISH:
TOLERANCES:
LINEAR:
ANGULAR:
FINISH:
DEBUR AND BREAK SHARP EDGES
DO NOT SCALE DRAWING
REVISION
NAME
SIGNATURE
DATE
DRAWN
CHK'D
APP'V'D
MFG
Q.A
MATERIAL:
WEIGHT:
TITLE:
Perforated Pipes
DWG NO.
Pipe
A4
SCALE:1:5
SHEET 1 OF 1

Appendix D

Technical Drawings of H-Beam

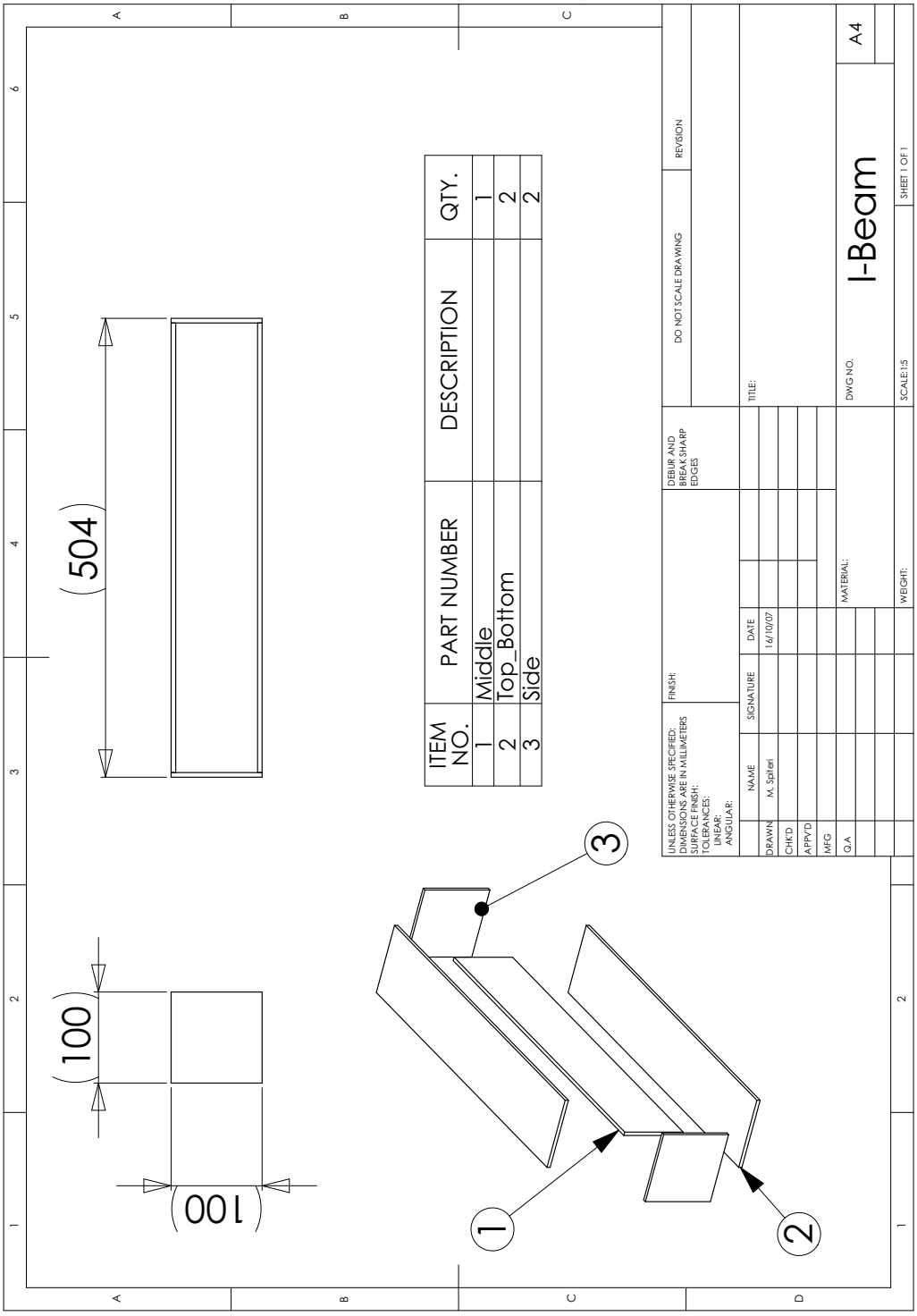
504
100
100
1
2
3
ITEM NO. | PART NUMBER | DESCRIPTION | QTY.
1 | Middle | | 1
2 | Top_Bottom | | 2
3 | Side | | 2
DO NOT SCALE DRAWING
REVISION
DEBUR AND BREAK SHARP EDGES
FINISH:
UNLESS OTHERWISE SPECIFIED:
DIMENSIONS ARE IN MILLIMETERS
SURFACE FINISH:
TOLERANCES:
LINEAR:
ANGULAR:
NAME | SIGNATURE | DATE
DRAWN M. Spiteri 16/10/07
CHK'D
APPV'D
MFG
Q.A
MATERIAL:
WEIGHT:
TITLE:
DWG NO. I-Beam
A4
SCALE:1:5
SHEET 1 OF 1

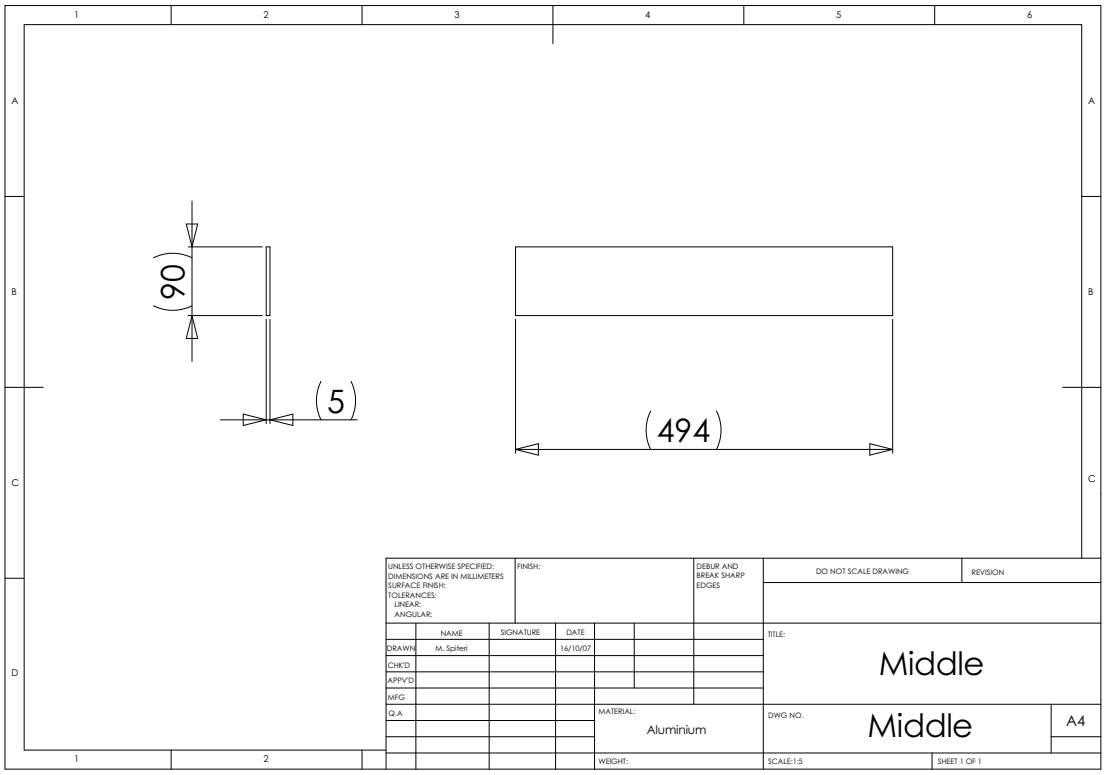
90
5
494
UNLESS OTHERWISE SPECIFIED:
DIMENSIONS ARE IN MILLIMETERS
SURFACE FINISH:
TOLERANCES:
LINEAR:
ANGULAR:
FINISH:
DEBUR AND BREAK SHARP EDGES
DO NOT SCALE DRAWING
REVISION
NAME
SIGNATURE
DATE
DRAWN
M. Spiteri
16/10/07
CHK'D
APPV'D
MFG
Q.A
TITLE:
Middle
MATERIAL:
Aluminium
DWG NO.
Middle
A4
WEIGHT:
SCALE:1:5
SHEET 1 OF 1

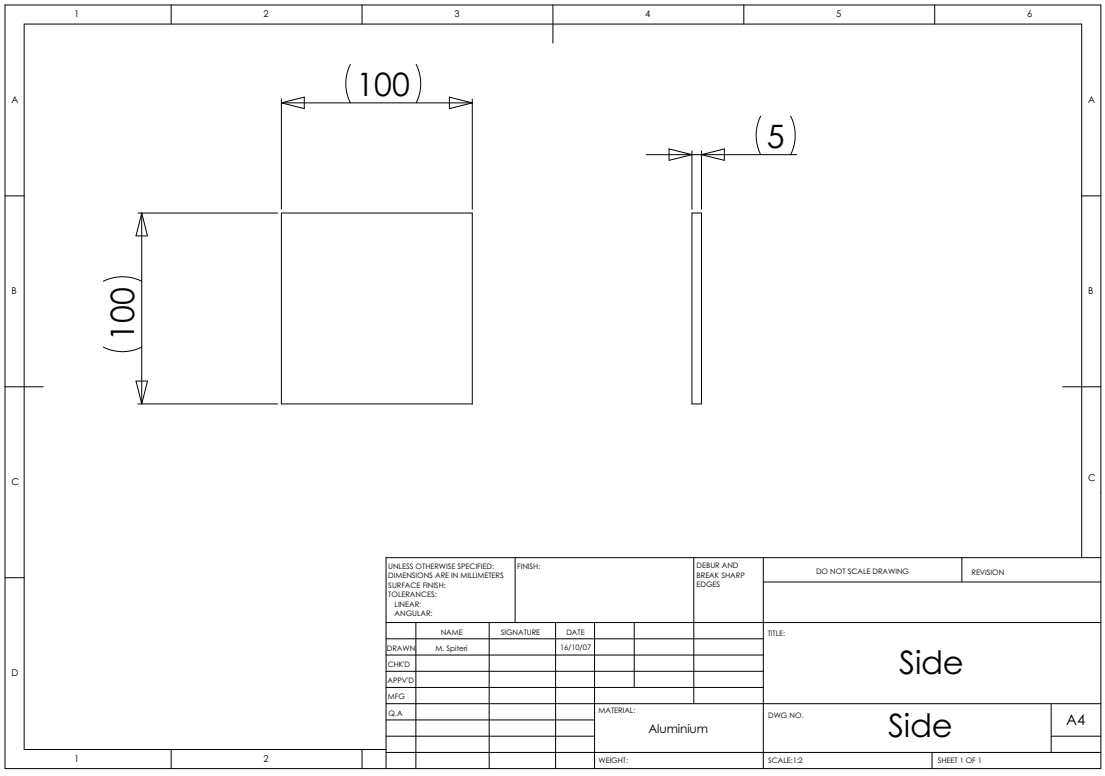
100
100
5
UNLESS OTHERWISE SPECIFIED:
DIMENSIONS ARE IN MILLIMETERS
SURFACE FINISH:
TOLERANCES:
LINEAR:
ANGULAR:
FINISH:
DEBUR AND BREAK SHARP EDGES
DO NOT SCALE DRAWING
REVISION
NAME
SIGNATURE
DATE
DRAWN
M. Spiteri
16/10/07
CHK'D
APPV'D
MFG
Q.A
TITLE:
Side
MATERIAL:
Aluminium
DWG NO.
Side
A4
WEIGHT:
SCALE:1:2
SHEET 1 OF 1

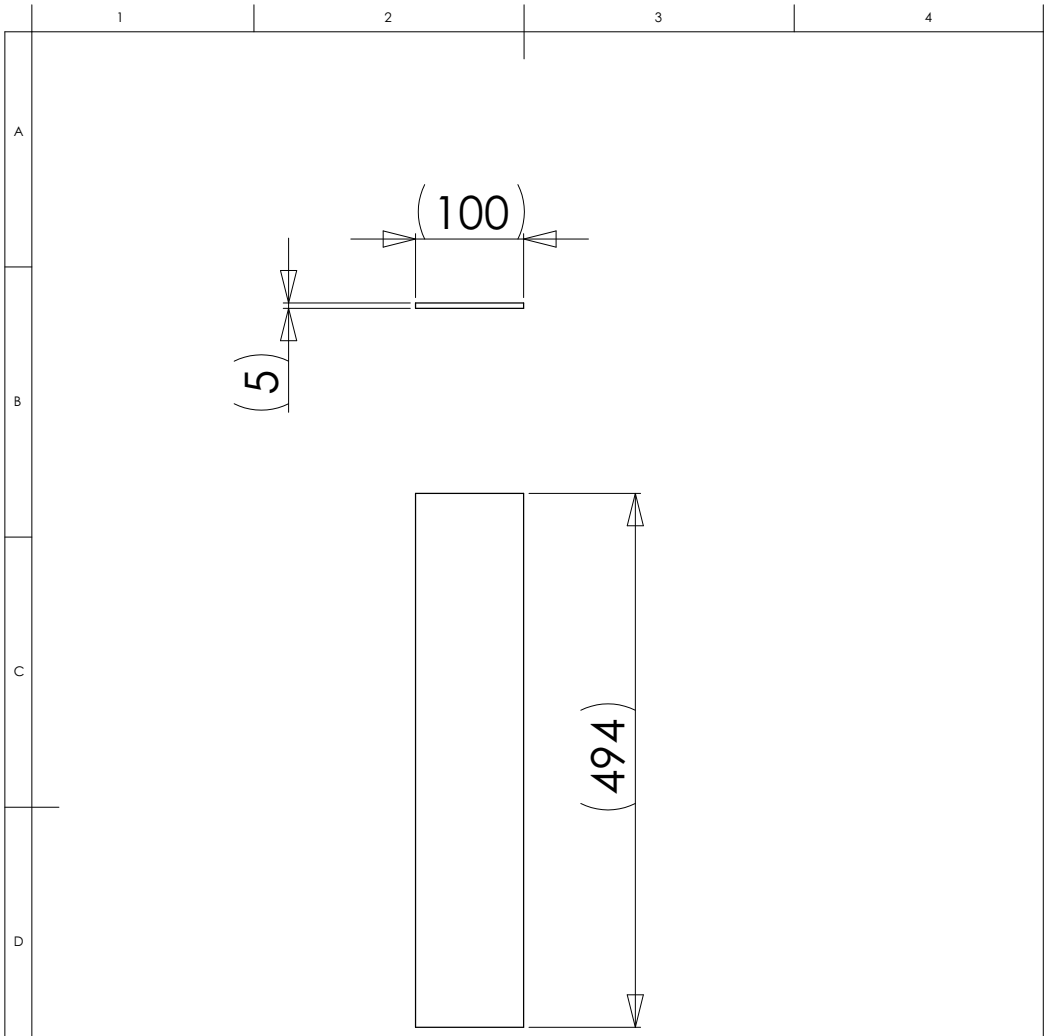

UNLESS OTHERWISE SPECIFIED: DIMENSIONS ARE IN MILLIMETERS SURFACE FINISH: TOLERANCES: LINEAR: ANGULAR:	FINISH:		DEBUR AND BREAK SHARP EDGES	DO NOT SCALE DRAWING	REVISION	
	NAME	SIGNATURE	DATE	TITLE:		
DRAWN	M. Spiteri		16/10/07	Top & Bottom		
CHK'D						
APPV'D						
MFG						
Q.A				MATERIAL: Aluminium	DWG NO. Top_Bottom	A4
				WEIGHT:	SCALE:1:5	SHEET 1 OF 1

References

[1] H.H. Heller and W.M. Dobrzynski. Sound radiation from aircraft wheel-well/landing-gear configuration. *Journal of Aircraft*, 14(2):768–774, 1977.

[2] R.L. Panton. *Incompressible flow*. Wiley-Interscience, 1984.

[3] J.H.M. Fransson, P. Koniecznyk, and P.H. Alfredsson. Flow around a porous cylinder subject to continuous suction or blowing. *Journal of Fluids and Structures*, 19:1031–1048, 2004.

[4] R.W. Stoker, Y. Guo, C. Streett, and N.J. Burnside. Airframe noise source location of a 777 aircraft in flight and comparisons with a past model scale test. *AIAA Paper*, 2003-3232, 2003.

[5] J.C. Ross. Progress in airframe noise reduction. *Canadian Aeronautics and Space Institute Annual Conference*, 2001.

[6] W.M. Dobrzynski, B. Schoning, L.C. Chow, C. Wood, M. Smith, and C. Seror. Design and testing of low noise landing gears. *AIAA Paper*, 2005-3008, 2005.

[7] W.M. Dobrzynski and H. Buchholz. Full-scale noise testing on airbus landing gears in the german dutch wind tunnel. *AIAA Paper*, 1997-1597, 1997.

[8] F.R. Grosche, G. Schneider, and H. Stiewitt. Wind tunnel experiments on airframe noise sources of transport aircraft. *AIAA Paper*, 1997-1642, 1997.

[9] J.F. Piet, L.C. Chow, F. Laporte, and H. Remy. Flight test investigation of high-lift devices and landing gear modifications to achieve airframe noise reduction. In *ECCOMAS, Jyvaeskylae, Finland*, 2004.

[10] J.F. Piet, R. Davy, G. Elias, H.A. Siller, L.C. Chow, C. Seror, and F. Laporte. Flight test investigation on add-on treatments to reduce aircraft airframe noise. *AIAA Paper*, 2005-3007, 2005.

[11] K. Boorsma, X. Zhang, and N. Molin. Perforated fairings for landing gear noise control. *AIAA Paper*, 2008-2961, 2008.

[12] M.J. Lighthill. On sound generation aerodynamically. I. general theory. *Proceedings of the Royal Society of London. Series A, Mathematical and Physical Sciences*, 211(1107):564–587, 1952.

[13] N. Curle. The influence of solid boundaries upon aerodynamic sound. *Proceedings of the Royal Society of London. Series A, Mathematical and Physical Sciences*, 231(1187):505–514, 1955.

[14] J.E. Ffowcs Williams and D.L. Hawkings. Sound generation by turbulence and surfaces in arbitrary motion. *Philosophical Transactions of the Royal Society of London*, 342:264–321, 1969.

[15] C.W. Horne, K.D. James, and B.L. Storms. Flow survey of the wake of a commercial transport main landing gear. 2002-2407, 2002.

[16] B.S. Lazos. Mean flow features around the inline wheels of four-wheel landing gear. *AIAA Paper*, 40(2):193–198, 2002.

[17] R.K. Amiet. Correction of open-jet wind tunnel measurments for shear layer refraction. *AIAA Paper*, 1975-532, 1975.

[18] G.J.J. Ruijgrok. *Elements of Aviation Acoustics*. Delft University Press, 1993.

[19] J. Piet and G. Elias. Airframe noise source localization using a microphone array. *AIAA Paper*, 1997-1643, 1997.

[20] S.M. Jaeger, N.J. Burnside, P.T. Soderman, W.C. Horne, and K.D. James. Array assessment of an isolated, 26% -scale, high-fidelity landing gear. *AIAA Paper*, 2002-2410, 2002.

[21] NN. *International standards and recommended practices, environmental protection, annex 16, the convention on international civil aviation*, volume 1, chapter Aircraft Noise. 3rd edition, 1993.

[22] Y.P. Guo, K.J. Yamamoto, and R.W. Stoker. An empirical model for landing gear noise prediction. *AIAA Paper*, 2004-2888, 2004.

[23] H.E. Bass, L.C. Sutherland, and A.J. Zuckerwar. Atmospheric absorption of sound: Update. *J. Acoust. Soc. Am.*, 88(4):2019–2021, 1990.

[24] Y. Guo. A statistical model for landing gear noise prediction. *AIAA Paper*, 2003-3227, 2003.

[25] M.R. Fink. Airframe noise prediction method. Technical Report 77-29, FAA-RD, 1979.

[26] M.G. Smith and L.C. Chow. Prediction method for aerodynamic noise from aircraft landing gear. *AIAA Paper*, 1998-2228, 1998.

[27] M.G. Smith and L.C. Chow. Validation of prediction model for aerodynamic noise from aircraft landing gear. *AIAA Paper*, 2002-2581, 2002.

[28] R. Franke, W. Rodi, and B. Schonung. Numerical calculation of laminar vortex-shedding flow past cylinders. *Journal of Wind Engineering and Industrial Aerodynamics*, 35:237–257, 1990.

[29] M.R. Visbal. Evolution of an implicit Navier-Stokes solver for some unsteady seperated flows. *AIAA Paper*, 1986-1053, 1986.

[30] R. Mittal and Balachandar. S. Effect of three-dimensionality on the lift and drag of nominally two-dimensional cylinders. *Physics of Fluids*, 7(8):1841–1865, 1995.

[31] A. Belov, A. Jameson, and L. Martinelli. Three dimensional unsteady incompressible flow calculations using multigrid. *AIAA Paper*, 1997-0443, 1997.

[32] S. Szepessy and P.W. Bearman. Aspect ratio and end plate effects on the vortex shedding from a circular cylinder. *Journal of Fluid Mechanics*, 234:191–127, 1992.

[33] L.S. Hedges, A.K. Travin, and P.R. Spalart. Detached-eddy simulation over a simplified landing gear. *Journal of Fluids Engineering*, 124:413–423, 2002.

[34] P.R. Spalart. Stratergies for turbulence modelling and simulations. *Int. J. Heat Fluid Flow*, 21:161–168, 2000.

[35] M.L. Shur, P.R. Spalart, M.KH. Strelets, and A.K. Travin. Detached-eddy simulation of an airfoil at high angle of attack. *Rodi, W., and Laurence, D. ecds. 4th Int. Symp. Eng. Turb. Modelling and Measurement, pp. 669-678. May 24, Corsica, Elsevier, Amsterdam*, 1999.

[36] J.S. Cox, C.L. Rumsey, K.S. Brenter, and A.B. Younis. Computation of sound generated by viscous flow over a circular cylinder. *NASA Technical Memorandum*, 110339, 1997.

[37] M.L. Shur, P.R. Spalart, M.KH. Strelets, and A.K. Travin. Navier-Stokes simulation of shedding turbulent flow past a circular cylinder and a cylinder with a backward splitter plate. Technical Report 1996, ECCOMAS, 1996.

[38] L. Mathelin, F. Bataille, and A. Lallemand. The effect of uniform blowing on the flow past a circular cylinder. *Journal of Fluids Engineering*, 124:452–464, 2002.

[39] D.P. Lockard, M.R. Khorrami, and F. Li. High resolution calculation of a simplified landing gear. 2004-2887, 2004.

[40] D.P. Lockard, M.R. Khorrami, and F. Li. Aeroacoustic analyisis of a simplified landing gear. *AIAA Paper*, 2003-3111, 2003.

[41] B.A. Singer and Y. Guo. Development of computational aeroacoustic tools for airframe noise calulations. *International Journal of Computational Fluid Dynamics*, 18(6):455–469, 2004.

[42] F.J. Souliez, L.N. Long, P.J. Morris, and A. Sharma. Landing gear aerodynamic noise prediction using unstructured grids. *International Journal of Aeroacoustics*, 1(2):115–135, 2002.

[43] W. Dobrzynski, L.C. Chow, P. Guion, and D. Shiells. A European study on landing gear airframe noise sources. *AIAA Paper*, 2000-1971, 2000.

[44] W. Dobrzynski, M. Pott-Pollenske, D. Foot, and M. Goodwin. Landing gears aerodynamic interaction noise. Technical Report 2004, ECCOMAS, 2004.

[45] M.S. Howe. *Theory of vortex sound*. Cambridge University Press, 1st edition, 2002.

[46] G.M. Lilley. The prediction of airframe noise and comparison with experiments. *Journal of Sound and Vibration*, 239(4):849–859, 2001.

[47] W. Dobrzynski, L.C. Chow, P. Guion, and D. Shiells. Research into landing gear airframe noise reduction. *AIAA Paper*, 2002-2409, 2002.

[48] V. Strouhal. Über eine be sondere art von tonerregung. *Annalen fur Physik und Chemie*, New Series 5:216–251, 1878.

[49] T. Kármán. Über der mechanismus des wiederstandes. *den ein bewegter Körper in einer Flüssigkeit erfahrt. Göttingen Nachrichten, Mathematisch-Physikalische Klasse*, 2:547–556, 1912.

[50] M.M. Zdravkovich. *Flow around circular cylinders*, volume 1: Fundamentals.

[51] C. Norberg. Fluctuating lift on a circular cylinder: Review and new measurements. *Journal of Fluids and Structures*, 17:57–96, 2003.

[52] E. Berger. Supression of vortex shedding and turbulence behind oscillating cylinders. *Physics of Fluids*, 10:S191–S193, 1967.

[53] C. Homescu, I.M. Navon, and Z. Li. Suppression of vortex shedding for flow around a circular cylinder using optimal control. *Int. J. Numer. Meth. Fluids*, 38:43–69, 2002.

[54] A.B. Wang, Z. Travnicek, and K.C. Chia. On the relationship of effective reynolds number and strouhal number for the laminar vortex shedding of a heated circular cylinder. *Physics of Fluids*, 12:1401–1410, 2000.

[55] T. Masouka, Y. Takatsu, K. Naganuma, and T. Tsuruta. Suppression of the Karman vortex street by wake heating. *Heat Transfer 1998, 11th IHTC, 5 Kyongju, Korea*, 12, 1998.

[56] K. Roussopoulos. Feedback control of vortex shedding at low reynolds numbers. *J. Fluid Mech.*, 248:267–296, 1993.

[57] D. S. Park, D. M. Ladd, and E. W. Hendricks. Feedback control of von Karman vortex shedding behind a circular cylinder at low reynolds numbers. *Phys. Fluids*, 6(7):2390–2405, 1994.

[58] A. Roshko. On the wake and drag of bluff bodies. *Journal of the Aeronautical Sciences*, 22:124–132, 1955.

[59] A. Roshko. Experiments on the flow past a circular cylinder at a very high reynolds number. *Journal of Fluid Mechanics*, 10:345–356, 1961.

[60] P.T. Takumaru and P.E. Dimotakis. Rotary oscillation control of a cylinder wake. *Journal of Fluid Mechanics*, 224:77–90, 1991.

[61] D. Shields and A. Leonard. Investigations of a drag reduction on a circular cylinder in rotary oscillation. *Journal of Mechanics*, 431:297–322, 2001.

[62] F.O. Thomas, A. Kozlov, and T.C. Corke. Plasma actuators for bluff body flow control. *AIAA Paper*, 2006-2845, 2006.

[63] F.O. Thomas, A. Kozlov, and T.C. Corke. Plasma actuators for landing gear noise control. *AIAA Paper*, 2005-3010, 2005.

[64] R.C. Pankhurst and M.A. Thwaites. Experiments on the flow past a porous circular cylinder fitted with a thwaites flat. *British Aernautical Research Council, Reports and Memoranda No. 2787*, 1950.

[65] D.G. Hurley and M.A. Thwaites. Investigations of a drag reduction on a circular cylinder in rotary oscillation. *British Aeronautical Research Council, Reports and Memoranda No. 2829*, 1951.

[66] L. Mathelin, F. Bataille, and A. Lallemand. Near wake of a circular cylinder submitted to blowing part 1-2. *Int. J. Heat Mass Transf.*, 44(19):3701–3719, 2000.

[67] A. Glezer and M. Amitay. Synthetic jets. *Annual Review of Fluid Mechanics*, 34:503–529, 2002.

[68] J.H. Gerrard. The mechanics of the formation region of vortices behind bluff bodies. *Journal of Fluid Mechanics*, 25:401–413, 1966.

[69] C.J. Apelt and G.S. West. The effects of wake splitter plates on bluff-body flow in the range $10^4 < r < 5 \times 10^4$. part 2. *Journal of Fluid Mechanics*, 71:145–160, 1975.

[70] A. Roshko. On the drag and shedding frequency of two-dimensional bluff bodies. *NACA TN no. 3169*, 1954.

[71] G.S. West and C.J. Apelt. The effects of tunnel blockage and aspect ratio on the mean flow past a circular cylinder with reynolds numbers between 10^4 and 10^5. *Journal of Fluid Mechanics*, 114:361–377, 1982.

[72] Y.C. Fung. Fluctuating lift and drag acting on a cylinder in a flow of supercritical reynolds number. *Journal of the Aerospace Science*, 27(11):801–814, 1960.

[73] ESDU 81039. Flow of liquids, pressure losses across orifice plates, perforated plates and thick orifice plates in ducts. Technical report, ESDU, 1982.

[74] R.J. Wells. Acoustical plenum chambers. *Noise Control*, 4:9–15, 1958.

[75] C. Cant, N. Hankins, R. Mason, and E. Lait. Design, construction and comissioning of a multifunctional aerodynamic facility. MEng group design project 2000, University of Southampton, School of Engineering Sciences, Ship Science Department, 2000.

[76] I.P. Castro. Hot wire anemometry with the Newcastle, NSW bridges. Technical report, November 2001.

[77] R.J. Pattenden. *An Investigation of the Flow Field around a Truncated Cylinder.* Phd disseration, University of Southampton, Faculty of Engineering, School of Engineering Sciences, Fluid Structure Interaction Research Group, April 2004.

[78] J.H. Gerrard. A disturbance sensitive Reynolds number range of the flow past a circular cylinder. *Journal of Fluid Mechanics*, 22:187–196, 1965.

[79] P.O.A.L. Davies. The new 7 by $5\frac{1}{2}$ ft. and 15 by 12 ft. low speed wind tunnel at the University of Southampton. Technical Report 202, A.A.S.U, 1961.

[80] T. Chong, P. Joseph, and P. Davies. Design of a quiet open-jet facility for the measurements of airfoil noise. *AIAA Paper*, 2007-3473, 2007.

[81] R.J. Moffat. Describing the uncertainties in experimental results. *Experimental Thermal and Fluid Science*, 1:3–17, 1988.

[82] E.I. Maina. *The development of passive flow control vortices.* PhD thesis, University of Southampton, 2004.

[83] B. Fenech and K. Takeda. Sotonarray: Southampton university wind tunnel microphone array system guide. Technical Report AFM 07/03, 2007.

[84] G.B. Brown. The vortex motion causing edge tones. *Proceeding of the Phyiscal Society*, 49(5):493–507, 1937.

[85] G.B. Brown. The mechanism of edge tone production. *Proceeding of the Phyiscal Society*, 49(5):508–521, 1937.

[86] P.A. Nelson. Noise generated by flow over perforated surface. *Journal of Sound and Vibration*, 83(1):11–26, 1982.

[87] D.C. Wilcox. *Turbulence Modeling for CFD.* Cambridge University Press, 2nd edition, 1992.

[88] J. Dacles-Mariani, G.G. Zilliac, J.S. Chow, and P. Bradshaw. Numerical/-experimental study of a wingtip vortex in the near field. *AIAA Journal*, 33(9):1561–1568, 1995.

[89] C.L. Rumsey, M.D. Sanetrik, R.T. Biedron, N.D. Melson, and E.B. Parlette. Efficiency and accuracy of time-accurate turbulent Navier-Stokes computations. *Computers and Fluids*, 25(2):217–236, 1996.

[90] A. Travin, M. Shur, M. Strelets, and P. Spalart. Detached-eddy simulations past a circular cylinder. *Flow, Turbulence and Combustion*, 63:293–313, 1999.

[91] P.R. Spalart. Young-person's guide to detached-eddy simulation grids. Technical report, 2001.

[92] Fluent Inc. *Fluent 6.0 User's Guide*, 2001.